Particle Therapy Co-Operative Group

PTCOG Report 1

PTCOG Publications Sub-Committee Task Group on Shielding Design and Radiation Safety of Charged Particle Therapy Facilities

PTCOG REPORT 1 (Final version, 15th January 2010)

SHIELDING DESIGN AND RADIATION SAFETY OF CHARGED PARTICLE THERAPY FACILITIES

PTCOG Publications Sub-Committee Task Group:

N.E. Ipe (Leader), Consultant, Shielding Design, Dosimetry & Radiation Protection, San Carlos, California, U.S.A.
G. Fehrenbacher, G.S.I. Darmstadt, Germany
I. Gudowska, Stockholm University, Sweden
H. Paganetti, Massachusetts General Hospital, Boston, Massachusetts, USA
J.M. Schippers, PSI, Villigen, Switzerland
S. Roesler, CERN, Geneva, Switzerland
Y. Uwamino, RIKEN, Saitama, Japan

Advisors

D. T. L. Jones, Proton Therapy Centre, Ružomberok, Slovak Republic and Department of Human Biology, University Cape Town, South Africa
A. Mazal, Institut Curie, Paris, France
A. Smith, M.D. Anderson Cancer Center, Houston, Texas, U.S.A.

Consultants

S. Ban, Radiation Science Center, High Energy Accelerator Research Organization (KEK), Japan
H. Yashima, Division of Nuclear Engineering Science, Research Reactor Institute, Kyoto University, Japan

SHIELDING DESIGN AND RADIATION SAFETY OF CHARGED PARTICLE THERAPY FACILITIES

CONTENTS

ACKNOWLEDGEMENTS

Dr. Nisy Elizabeth Ipe notes, "Sincere gratitude is expressed to the task group members for all their outstanding work and great efforts in writing the chapters and reviewing the report: to the advisors for reviewing the report; to the consultants for their contribution to Chapter 5; to Kory Stamper for her outstanding and timely editorial assistance; to Al Smith for his unwavering support and encouragement; and to the PTCOG Publications Subcommittee for giving me the opportunity to lead this effort."

Dr. Yoshitomo Uwamino would like to thank Prof. S. Ban, High Energy Accelerator Research Organization (KEK), and Dr. H. Yashima, Kyoto Univ. Research Reactor Institute, for their invaluable assistance in the writing of Chapter 5.

Dr. Jacobus Maarten Schippers notes, "At PSI, many people have been involved in the conceptual design and building of the systems described here and in understand the regulations. B. Amrein, A. Coray, G. Dzieglewski, A. Fuchs, C. Hilbes, M. Hofer, T. Korhonen, A. Mezger, and W. Roser are acknowledged for their help with the preparation of this overview and their valuable input and feedback. Based on the pioneering work of E. Pedroni, several of these people, as well as E. Egger, T. Lomax, M. Grossmann, G. Goitein, the group of S. Hirschberg, I. Jirousek, M. Rejzek, J. Verwey, and many others have contributed to the design of the concepts, analysis of risks, and the realization of the now working systems."

PREFACE

The current report on shielding and radiation protection for charged particle therapy facilities is the first report produced by the Publications Subcommittee of the Particle Therapy Co-Operative Group (PTCOG). The PTCOG Publications Subcommittee was authorized at the PTCOG 46 Steering Committee meeting in Wanjie, China, and has the following membership:

Co-Chairpersons:	Al Smith and Erik Blomquist
Members:	Masayuki Mumada
	Takashi Ogino
	Thomas Delaney
	Eugen Hug
	Carl Rossi
	Thomas Bortfeld
De Facto Members:	Hirohiko Tsujii, PTCOG Steering Committee Chariman
	Martin Jermann, PTCOG Secretary/Treasurer

The Publications Subcommittee was charged with defining topics of interest to PTCOG members and establishing Task Groups to develop reports on such topics. The first Task Group to be established was Task Group I: Shielding Design and Radiation Protection of Charged Particle Therapy Facilities. The Task Group has the following members:

Task Group Leader: Nisy Ipe, Shielding Consultant, San Carlos, CA USA

Task Group Members:

Georg Fehrenbacher, G.S.I., Darmstadt, Germany

Irena Gudowska, Stockholm University, Sweden

Harald Paganetti, Francis H. Burr Proton Therapy Center, Boston, MA, US

Jacobus Maarten Schippers, P.S.I., Switzerland

Stefan Roesler, CERN, Switzerland

Yoshitomo Uwamino, RIKEN, Japan

Task Group Advisers

Dan Jones, iThema Laboratory, S. Africa

Alejandro Mazal, Institut Curie, France

Al Smith, M. D. Anderson Cancer Center, USA

Consultants

Shuichi Ban, Radiation Science Center, High Energy Accelerator Research Organization (KEK), Japan

Hiroshi Yashima, Division of Nuclear Engineering Science, Research Reactor Institute, Kyoto University, Japan

The topic of shielding and radiation protection was proposed by a number of PTCOG members and was deemed to be important to all particle therapy facilities. The topic is, however, somewhat difficult to address due to the variety of particle accelerators, treatment delivery systems, and regulations encountered throughout the world. Because of these differences, some of the material in the report is, by necessity, more general than would have been the case if specific circumstances were being addressed.

We have tried, as far as possible, to describe modern and up-to-date methodology, procedures, and instrumentation used in shielding calculations and radiation measurements. That said, we have not attempted to be exhaustive and therefore have not covered every possible technique and every new technology. We have focused on the "tried and proven" with the assumption that this approach would provide the most useful document for particle therapy users and developers. It is our intent, however, to periodically update the document in order to keep it current with the latest thinking experience and technologies. The document is being published electronically and is available on the PTCOG web site: http://ptcog.web.psi.ch.

We encourage PTCOG members, and others, to send comments, critiques, and corrections to the address specified in the PTCOG Publication Subcommittee link on the PTCOG web site. We will attempt to address corrections in a timely manner. Comments and critiques will be addressed as time permits.

I am greatly appreciative of the work done by each of the Task Group members, consultants, and reviewers. Everyone involved in the production of this document has been a volunteer and therefore has not received any tangible compensation for their work. Everyone reading the document will realize that a tremendous amount of work went into each individual effort. I especially want to thank Nisy Ipe who organized and led this tremendous effort. The document was brought to conclusion on time and on zero budget (except for the services of the editorial assistant), in spite of the demands of her private consulting business. I would also like to acknowledge Kory Stamper for the editorial assistance.

Now that this initial effort has been brought to a successful conclusion, the Publications Subcommittee intends to identify other topics of general interest to the PTCOG community and publish additional reports. We look forward to your feedback and assistance.

Al Smith

September 2009

1. Introduction

Nisy Elizabeth Ipe

1.1 Brief Overview of Charged Particle Therapy Facilities

Charged particle therapy facilities might use protons and various ions such as helium, lithium, boron, carbon, nitrogen, oxygen, neon, and argon to treat malignant and nonmalignant diseases. Particle energies are required that allow penetration of 30 cm or more in tissue. In this report, the primary emphasis will be on protons and carbon ions. There are currently about thirty operational particle therapy facilities (both proton and carbon) worldwide (PTCOG, 2009). Another twenty-three facilities or so are in the planning, design, or construction stage at the time of writing this report.

A typical large particle therapy (PT) facility might consist of an injector, a cyclotron or a synchrotron to accelerate the particles, a high-energy beam transport line, several treatment rooms including fixed beam and 360° gantry rooms, and, often, a research area (ICRU, 2007). Recently, single-room therapy systems with a synchrocyclotron integrated in the treatment room have also become available. These and other novel technologies are discussed in Chapter 2. Several vendors offer single-room systems with the accelerator outside the treatment room; such facilities usually have the ability to add additional treatment rooms in future facility expansions. For both cyclotron- and synchrotron-based systems, dose rates of 1 to 2 Gy/min are typically used for patient treatment using "large" fields in the order of 30 cm x 30 cm. Special beam lines devoted to eye treatments use dose rates in the order of 15 to 20 Gy/min but for smaller fields of about 3 cm diameter. There are a few systems used specifically for radiosurgery techniques that use dose rates and field sizes intermediate to those for large field treatments and eye treatments.

During the operation of particle therapy facilities, secondary radiation is produced at locations where beam losses occur. Such losses may occur in the synchrotron and cyclotron along the beam line during injection, acceleration, extraction, energy degradation, and transport of the particles in the beam line to the treatment room, and in the beam shaping devices in the treatment nozzle. In addition, the deposition of beam proton interactions in the patient, beam stop, or dosimetry phantom also results in radiation production. Thus, the entire facility requires shielding. The interaction of protons and carbon ions with matter results in “prompt” and “residual” radiation. Prompt radiation persists only during the time that the beam is present. Residual radiation from activation continues after the beam is shut off. For charged particle therapy facilities, neutrons dominate the prompt radiation dose outside the shielding.

Proton energies in therapy facilities typically range from about 230 MeV to 250 MeV, while carbon ions may have maximum energies of 320 MeV u^{-1} to 430 MeV u^{-1}. For ions, it is customary to use the specific energy defined as the ratio of the total energy to the atomic mass number (MeV amu^{-1} or MeV u^{-1}) (NCRP, 2003). The specific energy is generally considered equivalent to the kinetic energy per nucleon. Because there are 12 carbon nucleons the total energy available for interactions is 5.16 GeV for 430 MeV u^{-1} carbon ions. Thus, the maximum neutron energy will exceed 430 MeV in this case. For carbon ion beams, the maximum energy of the neutrons is approximately two times the energy of the carbon ion (Kurosawa *et al.*, 1999). For proton beams, the neutron energies extend to a maximum, which is the energy of the incident proton.

Figure 1.1 shows a schematic of a cyclotron-based PT facility capable of accelerating protons or carbon ions. Figure 1.2 shows an example of a synchrotron-based PT facility.

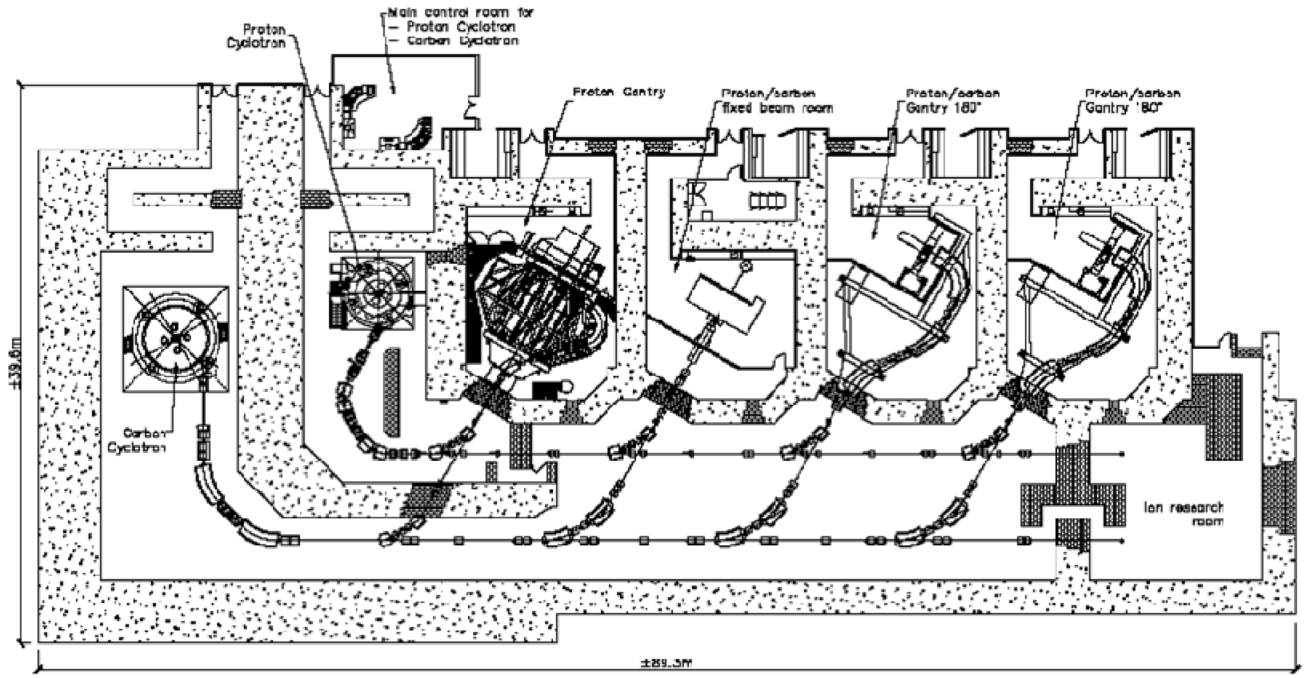

Figure 1.1. Schematic of a cyclotron-based particle therapy facility (Courtesy of IBA[1])

[1] Ion Beam Applications, Belgium

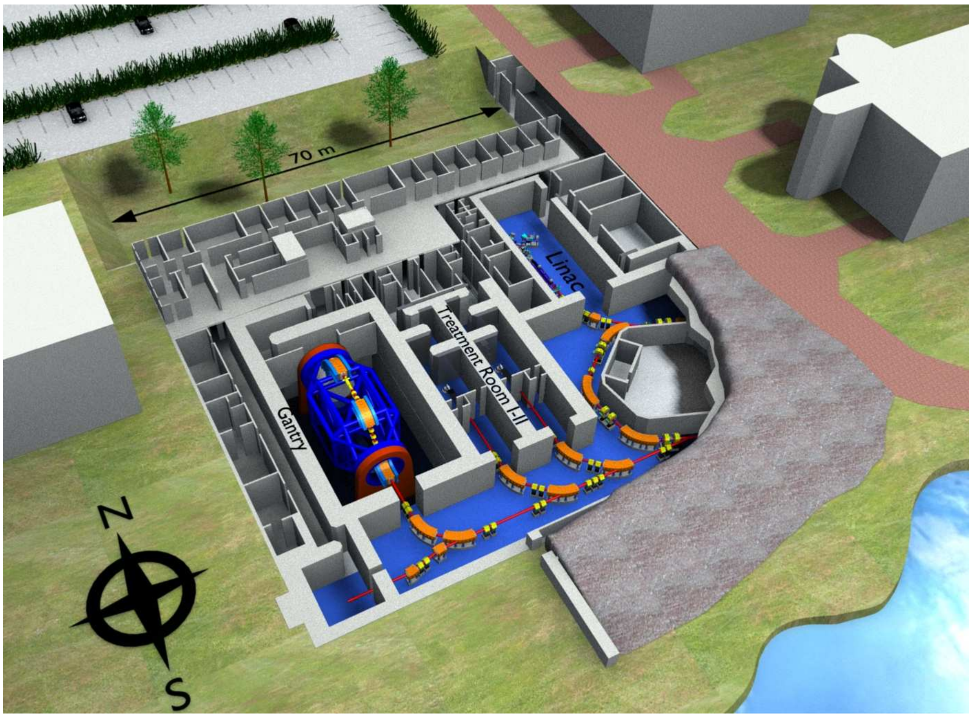

Figure 1.2. Heidelberg Ion Therapy Center (Courtesy of G. Fehrenbacher)

1.2 Overview of Particle Accelerator Shielding

The history of particle accelerator shielding dates back to the 1930s, with the construction and operation of particle accelerators at Cambridge by Cockroft and Walton, and at Berkeley by Lawrence and Livingstone (Stevenson, 1999; IAEA, 1988). The early accelerators were of low energy and intensity, and many of them were constructed underground. However, as larger accelerators producing particles with much higher energies were developed (*e.g.*, the Cosmotron at Brookhaven and the Bevatron at Berkeley), knowledge of the prompt radiation fields and the requirements for effective shielding design became necessary. An understanding of the generation of prompt and residual radiation requires knowledge of the nuclear reactions that occur in the energy range of interest. These are discussed in Chapter 2.

The prompt radiation field produced by protons (67 MeV to 250 MeV) encountered in proton therapy is quite complex, consisting of a mixture of charged and neutral particles as well as photons. When these protons react with matter, a hadronic or nuclear cascade (spray of particles) is produced in which neutrons have energies as high as the proton energy (ICRU, 2000). Further discussion can be found in Chapter 2. This high-energy component with neutron energies (E_n) above 100 MeV propagates the neutrons through the shielding; and continuously regenerates lower-energy neutrons and charged particles at all depths in the shield *via* inelastic reactions with the shielding material (Moritz, 2001). Thus, the neutron energy distribution consists of two components, high-energy neutrons produced by the cascade and evaporation neutrons with energy peaked at ~ 2 MeV. The high-energy neutrons are forward peaked but the evaporation neutrons are isotropic. The highest-energy neutrons detected outside the shielding are those that arrive without interaction, or that have undergone only elastic scattering or direct inelastic scattering with little loss of energy, and a small change in direction. Low-energy neutrons and charged particles detected outside the shielding are those that have been generated at the outer surface of the shield. Thus, the yield of high-energy neutrons (E_n > 100 MeV) in the primary collision of the protons with the target material determines the magnitude of the prompt radiation field outside the shield for intermediate-energy protons. The high-energy neutrons are anisotropic and are forward peaked. In the therapeutic energy range of interest, the charged particles produced by the protons will be absorbed in shielding that is sufficiently thick to protect against neutrons. Thus, neutrons dominate the radiation field outside the shielding. Degraded neutrons might undergo capture reactions in the shielding, giving rise to neutron-capture gamma rays.

The prompt radiation field produced by carbon ions is also dominated by neutrons with much higher energies than is the case with protons. Dose contributions from pions, protons, and photons are significantly lower than from neutrons. Additional information is provided in Chapter 2.

The goal of shielding is to attenuate secondary radiation to levels that are within regulatory or design limits for individual exposure, and to protect equipment from radiation damage, which should be done at a reasonable cost and without compromising the use of the accelerator for its intended purpose (Stevenson, 2001). This requires knowledge of the following parameters (Ipe, 2008), some of which are discussed in detail in Chapter 3.

1. Accelerator type, particle type, and maximum energy
2. Beam losses and targets
3. Beam-on time
4. Beam shaping and delivery
5. Regulatory and design limits
6. Workload, including number of patients to be treated, energies for treatment, field sizes, dose per treatment

7. Use factors
8. Occupancy factors

There are several powerful computer codes discussed in Chapter 6 that are capable of providing detailed spatial distributions of dose equivalent outside the shielding. However, it is often desirable to perform simpler calculations, especially during the schematic design of the facility. Shielding can be estimated over a wide range of thickness by the following equation for a point source, which combines the inverse square law and an exponential attenuation through the shield, and is independent of geometry (Agosteo *et al.*, 1996a):

$$H(E_p, \theta, d/\lambda(\theta)) = \frac{H_0(E_p, \theta)}{r^2} \exp\left[-\frac{d}{\lambda(\theta) g(\theta)}\right] \quad (1.1)$$

where:

H is the dose equivalent outside the shielding;

H_0 is source term at a production angle θ with respect to the incident beam and is assumed to be geometry independent;

E_p is the energy of the incident particle;

r is the distance between the target and the point at which the dose equivalent is scored;

d is the thickness of the shield;

$d/g(\theta)$ is the slant thickness of the shield at an angle θ;

$\lambda(\theta)$ is the attenuation length for dose equivalent at an angle θ and is defined as the penetration distance in which the intensity of the radiation is attenuated by a factor of e;

$g(\theta) = \cos\theta$ for forward shielding;

$g(\theta) = \sin\theta$ for lateral shielding;

$g(\theta) = 1$ for spherical geometry.

Approximation of the radiation transmission by an exponential function works well over a limited range of thickness (NCRP, 2003). The attenuation length is usually expressed in cm (or m) and in g cm^{-2} (or kg m^{-2}) when multiplied by the density (ρ) and will be referred to hereafter as λ. For thicknesses (ρd) that are less than ~ 100 g cm^{-2}, the value of λ changes with increasing depth in the shield because the "softer" radiations are more easily attenuated, and the neutron spectrum hardens. Figure 1.3 shows the variation of attenuation length ($\rho\lambda$) for monoenergetic neutrons in concrete as a function of energy. The attenuation length increases with increasing neutron energy at energies greater than ~ 20 MeV . In the past, it has typically been assumed that the attenuation length reaches a high-energy limiting value of about 120 g cm$^{-2.}$, even though the data in Fig. 1.3 show a slightly increasing trend above 200 MeV.

Figures 1.4a and 1.4b show the comparison of neutron dose attenuation lengths measured at various facilities, for concrete and iron, respectively, as a function of the effective maximum energy (E_{max}) of the source neutrons, for neutrons with energies from thermal to maximum. Figures 1.5a and 1.5b show the comparison of neutron dose attenuation lengths measured at various facilities, for concrete and iron, respectively, as a function of the effective maximum energy (E_{max}) of the source neutrons, for neutrons with energies greater than 20 MeV. As expected, the attenuation lengths in the latter case are larger than for neutrons with energies greater than thermal energy. The experiments are described in a paper by Nakamura and include measurements for E_{max} ranging from 22 MeV to 700 MeV, and various production angles for a variety of neutron sources (Nakamura, 2004). Table 1.1 summarizes the site and properties of the neutron source, shielding material, and the detectors. According to Nakamura, the measured neutron dose attenuation length (thermal to maximum energy) for concrete lies between 30 g cm^{-2} and 40 g cm^{-2} from about 22 MeV to 65 MeV in the forward direction and then gradually increases above 100 MeV to a maximum value of about 130 g cm^{-2}, which may be the high-energy limit. For 400 MeV u^{-1} carbon ions, the measured attenuation length in the forward direction for concrete (0° production angle) for a maximum neutron energy of 700 MeV is 126 ± 9 g cm^{-2}, while the calculated value is 115.2 ± 9 g cm^{-2}. The corresponding measured and calculated attenuation lengths for iron in the forward direction were 211± 9 g cm^{-2}, and 209.2 ± 1.5 g cm^{-2}, respectively. Monte Carlo calculations by Ipe and Fasso (Ipe and Fasso, 2006) yielded a total dose (from all particles) attenuation length in the forward direction of 123.8± 0.5 g cm^{-2} for 430 Mev u^{-1} carbon ions in concrete. Steel is much more effective than concrete for the shielding of high-energy neutrons. It is important to note that, in addition to energy and production angle (θ), λ also depends upon the material composition and density. Monte Carlo calculations by Ipe indicate that, for concrete, shielding for 250 MeV protons in the forward direction can differ by about 30 cm for shielding thicknesses of the order of 2 m to 3 m when two concretes with the same density but differing compositions are used. Thus, all concretes will not have the same λ at a given angle and energy, and the differences can be quite pronounced, especially in the forward direction for concretes with different compositions and densities. More information on shielding is provided in Chapter 3.

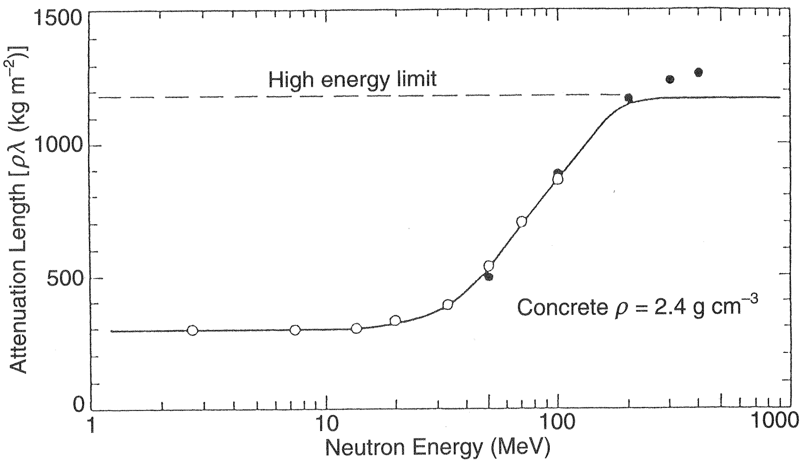

Figure 1.3. The variation of attenuation length ($\rho\lambda$) for monoenergetic neutrons in concrete of density ρ = 2400 kg m^{-3} (NCRP, 2003). Reprinted with permission of the National Council on Radiation Protection and Measurements, http://NCRPonline.org

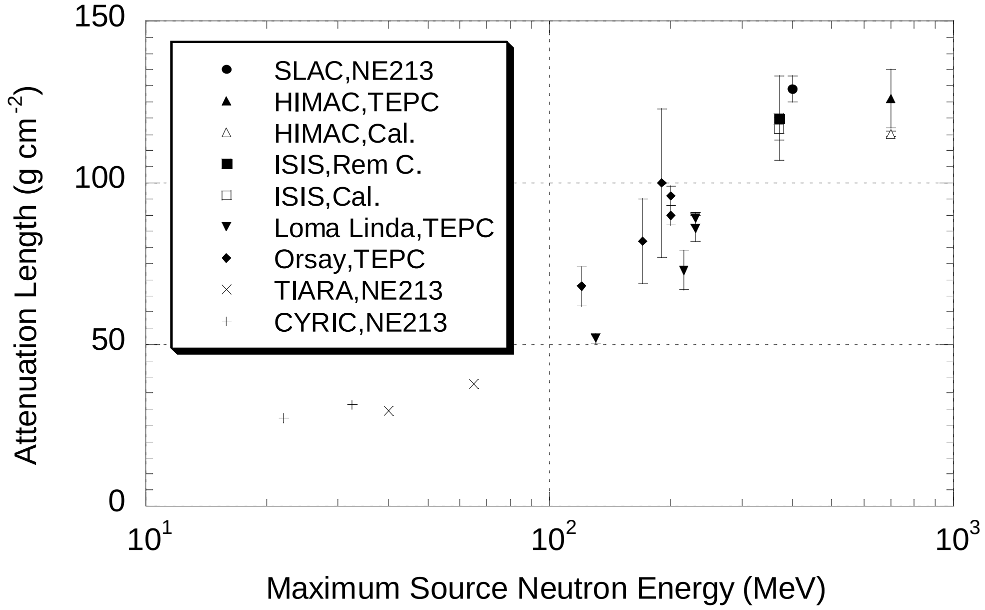

Figure 1.4a. Comparison of measured neutron dose attenuation lengths in concrete for neutrons of energy from thermal to maximum source energy (Nakamura, 2004)

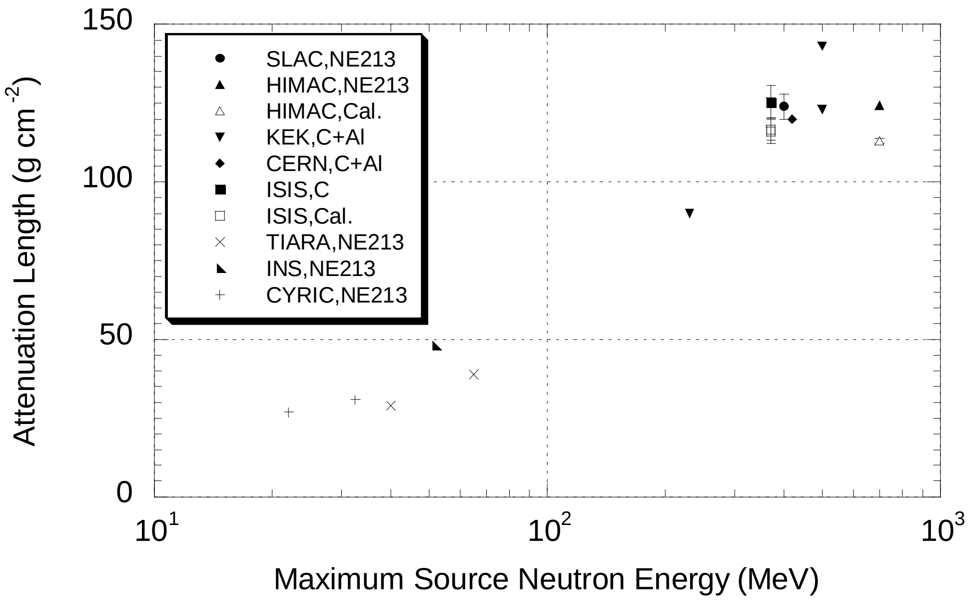

Figure 1.4b. Comparison of measured neutron dose attenuation lengths in concrete for neutrons of energy greater than 20 MeV (Nakamura, 2004)

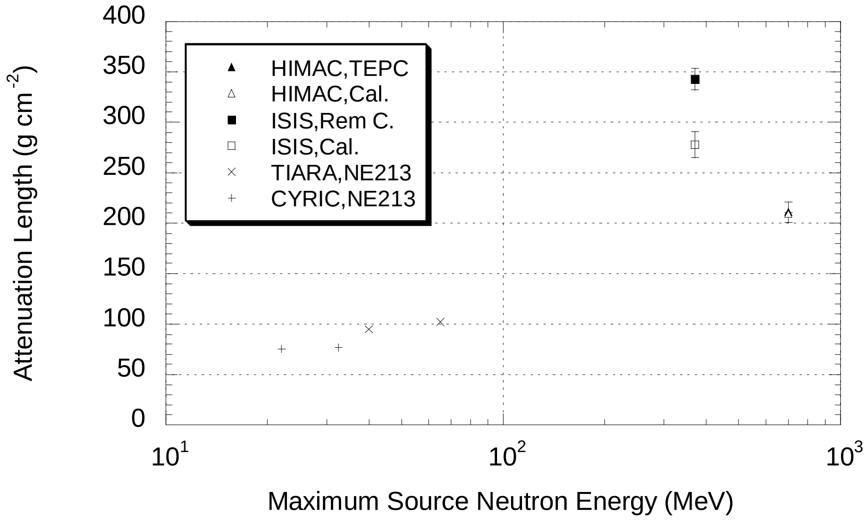

Figure 1.5a. Comparison of measured neutron dose attenuation lengths in iron for neutrons with energy from thermal to maximum source energy (Nakamura, 2004)

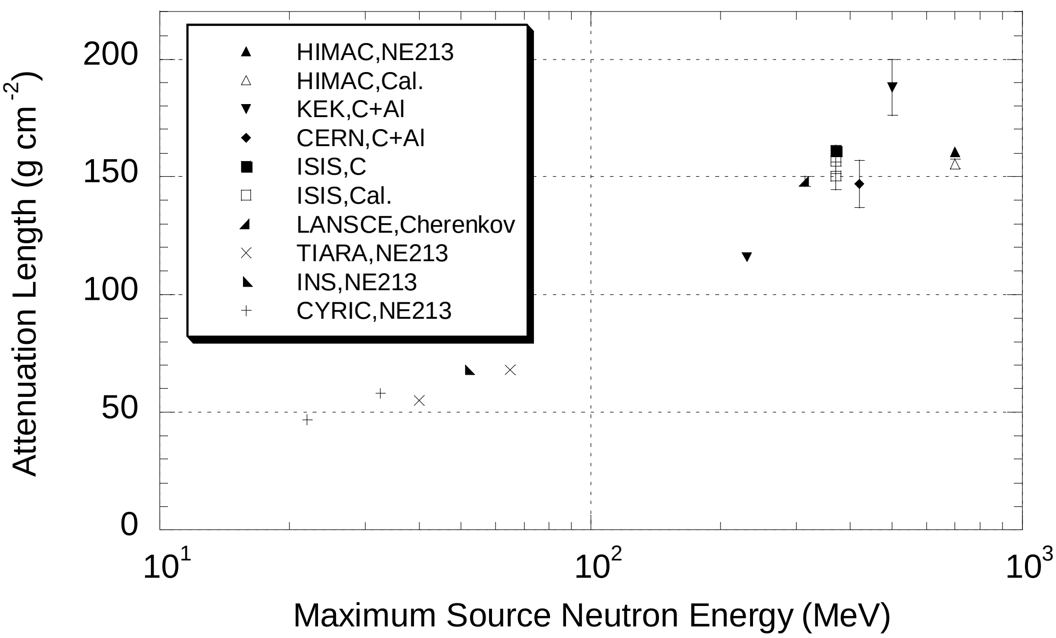

Figure 1.5b. Comparison of measured neutron dose attenuation lengths in iron for neutrons with energy greater than 20 MeV (Nakamura, 2004)

Table 1.1. Summary of site, neutron source, shielding material, and detector properties

Site	Projectile	Target (thickness)	Neutron source and measured angle	Shield material (thickness)	Detector
Cyclotron and Radioisotope Center (CYRIC), Tohoko University, Japan	25 , 35 MeV proton	Li (2 mm)	Quasi-monoenergetic collimated beam at 0°	Concrete (10 cm to 40 cm) Iron (25 cm to100 cm)	NE213 proton recoil proportional counter Bonner Ball with ^{3}He counter
TIARA proton cyclotron facility, Japan Atomic Energy Research Institute (JAERI), Japan	43 MeV proton	Li (3.6 mm)	Quasi-monoenergetic collimated beam at 0°	Concrete (25 cm to 200 cm) Iron (10 to 30 cm)	BC501A Bonner Ball with ^{3}He counter
	68 MeV proton	Li (5.2 mm)			
Loma Linda University Medical Center, U.S.A.	230 MeV proton	Al, Fe, Pb (stopping length, 10.2- cm diameter)	White spectrum (0°, 22°, 45°, 90°)	Concrete (39 g cm^{-2} 515 g cm^{-2} , 1.88 g cm^{-3} density)	Tissue Equivalent Proportional Counter (TEPC)
Orsay Proton Therapy Center, France	200 MeV proton	Al (15 cm long, 9 cm diameter) Water (20 cm x 20 cm x 32 cm)	White spectrum (0°, 22°, 45°, 67.5°, 90°)	Concrete (0 cm to 300 cm)	Ion chamber TEPC Rem counter Rem counter with lead (LINUS) LiF TLD with moderators
HIMAC, National Institute of Radiological Sciences (NIRS), Japan	400 MeV u^{-1} C	Cu (10 cm x 10 cm x 5 cm)	White spectrum (0°)	Concrete (50 cm to 200 cm) Iron (20 cm to 100 cm)	TEPC NE213 Activation detectors (Bi, C) Self-Time of Flight (TOF) detector
National Superconducting Cyclotron Laboratory (NSCL), U.S.A.	155 MeV u^{-1} He, C, O	Hevimet (5.08 cm x 5.093 cm)	White spectrum (44°-94°)	Concrete (308 to 1057 g cm^{-2} , 2.4 g cm^{-3} density)	Bonner Ball with LiI (Eu)
TRIUMF, Canada	500 MeV proton		White spectrum	Concrete	Bonner Ball with LiI (Eu) ^{11}C activation of NE102A
KENS, High Energy Accelerator Research Organization (KEK), Japan	500 MeV proton	W (stopping length)	White spectrum (0°)	Concrete(0 m to 4 m)	Activation detectors (Bi, Al, Au)
LANSCE, Los Alamos National Laboratory (LANL), U.S.A.	800 MeV proton	Cu (60 cm long, 21 cm diameter)	White spectrum (90°)	Iron (4 to 5 m)	6 ton water Cherenkov detector
ISIS, Rutherford Appleton Laboratory (RAL), U.K.	800 MeV proton	Ta (30 cm long, 9 cm diameter)	White spectrum (90°)	Concrete (20 cm to 120 cm) Iron (10 cm to 60 cm) After 284 cm thick iron and 97 cm thick concrete	Bonner Ball with LiI (Eu) Rem counter
AGS, Brookhaven National Laboratory, U.S.A.	1.6, 12, 24 GeV proton	Hg (130 cm long, 20 cm diameter)	White spectrum (0°)	Steel (0 m to 3.7 m)	Activation detectors (Bi, Al, Au)
			White spectrum (90°)	Concrete (0 m to 5 m) Steel (0 to 3.3 m)	
SLAC, Stanford National Accelerator Laboratory, U.S.A.	28.7 GeV electron	Al (145 cm long, 30 cm diameter)	White spectrum (90°)	Concrete (274, 335, 396 cm)	NE213 Bonner Ball with LiI (Eu)
CERN, Switzerland	120, 205 GeV/c proton	Cu (50 cm long, 7 cm diameter)	White spectrum (90°)	Iron (40 cm) Concrete (80 cm)	TEPC (HANDI) Bonner Ball with LiI (Eu) LINUS ^{209}Bi and ^{232}Th fission chambers
	160 Gev u^{-1} lead	Pb	White spectrum	Concrete	

The attenuation length of neutrons in the shielding material determines the thickness of shielding that is required to reduce the dose to acceptable levels. Shielding for neutrons must be such that sufficient material is interposed between the source and the point of interest, and neutrons of all energies must be attenuated effectively (Moritz, 2001). Dense material of high-atomic mass such as steel meets the first criterion, and hydrogen meets the second criterion because of effective attenuation by elastic scattering. However, steel is transparent to neutrons of energy ~ 0.2 MeV to 0.3 MeV. Therefore, a layer of hydrogenous material must always follow the steel. Alternatively, large thicknesses of concrete or concrete with high-z aggregates can be used as discussed in Chapter 3.

1.3 Dose Quantities and Conversion Coefficients

1.3.1 Protection and Operational Dose Quantities

The interaction of radiation with matter is comprised of a series of events (collisions) in which the particle energy is dissipated and finally deposited in matter. The dose quantities that are used in shielding calculations and radiation monitoring are discussed below.

Shielding calculations and radiation monitoring are performed solely for radiation protection. The former are performed to ensure that the facility is designed so that exposures of personnel and the public are within regulatory limits. The latter is performed to demonstrate compliance with design or regulatory limits (NCRP, 2003). Thus, the calculations and measurements must be expressed in terms of quantities in which the limits are defined. The International Commission on Radiological Protection (ICRP) defines dose limits. They are expressed in terms of protection quantities measured in the human body. Compliance with these limits can be demonstrated by measurement of the appropriate operational quantity defined by the International Commissions on Radiological Units and Measurements (ICRU).

ICRP Publication 60 (ICRP, 1991) recommended the use of equivalent dose (H_T) and effective dose (E) as protection quantities. However, these quantities are not directly measurable. For external individual exposure the accepted convention is the use of operational quantities, ambient dose equivalent $H^*(d)$, the directional dose equivalent $H(d,\Omega)$, and personal dose equivalent $H_p(d)$, defined by ICRU. The two sets of quantities might be related to the particle fluence and, in turn, by conversion coefficients to each other. Note that the term “dose” might be used in a generic sense throughout this document to refer to the various dose quantities. The definitions of protection and operational quantities taken from ICRU Report 51 (ICRU, 1991), ICRP Publication 60 (ICRP, 1991) and ICRP Publication 103 (ICRP, 2007) are as follows:

The **absorbed dose**, D, is the quotient of $D = \frac{d\bar{\varepsilon}}{dm}$ where $d\bar{\varepsilon}$ is the mean energy imparted by ionizing radiation to matter of mass dm. The unit is J kg^{-1} .The special name for the unit of absorbed dose is the gray (Gy).

The **dose equivalent,** H, is the product of Q and D at a point in tissue, where D is the absorbed dose and Q is the quality factor at that point. Thus, $H = Q D$. The unit of dose equivalent in the SI system of units is joules per kilogram (J kg^{-1}) and its special name is the sievert (Sv).

The dose equivalent was specified in ICRP Publication 21 (ICRP, 1973). ICRP Publication 60 (ICRP, 1991) introduced the concept of equivalent dose. ICRP Publication 103 (ICRP, 2007) modified the weighting factors.

The **equivalent dose,** H_T, in a tissue or organ is given by $H_T = \sum_R w_R D_{T,R}$, where $D_{T,R}$ is the mean absorbed dose in the tissue or organ, *T*, due to radiation, *R*, and w_R is the corresponding radiation weighting factor. The unit of equivalent dose is the sievert (Sv).

The weighting factor, w_R for the protection quantities recommended by ICRP Publication 103 (ICRP, 2007) is shown in Table 1.2. In the case of neutrons, w_R varies with energy and therefore the computation for the protection quantities is made by integration over the entire energy spectrum.

Table 1.2. Radiation weighting factors recommended by ICRP Publication 103

Radiation Type	**Energy Range**	$\boldsymbol{w_R}$
Photons, electrons and muons	All energies	1
Neutrons	< 1 MeV	$W_R = 2.5 + 18.2\exp[-\frac{(\ln(E))^2}{6}]$
Neutrons	1 MeV to 50 MeV	$W_R = 5 + 17\exp[-\frac{(\ln(2E))^2}{6}]$
Neutrons	> 50 MeV	$W_R = 2.5 + 3.5\exp[-\frac{(\ln(0.04E))^2}{6}]$
Protons, other than recoil protons	> 2 MeV	2
Alpha particles, fission fragments and heavy nuclei	All energies	20

The **effective dose**, E, is given by $E = \sum_{R} w_T H_T$, where H_T is the equivalent dose in the tissue or organ, T, and w_T is the corresponding tissue weighting factor. The effective dose is expressed in Sv.

The **ambient dose equivalent,** *H*(d)*, at a point in a radiation field, is the dose equivalent that would be produced by the corresponding expanded and aligned field, in the ICRU sphere (diameter = 30 cm, 76.2 % O, 10.1 % H, 11.1 % C and 2.6 % N) at a depth, *d*, on the radius opposing the direction of the aligned field (ICRU, 1993). The ambient dose equivalent is measured in Sv. For strongly penetrating radiation, a depth of 10 mm is recommended. For weakly penetrating radiation, a depth of 0.07 mm is recommended. In the expanded and aligned field, the fluence and its energy distribution have the same values throughout the volume of interest as in the actual field at the point of reference, but the fluence is unidirectional.

The **directional dose equivalent**, $H'(d, \Omega)$, at a point in a radiation field, is the dose equivalent that would be produced by the corresponding expanded field in the ICRU sphere at a depth, *d*, on the radius in a specified direction, Ω (ICRU, 1993). The directional dose equivalent is measured in Sv. For strongly penetrating radiation, a depth of 10 mm is recommended. For weakly penetrating radiation, a depth of 0.07 mm is recommended.

The **personal dose equivalent**, $H_p(d)$, is the dose equivalent in soft tissue, at an appropriate depth, *d*, below a specified point on the body. The personal dose equivalent is measured in Sv. For strongly penetrating radiation, a depth of 10 mm is recommended. For weakly penetrating radiation, a depth of 0.07 mm is recommended.

1.3.2 Conversion Coefficients

Conversion coefficients are used to relate the protection and operational quantities to physical quantities characterizing the radiation field (ICRU, 1998). Frequently radiation fields are characterized in terms of absorbed dose or fluence. The **fluence**, Φ, is the quotient of $d\underline{N}$ *by* $d\underline{a}$ where $d\underline{N}$ is the number of particles incident on a sphere of cross-sectional area $d\underline{a}$. The unit is m^{-2} or cm^{-2}. Thus, for example, the effective dose can be obtained by multiplying the fluence with the fluence-to-effective dose conversion coefficient.

The fluence-to-dose conversion coefficients at high energies are the basic data for shielding calculations. Conversion coefficients for electrons with energies up to 45 MeV, photons with energies up to 10 MeV and neutrons with energies up to 180 MeV can be found in ICRU Report 57 (ICRU, 1998). Fluence-to-effective dose and fluence-to-ambient dose equivalent conversion coefficients have been calculated by the Monte Carlo transport code FLUKA (Ferrari, 2005; Battistoni *et al.*, 2007) for many types of radiation (photons, electrons, positrons, protons, neutrons, muons, charged pions, kaons) and incident energies (up to 10 TeV). The data are summarized in a paper by Pelliccioni (Pelliccioni, 2000). Conversion coefficients for high-energy electrons, photons, neutrons, and protons have also been calculated by others using various Monte Carlo codes. These references are cited in ICRU Report 57 (ICRU, 1998) and Pelliccioni (2000). Figure 1.5 shows the fluence-to effective dose conversion coefficients for anterior-posterior (AP) irradiation for various particles as a function of particle energy (Pelliccioni, 2000). Figure 1.6 shows the fluence-to ambient dose equivalent conversion coefficients. Figure 1.7 shows the fluence-to effective dose conversion coefficients for isotropic (ISO) irradiation.

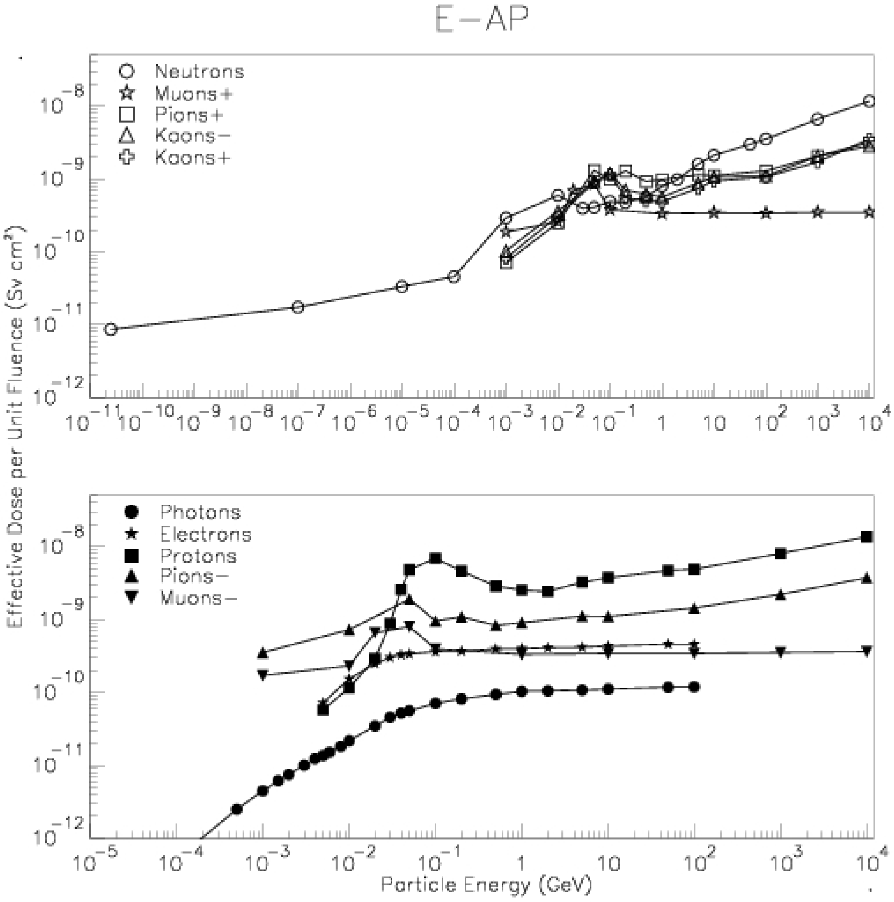

Figure 1.5. Fluence-to-effective dose conversion coefficients for AP irradiation as a function of energy for various types of radiation (Pelliccioni, 2000)

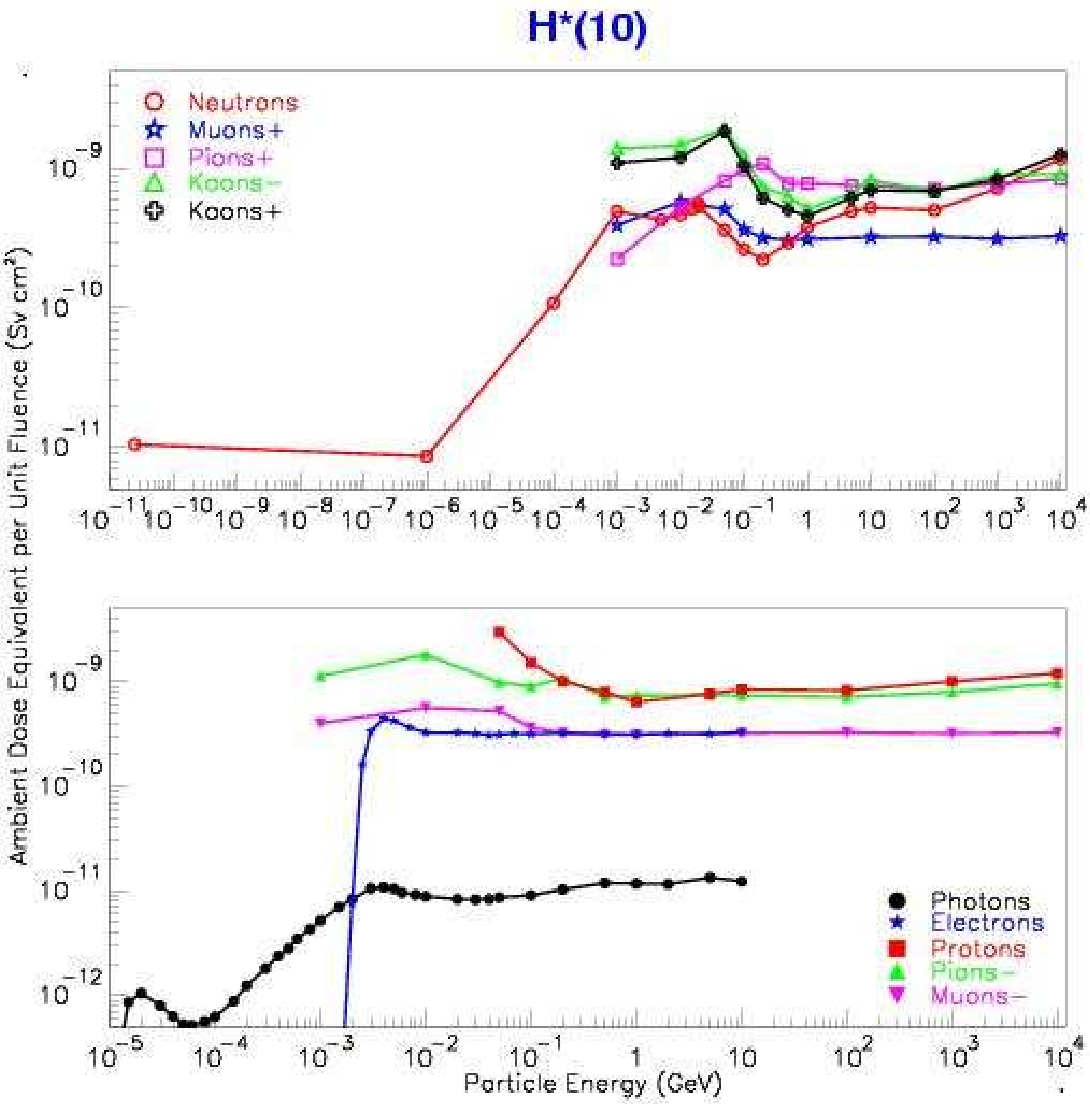

722
723 Figure 1.6. Fluence-to-ambient dose conversion coefficients as a function of energy for various types of
724 radiation (Courtesy of M. Pellicioni; Pelliccioni, 2000)

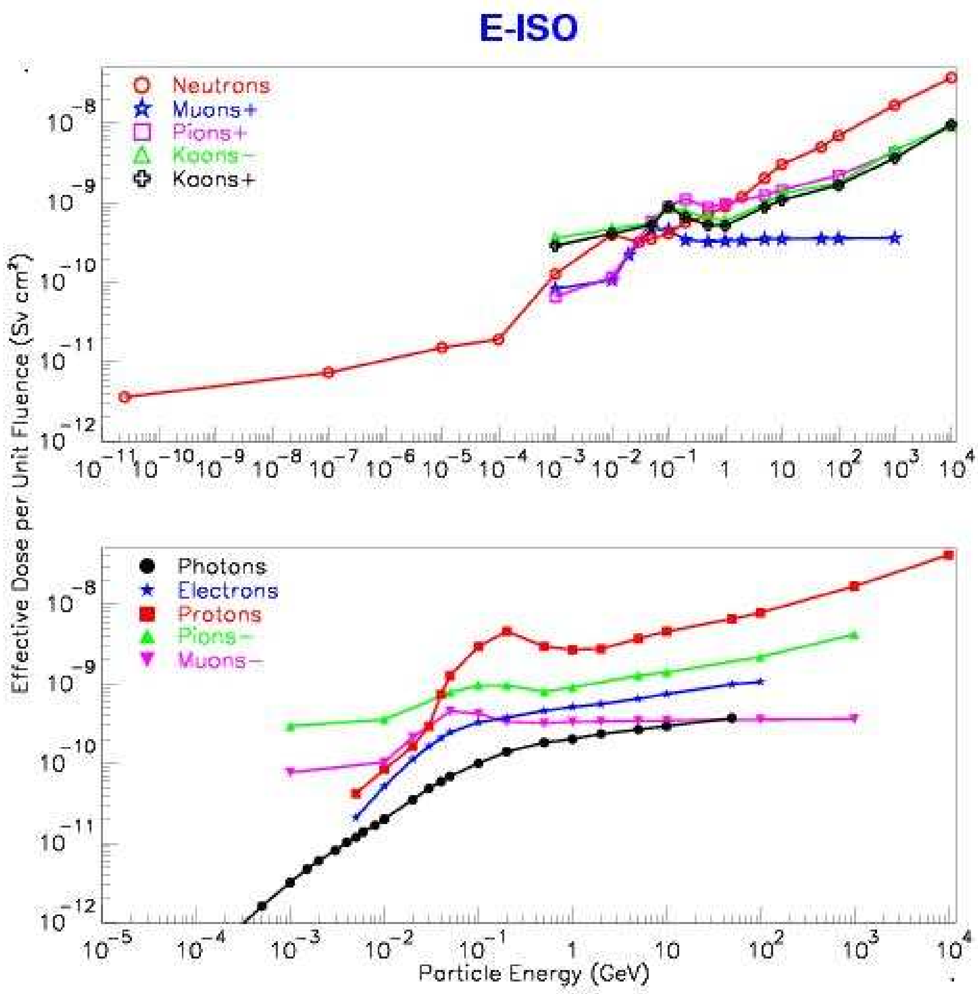

725

726 Figure 1.7. Fluence-to-effective dose conversion coefficients for ISO (isotropic) irradiation as a

727 function of energy for various types of radiation (Courtesy of M. Pelliccioni)

1.4 Shielding Design and Radiation Safety

The remainder of this report is devoted to shielding design (Chapters 2 and 3) and radiation safety (chapters 4-6) of charged particle therapy accelerators. The literature is replete with data and information for high-energy proton accelerators (> 1 GeV); however, such information is sparse for intermediate-energy protons and carbon ions. The purpose of this report is to provide sufficient information for the design of new facilities; therefore, it does not necessarily provide a comprehensive citation of all related references for proton and carbon ion.

2. Radiological Aspects of Particle Therapy Facilities

Nisy Elizabeth Ipe

2.1 Charged Particle Interactions

The literature is replete with the physics of high-energy particle accelerator shielding, but there is a dearth of related information for intermediate energy charged particle accelerators. The first section of this chapter provides a summary of the particle interactions with the emphasis placed mainly on the interactions pertaining to shielding of charged particle therapy facilities.

The interaction of an accelerated beam of charged particles with matter results in the production of different types of radiation (NCRP, 2003). The yield (number of secondary particles emitted per incident primary particle) and types of secondary radiation generally increase with increasing kinetic energy of the incident particle. The processes that are important in energy deposition include the strong (or nuclear) interaction, the electromagnetic interaction, and the weak interaction (ICRU, 1978). The electromagnetic interaction is comprised of the direct interactions that are long range and that occur between particles that carry charge or have a magnetic moment, and the interactions in which photons are emitted or absorbed. The strong interaction occurs only between hadrons or between photons and hadrons. It is the strongest of all the interactions but occurs over a short range ($<10^{-13}$ cm). It is responsible for the binding of protons and neutrons in the atomic nucleus.

Hadrons comprise the majority of all known particles and interact *via* strong interactions (ICRU, 1978). They consist of baryons and mesons. Baryons are particles with mass equal to or greater than that of the proton and have a half-integral spin. They include protons and neutrons. Mesons are particles that have an integral or zero spin, and include pions (pi-mesons, π) and kaons (k-mesons, K). Pions are produced in high-energy reactions and charged pions play a dominant role in the propagation of the hadronic cascade (described in section 2.1.2). They decay to muons in air or a vacuum, but have a high probability of stopping in condensed matter. Positive pions will decay and negative pions will be captured, forming pi-mesic atoms. In the latter case, the atoms will quickly de-excite and emit characteristic x rays, while the pions will be captured by the nucleus. The interactions of pions with nuclei lead to nuclear break-up and the subsequent emission of low-energy protons (p), alpha particles (α) and high-LET nuclear fragments. Heavier mesons and baryons are also produced, but the probability of their production is significantly lower than that of pions. Hadrons interact with each other *via* strong interactions when their distance of separation is less than 10^{-13} cm. At distances larger than this, they can interact *via* electromagnetic interactions such as proton scattering and proton energy-loss by ionization.

The interactions of charged particles include electromagnetic interactions with atomic electrons and the nucleus, nuclear reactions and the production of secondary hadrons, nuclear reactions of secondary hadrons, and the electromagnetic cascade. These are described in the following sections.

2.1.1 Electromagnetic Interactions of Charged Particles

Interaction of charged particles with atomic electrons and the nucleus are briefly described in the following sections.

2.1.1.1 Interaction of Charged Particles with Atomic Electrons. A heavy charged particle loses energy mainly through ionization and excitation of atoms as it traverses matter. Except at low velocities, it loses a negligible amount of energy in nuclear collisions. Its encounters with atomic electrons can be divided into two categories: hard collisions, where the energy imparted is much greater than the binding energy of the electron; and soft collisions, where the energy imparted to the electron is similar in magnitude to its binding energy (ICRU, 1978). In the derivation of the formulae for energy loss, it is assumed that the incident particle is moving at a speed *v* that is much greater than the mean velocity of the electrons in their atomic orbits.

For hard collisions, the energy transferred is very large compared to the electron binding energy. Thus, the atomic electrons are considered initially at rest and free (unbound). The maximum energy T_{max} that can be imparted by a charged particle to an electron in a head-on collision is given by:

$$T_{\max} = 2mc^2 \frac{p^2c^2}{m^2c^4 + M^2c^4 + 2mc^2E} \tag{3.1}$$

where *m* is the electron rest mass, *c* is the speed of light in vacuum, *p* is the momentum of the incident particle, *M* is the rest mass of the particle, and *E* is the total energy of the particle.

When *M* is much greater than m, as in the case of mesons or protons, and when $pc << (M/m)Mc^2$,

$$T_{\max} \approx 2mc^2 \frac{\beta^2}{1-\beta^2} \tag{3.2}$$

where $\beta = v/c$ is the relative velocity of the particle.

At very high energies, T_{max} approaches *pc* or *E*, and does not depend on the value of *M*. Thus, there is a small probability that the knock-on electron can carry off almost all the kinetic energy of the incident particle.

The linear rate of energy loss to atomic electrons along the path of a heavy charged particle in a medium (expressed as MeV/cm or MeV/m) is the basic physical quantity that determines the dose delivered by the particle in the medium (Turner, 1980). This quantity referred to as *-dE/dx* is called the stopping power of the medium for the particle and is given by the Bethe formula:

$$-\frac{dE}{dx}=\frac{4\pi z^2 e^4 n}{mc^2\beta^2}\left[\ln\frac{2mc^2\beta^2}{I(1-\beta^2)}\right]-\beta^2 \tag{3.3}$$

where *z* is the atomic number of the heavy particle, *e* is the magnitude of electron charge, *n* is the number of electrons per unit volume in the medium, and *I* is the mean excitation energy of the medium.

The stopping power depends only on the charge *ze* and the relative velocity *β* of the heavy particle, and on the relevant properties of the medium such as its mean excitation energy *I* and the electronic density *n*.

The range of a charged particle is the distance that it travels before coming to rest. The distance traveled per unit energy loss is given by the reciprocal of the stopping power. Thus, the range *R*(*T*) of a particle of kinetic energy (*T*) is the integral of the reciprocal of the stopping power down to zero energy, and can be written in the following form (Turner, 1980):

$$R(T)=\frac{M}{z^2}f(\beta) \tag{3.4}$$

It is important to note that the mean range of particles of a given speed is proportional to the mass and varies as the inverse square of their charge. The dependence of the Bethe formula on z^2 implies that particles with the same mass and energy but opposite charge (such as pions and muons) have the same stopping power and range. However, departures from this prediction have been measured and theoretically explained by the inclusion of higher powers of *z* in the Bethe formula. Statistical fluctuations in the energy-loss process can also result in an r.m.s. (root mean square) spread in the actual range of individual monoenergetic particles, resulting in “range straggling.”

2.1.1.2 Interaction of Charged Particles with Nucleus. A charged particle is also scattered when it passes near a nucleus (ICRU, 1978). The scattering process is generally considered an elastic one, because of the relatively small probability of a photon being emitted with an energy comparable to the kinetic energy of the charged particle. When a charged particle penetrates an absorbing medium, most of the scattering interactions lead to small deflections. Small net deflections occur because of a large number of very small deflections and are referred to as multiple scattering. Large net deflections are the result of a single large-angle scatter plus many very small deflections and are referred to as single scattering. The intermediate case is known as plural scattering.

2.1.2 Nuclear Interactions

Nuclear interactions include nucleon-nucleus interactions and heavy ion-nucleus interactions.

2.1.2.1 Nucleon-Nucleus Interactions. The incident nucleon enters the nucleus, is deflected by the nuclear potential, and emerges again at a different angle but with the same energy (Moritz, 2001). This is known as direct elastic scattering. The nucleon can also directly collide with a target nucleon and excite it to form a compound state. There are two possibilities:

- Either one or both nucleons have energy greater or less than their separation energy. In the former case, the nucleon with energy greater than the separation energy leaves the nucleus without further interaction, other than being deflected. If the change in mass is zero, the reaction is either an inelastic scattering or a charge-exchange reaction. This is considered a direct reaction. When the change in mass is not zero, the reactions are either transfer or knock-out reactions. The angular distribution of the scattered particles is anisotropic and forward peaked.

- The nucleons will undergo further collisions in the compound nucleus, thus spreading the excitation energy over the entire nucleus. The nuclear state becomes complex during the pre-equilibrium phase but eventually attains statistical equilibrium. Sufficient energy is concentrated on one nucleon, which may escape the nucleus or "boil off." Similarly, the kinetic energy may be concentrated on a group of nucleons, and deuterons, tritons, and alpha particles may be emitted. Heavy fragments may also be emitted. The emission of the particles is described by an evaporation process similar to the evaporation of a molecule from the surface of a liquid. For example, the spectrum of the emitted neutrons may be described by a Maxwellian distribution of the form:

$$\frac{dN}{dE_n} = BE_n \exp(-E_n / T) \tag{3.4}$$

  where E_n is the energy of the neutron, B is a constant, and T is the nuclear temperature. The nuclear temperature is characteristic of the target residual nucleus and its excitation energy, and has dimensions of energy. Its value lies between 2 and 8 MeV. When the spectra are plotted as $\ln(E_n^{-1} x\ dN/dE)$ *versus* E_n, the Maxwellian distribution appears on a semi logarithmic scale as a straight line with a slope of $-1/T$. The evaporated particles are emitted isotropically and the energy distribution of the neutrons extends up to about 8 MeV. Compound reactions may also occur during the pre-equilibrium phase, in which case the angle of emission will be strongly correlated with the direction of the incident particle. After statistical equilibrium has been attained, the emitted particles will have an isotropic distribution.

All the scattered and emitted particles can interact again resulting in an intra-nuclear cascade. Above the pion production threshold (135 MeV), pions also contribute to the nuclear cascade. Neutral pions decay into a pair of gamma rays after traversing a short distance. Charged pions will decay into muons and then electrons if they have a clear flight path (*i.e.*, no further interactions), resulting in an electromagnetic cascade. Neutrons or protons can also induce fission in high-atomic-mass nuclei.

2.1.2.2 Heavy Ion-Nucleus Interactions. Nuclear interactions of heavy ions as they pass through matter arise from grazing or head-on collisions (Raju, 1980). In grazing collisions, fragmentation of either the incident heavy ion or the target nucleus occurs. Fragmentation is the major nuclear interaction. Head-on collisions are less frequent, but in such collisions, large amounts of energy are transferred compared to grazing collisions. In heavy-ion interactions, many secondary particles are created from nucleus-nucleus interactions. Nucleus-nucleus interactions have features that are different from typical hadron-nucleus interactions at either the same total energy or energy per nucleon (ICRU, 1978). The cross section for nuclear collisions between two nuclei is larger than that between a single hadron and either nucleus. When two high-energy nuclei interact, only the segments that interpenetrate each other undergo a significant interaction and mutual disintegration. The remainder of each nucleus is uninvolved even though each is likely to have become highly excited, as is evidenced by the fact that a substantial fragment is usually observed traveling in the same direction and at a similar speed to the incident primary ion. Even though the part of the nucleus that escapes the severe interaction becomes highly excited, it does not undergo evaporation to the extent that it breaks up into fragments with $Z < 3$ (ICRU, 1978). It is only in a head-on collision that the projectile breaks up into many small pieces, so that no high-velocity fragment survives. The residual nucleus and the alpha particles that evaporate from the primary fragment are concentrated about the incident direction.

The process of fragmentation is frequently described as an abrasion-ablation process and is schematically illustrated in Fig. 2.1 (Gunzert-Marx, 2004). The first step is known as abrasion. In grazing collisions, a small fraction of the nuclear material overlaps and this overlapping zone is known as the fireball. The abraded projectile pre-fragment keeps most of its initial energy while the abraded pre-fragment target remains at rest. The fireball recoils with an intermediate velocity. During ablation, the second step of fragmentation, the pre-fragments and the highly excited fireball evaporate nucleons and light clusters.

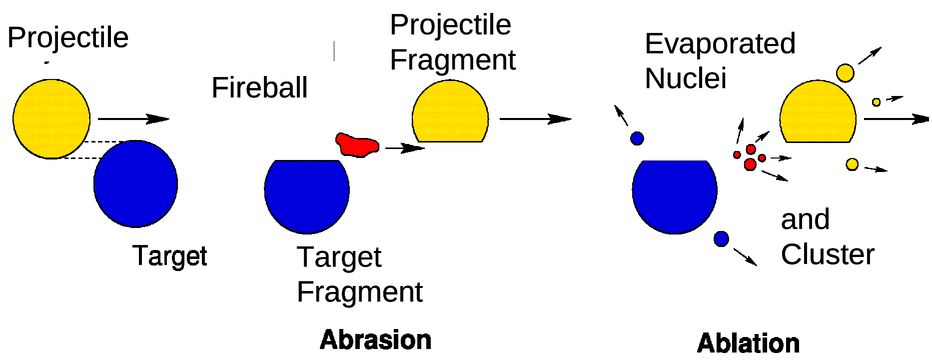

Figure 2.1. Schematic illustration of fragmentation in a target (Courtesy of GSI)

The average number of mesons produced in a nucleus-nucleus interaction is larger than that produced in a proton collision. The number of mesons produced in a single collision between heavy nuclei fluctuates significantly due to the varying degree of overlap between the two nuclei. At high energies (> ~ 200 MeV/nucleon), the probability and type of fragmentation does not depend on the incident energy. At low energies, the cross sections for fragmentation decrease significantly. At still lower energies, there is a higher probability that the nuclei come to rest without any interaction. At very low energies (~ [1 to 2] MeV/nucleon) the colliding nuclei may interact as a whole, resulting in the production of a compound nucleus.

At high energies (Moritz, 1994), heavy ion interactions may be treated as interactions between individual nucleons, *i.e.*, Z protons and (A-Z) neutrons acting independently approximate a heavy ion (Moritz, 1994). Most of the ion interactions occur at a finite impact parameter (the perpendicular distance between the velocity vector of a projectile and center of the target that it is approaching). Therefore, part of the ion may shear off and continue forward as a nuclear fragment. Thus, less than A nucleons are available for further interactions. However, interaction cross sections are large. Therefore the fragmented ion may interact very close to the initial interaction point. Thus, it may appear that all nucleons interact at a single point.

Agosteo *et al.* (2004a; 2004b) point out that the approach of considering an ion of mass A equivalent to A protons is not a good approximation in shielding calculations for ions in the therapeutic range of interest, but is correct at ultra-relativistic energies, *i.e.*, hundreds of GeV/nucleon. At low energies, the above-mentioned approach leads to an underestimate of shielding thicknesses, with the underestimation increasing with larger shielding thicknesses especially in the forward direction. This can be attributed to the fact that secondary neutrons generated from ion interactions have energies that extend to a maximum of about two times the specific energy of the ion.

Experimental data from heavy ion reactions for ions with specific energy greater than 100 MeV/nucleon have been tabulated in a handbook (Nakamura and Heilbron, 2006). This handbook includes thick-target secondary neutron yields, thin-target secondary neutron production cross sections, measurements of neutron penetration behind shielding, spallation product cross sections and yields, and parameterizations of neutron yields.

2.1.3 Hadron Interactions

The hadronic cascade and proton interactions are discusses in the following sections.

2.1.3.1 Hadronic or Nuclear Cascade. Figure 2.2 provides a schematic representation of the hadronic or nuclear cascade (ICRU, 1978; NCRP, 2003). The typical energy per particle in the figure refers to the energy of the outgoing particle, and not the energy of the incoming particle.

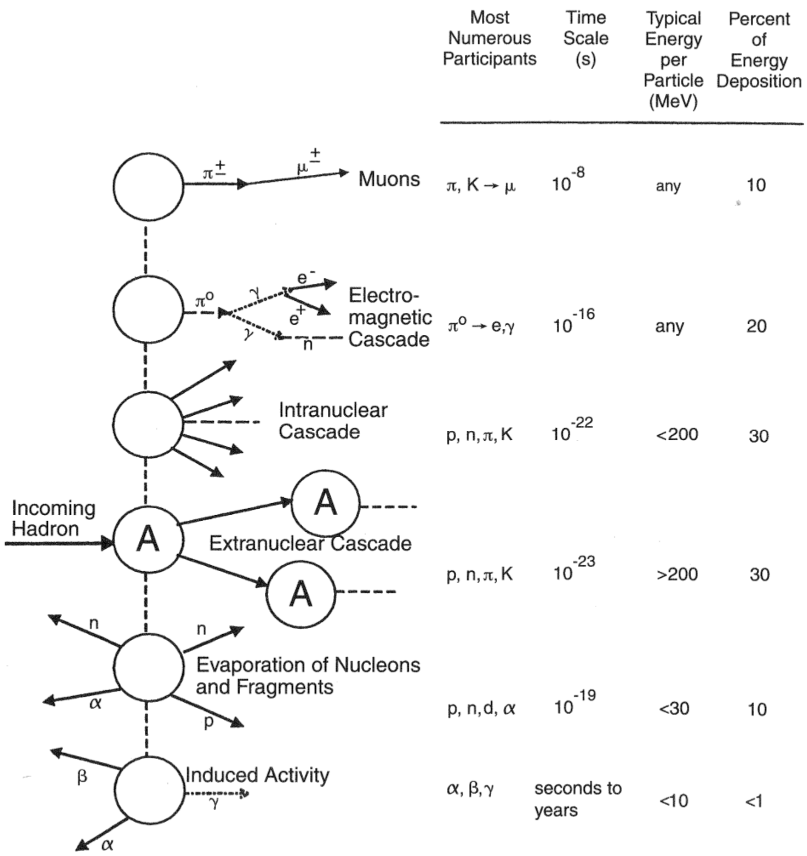

Figure 2.2. Six levels of hadronic cascade (NCRP, 2003). Reprinted with permission of the National Council on Radiation Protection and Measurements, http://NCRPonline.org.

Six distinct and independent processes characterize the hadronic cascade. The extra-nuclear cascade is the most important process and feeds all other processes. The hadrons (p, n, $\pi^{\pm}$, etc) propagate this cascade. When a baryon or a meson interacts with a nucleus as a whole, it will release fast forward-directed baryons and mesons, which will propagate the shower by collisions with other nuclei. With each interaction the number of particles increases.

An intra-nuclear cascade may also occur when the particles in the extra-nuclear cascade interact with individual nucleons inside the struck nucleus. This gives rise to similar reaction products, but of lower energy, and emitted at wider angles. These particles may also contribute to the extra-nuclear cascade, but to a much lesser extent. The intra-nuclear cascade process occurs within ~ 10^{-22} s. Above the pion production threshold (135 MeV), pions also contribute to the nuclear cascade. The neutral pions (π^0) from the extra- and intra-cascades decay into two photons, which in turn can initiate an electromagnetic cascade. The energy transferred is deposited by ionization losses within a distance of several radiation lengths. The radiation length X_0 is the mean path length required to reduce the energy of a relativistic charged particle by a factor of *e*. The neutral pion decay occurs within ~ 10^{-16} s. Some of the charged pions and kaons ($\pi^{\pm}$, $K^{\pm}$) will decay before they have dissipated all their energy, releasing one muon ($\mu^{\pm}$) from each meson decay. Muons are very penetrating particles and deposit their energy mainly by ionization. Muon photonuclear reactions are also possible. The charged pion and kaon decays occur within ~ 10^{-8} s.

After interaction with the incoming hadron, the prefragment, *i.e.*, what remains of the original nucleus, is left in an excited state. It de-excites by emitting particles, mainly neutrons and protons, that do not contribute to the cascade or are involved with any of the other processes. These low-energy neutrons travel long distances, continuously depositing energy. The proton energy is deposited locally.

The evaporation of nucleons takes place within ~ 10^{-19} s. The de-excited nucleus may be radioactive, thus leading to residual radiation.

Thus, the interaction of a high-energy hadron with a nucleus results in the production of a large number of particles, mainly nucleons, pions, and kaons. A large fraction of the incident energy may be transferred to a single nucleon, that can be considered the propagator of the cascade. Energy transfer mainly occurs by the interaction of high-energy nucleons with energies greater than ~ 150 MeV, and these particles propagate the cascade. Nucleons with energies between 20 MeV and 150 MeV also transfer their energy by nuclear interactions, but the energy is transferred to a large number of nucleons instead of to a single nucleon. Therefore, each nucleon receives on average only a fraction of the total energy transferred and therefore has a low kinetic energy of ~ 10 MeV. Charged particles at these energies are quickly stopped by ionization. Thus, neutrons predominate at low energies. Charged pions and kaons decay into muons and neutrinos. Because muons are not subject to the strong interaction, they are primarily stopped in matter by ionization energy losses. Energetic gamma rays produced by the decay of neutral pions initiate electromagnetic cascades. However, the attenuation length (defined in Chapter 1) of these cascades is much shorter than the absorption length (distance traveled in which the intensity of the particles is reduced by a factor of *e* due to absorption) of strongly interacting particles; therefore, they do not contribute significantly to the energy transport. Thus, with increasing depth in the shield, neutrons are the principal propagators of the cascade because protons and pions with energies less than ~ 450 MeV have a high rate of energy loss.

2.1.3.2 Proton Interactions. The interactions of protons with matter result in the degradation of the energy of the protons, and the production of a spray or cascade of secondary particles known as the hadronic or nuclear cascade, as described in the previous section. The extra-nuclear cascade occurs at primary proton energies above a few GeV (Moritz, 1994), and is followed by an intra-nuclear cascade.

The intra-nuclear cascade takes place at proton energies between 50 MeV and 1000 MeV. Therefore, the intra-nuclear cascade is of importance for shielding in the proton therapeutic energy range of interest (67 to 250 MeV), and the yield of low-energy neutrons increases as the primary proton energy increases (ICRU, 1978). However, the greater yield is more than compensated for by greater attenuation in the shield due to a higher cross section at low energy. Shielding studies indicate that the radiation field reaches an equilibrium condition beyond a few mean-free paths within the shield. Neutrons with energies greater than 150 MeV regenerate the cascade even though they are present in relatively small numbers. They are accompanied by numerous low-energy neutrons produced in the interactions. The shape of the neutron spectrum observed at the shield surface is very similar to that which exists in the shield. The presence of holes or penetrations in the shielding may perturb the shape of the neutron spectrum, with an increased number of low-energy neutrons in the vicinity of the penetrations. Both experiments and calculations confirm that for a well-developed cascade the shape of the spectrum is rather independent of the location within the shield, the incident energy, or even the shielding material, as long as the hydrogen content is essentially the same (ICRU, 1978). The typical neutron spectrum observed outside a thick concrete shield consists of peaks at a few MeV and at ~ 100 MeV.

At proton energies below 10 MeV, the proton is absorbed into the target nucleus and creates a new compound nucleus, as explained in section 2.1.2.1 (IAEA, 1988).

Photons are produced by inelastic neutron scattering and neutron capture by hydrogen within the concrete wall, and the inelastic scattering of evaporation neutrons in the target. The contribution of dose from photons produced in the shield is important only for primary neutrons with energies below 25 MeV and for thick concrete shields. The total photon dose is much lower than the neutron dose for proton energies higher than 150 MeV and for a sufficiently thick shield.

The energy loss at the lowest proton energy is mainly due to ionization of the material in which the protons are stopped. The lowest-energy proton produces the greatest specific ionization resulting in the formation of the Bragg peak at the end of the proton range. This property has been exploited in proton therapy. Protons can penetrate the Coulomb barrier when their kinetic energy is sufficiently high. In this case, nuclear reactions are also possible in addition to Coulomb scattering. As the energy of the protons increase, the nuclear reactions compete with the electromagnetic interactions.

2.1.4 Electromagnetic Cascade

Electromagnetic cascades are initiated by pion decay as shown in Fig. 2.2; however, the intra-nuclear cascade dominates for protons in the therapeutic range of interest. When a high-energy electron interacts with matter, only a small fraction of the energy is dissipated as a result of collision processes. A large fraction is spent in the production of high-energy photons or bremsstrahlung. These photons interact through pair production or Compton collisions resulting in the production of electrons. These electrons radiate more photons, which in turn interact to produce more electrons. At each new step, the number of particles increases and the average energy decreases. This process continues until the electrons fall into the energy range where radiation losses can no longer compete with collision losses. Eventually, the energy of the primary electron is completely dissipated in excitation and ionization of the atoms, resulting in heat production. This entire process resulting in a cascade of photons, electrons, and positrons is called an electromagnetic cascade. A very small fraction of the bremsstrahlung energy in the cascade is utilized in the production of hadrons such as neutrons, protons, and pions.

2.2 Secondary Radiation Environment

The secondary radiation environment for charged particle therapy accelerators is comprised of:

1. Neutrons; charged particles like pions, kaons, ions; and nuclear fragments emitted in inelastic hadronic interactions;
2. Prompt gamma radiation from the interaction of neutrons or ions with matter;
3. Muons and other particles;
4. Characteristic x rays due to transfer of energy from the charged particle to an electron in the bound state and the subsequent emission of a photon from the decay of the excited state;
5. Bremsstrahlung radiation produced by the transfer of energy from the accelerated charged particle to a photon in the electromagnetic field of an atom; and
6. Residual radiation from radioactivation produced by nuclear reactions of the particle with atomic nuclei.

Neutrons dominate the prompt radiation field for proton and ion accelerators outside the shielding. In general, the radiation dose outside the shielding depends upon the energy, type of incident particle, the beam-on time, the target material and dimensions, and the shielding itself.

2.2.1 Neutron Energy Classifications

For radiation protection purposes the neutrons can be classified as follows:

Thermal: $\bar{E}_n =$ 0.025 eV at 20° C, typically $E_n \leq 0.5$ eV (cadmium resonance)

Intermediate: 0.5 eV $< E_n \leq 10$ keV

Fast: 10 keV $< E_n \leq 20$ MeV

Relativistic or high-energy: $E_n > 20$ MeV

where $\bar{E}_n$ is the average energy of the neutrons and E_n is the energy of the neutrons.

2.2.2 Neutron Interactions

Because neutrons are uncharged, they can travel appreciable distances in matter without undergoing interactions. When a neutron collides with an atom, it can undergo an elastic or an inelastic reaction (Turner, 1986). An elastic reaction is one in which the total kinetic energy of the incoming particle is conserved. In an inelastic reaction, the nucleus absorbs some energy and is left in an excited state. The neutron can also be captured or absorbed by a nucleus in reactions such as (n,p), (n,2n), (n,α) or (n,γ).

Thermal neutrons (n_{th}) are in approximate thermal equilibrium with their surroundings and gain and lose only small amounts of energy through elastic scattering. They diffuse about until captured by atomic nuclei. Thermal neutrons undergo radiative capture, *i.e.*, neutron absorption followed by the immediate emission of a gamma ray, such as in the $^{1}H(n_{th},\gamma)^{2}H$ reaction. The gamma ray has an energy of 2.22 MeV. The capture crosssection is 0.33×10^{-24} cm^2. This reaction occurs in shielding materials such as polyethylene and concrete. Borated polyethylene is used because the cross section for capture in boron is much higher (3480 x 10^{-24} cm^2) and the subsequent capture gamma ray from the $^{10}B(n_{th},\alpha)^{7}Li$ is much lower energy (0.48 MeV). The capture cross sections for low-energy neutrons (< 1 keV) decrease as the reciprocal of the velocity or as the neutron energy increases.

Intermediate energy neutrons lose energy by scattering and are absorbed.

Fast neutrons include evaporation neutrons from charged particle accelerators. They interact with matter mainly through a series of elastic and inelastic scattering, and are finally absorbed after giving up their energy (ICRU, 1978). On the average, approximately 7 MeV is given up to gamma rays during the slowing down and capture process. Above 10 MeV, inelastic scattering is the dominant process in all materials. At lower energies elastic scattering dominates. Below 1 MeV, elastic scattering is the principle process by which neutrons interact in hydrogenous materials such as concrete and polyethylene. When high-Z material such as steel is used for shielding, it must always be followed by hydrogenous material because the energy of the neutrons may be reduced by inelastic scattering to an energy where they may be transparent to the non-hydrogenous material. For example, as stated in Chapter 1, steel is transparent to neutrons of energy ~ 0.2 MeV to 0.3 MeV.

Relativistic neutrons arise from cascade processes in proton accelerators, and nuclear and fragmentation processes at ion accelerators, and are important in propagating the radiation field. This high-energy component with neutron energies (E_n) above 100 MeV propagates the neutrons through the shielding; and continuously regenerates lower-energy neutrons and charged particles at all depths in the shield *via* inelastic reactions with the shielding material (Moritz, 2001). For neutrons with energies between 50 and 100 MeV, reactions occur in three stages (NCRP, 1971). An intra-nuclear cascade develops in the first stage. The incident high-energy neutron interacts with an individual nucleon in the nucleus. The scattered and recoiling nucleons from the interaction proceed through the nucleus. Each of these nucleons may in turn interact with other nucleons in the nucleus, leading to the development of a cascade. Some of the cascade particles that have sufficiently high energy escape from the nucleus, while others do not. In the second stage, the energy of those particles that do not escape is assumed to be distributed among the remaining nucleons in the nucleus, leaving it in an excited state. The residual nucleus evaporates particles such as alpha particles and other nucleons. In the third stage, after particle emission is no longer energetically possible, the remaining excitation energy is emitted in the form of gamma rays.

2.2.3 Protons: Neutron Yield, Energy Spectra, and Angular Distributions

As stated in Chapter 1, the prompt radiation field produced by protons of energies up to 250 MeV encountered in proton therapy is quite complex, consisting of a mixture of charged and neutral particles as well as photons. Neutrons dominate the prompt radiation field. As the proton energy increases, the threshold for nuclear reactions is exceeded and more nuclear interactions can occur. At energies above 200 MeV, the nuclear cascade process occurs. Between proton energies of 50 and 500 MeV the neutron yields increase as approximately E_P^2 where E_P is the energy of the incident proton (IAEA, 1988). Calculations and measurements of neutron yields, energy spectra, and angular distributions for protons of various energies incident on different types of materials can be found in the literature (Agosteo *et al.*, 1995; Agosteo *et al.*, 1996; Agosteo *et al.*, 2007; Kato *et al.*, 2002; Nakashima *et al.*, 1995; NCRP, 2003; Tayama *et al.*, 2002; Tesch, 1985). Comparisons between calculations and measurements can be found in the papers by Kato *et al.* (2000), Nakashima *et al.* (1995), and Tayama *et al.* (2002).

Thick targets are targets in which the protons or ions are stopped, *i.e.*, the thickness is greater than or equal to the particle range. Thin targets are targets with thicknesses that are significantly less than the particle range. Thus, for example, the protons lose an insignificant amount of energy in the target, and the kinetic energy available for neutron production in the target is the full incident proton energy (IAEA, 1988).

The neutron yield of a target is defined as the number of neutrons emitted per incident primary particle. Table 2.1 shows the neutron yield (integrated over all angles) from 100 MeV to 250 MeV protons impinging on a thick iron target, based on calculations with the Monte Carlo code, FLUKA (Agosteo *et al.*, 2007; Ferrari, 2005). FLUKA is described in Chapter 6. The total yield (n_{tot}), and yields for neutron energy (E_n) less than, and greater than 19.6 MeV are shown. As expected, the neutron yield increases with increasing proton energy.

Table 2.1. Neutron yields for 100 MeV to 250 MeV protons incident on a thick iron target (Agosteo *et al.*, 2007)

Proton Energy E_P (MeV)	Range (mm)	Iron Target Radius (mm)	Iron Target Thickness (mm)	Neutron Yield (neutrons per proton)		
				E_n < 19.6 MeV	E_n >19.6 MeV	n_{tot}
100	14.45	10	20	0.118	0.017	0.135
150	29.17	15	30	0.233	0.051	0.284
200	47.65	25	50	0.381	0.096	0.477
250	69.30	58	75	0.586	0.140	0.726

The average neutron energies ($\bar{E}_n$) for various emission angles are shown in Table 2.2 for the targets described in Table 2.1. As the proton energy increases, the spectra in the forward direction (0° to 10°) hardens as is evidenced by the increasing average neutron energy. However, at very large angles (130° to 140°) the average energy does not change significantly with increasing proton energies.

Table 2.2. Average neutron energies for various emission angles as a function of proton energy (Agosteo *et al.*, 2007)

Proton Energy (MeV)↓	Average Neutron Energy, $\bar{E}_n$ (MeV)			
Emission Angles→	0° to 10°	40° to 50°	80° to 90°	130° to 140°
100	22.58	12.06	4.96	3.56
150	40.41	17.26	6.29	3.93
200	57.73	22.03	7.38	3.98
250	67.72	22.90	8.09	3.62

Table 2.3 shows the neutron yield as a function of target dimensions for 250 MeV protons. As the target radius increases, the total neutron yield increases, but the yield for E_n >19.6 MeV decreases. Thus, the average neutron energy also decreases, as seen in Table 2.4. The total neutron yield increases with increasing target thickness, but the yield for E_n >19.6 MeV decreases. The data shows that the average energy increases at the 0° to 10° and 40° to 50° emission angles, but decreases for emission angles larger than 80° to 90°. As the target thickness increases, the proton interactions increase and the secondary neutron yield increases. Initially the yield is dominated by the high-energy neutrons. As the thickness is further increased, the high-energy neutrons interact, producing more low-energy neutrons. Thus, the high-energy neutron yield decreases and the low-energy neutron yield increases, while the overall neutron yield increases. With further increasing thickness, the low-energy neutrons get attenuated in the target. The net result of this competing process is an increase in total neutron yield with increasing target thickness until it reaches a maximum and then it is expected to decrease due to the attenuation of low-energy neutrons in the target material.

Table 2.3. Neutron yield for 250 MeV protons as a function of iron target dimensions (Agosteo *et al.*, 2007)

Iron Target Radius (mm)	Iron Target Thickness (mm)	Neutron Yield (neutrons per proton)		
		E_n < 19.6 MeV	E_n >19.6 MeV	n_{tot}
37.5	75.0	0.567	0.148	0.715
58.0	75.0	0.586	0.140	0.726
75.0	75.0	0.596	0.136	0.732
75.0	150.0	0.671	0.111	0.782

Table 2.4. Average neutron energies at 250 MeV for various emission angles as a function of iron target dimensions (Agosteo *et al.*, 2007)

Iron Target Radius (mm) ↓	Iron Target Thickness (mm)	Average Neutron Energy, $\bar{E}_n$ (MeV)			
Emission Angles →		0° to 10°	40° to 50°	80° to 90°	130° to 140°
37.5	75.0	73.6	25.9	8.1	3.9
58.0	75.0	67.7	22.9	8.1	3.6
75.0	75.0	64.7	21.3	8.1	3.5
75.0	150.0	70.3	23.5	6.9	3.2

Figures 2.3 and 2.4 show the double differential neutron spectra as lethargy (logarithm of energy decrement) plots calculated with FLUKA for neutrons at various emission angles, produced by 100 MeV and 250 MeV protons incident on thick iron targets (without any concrete shielding) described in Table 2.1 (Agosteo *et al.*, 2007). The energy distributions in these figures are typically characterized by two peaks: a high-energy peak (produced by the scattered beam particle) and an evaporation peak at ~ 2 MeV. As the proton energy increases, the high-energy peaks shift to higher energies, which are particularly evident in the forward direction (0° to 10°). The high-energy peak for the unshielded target is not the usual 100 MeV peak that is observed outside thick concrete shielding as described in Section 2.1.3.2. Thus, it is important to use wide-energy range instruments for neutron monitoring, as discussed in Chapter 4.

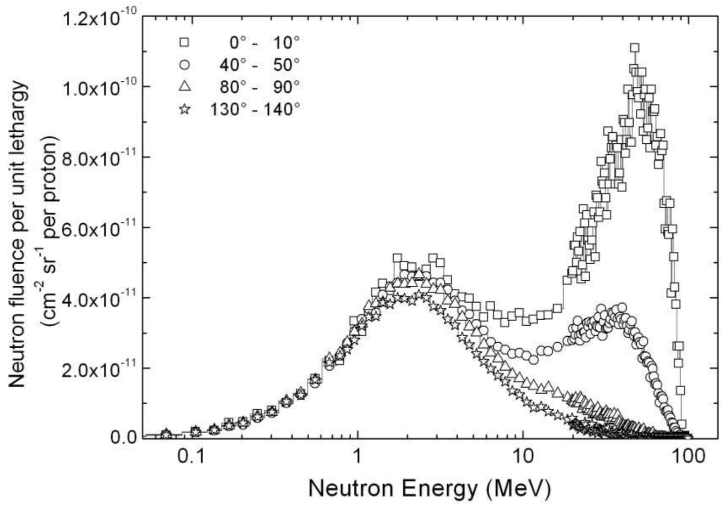

Figure 2.3. Double differential neutron spectra for 100 MeV protons incident on a thick iron target (Courtesy of S. Agosteo, Agosteo *et al.*, 2007)

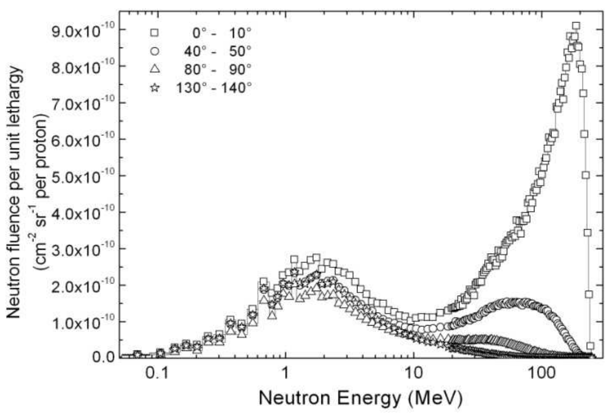

Figure 2.4. Double differential neutron spectra for 250 MeV protons incident on a thick iron target (Courtesy of S. Agosteo, Agosteo *et al.*, 2007)

2.2.4 Ions: Neutron Yields, Energy Spectra, and Angular Distribution

Neutrons dominate the radiation field of ion accelerators. The contributions from photons, protons, and pions are small, as discussed in Chapter 3. Calculations and measurements of neutron yields, energy spectra, and angular distribution for ions of various energies incident on different types of materials can be found in the literature (Gunzert-Marx, 2004; Kato *et al.*, 2002; Kurosawa *et al.*, 1999; Nakamura, 2000; Nakamura *et al.*, 2002; Nakamura *et al.*, 2006; NCRP, 2003; Porta *et al.*, 2008; Shin *et al.*, 1997).

Figure 2.5 shows the total secondary neutron yield produced in tissue as a function of kinetic energy of the projectile (kinetic energy per nucleon × number of nucleons) for various ions; protons (200 MeV), helium (202 MeV/nucleon), lithium (234 MeV/nucleon), boron (329 MeV/nucleon), carbon (400 MeV/nucleon), nitrogen (430 MeV/nucleon), and oxygen (468 MeV/nucleon) (Porta *et al.*, 2008). The results are based on calculations with FLUKA for ions incident on an International Commission on Radiation Units and Measurements (ICRU) tissue phantom (composition: 76.2 % O, 10.1 % H, 11.1 % C and 2.6 % N). The phantom was 40 cm in height and 40 cm in diameter, and the beam diameter was 10 mm. The energy of each ion was chosen so that the range in water was 26.2 cm.

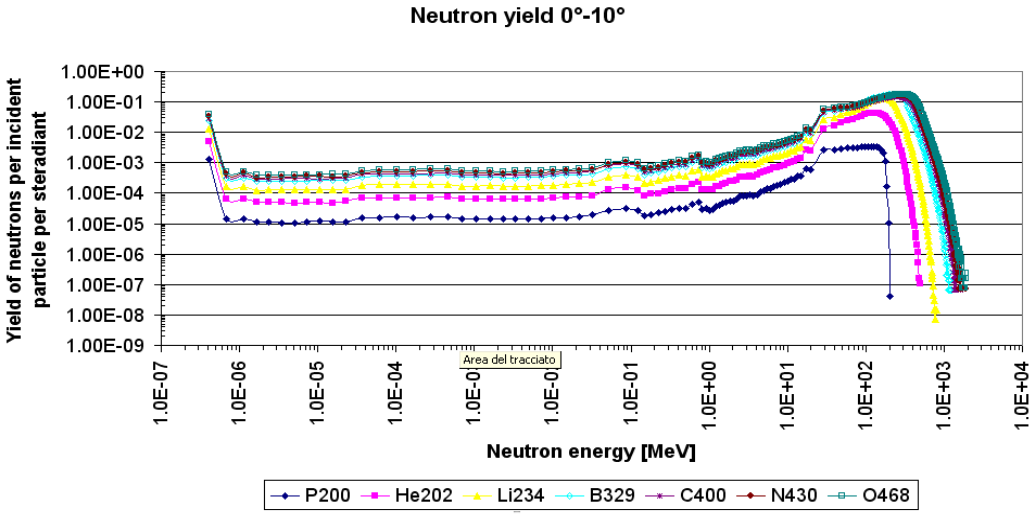

Figure 2.5. Total neutron yield expressed as neutrons per unit of solid angle and per incident particle in the 0° to 10° angular bin (Courtesy of A. Porta, Porta *et al.*, 2008).

Only carbon ions will be discussed in this section. Figures 2.6, 2.7, and 2.8 show the measured neutron spectra from 180 MeV/nucleon and 400 MeV/nucleon carbon ions incident on copper and carbon targets (Kurosawa *et al.*, 1999). The dimensions of the carbon target were 10 cm × 10 cm × 2 cm for 180 MeV/nucleon and 10 cm × 10 cm × 20 cm for 400 MeV/nucleon carbon ions, respectively. The dimension of the copper target was 10 cm × 10 cm × 1.5 cm. The spectra in the forward direction have a peak at the high-energy end that broadens with angle of emission. The peak energy is ~ 60 % to 70 % of the specific energy (140 MeV for 180 MeV/nucleon and 230 MeV for 400 MeV/nucleon). This data together with other data in the paper by Kurosawa *et al.* indicate that the high-energy neutron component produced in the forward direction by a break-up process and the momentum transfer from projectile to target nuclei are higher for both lighter target nuclei and higher projectile energy than for heavier target nuclei and lower projectile energy.

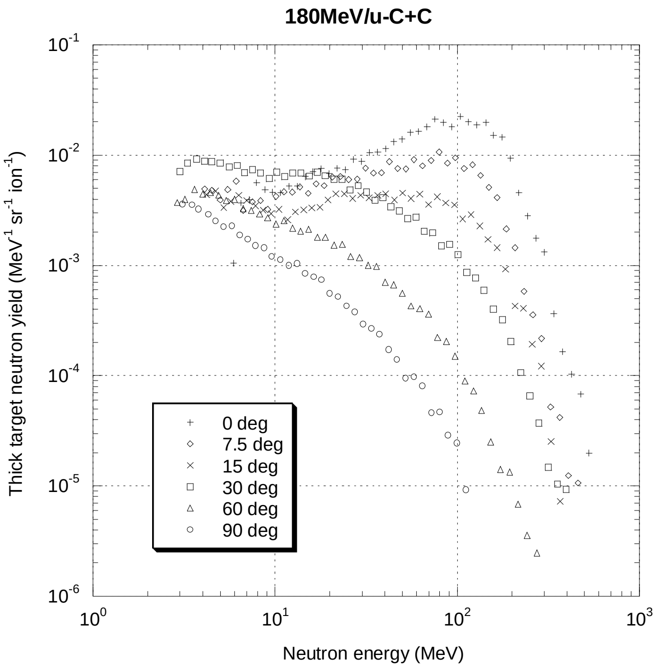

Figure 2.6. Neutron spectra from 180 MeV/nucleon C ions incident on a C target (Kurosawa *et al.*, 1999)

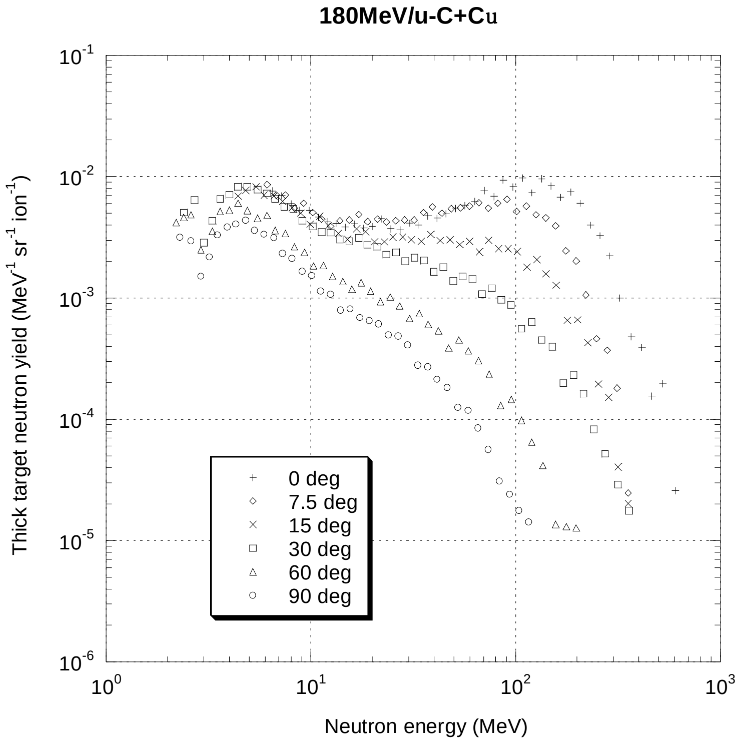

Figure 2.7. Neutron spectra from 180 MeV/nucleon C ions incident on a Cu target (Kurosawa *et al.*,1999)

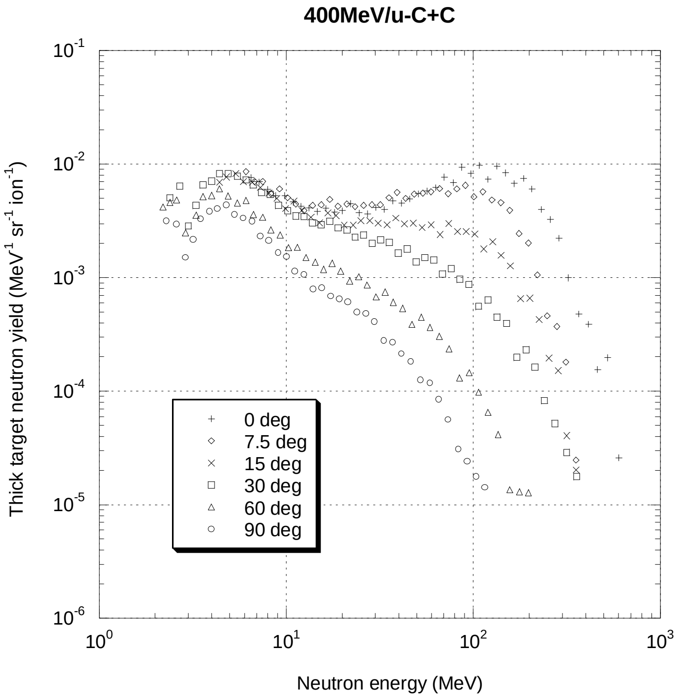

Figure 2.8. Neutron spectra from 400 MeV/nucleon C ions incident on a C target (Kurosawa *et al.*, 1999)

2.3 Beam Losses and Sources of Radiation

During the operation of particle therapy facilities, the interaction of the particles with beam-line components and the patient results in the production of radiation with neutrons being the dominant component. Typically the shielding thicknesses for various parts of the facility may range from about 60 cm to about 7 m of concrete. Effective shielding can only be designed if the beam losses and sources of radiation for the charged particle therapy facilities are well understood. This requires knowledge of how the accelerators operate and deliver beam to the treatment rooms. Specific details of beam losses, duration, frequency, targets, and locations should be provided by the equipment vendor so that all sources of radiation are considered in the shielding design. It is important to note that higher beam losses will occur during start-up and commissioning as the beam is tuned and delivered to the final destination, and should be planned for. Both cyclotrons and synchrotron-based systems are discussed below.

2.3.1 Cyclotrons

Cyclotrons are used for both proton and ion acceleration and produce essentially continuous beams. Fixed-energy machines are used for therapy and are designed to operate at energies required to reach deep-seated tumors (Coutrakron, 2007). The principle of operation for a proton cyclotron is as follows: protons are extracted from the ion source located at the center of the and are injected into the cyclotron. The cyclotron is comprised of a large magnet (or several sector magnets) with an internal vacuum region located between the poles of the magnet(s). The maximum radius of a commercial room-temperature therapy cyclotron is about 1 m. There are large D-shaped electrodes commonly referred to as "dees." A sinusoidal-alternating voltage with a frequency equal to the revolution frequency of the protons (or a multiple thereof) is applied across the dees as the protons travel in their orbit. Thus, as the protons cross a gap between the electrodes, they are further accelerated and begin to spiral outwards. The orbit radius is determined by the magnetic field. Figure 2.8 shows the inside view of the C-230 IBA cyclotron, which has four spiral-shaped electrodes. The protons are injected from the ion source below into the center of the cyclotron. The magnetic field of the cyclotron increases as the orbit radius increases to compensate for the relativistic mass increase, and the turn-by-turn separation decreases at higher energies. All the particles travel at the same revolution frequency, regardless of their energy or orbit, because the cyclotron is isochronous. The protons exit the cyclotron through a hole in the return yoke after passing through the electrostatic extraction plates.

During acceleration, continuous beam losses occur in the cyclotron. Depending upon the beam optics, about 20 % to 50 % of the accelerated beam particles can be lost in the cyclotron. The magnet yoke is made of steel and provides significant self-shielding, except in regions where there are holes through the yoke. These holes need to be considered in the shielding design. Losses at very low proton energies are not of concern for prompt radiation shielding, but can contribute to activation of the cyclotron. The beam losses of concern in the shielding design are those that occur at higher energies, and those due to protons that are close to their extraction energy (230 MeV to 250 MeV depending upon the cyclotron type) striking the dees and the extraction septum which are made of copper. These beam losses also result in activation of the cyclotron.

Figure 2.9. Inside view of C-230 IBA cyclotron (Courtesy of IBA)

2.3.1.1 Energy Selection System (ESS). For the treatment of tumors at shallow depths, the proton energy extracted from the cyclotron has to be lowered. This is typically achieved by using an energy selection system (ESS) after extraction. Figure 2.10 shows an ESS that is comprised of an energy degrader, a tantalum collimator, nickel energy slits and collimator, and a nickel beam stop. The energy degrader consists of a variable-thickness material, typically graphite, arranged in a wheel that is rotated into position, thus reducing the proton energy down to the energy of interest. In principle, the proton beam energy can be reduced to 75 MeV in the equipment described here. However, sometimes range shifters are used inside the nozzles in treatment rooms to achieve these lower energies. The intensity from the cyclotron has to be increased as the degraded energy is decreased in order to maintain the same dose rate at the patient. Thus, large amounts of neutrons are produced in the degrader, especially at the lower energies, resulting in thicker local shielding requirements in this area. The degrader scatters the protons and increases the energy spread. Most of the scattered beam from the degrader is collimated in a tantalum collimator, in order to reduce the beam emittance. A magnetic spectrometer and energy slits are used to reduce the energy spread. Beam stops are used to tune the beam. Neutrons are also produced in the collimator and slits. Losses in the ESS are large, and they also result in activation.

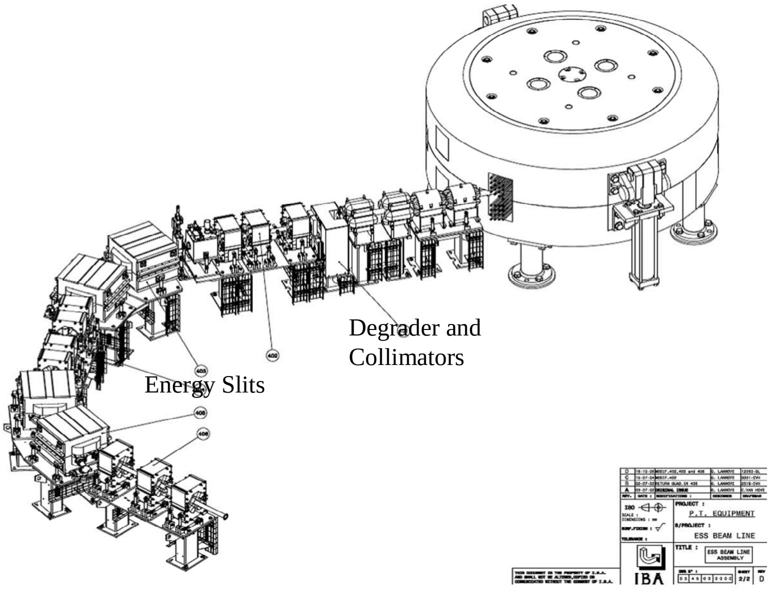

Figure 2.10. Energy Selection System (Courtesy of IBA)

2.3.2 Synchrotrons

Synchrotrons are designed to accelerate protons and ions to the exact energy needed for therapy, thus eliminating the need for energy degraders. This in turn results in less local shielding and activation of beam-line components. Synchrotrons however, are pulsed machines. For synchrotrons, the orbit radius is held constant and the magnetic field is increased as the particle energy increases. Maximum proton energy for therapy is ~ 250 MeV with about 10^{11} protons/spill, while maximum carbon energies range from (320 to 430) MeV/nucleon with (0.4 to 1.0) $\times$ 10^9 ions/spill. A spill typically lasts from 1 s to 10 s. Thus, proton intensities can be up to 250 times higher than carbon intensities.

Figure 2.11 shows a typical injector system for a synchrotron. There are two ion sources (ECRIS), one for protons and one for carbon. Proton facilities, of course, have only one ion source. A switching magnet allows the selection of either carbon ions or protons. The particles are then accelerated from 8 keV/nucleon by the RFQ (radiofrequency quadrupole) and by the IH (inter digital H-type structure) drift tube linear accelerator (linac) combination to 7 MeV/nucleon. The stripper foil produces fully stripped ions, thus eliminating all contamination, and the beam is delivered to the synchrotron. Sources of radiation include x rays from the ion source, x rays produced by back-streaming electrons striking the linac structure; and neutrons produced by the interaction of the ions with the linac structure at the end of the linac. The target material is typically copper or iron. The production of x rays from back-streaming electrons will depend upon the vacuum conditions and the design of the accelerator (NCRP, 1977). The use of a Faraday cup to intercept the beam downstream of the linac must also be considered in the shielding design.

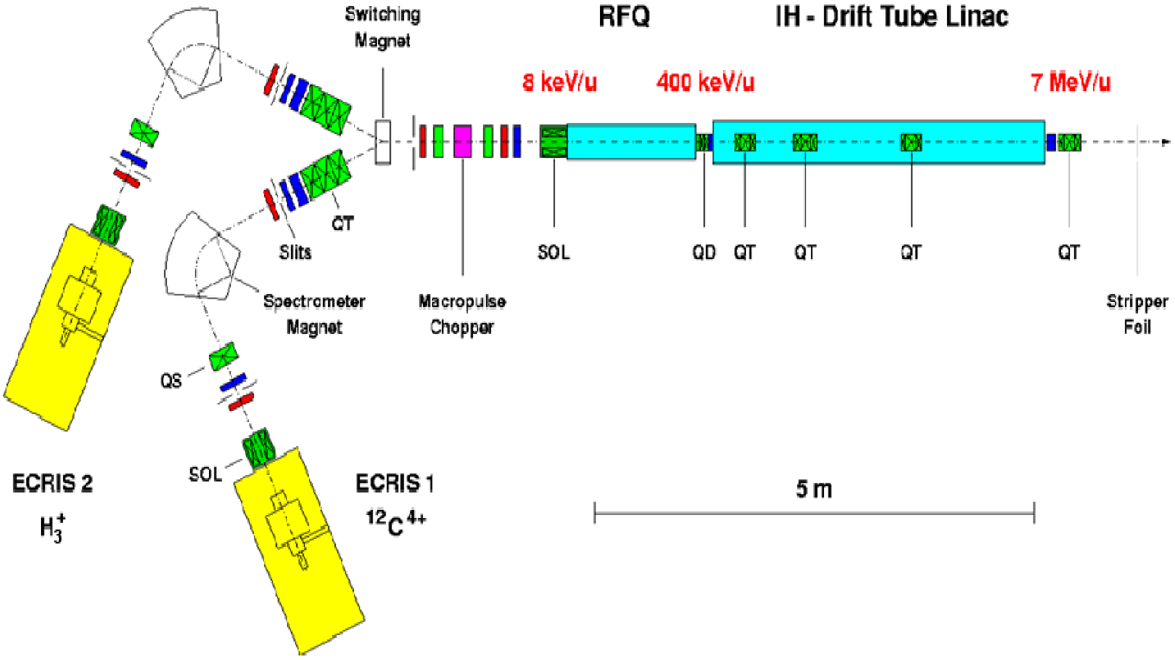

Figure 2.11. Typical injector for synchrotron (Courtesy of *Gesellschaft für Schwerionenforschung*)

Figure 2.12 shows the synchrotron , high energy beam transport (HEBT), and transport to treatment rooms for a typical Siemens particle therapy facility. The synchrotron is capable of accelerating carbon ions to 430 MeV/nucleon and protons to 250 MeV. The synchrotron is filled using a multi-turn injection scheme. The beam is accelerated to the desired energy in less than 1 s. More than 200 beam energies can be requested from cycle to cycle. A slow extraction technique is used to extract the beam and the extraction time varies from 1 s to 10 s.

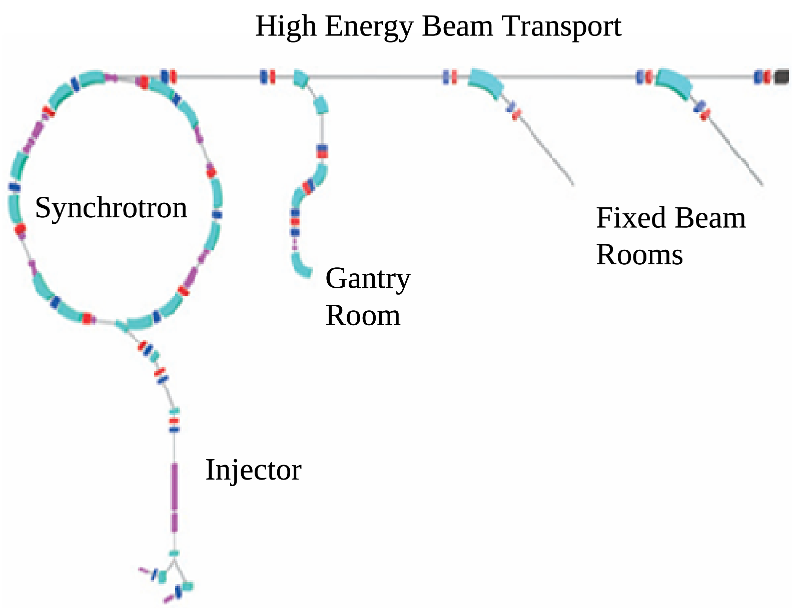

Figure 2.12. Synchrotron, HEBT, and transport to treatment rooms (Courtesy of Siemens Medical Systems)

For synchrotrons in general, beam losses can occur during the injection process, RF capture and acceleration, and during extraction. Some of these losses may occur locally while others may be distributed around the synchrotron. The target material is typically copper or iron. Losses will be machine-specific and therefore the equipment vendor should provide this information. Particles that are not used in a spill may be deflected on to a beam dump or stopper and will need to be considered in the shielding design and activation analysis. In some cases these particles are decelerated before being dumped and therefore are not of concern in the shielding design or activation analysis.

X rays are produced at the injection and extraction septa due to the voltage applied across electrostatic deflectors, and may need to be considered in the exposure to personnel working in the vicinity of the synchrotron components during commissioning.

2.3.3 Beam Transport Line

For both cyclotron- and synchrotron-based systems losses occur in the beam transport line. These losses are usually very low (~ 1 %) and distributed along the beam line, but need to be considered for shielding design. The target material is typically copper or iron. During operation, the beam is steered onto Faraday cups, beam stoppers, and beam dumps, all of which need to be considered in the shielding design.

2.3.4 Treatment Rooms

The radiation produced from the beam impinging on the patient (or phantom) is a dominant source for the treatment rooms. Thus, a thick-tissue target should be assumed in computer simulations for shielding calculations. In addition, losses in the nozzle, beam-shaping, and range-shifting devices must also be considered in the shielding design. The contributions from adjacent areas, such as the HEBT and other treatment rooms, should also be considered

Typically, the treatment rooms do not have shielded doors, and therefore the effectiveness of the maze design is critical. A full computer simulation for the maze is recommended. Mazes are discussed in more detail in Chapter 3. Treatment rooms either have fixed beams rooms or gantries.

2.3.4.1 Fixed Beam Rooms. In fixed beam rooms, either a single horizontal fixed beam or dual (horizontal and vertical or oblique) beams are used. For a facility with both protons and carbon ions, both particles have to be considered for shielding design. Although the proton intensity is much higher than the carbon intensity for synchrotron-based facilities, the neutron dose rate in the forward direction is higher for the carbon ions. Shielding walls in the forward direction are much thicker than the lateral walls and the walls in the backward direction. At large angles and at the maze entrance, the neutron dose from protons is higher than that from carbon ions. Figure 2.13 shows a fixed beam room with a horizontal and a 45° vertical beam. The Use Factor (U) is defined as the fraction of time that the primary proton or carbon ion beam is directed towards the barrier. For rooms with dual beams the Use Factor for the wall in the forward (0°) direction for each beam should be considered. This may be either 1/2 for both beams or 2/3 for one beam and 1/3 for the other. For a single beam, the Use Factor is one for the wall in the forward direction.

1403

1404

1405

1406 Figure 2.13. Fixed beam room with dual beams (Courtesy of Siemens Medical Systems)

2.3.4.2 Gantry Rooms. In gantry rooms, the beam is rotated about the patient. On average, it can be assumed that the Use Factor for each of the four barriers (two walls, floor and ceiling) is 0.25. In some designs, the gantry counterweight (made of large thicknesses of steel) acts as a stopper in the forward direction, but it covers a small angle and is asymmetric. The ceiling, lateral walls, and floor are exposed to the forward-directed radiation. However, because of the lower Use Factor, walls in the forward direction can be thinner than for fixed beam rooms.

2.3.5 Beam Shaping and Delivery

Various methods are used to shape and deliver the beam to the patient. They can be divided primarily into two categories: passive scattering and pencil beam scanning.

In passive scattering, a range modulation wheel or a ridge filter located in the nozzle is used to produce a spread-out Bragg peak (SOBP) (Smith, 2009). Scatterers located downstream spread the beam out laterally. A single scatterer is usually used for small fields and a double scatterer is used for large fields. Between the nozzle exit and the patient, a collimator (specific to the treatment field) is used to shape the field laterally, while a range compensator is used to correct for the shape of the patient surface, inhomogeneities in the tissues traversed by the beam, and the shape of the distal target volume. Since there are losses due to the incidence of the primary beam on the various delivery and shaping devices, a much higher beam current is required at the nozzle entrance when compared to the other delivery techniques. The efficiency of a passive scattering system is typically about 45 %. Therefore, more shielding is required for passive scattering as compared to pencil beam scanning. This technique also results in higher secondary dose to the patient as discussed in Chapter 7.

In pencil beam scanning, horizontal and vertical magnets are used to scan the beam in a plane perpendicular to the beam axis. The range of the beam in the patient is adjusted by changing the beam energy. In synchrotrons, this is achieved by changing the accelerator energy. In cyclotrons, the ESS is used to change the energy. Additionally, energy absorbers can also be used in the nozzle for range shifting and/or range modulation. However, and unlike in passive scattering, there are fewer scatterers and therefore fewer beam losses; thus, the resulting production of secondary radiation is minimized.

2.4 New Technologies

There have been several advances in accelerator technology and some of these are summarized in a paper by Smith (2009). They include single-room systems: cyclotron- or synchrotron-based; Dielectric Wall Accelerator (DWA); Fixed-Field Alternating-Gradient Accelerators (FFAG); and Laser Accelerated Protons.

2.4.1 Single-Room Systems

Figure 2.14 shows a schematic of the proton gantry of a single-room synchrocyclotron-based system that is now commercially available. The maximum proton energy at the exit of the cyclotron is 250 MeV. The 250 MeV beam is scattered or spread in the treatment room by the field shaping system, comprised of the first and second scatterers, energy degrader, and range modulator, which are located in the gantry. Since the cyclotron is super-conducting, it is small and incorporated into the gantry head. The gantry is capable of rotating ± 90 degrees about the patient plane. Therefore only the ceiling, one lateral wall, and the floor intercept the forward-directed radiation, and each of these barriers can be assumed to have a Use Factor of 1/3.

Figure 2.15 shows a 3-D rendition of a single-room cyclotron based facility. The room has two levels with entrances: a patient treatment level, and a sub-level. Thus, there are two entrance mazes, one at each level. Both mazes will require shielded doors due to maze-scattered neutrons and neutron-capture gamma rays. The beam losses to be considered include the primary beam stopped in the patient or phantom, and leakage from the cyclotron and field shaping systems located in the gantry head. The thicknesses of the barriers range from about 1.5 m to 4.0 m of concrete .

Figure 2.16 shows a synchrotron-based single room facility.

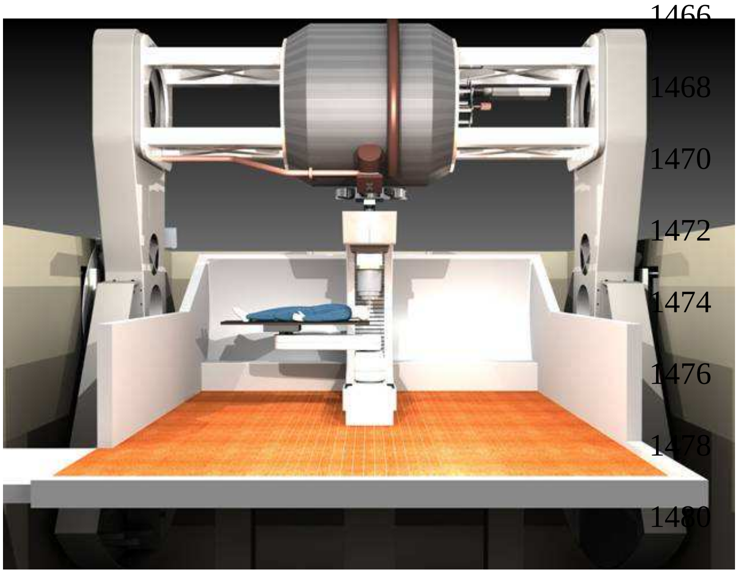

Figure 2.14. Proton therapy gantry including a synchrocyclotron (Courtesy of Still River Systems, Littleton, MA)

Figure 2.15. Architect's 3-D rendition of a synchrocyclotron-based single-room facility (Courtesy of The Benham Companies, An SAIC Company, Oklahoma City, Oklahoma)

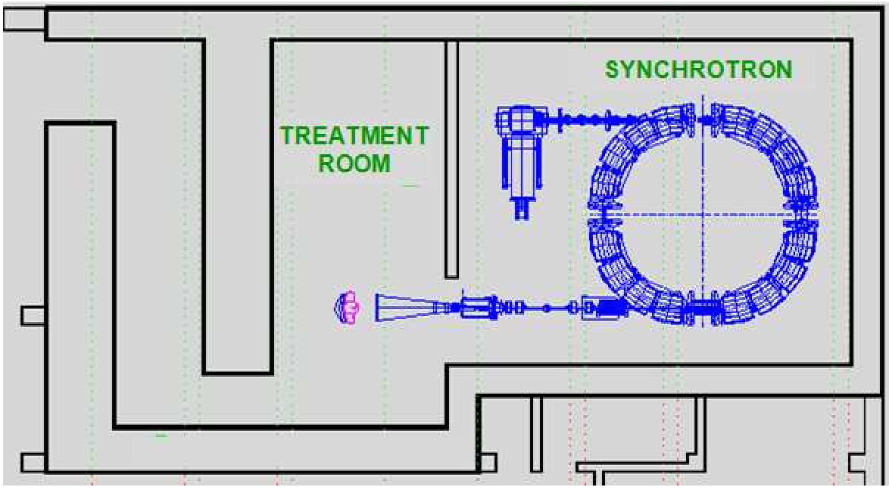

Figure 2.16. Schematic layout of single-room synchrotron-based proton therapy system (Courtesy of ProTom International, Flower Mound, Texas)

Conventional accelerator cavities have an accelerating field only in their gaps, which occupy only a small fraction of the cavity length, and have an accelerating gradient of approximately 1 MeV/m to 2 MeV/m. In contrast, dielectric wall accelerators (DWA) have the potential of producing gradients of approximately 100 MeV/m (Caporasa, 2009). In a DWA, the beam line is replaced by an insulating wall so that protons can be accelerated uniformly over the entire length of the accelerator. Figure 2.17 shows the schematic of a compact proton DWA. Protons can be accelerated to 200 MeV in 2 m. The linac is modular and hence the energy of the protons can be changed easily. The energy, intensity, and spot width can be varied from pulse to pulse with pulse widths of the order of nanoseconds at a repetition rate of 50 Hz. Losses along the linac are minimal since the linac aperture is much larger than the beam size. The primary source of secondary radiation is from the proton beam incident on the patient or the phantom. Since it is a traveling wave linac, bremsstahlung from back-streaming electrons is also not an issue. The linac has the capability of being rotated through at least 200°.

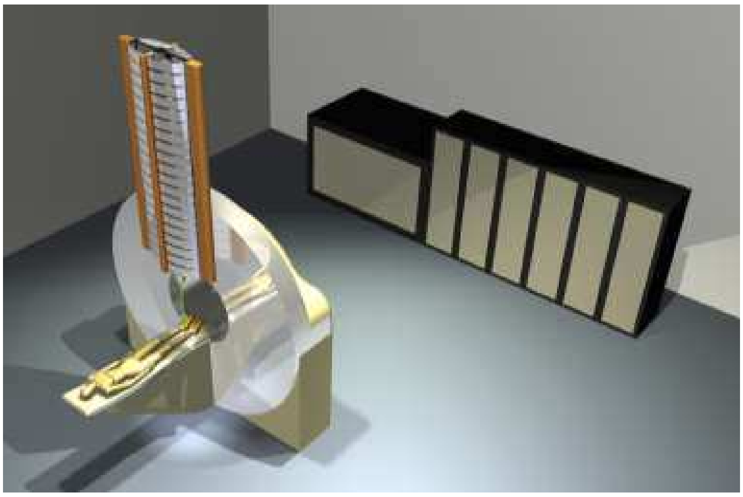

Figure 2.17. Compact proton dielectric wall accelerator (Caporaso, 2009)

2.4.2 FFAG

FFAG accelerators have fixed magnetic fields (as in cyclotrons) and pulsed acceleration (as in synchrotrons). For these accelerators, beam losses discussed in previous sections for synchrotrons and cyclotrons will apply.

2.4.3 Laser Acceleration

A laser pulse interacting with high-density hydrogen-rich material ionizes it, and subsequently interacts with the created plasma. Protons are accelerated by focusing a high-power laser (~10^{21} W cm^{-2}) on a very thin target (~ 0.5 μm to 1 μm thick) with electron densities $n_e = 5 \times 10^{22}$ cm^{-3} (Fan, 2007; Smith, 2009). The resulting high peak power intensity produced by the extremely short pulse width (~ 50 fs) creates a huge burst of ionization in the target, thus expelling a large number of relativistic electrons. The sudden loss of electrons results in a high positive charge on the target. The transient positive field accelerates protons to high energies, resulting in a broad energy spectrum and a large angular distribution. Protons with energies of 200 MeV or higher can be produced. Special particle selection and collimation devices are needed to generate the desired proton beams for treatment. Thus, a large number of unwanted protons and electrons are produced during laser acceleration. For a laser-proton therapy unit, the target foil assembly and the beam selection device are placed inside the rotating gantry. The laser is transported to the gantry directly and to the target foil through a series of mirrors. The electron and proton emission from the target foil are forward-peaked along the axis of the laser beam and have a wide angular spread. Most of the primary charged particles are stopped in the primary collimator. A small fraction passes into the particle selection system. The interaction of these high-energy protons with the selection and collimation devices results in the production of neutrons. The neutrons can further interact with the shielding to produce neutron capture gamma rays. Bremsstrahlung radiation from electrons must also be considered in the shielding design since nearly half of the incident laser energy transfers to electrons, which have a maximum energy that is almost the same as protons. Thus, the leakage radiation consists of neutrons and photons. In addition to leakage, the deposition of the proton beam in the patient, phantom or beam stop must also be considered for room shielding.

3. Shielding Design Considerations

Georg Fehrenbacher and Nisy Elizabeth Ipe

3.1 Regulatory Requirements

The use of charged particle beams for therapy purposes is associated with the generation of ionizing radiation which might expose the facility personnel or the public. Patients can also be exposed to unintended radiation. As stated in previous chapters, neutrons are the main source of secondary radiation to be considered in the shielding design of such facilities. The protection of the following different groups of individuals exposed to secondary radiation has to be considered:

- Occupationally exposed workers
- Members of the public (visitors to the clinic and the public in the vicinity of the facility)
- Patients

Most of the national radiation protection regulations are based on international guidelines or standards. For example, standards are formulated by the International Commission on Radiological Protection ICRP (ICRP, 1991; 2007), which are adapted into international rules such as the EURATOM regulations (EURATOM, 1996) and then incorporated into the European national regulations. The international regulations set a minimum level of standards that can be surpassed by the corresponding national laws. Thus, the national radiation protection regulations are comparable for the countries of the European Union.

In some countries, such as Germany, occupationally exposed workers are further classified into categories depending upon the annual effective dose that they receive: Category A (6 mSv per year) and Category B (20 mSv per year). In this chapter, only the radiation protection for occupational workers and the public are considered. Chapter 7 covers patients. Dose limits are defined for the exposure by external radiation and for the intake of radionuclides leading to an internal exposure.

In the U.S., medical facilities are subject to state regulations. These regulations are based on standards of protection issued by the U.S. Nuclear Regulatory Commission (USNRC, 2009).

The dose limits enforced by national radiation protection regulations are specified in the quantity, effective dose (defined in Chapter 1). Further limits are applied for the exposure of single organs or tissues like the lens of the eye or the skin (ICRP, 1991). Because regulations vary from country to country, it is not possible to list all of them. *However, it is up to each facility to comply with their local, state, or national regulations*. A few examples are given in the sections below.

3.1.1 Radiological Areas

In the U.S., radiological areas are defined as shown below (USNRC, 2009):

> *Radiation Area* means any area accessible to individuals, in which radiation levels could result in an individual receiving a dose equivalent in excess of 0.05 mSv in 1 hour at 30 centimeters from the source of radiation or from any surface that the radiation penetrates.

> *High Radiation Area* means an area accessible to individuals, in which radiation levels from radiation sources external to the body could result in an individual receiving a dose equivalent in excess of 1 mSv in 1 hour at 30 centimeters from any source of radiation or 30 centimeters from any surface that the radiation penetrates.

> *Very High Radiation Area* means an area accessible to individuals, in which radiation levels from radiation sources external to the body could result in an individual receiving an absorbed dose in excess of 5 Gy in 1 hour at 1 meter from a source of radiation or 1 meter from any surface that the radiation penetrates

In addition, radiological areas in the U.S. are classified as *Controlled Areas* when the access, occupancy, and working conditions are controlled for radiation protection purposes (NCRP, 2005). The personnel working in the areas are those who have been specifically trained in the use of ionizing radiation and who are individually monitored. *Unrestricted Area* (or *Uncontrolled Area*) means an area, access to which is neither limited nor controlled by the licensee are areas that have no restriction of access, occupancy or working conditions. These areas are often referred to as *Public Areas*. Individuals who occupy *Uncontrolled Areas* include patients, visitors, service personnel, and employees who do not work routinely with or around radiation sources. Therefore, these individuals do not require individual monitoring. *Restricted Area* means an area, access to which is limited for the purpose of protecting individuals against undue risks from exposure to radiation and radioactive materials.

In Germany, Italy, and Switzerland, the classification of radiological areas is based on the concepts formulated in the IAEA Safety Series No. 115 (IAEA, 1996). A *Controlled Area* is any area in which specific protection measures and safety provisions are or could be required for controlling normal exposures or preventing the spread of contamination during normal working conditions, and preventing or limiting the extent of potential exposures. A *Supervised Area* is any area not designated as a controlled area, but for which occupational exposure conditions are kept under review even though specific protective measures and safety provisions are not normally needed (IAEA, 1996; 2006). The *Interdicted Area* or *Restricted Area* is defined as a part of the controlled area where an increased dose rate level or contamination must be considered. Only in some countries is there an explicit definition of these areas in the radiation protection legislation. Interdicted areas are usually determined by the local radiation safety management. In some countries the concept of *Intermittent Area* is used for the situations where the same area changes the status; for example, the treatment rooms (*Interdicted* during use of the beam, and *Controlled* or *Supervised* the rest of the time).

The radiological areas for a particle therapy facility (in Germany, Italy, and Switzerland) are shown in Figure 3.1. All parts of the accelerator where the particle beam is transported are inaccessible areas (shown in dark blue) while there is beam in the areas. Areas surrounding the accelerator are controlled areas (shown in light blue) or supervised areas (shown in yellow). The dose limits for the public may be applied outside the building (shown in green), which is usually accessible to the public.

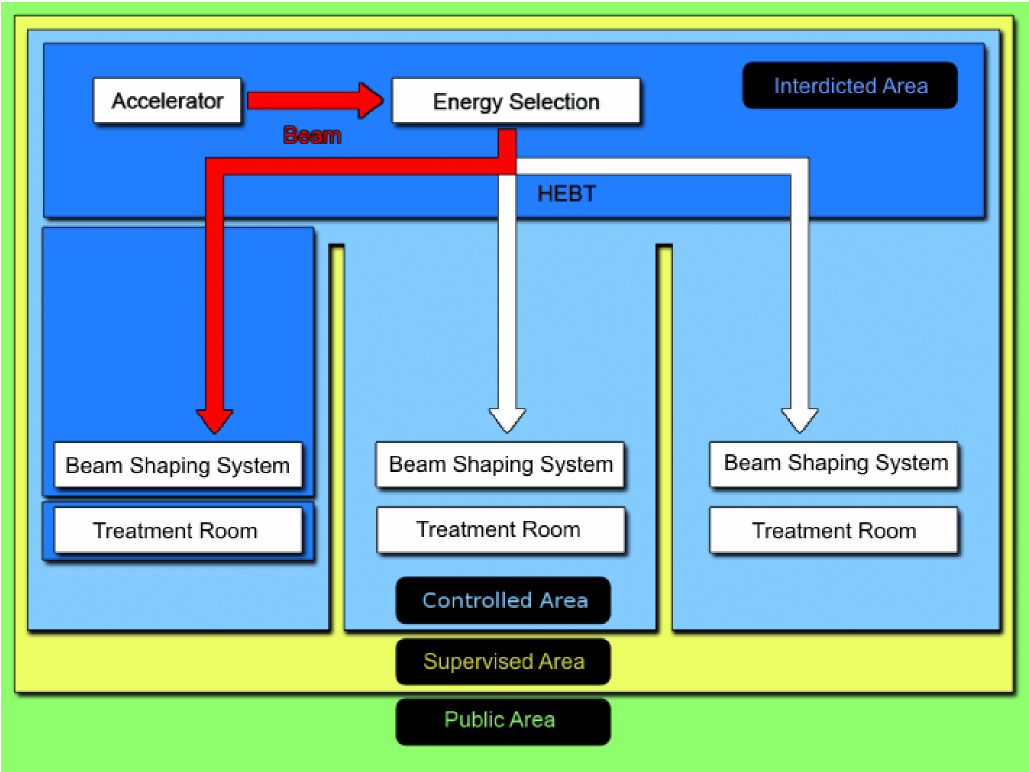

Figure 3.1. Radiological areas for a particle therapy facility (Courtesy of G. Fehrenbacher, J. Goetze, T. Knoll, GSI (2009)).

3.1.2 Dose Limits for Various Countries

Table 3.1 shows the radiological areas and the dose limits for a few countries as an example. The dose limits for the countries in the European Union (Italy and Germany) are similar for controlled, supervised and public areas. In Germany, areas with dose rates > 3 mSv/h are defined as restricted areas. France further classifies the restricted areas as shown in the table. In the U.S., controlled areas have dose limits which are much lower than the dose limits for other countries. Thus, for example, while in the U.S. the control room adjacent to the treatment room has a design dose limit of 5 mSv/yr, dose limits for controlled areas in other countries are much higher. Therefore, a cookie-cutter design originating in one country could potentially underestimate or overestimate the shielding in some areas for a charged particle therapy facility in another country assuming similar patient workload, usage, and beam parameters.

Table 3.1. Examples of classification of radiological areas in some countries. Data sources are cited for each country.

Area	**USA** (USNRC, 2009)	**Japan** (JRPL, 2004)	**South Korea** (Lee, 2008)	**Italy** (IRPL, 2000)	**Switzerland** (BfG, 2004)	**Germany** (GRPO, 2005)	France (JORF, 2006)
Restricted	-	-	-	No general regulation (RSO[1] judgement)	-		Forbidden: >100mSv/h Orange: <2 to100 mSv/h Yellow: < 25 μSv to 2 mSv/h
Controlled	≤ 5 mSv/y	<1 mSv/week	-		<20 mSv/y	<3 mSv/h	Green: 7.5 to 25 μSv /h
Supervised (area near controlled area)		<1.3 mSv/3 months at boundary of controlled area	<0.4 mSv/week (based on 20 mSv/y for radiation workers)	< 6 mSv/y	<5 mSv/y	< 6 mSv/y	< 7.5 μSv /h
Public	≤ 1 mSv/y, 20 μSv in 1 h with T=1	<250 μSv/3 months (outside of site boundary)	< 1 mSv/y	<1mSv/y Recommended operational limit = 0.25 mSV/y	<1mSv/y	<1 mSv/y	< 80 μSv /month

[1](RSO=Radiation Safety Officer)

3.2 Primary and Secondary Shielding Barriers

In photon therapy, the radiation consists of primary and secondary radiation (NCRP, 2005). The primary radiation (also referred to as the useful beam) is the radiation emitted directly from the equipment that is used for patient therapy. The primary barrier is a wall, ceiling, floor, or other structure that will intercept the primary radiation emitted directly from the equipment. The secondary barrier intercepts the leakage radiation from the protective housing of the source, as well as any radiation scattered by the patient or other objects.

For the purposes of this report, for charged particle therapy facilities, we will refer to the protons or carbon ions as the "primary beam." The "secondary radiation" will include all the radiation produced by the interaction of the primary beam with any target including the patient, leakage radiation from the machine, as well as any scattered radiation. Hence, a primary barrier is defined as a shielding wall, ceiling, floor, or other structure toward which the primary proton or carbon beam is directed. The primary barrier intercepts the 0° secondary radiation produced by the interaction of the primary beam with any target, including the patient. If the primary beam is directed toward the corner of a wall, then the corner becomes the primary barrier. The secondary barrier is defined as any wall, floor, or ceiling which is not the primary barrier, *i.e.*, it does not intercept the 0° secondary radiation.

3.3 Use Factors

For photon therapy, the "use factor" as a function of gantry angle [U(G)] gives the fraction of the weekly workload for which the gantry or beam is oriented in an angular interval centered about angle G (NCRP, 2005). The IAEA defines the use factor for photon therapy as the fraction of the time during which the radiation under consideration is directed at a particular barrier (IAEA, 2006). For charged particle therapy facilities, the use factor (U) may be defined as the fraction of beam operation time during which the primary proton or carbon ion beam is directed toward a primary barrier. For a gantry room where the beam rotates 360° about an isocenter, the distribution of gantry treatment angles will be symmetrical and therefore one can assume a use factor of 1/4 for each of the primary barriers, *i.e.*, two walls, ceiling, and floor which directly intercept the primary beam. For a gantry that rotates ± 90° about the isocenter, a use factor of 1/3 can be assumed for each of the primary barriers, *i.e.*, one wall, ceiling, and floor. For a horizontal fixed beam room, the primary beam direction is fixed, and the use factor is 1 for the barrier toward which the primary beam is directed. Thus, the shielding thickness of each of the four primary barriers for a gantry room will be less than the thickness required for a fixed beam primary barrier, because the use factor is only 1/4.

3.4 Occupancy Factor

The occupancy factor (T) for an area is the average fraction of the time that the maximally exposed individual is present in the area while the beam is on (NCRP, 2005). If the use of the machine is spread out uniformly during the week, the occupancy factor is the fraction of the working hours in the week during which the individual occupies the area. For instance, corridors, stairways, bathrooms, or outside areas have lower occupancy factors than offices, nurse's stations, wards, staff, or control rooms. The occupancy factor for controlled areas is typically assumed to be 1, and is based on the premise that a radiation worker works 100 % of the time in one controlled area or another. However, there can be exceptions where access to a controlled area is restricted for a radiation worker when radiation is being produced. In such a case, a lower occupancy factor may be deemed appropriate by the qualified expert (defined in Section 3.11). The NCRP and IAEA list occupancy factors for various areas (IAEA 2006, NCRP 2005).

3.5 Workload

The concept of workload (W) for photon radiotherapy is defined as the time integral of the absorbed dose rate determined at the depth of the maximum absorbed dose in the patient, at a distance of 1 m from the source (NCRP, 2005). It is usually specified as the absorbed dose from photons delivered to the isocenter in a week, is based on the projected use, and is estimated from the average number of patients (or fields) treated in a week and the absorbed dose delivered per patient (or field). It also includes the average weekly absorbed dose delivered during calibrations, quality controls, and physics measurements. This concept of workload cannot be directly applied to charged particle therapy facilities for the following reasons:

1. In photon therapy, the workload is defined in terms of the primary beam photon dose rate at the isocenter in a treatment room. Photoneutrons are produced only when the incident photon energy is higher than about 6 MV. The average energies of the photoneutrons are 1 MeV to 2 MeV. (NCRP, 2005). Photoneutrons are produced mainly in the accelerator head and any external high-*Z* target such as lead shielding, *etc*. The photoneutron dose equivalent rate (from neutrons produced in the accelerator head) is less than 0.1 % of the primary beam photon dose at the isocenter. The photon leakage dose rate from the accelerator head is also less than 0.1 % of the primary photon beam dose rate at the isocenter. The tenth value layer of the primary photons and leakage photons is significantly greater than tenth value layer of the photonneutrons. Therefore, if the facility is shielded for photons with concrete, it will be more than adequately shielded for photoneutrons. For charged particle therapy, any target that intercepts the primary beam becomes a source of secondary high-energy radiation which must be shielded. For

example, during treatment the proton or ion beam (primary beam) is completely stopped in the patient tissue, and that then becomes a source of secondary radiation. Further, secondary radiation production can also occur in beam shaping devices and the beam nozzle. The secondary radiation dominated by high-energy neutrons determines the shielding of the treatment room.

2. An important distinction needs to be made when comparing photon therapy and charged particle therapy. For example, in a gantry room, even though the dose is delivered to the patient (located at the isocenter of a gantry room), the secondary radiation dose is defined at 1 m from the isocenter and not at the isocenter, as in photon therapy. Furthermore, in charged particle therapy the distribution of secondary radiation dose is forward-peaked and has an angular profile and spectra, unlike in photon therapy, where the photoneutrons have an almost isotropic distribution.

3. Depending upon the chosen irradiation technique, the energy of the ion beam changes (*e.g.*, the energy selection system (ESS) for protons from cyclotrons or the use of synchrotrons for protons and heavy ions).

4. For photon therapy there is only one shielded treatment room. For charged particle therapy, in addition to shielded treatment rooms, the cyclotron or synchrotron, the beam transport lines, and the research rooms are also shielded. These areas may have beam when there is no beam in the treatment room.

5. For charged particle therapy facilities, the distinction of the type of primary particle type is important, because the different energy-angular distributions of the secondary neutrons influence the shielding design.

6. The time structure of the charged particle therapy beam can be rather complicated in comparison to a photon therapy linear accelerator. Therefore, one has to take into account the fact that the produced radiation may have a highly discontinuous time structure.

7. In charged particle therapy, the patient dose is expressed in the unit Gy equivalent, with RBEs which have values higher than 1 for heavier ions (like carbon). The shielding design is essentially based on the (averaged) spectral neutron energy fluence weighted with dose conversion coefficients (spectral dose distribution). The same dose value for the irradiated tissue can be associated with significant differing spectral dose distributions.

Thus, the workload must be used in a generic sense to include for each treatment room, each particle type, each energy, the beam shaping method, the number of fractions per week and the time per fraction, the dose per fraction, and the proton or carbon ion current required to deliver a specific dose rate. Once the workload for the treatment room has been established, one must work backwards to determine the energies and currents from the cyclotron or the synchrotron. The workload for the cyclotron or synchrotron can then be determined. The workload for each facility will be site-specific. Further the beam losses, targets and their locations, and associated currents are equipment-specific and will vary from one equipment vendor to the other.

3.5.1 Example for Workload Calculations and Usage Assumptions

An example for workload calculations and usage assumptions, assuming 100 % uniform scanning for a proton cyclotron facility with a maximum proton energy of 230 MeV, is shown below. The reader is cautioned against blindly using the example below because it may not be applicable to his or her facility.

In the following example, we assume a proton cyclotron facility with one gantry room, one inclined beam room, and one fixed beam room. In each of the three rooms, we assume a total of 25 treatments or fractions per 8 hour day. Treatments are performed at different energies, and 100 % uniform scanning is assumed. For each energy, the proton current (in nA) required for a 2 Gy/min dose rate in the patient is provided by the equipment vendor. We assume that each treatment delivers a dose of 2 Gy, which corresponds to a 1 minute irradiation time. A stopping tissue target is assumed in each treatment room. Based on the treatments, we determine the fraction of time the cyclotron operates at each energy. The beam losses and targets in the cyclotron, energy selection system and target, and beam transport line are provided by the equipment vendor.

1. Gantry room and inclined beam rooms:
    a) Beam-on time for 2 Gy = 25 fractions/8 h x 40 h/week x 1 min/fraction = 125 min/week
    b) Treatments and beam parameters
        i. 20 % of treatments at 180 MeV, 3.3 nA at 2 Gy/min
        ii. 60 % of treatments at 130 MeV, 2.3 nA at 2 Gy/min
        iii. 20 % of treatments at 88.75 MeV, 3.09 nA at 2 Gy/min

2. Horizontal beam room:
    a) Beam-on time for 2 Gy = 25 fractions/8 h x 40 h/week x 1 min/fraction = 125 min/week

    b) Treatments and beam parameters
        i. 80 % of treatments at 216 MeV, 4 nA at 2 Gy/min
        ii. 20 % of treatments at 180 MeV, 3.3 nA at 2 Gy/min

3. Cyclotron
    a) Beam-on time = 20 h/week
    b) Beam energies
        i. 20 % at 216 MeV
        ii. 20 % at 180 MeV
        iii. 45 % at 130 MeV
        iv. 15 % at 130 MeV (88.75 MeV at patient)
    c) Beam losses in cyclotron
        i. Transmission efficiency = 35 %
        ii. Losses at 10 MeV (20 %), ignored because of low energy (10 MeV)
        iii. 4 counter dees (20 % loss), 10 % at 230 MeV, 10 % at 150 MeV
        iv. Septum (35 % loss), all at 230 MeV
        v. 5 % loss between cyclotron and degrader

4. ESS (Energy selection system)
    a) Energies
        i. Carbon degrader: 230 MeV
        ii. Tantalum collimator: 216 MeV, 180 MeV, 130 MeV
    b) Beam loss varies depending upon energies requested. Maximum beam loss occurs at ESS.

5. BTL (Beam transport line)

a) Beam-on time = 20 h/week
b) Beam Loss = 5 %
c) Beam Energies
   i. 20 % operation at 230 MeV
   ii. 20 % operation at 180 MeV
   iii. 45 % operation at 130 MeV
   iv. 15 % operation at 130 MeV (88.75 MeV at patient)

3.5.2 Beam Parameters Used for Shielding Calculations

Table 3.2 shows, for the above example, the beam parameters as provided by the equipment vendor and the calculated parameters using the vendor's data that are required for shielding calculations. Column 1 shows the energy of the proton beam at the degrader. Column 2 shows the thickness of the carbon degrader in the ESS. Column 3 shows the degrader energy. Column 4 shows the thickness of the carbon range shifter in the nozzle. The range shifter is used only to degrade 130 MeV to 88.75 MeV in the nozzle. Column 5 shows the proton beam energy at the nozzle exit. Column 6 shows the range in patient. Column 7 shows the beam size. Column 8 shows the beam current at the cyclotron exit. Column 9 shows the ESS transmission obtained by interpolating data from the equipment vendor for uniform scanning. Column 10 shows the beam currents at the nozzle entrance. Column 11 shows the beam current in the BTL calculated backwards, *i.e.* dividing the currents in Column 10 by 0.95 to account for 5 % loss in the BTL. The columns in italics show information provided by the vendor.

For shielding calculations, the currents shown in Column 8 are used for the cyclotron calculations, while the currents shown in Column 10 are used for treatment rooms and the currents shown in Column 11 are used for BTL. All the losses in the carbon degrader occur at 230 MeV but with varying thicknesses as shown in Table 3.2. For the septum and the counter dees, a copper stopping target is assumed. For losses in the counter dees, 50 % of the losses occur at 230 MeV, while the remaining 50 % occur at 150 MeV.

The contribution of multiple sources to dose at any given location must be considered in the shielding design. For example, a room in the vicinity of one treatment room may also see dose from the adjacent treatment room.

Table 3.2. An example of beam parameters used for shielding calculations.

Beam Energy at Cyclotron Exit and Degrader (MeV)	ESS Carbon Degrader Thickness (mm)	Beam Energy at Tantalum Collimator and Nozzle Entrance (MeV)	Carbon Range Shifter Thickness in Nozzle (g/cm^2)	Beam Energy at Nozzle Exit (MeV)	Range in Patient (g/cm^2)	Beam Size (cm x cm)	Beam Current at Cyclotron Exit (nA)	ESS Transmission	Beam Current at Nozzle Entrance (nA)	Beam Current in BTL Calculated Backwards Assuming 5 % Loss in Iron Target
230		130	*4.1*	88.75	*6.24*	30 x 30	*90.35*	*0.0068*	*3.09*	3.25
230	*130*	130		130	*21.3*	30 x 30	*51.0*	*0.0068*	*2.3*	2.42
230	*74.4*	180		180		30 x 30	*15.83*	*0.0455*	*3.3*	3.47
230	*26.51*	216		216	*22*	30 x 30	*7.5*	*0.1916*	*4*	4.21
230	*0.0*	230		230	*31.8*	30 x 30	*4.72*	*0.446*	*3.77*	3.97

Table 3.3 shows a summary of a survey of beam losses at various synchrotron and cyclotron particle therapy facilities.

Table 3.3. Survey of beam losses at various synchrotron and cyclotron particle therapy facilities. Data sources are given for each survey.

Accelerator Type	**Synchrotron**		**Cyclotron**
Particle Type	Carbon		Proton
Injection LINAC-Synchrotron	60 % (Noda, 2004)		-
Loss in the accel.	36 % (Noda, 2004) 5 % (Agosteo, 2001)		50 % (Avery, 2008) 55 % (Geisler, 2007) 65 % (Newhauser, 2002)
Extraction	10 % (Noda, 2004) 5 % (Agosteo, 2001)		50 % (Avery, 2008) 20 % (Geisler, 2007) or higher
HEBT (High Energy Beam Transport)	~ 5 % (Noda, 2004) ~ 4 to 7 % (Agosteo, 2001)		~ 5 % 1% (Newhauser, 2002)
Beam Shaping	**Active**	**Passive**	**Passive**
ESS (Energy Selection System)	-	70 % (Noda, 2004)	> 55 % (99 %) (Geisler, 2007), (Rinecker, 2005) 63 % (Newhauser, 2002)

3.6 Self-Shielding of Beam Line Components

The beam lines are comprised of massive beam optics elements such as dipoles, quadrupoles, sextupoles, *etc.* As expected, beam losses may occur in these magnets when the particles deviate from their predetermined path. The elements are typically made of materials such as steel and copper which provide a large amount of self-shielding. The exact amount of beam losses in these magnets is usually unknown, and the details of these magnets are not usually provided by the equipment vendor. Self-shielding of accelerator components can be taken into account by using known beam losses and a (simplified) model of the magnets in Monte Carlo calculations. When self-shielding is neglected in shielding calculations, the measured radiation doses are significantly lower than calculated doses. The cyclotron and the gantry also have a large amount of self-shielding. The self-shielding of the cyclotron is usually considered in the shielding design, except at the location where there are openings in the magnet yoke.

3.7 Calculational Methods

3.7.1 Analytical Methods

Most analytical models can be described as line-of-sight (also called point kernel) models which incorporate the following parameters and assumptions:

1. Point loss;
2. Distance of the point source to reference point (r);
3. Angle of the incident beam (line) and the direction to the reference point (θ);

4. Angular specific source term $H_0(E_p,\theta)$ which depends on the ion type and target type, as well as E_p, the particle energy;
5. Exponential attenuation in shielding material of thickness d_0, where d ($d_0/\sin(\theta)$) is the slant thickness, and $\lambda(\theta)$ is the attenuation length. λ depends on the angle θ, because the neutron energy distribution changes with the angle θ.

Figure 3.2 shows the geometry for the line-of-sight-model.

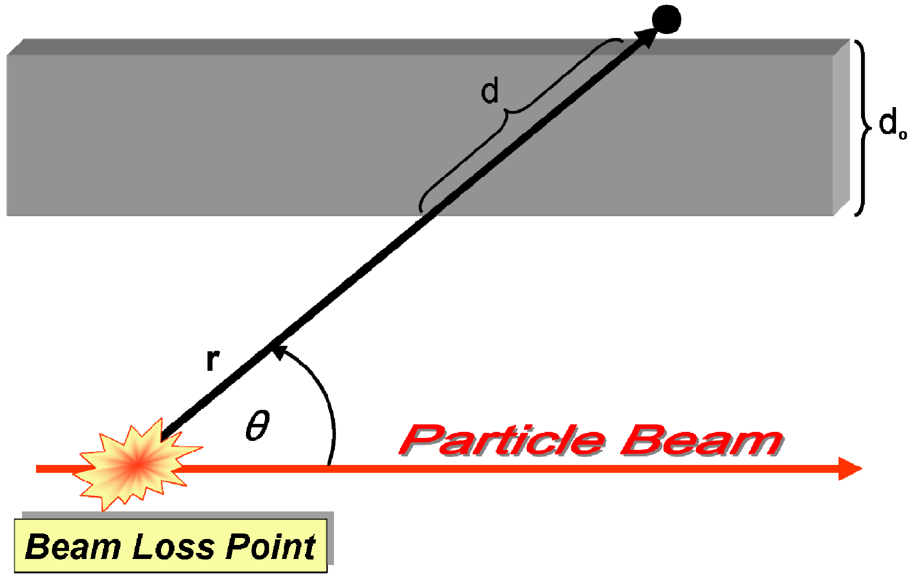

Figure 3.2. Application of the line-of-sight models to simple bulk shielding geometries (Courtesy of G. Fehrenbacher, J. Goetze, T. Knoll, GSI (2009)).

The dose (rate) at the reference point is derived from the source term H_0 and geometrical quantities. The dose $H(E_p, d, \theta)$ at the reference point can then be estimated as follows:

$$H(E_p, d, \theta) = H_0(E_p, \theta) \cdot \tfrac{1}{r^2} \cdot \exp\left(-\tfrac{d}{\lambda(\theta)}\right) \tag{3.1}$$

In 1961, Burton Moyer developed a semi-empirical method for the shield design of the 6 GeV proton Bevatron (NCRP, 2003). Design studies of the proton synchrotron at Fermi National Accelerator Laboratory (FNAL, Batavia, Illinois) and the Super Proton Synchrotron (SPS, CERN, Geneva) led to the improvement of the Moyer model. This model is only applicable to angles close to 90° and the transverse shielding for a high-energy proton accelerator is determined using the following simple form of the Moyer model (Thomas, 1993):

$$H = \frac{H_0}{r^2}\left[\frac{E_P}{E_0}\right]^{\alpha} \exp\left[-\frac{d}{\lambda}\right] \tag{3.2}$$

where H = maximum dose equivalent rate at a given radial distance (r) from the target, d = shield thickness, E_P = proton energy, E_0 = 1 GeV, H_0 = 2.6 x 10^{-14} Sv m^2, and α is about 0.8.

This model is effective in the GeV region because the neutron dose attenuation length (λ) is nearly constant regardless of energy (see Fig. 1.3). However, the model is restricted to the determination of neutron dose equivalent produced at an angle between 60° to 120°. At proton energies in the therapeutic range of interest, the neutron attenuation length increases considerably with energy as shown in Fig. 1.3. Clearly, such empirical models are limited in their use because they are limited to transverse shielding, and do not account for changes in energy, angle of production, target material and dimensions, and concrete material composition and density. In the past, the Moyer model has been used in the shielding design of some proton therapy facilities; however, it is not appropriate for such use.

Kato and Nakamura have developed a modified version of the Moyer model which includes changes in attenuation length with shield thickness, and also includes a correction for oblique penetration through the shield (Kato, 2001). Tesch has also developed a model for proton energies from 50 MeV to 1 GeV (Tesch, 1985). In the past, high-energy accelerators were shielded using analytical methods. However, with the advent of powerful computers and sophisticated Monte Carlo codes, computational methods have superseded analytical methods. Analytical methods may be used for the planning of the bulk shielding, but do not provide a very precise prediction of the dose rate levels outside the shielding. The advantages of analytical methods are their ease of use and the comparatively high efficiency in obtaining results. Their drawbacks are the very simplistic assumptions, limited applicability to simple planar geometries, and limitations of target materials and geometry.

3.7.2 Monte Carlo Calculations

Monte Carlo codes are described in detail in Chapter 6, and are used extensively for shielding calculations. These codes can be used to do a full simulation, modeling the accelerator or beam line and the room geometry in its entirety. They can also be used to derive computational models as discussed in the next section. Monte Carlo codes have been used for shielding design of rooms or mazes at several facilities (Agosteo *et al.*, 1996b; Avery *et al.*, 2008; Dittrich and Hansmann, 2006; Hofmann and Dittrich, 2005; Kim *et al.*, 2003; Porta *et al.*, 2005; Stichelbaut, 2009). Monte Carlo codes can be used to generate isodose curves (dose contours), which provide a visualization of the secondary radiation field that helps facilitate the shielding design (Hofmann and Dittrich, 2005). It is important to note that when comparing Monte Carlo calculations to experimental data, the actual experimental configuration should be modeled, including the instrument response and the concrete composition. Further, the experiment should have been performed using the appropriate instrumentation. If there are any deviations from the above conditions, there will be large discrepancies between measurements and simulations. Unfortunately, there is hardly any published data for charged particle therapy facilities that meets all these conditions.

3.7.3 Monte Carlo Computational Models

Monte Carlo computational models that are independent of geometry typically consist of a source term and an exponential term that describes the attenuation of the radiation. Both the source term and the attenuation length are a dependent on particle type and are a function of energy and angle. Agosteo *et al.* (1996b) first derived such models using experimental double differential neutron spectra, but the data is now obsolete (Agosteo, 2007). Ipe and Fasso (2006) have published source terms and attenuation lengths for composite barriers with 430 MeV carbon ions incident on a 30 cm ICRU sphere. As discussed in Chapter 1, computational models are useful especially during the schematic phase of the facility design, when the design undergoes several changes, to determine the bulk shielding. In this case, the entire room geometry is not modeled but usually spherical shells of shielding material are placed around the target, and dose is scored at given angular intervals and in each shell of shielding material. The dose at each angle can be plotted as a function of shielding thickness and the data can be fitted to obtain source terms and attenuation lengths as a function of angle, and at the energies of interest, with the appropriate target using Monte Carlo methods. The source terms and attenuation lengths will depend upon the composition and density of the shielding material. A stopping target can be used to determine dose rates from the beam incident on the patient. However, the use of a stopping target is not necessarily conservative in all cases, because for a thin target, the hadron cascade may propagate in the downstream shielding. Ray traces can be performed at various angles and the source terms and attenuation lengths can be used for dose calculations. These models are also useful in identifying thin shielding and facilitates improved shield design. The qualified expert should not rely on published models but should derive computational models for energies, targets and concrete composition that are site specific.

3.7.3.1 Carbon Ions. Ipe and Fasso (2006) describe Monte Carlo calculations performed using FLUKA to derive computational models for 430 MeV/u carbon ions incident on tissue. The simulations were performed so that source terms and attenuation lengths in concrete and composite barriers (concrete plus iron) could be determined for 430 MeV/u carbon ions incident on an ICRU tissue sphere (15 cm radius, 76.2 % O, 10.1 % H, 11.1 % C, and 2.6 % N). The concrete was assumed to be Portland cement with a density of 2.35 g cm^{-3}.

Figure 3.3 shows the total ambient dose equivalent from all particles in picosieverts per carbon ion normalized to a distance of 1 m from the target ($pSv\text{-}m^2$) as a function of shielding thickness. The dose at any distance *d* from the tissue target is obtained by dividing the dose at 1 m by d^2. Also shown is the dose equivalent in vacuum. It is important to note that there is a dose build-up in the first few layers of the shielding before attenuation takes place. Therefore, dose equivalent rates in vacuum should not be used to determine shielding thicknesses. The errors are not shown but are typically within 20 %. The attenuation length, λ, changes with shielding depth and reaches equilibrium after about 1.35 m of shielding thickness. The data in Figure 3.3 were fitted with the classical two parameter formula as shown in Equation 1.1. The equilibrium attenuation length, λ_e, is given by the reciprocal of the exponent. The results are shown in Table 3.4 together with the parameters for two other polar angles (10° to 30° and 40° to 50°). The source terms and attenuation lengths are valid for shielding thicknesses greater than 1.35 m. The attenuation lengths shown are the dose equivalent attenuation lengths for all particles and not just for neutrons. The attenuation length in the 10° to 30° range is higher than in the forward direction. A similar observation was made by Agosteo *et al.* (1996b) for 400 MeV/u carbon ion data. This may be attributed to the fact that head-on collisions for carbon ions are less frequent than grazing collisions (Raju, 1980).

In general, it can be observed that the addition of 30 cm of iron provides a reduction in the source term by a factor of about 2. In the forward direction (0° to 30°), there is a softening of the spectrum with the addition of iron, as can be observed by the change in attenuation length. At large angles (40° to 60°), the iron does not appear to provide any significant softening of the spectrum. It is important to note that the source terms and attenuation lengths will depend upon the particle energy, the material and dimensions of the target, the angle of production, the fluence to dose equivalent conversion factors, and the composition and density of the shielding material. Additionally the source terms and attenuation lengths will also depend on how good the fit is. There is no other published data on source terms and attenuation lengths (computational or experimental) for 430 MeV/u carbon ions.

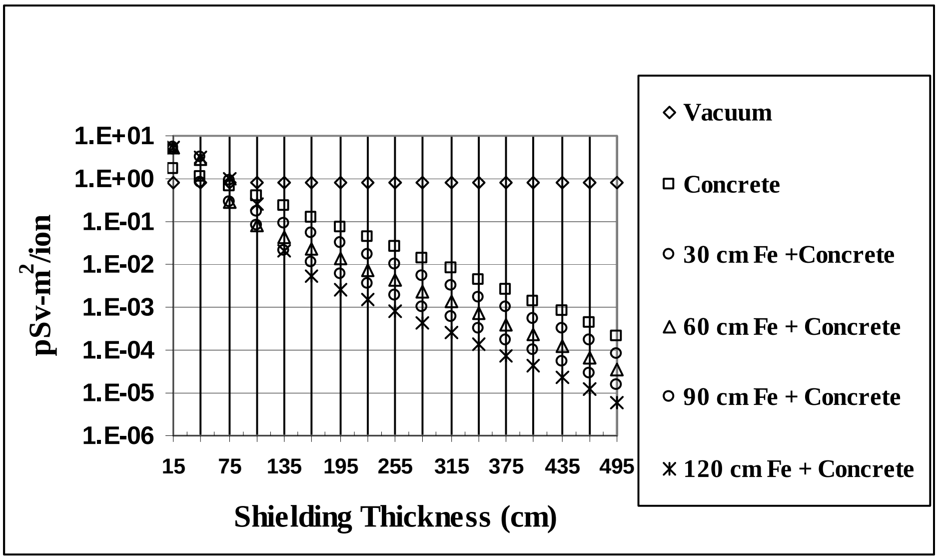

Figure 3.3. Dose equivalent per carbon ion (0° to 10°) as a function of shielding thickness for 430 MeV/u carbon ions incident on ICRU tissue sphere for composite shield (Ipe and Fasso, 2006).

Table 3.4 Computational models for concrete and composite shield (concrete and iron) for 430 MeV/u carbon ions incident on ICRU tissue sphere (15 cm radius) valid for shielding thickness > 1.35 m (Ipe and Fasso, 2006).

Iron Thickness (cm)	0° to 10°		10° to 30°		40° to 60°	
	H_0 ($Sv\text{-}m^2$/ion)	λ_e (g/cm^2)	H_0 ($Sv\text{-}m^2$/ion)	λ_e (g/cm^2)	H_0 ($Sv\text{-}m^2$/ion)	λ_e (g/cm^2)
0	$(3.02 \pm 0.04) \times 10^{-12}$	123.81 ± 0.48	$(4.81 \pm 0.06) \times 10^{-13}$	133.09 ± 0.74	$(4.71 \pm 0.21) \times 10^{-14}$	117.64 ± 1.32
30	$(1.25 \pm 0.02) \times 10^{-12}$	123.12 ± 0.38	$(2.44 \pm 0.03) \times 10^{-13}$	$129.64. \pm 0.36$	$(1.91 \pm 0.08) \times 10^{-14}$	119.38 ± 0.48
60	$(6.05 \pm 0.03) \times 10^{-13}$	120.32 ± 0.46	$(1.11 \pm 0.04) \times 10^{-13}$	128.66 ± 0.70	$(8.29 \pm 0.66) \times 10^{-15}$	118.5 ± 0.80
90	$(2.77 \pm 0.09) \times 10^{-13}$	119.58 ± 1.25	$(5.27 \pm 0.29) \times 10^{-14}$	126.09 ± 0.80	$(3.29 \pm 0.69) \times 10^{-15}$	119.14 ± 1.34
120	$(1.33 \pm 0.05) \times 10^{-13}$	117.68 ± 0.91	$(2.48 \pm 0.24) \times 10^{-14}$	124.29 ± 0.94	$(1.34 \pm 0.68) \times 10^{-15}$	118.83 ± 2.89

Figures 3.4 and 3.5 show the dose per carbon ion in picosieverts per particle normalized to 1 m ($pSv\text{-}m^2$) as a function of concrete thickness for both iron (Fe) target and tissue targets in the 0° to 10° and 80° to 100° directions. In the forward direction, the doses in vacuum and concrete are higher for the tissue target when compared to the iron target, whereas at the large angles, the doses are lower for the tissue target when compared to the iron target. This is because the high-energy neutron components produced in the forward direction by a break-up process and the momentum transfer from projectile to target nuclei are higher for both lighter nuclei targets and higher projectile energy than for heavier nuclei targets and lower projectile energy (Gunzert-Marx *et al.*, 2004). Thus, more forward-directed neutrons will be produced in a stopping tissue target than in a stopping iron target. For both targets, there is a build up in dose in the first few layers of the concrete shield. The attenuation lengths reach equilibrium only after about a meter or more of concrete in the forward direction.

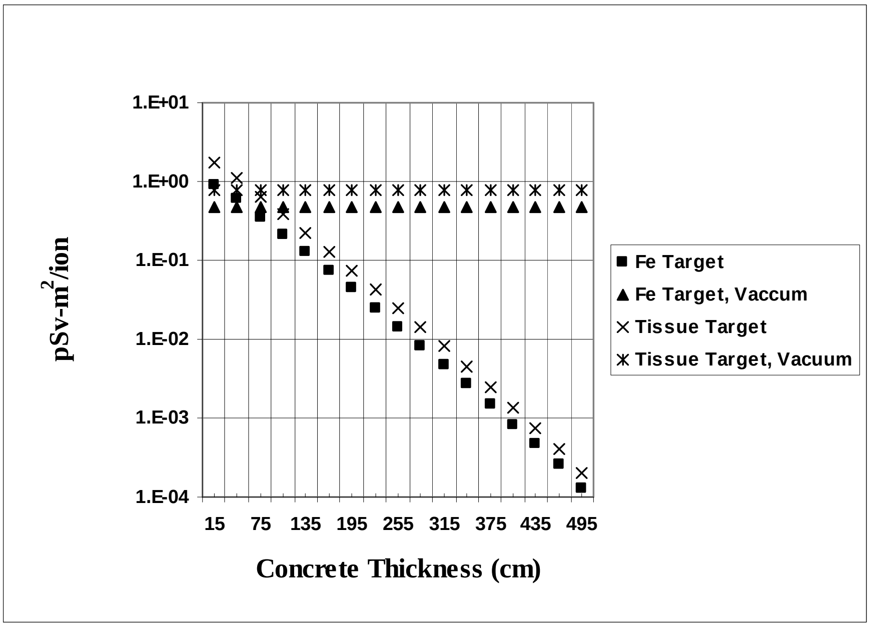

Figure 3.4. Dose equivalent per carbon ion (0° to 10°) as a function of concrete thickness for 430 MeV/u carbon ions incident on ICRU tissue and iron targets (Ipe and Fasso, 2006).

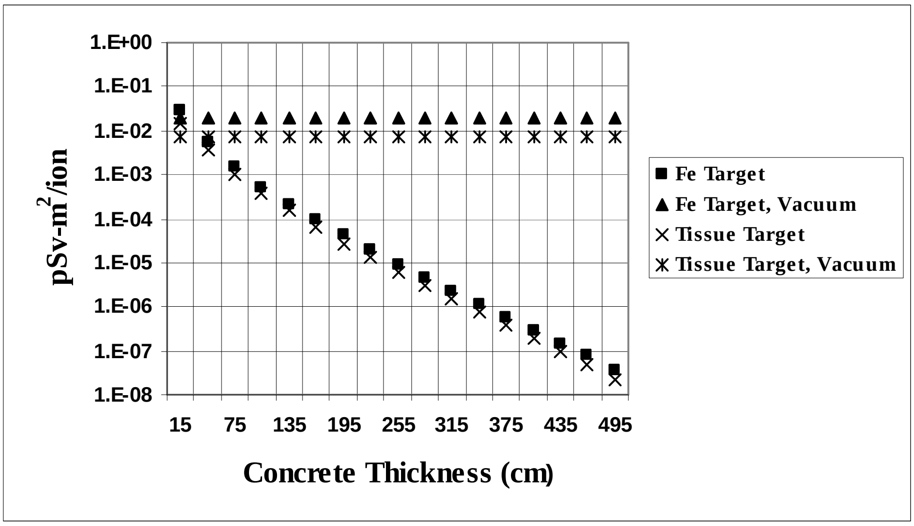

Figure 3.5. Dose equivalent per carbon ion (80° to100°) as a function of concrete thickness for 430 MeV/u carbon ions incident on ICRU tissue and iron targets (Ipe and Fasso, 2006).

Figure 3.6 shows the relative dose equivalent contributions of the various particles for 0° to 10° at 1 m from the target. Neutrons are the largest contributor to the total dose. At a depth of 15 cm in concrete, about 66 % of the dose is from neutrons, about 32 % from protons, less than 2 % from photons, and less than 0.2 % from charged pions. The neutron contribution increases to about 95 % at greater depths. At large angles (not shown in the figure), the neutron contribution remains fairly constant at all depths (96 %), while the proton contribution increases from less than 1 % to about 2 % with increasing depths. Thus, neutrons dominate the dose outside the shielding at all angles.

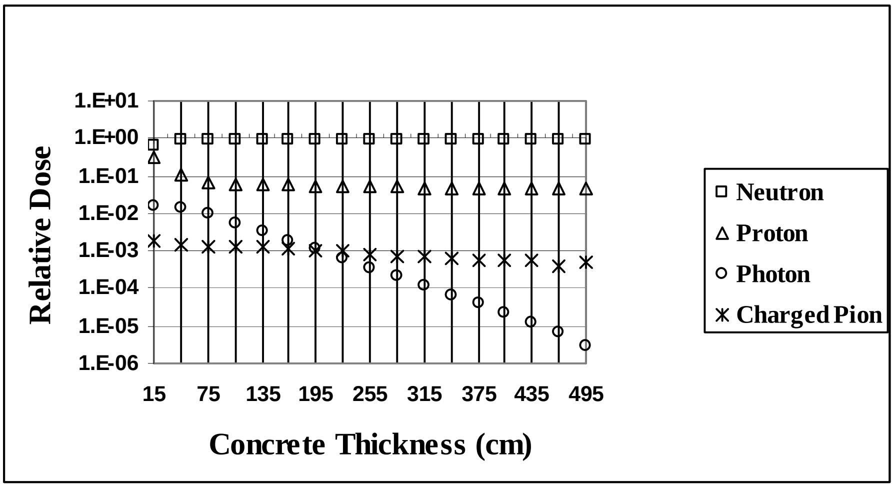

Figure 3.6. Relative dose equivalent contributions at 0° to 10° per carbon ion at 1 m from ICRU tissue sphere (Ipe and Fasso, 2006).

Figure 3.7 shows the neutron spectra from 430 MeV/u carbon ions incident on tissue at the concrete surface, for 0° to10° and for 80° to 90°. The errors are not shown but are typically within 20 %. The fluence is in lethargy units, *i.e.*, E x $d\varphi/dE$, where E is the neutron energy and $d\varphi/dE$ is the differential fluence. The neutron fluence in the forward direction (0° to 10°) is much greater than the neutron fluence at the large angles (80° to 100°) at the concrete surface. The neutron spectrum in the forward direction extends up to about 1 GeV in energy, while the spectrum at the large angle extends to about 0.4 GeV. In both spectra, the oxygen resonance peaks (from concrete) at 500 keV and the evaporation neutron peaks at about 2.3 MeV are observed. A high-energy neutron peak is observed at about 340 MeV in the forward direction, while a broad peak is observed between about 20 and 50 MeV at the large angles.

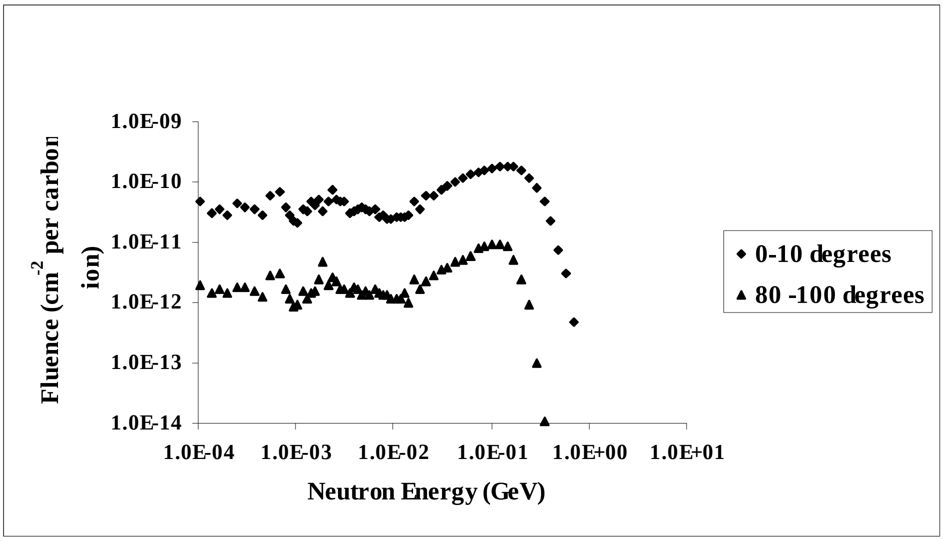

Figure 3.7. Neutron energy spectra incident at concrete surface for 430 MeV/u carbon ions incident on ICRU tissue sphere (Ipe and Fasso, 2006).

3.7.3.2 Protons. Agosteo *et al.* (2007) have derived computational models for concrete for 100, 150, 200, and 250 MeV protons incident on a thick iron target using the Monte Carlo code FLUKA, using the TSF 5.5 concrete with a density of 2.31 g cm^{-3} and a water content of 5.5 %. A single exponential fit was used for the data in the forward direction, and a double exponential fit was used at large angles (> 40°). The results are shown in Table 3.5. They have also made an extensive comparison of their Monte Carlo computational data with published experimental and computational data and conclude that "there is wide range of variability in the results, which reflects the large differences in the geometrical configurations (experimental or computational), material composition and techniques used. The concrete composition may have a substantial impact on the attenuation properties of a barrier" (Agosteo *et al.*, 2007). Teichmann (2006) has published computational models for 72 MeV and 250 MeV protons incident on a thick iron target, using the Monte Carlo code MCNPX (Pelowitz, 2005) for the TSF 5.5 concrete. Attenuation lengths calculated with FLUKA and MCNPX agree to within 10 %, whereas the source terms are significantly different. For example, MCNPX source term is 1.5 times lower than the FLUKA source term at 250 MeV in the 0° to 10° interval. Ipe (2008) has published the equilibrium attenuation lengths for 250 MeV protons incident on a tissue target for composite (iron plus concrete) barriers. Tayama *et al.* (2002) have published source terms and attenuation lengths based on MCNPX for concrete, for 52 MeV, 113 MeV and 256 MeV protons incident on a thick iron target. Tayama *et al.* (2002) also compare experimental source terms and attenuation lengths measured by Siebers (1993) for 230 MeV with MCNPX calculations. The calculated source term and attenuation length are within a factor of 2 and 35 %, respectively, of the measured values.

Table 3.5. Source term parameter and attenuation length for proton beams stopped in a thick iron target. The attenuation is computed for normal concrete (TSF-5.5) (Agosteo, 2007).

Energy (MeV)	Angular Bin	H_1**(10)** per proton (Sv m^2)	λ_1 (g cm^{-2})	H_2**(10)** per Proton (Sv m^2)	λ_2 (g cm^{-2})
100	0° to 10°			$(8.9 \pm 0.4) \times 10^{-16}$	59.7 ± 0.2
	40° to 50°	$(5.9 \pm 1.3) \times 10^{-16}$	47.5 ± 2.7	$(1.5 \pm 0.1) \times 10^{-16}$	57.2 ± 0.3
	80° to 90°	$(5.3 \pm 0.8) \times 10^{-16}$	33.7 ± 1.2	$(1.1 \pm 0.3) \times 10^{-17}$	52.6 ± 0.7
	130° to 140°	$(4.7 \pm 0.4) \times 10^{-16}$	30.7 ± 0.5	$(8.0 \pm 5.1) \times 10^{-18}$	46.1 ± 2.8
150	0° to 10°			$(3.0 \pm 0.2) \times 10^{-15}$	80.4 ± 0.5
	40° to 50°	$(1.2 \pm 0.2) \times 10^{-15}$	57.8 ± 3.4	$(3.3 \pm 0.8) \times 10^{-16}$	74.3 ± 1.4
	80° to 90°	$(10.0 \pm 2.2) \times 10^{-16}$	37.4 ± 2.7	$(1.2 \pm 0.3) \times 10^{-17}$	70.8 ± 1.3
	130° to 140°	$(7.8 \pm 2.0) \times 10^{-16}$	32.1 ± 1.5	$(2.1 \pm 0.6) \times 10^{-18}$	61.8 ± 1.1
200	0° to 10°			$(5.6 \pm 0.4) \times 10^{-15}$	96.6 ± 0.8
	40° to 50°	$(1.9 \pm 0.3) \times 10^{-15}$	68.3 ± 5.9	$(6.8 \pm 0.5) \times 10^{-16}$	86.4 ± 0.5
	80° to 90°	$(1.3 \pm 0.4) \times 10^{-15}$	43.8 ± 4.4	$(3.7 \pm 0.8) \times 10^{-17}$	78.3 ± 1.3
	130° to 140°	$(1.3 \pm 0.3) \times 10^{-15}$	32.8 ± 1.6	$(2.8 \pm 2.4) \times 10^{-18}$	70.0 ± 4.1
250	0° to 10°			$(9.8 \pm 1.0) \times 10^{-15}$	105.4 ± 1.4
	40° to 50°	$(2.3 \pm 0.5) \times 10^{-15}$	77.0 ± 7.9	$(1.2 \pm 0.1) \times 10^{-15}$	93.5 ± 0.5
	80° to 90°	$(1.4 \pm 0.4) \times 10^{-15}$	49.7 ± 5.7	$(9.0 \pm 2.5) \times 10^{-17}$	83.7 ± 2.0
	130° to 140°	$(1.9 \pm 0.6) \times 10^{-15}$	34.4 ± 3.4	$(6.5 \pm 2.6) \times 10^{-18}$	79.1 ± 3.4

3.7.4 Other codes

The ANISN code (Engle, 1967) was used for the design of the Hyogo (HIBMC) and Gunma University facilities.

The BULK-I code is a Microsoft Excel application and developed at the accelerator laboratory KEK in Japan (Tayama, 2004). The tool is applicable for proton beams in the energy range from 50 MeV to 500 MeV. The shielding can be computed not only for concrete but also for iron or combinations of both.

The BULK C-12 code, developed at the University of Applied Science in Zittau, Germany, in cooperation with AREVA, Erlangen, Germany (Norosinski, 2006), is capable of estimating neutron and photon effective dose rates from medium energy protons (50 MeV to 500 MeV) or carbon ions (155 MeV/u to 430 MeV/u). Shielding materials considered in the code are concrete walls or a combination of iron and concrete. The code is available from the Nuclear Energy Agency (NEA) (Norosinski, 2006).

3.8 Shielding Materials and Transmission

3.8.1 Shielding Materials

Earth, concrete, and steel are typically used for particle accelerator shielding (NCRP, 2003). Other materials such as polyethylene and lead are used to a limited extent. As previously stated, neutrons are the dominant secondary radiation, and when using steel a layer of hydrogenous material, must be used in conjunction with the steel.

3.8.1.1 Earth. Earth is often used as shielding material at underground accelerator facilities and must be compacted to minimize cracks and voids. Earth is primarily composed of silicon dioxide (SiO_2), which makes it suitable for shielding of both gamma radiation and neutrons (NCRP, 2003). It contains water which improves the shielding of neutrons. Because the water content (0% to 30%) of the earth and its density (1.7 g/cm^3 to 2.2 g/cm^3) can vary quite a bit, the soil characteristics of the site must be determined to ensure effective shielding design. The activation of the ground water must also be considered for underground facilities. Partial earth shielding is used at some particle therapy facilities (HIT facility in Heidelberg, CNAO in Pavia, Italy, and Gunma University in Japan). The only cost associated with earth is its transportation offsite.

3.8.1.2 Concrete and Heavy Concretes. Concrete is a mixture of cement, coarse and fine aggregates, water, and sometimes supplementary cementing materials and/or chemical admixtures (see http://www.cement.org/tech/faq_unit_weights.asp). The density of concrete varies depending on the amount and density of the aggregate, the amount of air that is entrapped or purposely entrained, and the water and cement contents (which in turn are influenced by the maximum size of the aggregate). Ordinary concrete has a density that varies between 2.2 and 2.4 g cm^{-3}.

Concrete has many advantages compared to other shielding materials (NCRP, 2005). It can be poured in almost any configuration and provides shielding for both photons and neutrons. It is relatively inexpensive. Because of its structural strength, poured-in-place concrete can be used to support the building and any additional shielding. Concrete blocks are also available. Water exists in concrete in the free and bound form. The water content of concrete plays a significant role in the shielding of neutrons. With time, the free water evaporates, but the concrete also hydrates (absorbs moisture from the surrounding environment) until it reaches some equilibrium. About 3 % of the water may evaporate in the first 30 days or so. For neutron shielding, a water content of about 5 % is recommended.

In the U.S., ordinary concrete is usually considered to have a density of 2.35 g cm^{-3} (147 lb $feet^{-3}$). Concrete used for floor slabs in buildings are typically lightweight with a density that varies between 1.6 and 1.7 g cm^{-3}.

The poured-in-place concrete is usually reinforced with steel rebar, which makes it more effective for neutrons. Because the steel rebar is not included in the concrete composition, measured radiation doses with heavily reinforced concrete will be lower than calculated doses. The disadvantage of concrete is that takes months to pour. The typical compositions of various types of concrete are shown in Table 3.6.

High-*Z* aggregates or small pieces of scrap steel or iron are sometimes added to concrete to increase its density and effective *Z*. These concretes are known as heavy concretes. Densities of up to about 4.8 g cm^{-3} can be achieved. However, the pouring of such high-*Z* enhanced concrete is a special skill and should not be undertaken by an ordinary concrete contractor because of settling, handling, and structural issues (NCRP, 2005). Ordinary concrete pumps are not capable of handling such dense concrete. The high-*Z* aggregates could sink to the bottom resulting in a non-uniform composition and density. Concrete trucks with greater capacity will be required for transportation. Heavy concretes made locally at the construction site may not be subject to industrial standards and will need to be checked. Prefabricated heavy concretes are subject to rigorous standards and are available as blocks or interlocking blocks. The high-*Z* aggregate enhanced concrete is also sold in the form of either interlocking or non-interlocking modular blocks. It is preferable to use the interlocking blocks to avoid the streaming of radiation. Concrete enhanced with iron ore is particularly effective for the shielding of relativistic neutrons. .

Ledite® is manufactured by Atomic International, Frederick, Pennsylvania, and is a modular pre-engineered interlocking high density block which has a high iron content. It is currently used in the shielding of photon therapy linear accelerators. It can be placed in existing structures and can be relocated and reused. Its use results in considerable time savings. Pouring of concrete takes months, whereas Ledite can be stacked in weeks. In order to study the space savings that could result from the use of Ledite, the transmission of three different compositions were investigated: Proshield Ledite 300 (ρ = 4.77 g cm^{-3}) which is was marketed by the manufacturer for particle therapy, and two previous compositions referred to as Ledite 293[2] (ρ = 4.77 g cm^{-3}) and Ledite 247[3] (ρ = 3.95 g cm^{-3}). The results are discussed in Section 3.8.2.

An important consideration in the choice of shielding materials is their susceptibility to radioactivation by neutrons, which can last for decades. Activation of concrete is discussed in Chapter 4. It has been observed that for short-lived radioactivity, ^{24}Na ($T_{1/2}$ = 15 h) is dominant, and for longer-lived radioactivity, ^{22}Na ($T_{1/2}$ = 2.6 a) and ^{152}Eu ($T_{1/2}$ = 12 a) are dominant. The steel rebars can also get activated. Higher activation may occur with some heavy concrete like barites (which are barium containing). Radioactive isotopes such as ^{133}Ba ($T_{1/2}$ = 10.7 a), ^{137}Cs ($T_{1/2}$ = 30.0 a), ^{131}Ba ($T_{1/2}$ = 12 d), and ^{134}Cs ($T_{1/2}$ = 2.1 a) can contribute significantly to the external dose rates (Sullivan, 1992). Studies by Ipe (2009b) indicate that activation in Ledite is not significantly greater than activation in concrete.

[2] Marketed as XN-288

[3] Marketed as XN-240

Table 3.6. Typical compositions of various types of concrete after curing (Chilton *et al.*, 1984; NCRP, 2003). The sum of partial densities is not exact the entire density of concrete due to missing element proportions.

Concrete Type	**Ordinary**	**Barytes**[a]	**Magnetite-Steel**
Density (g/cm^3)	2.35	3.35	4.64
Element		**Partial Density (g/cm^3)**	
Hydrogen	0.013	0.012	0.011
Oxygen	1.165	1.043	0.638
Silicon	0.737	0.035	0.073
Calcium	0.194	0.168	0.258
Carbon	-	-	-
Sodium	0.04	-	-
Magnesium	0.006	0.004	0.017
Aluminum	0.107	0.014	0.048
Sulfur	0.003	0.361	-
Potassium	0.045	0.159	-
Iron	0.029	-	3.512
Titanium	-	-	0.074
Chromium	-	-	-
Manganese	-	-	-
Vanadium	-	-	0.003
Barium	-	1.551	-

[a]Barytes with $BaSO_4$ ore as aggregate

3.8.1.3 Steel. Steel is an iron alloy and is useful for shielding photons and high-energy neutrons. The high density of steel (~ 7.4 g/cm^3) together with its physical properties leads to tenth-value thickness for high-energy neutrons of about 41 cm (Sullivan, 1992). Therefore, steel is often used when space is at a premium. Steel or iron are usually available in the form of blocks (NCRP, 2003). Natural iron is comprised of 91.7 % ^{56}Fe, 2.2 % of ^{57}Fe, and 0.3 % of ^{56}Fe. The lowest inelastic energy level of ^{56}Fe is 847 keV. Neutrons above 847 keV will lose their energy by inelastic scattering, while neutrons below 847 keV can lose their energy only by elastic scattering which is a very inefficient process for iron. Therefore, there is a build up of neutrons below this energy. This is also the energy region where the neutrons have the highest weighting factor. Natural iron also has two energy regions where the minimum cross section is very low because of the resonance in ^{56}Fe. They are at 27.7 keV (0.5 barn) and at 73.9 keV (0.6 barn). Thus, the attenuation length in this region is about 50 % higher than the high-energy attenuation length. Therefore, large fluxes of neutrons can be found outside steel shielding. For lower energy neutrons, only the elastic scattering process causes neutron energy degradation. As stated in Chapter 1, if steel is used for the shielding of high-energy neutrons, it must be followed by a hydrogenous material for shielding the low-energy neutrons which are generated.

Due to the large variety of nuclear processes, including neutron capture reactions of thermalized neutrons, steel can be highly activated. It is reported that the following radionuclides are produced in steel or iron by protons and neutrons: ^{52,54,56}Mn, ^{44,46}Sc, ^{56,57,58,60}Co, ^{48}V, ^{49,51}Cr, ^{22,24}Na, and ^{59}Fe (Freytag, 1972; Numajiri, 2007). Thermal neutrons cause ^{59}Fe and ^{60}Co activation. It is obvious that steel with less cobalt can reduce the production of cobalt isotopes.

3.8.1.4 Polyethylene and Paraffin. Polyethylene $(CH_2)_n$ and paraffin have the same percentage of hydrogen. Paraffin is less expensive but has a lower density and is flammable (NCRP, 2005). Therefore, polyethylene is preferred for neutron shielding even though it is more expensive. Attenuation curves in polyethylene of neutrons from 72 MeV protons incident on a thick iron target are reported by Teichmann (2006). The thermal neutron capture in polyethylene yields a 2.2 MeV gamma ray which is quite penetrating. Therefore, boron-loaded polyethylene can be used. Thermal neutron capture in boron yields a 0.475 MeV gamma ray. Borated polyethylene can be used for shielding of doors and ducts and other penetrations.

3.8.1.5 Lead. Lead has a very high density (11.35 g cm^{-3}) and is used mainly for the shielding of photons. Lead is available in bricks, sheets, and plates. Lead is malleable (NCRP, 2005) and therefore cannot be stacked to large heights because it will not support its own weight. Therefore, it will require a secondary support system. Lead is transparent to fast neutrons and it should not be used for door sills or thresholds for particle therapy facilities where secondary neutrons dominate the radiation field. However, it does decrease the energy of higher energy neutrons by inelastic scattering down to about 5 MeV. Below this, the inelastic cross section for neutrons drops sharply. Lead is toxic and should be encased in steel or other materials, or protected by paint.

3.8.2 Transmission

The transmission of a given thickness of shielding material is defined as the ratio of the dose at a given angle with shielding to the dose at the same angle without shielding. Transmission curves can also be used to determine shielding thicknesses.

Figures 3.8 through 3.10 show the total particle dose equivalent transmission (based on FLUKA calculations) of three different compositions of Ledite®, composite shields, and iron and concrete as a function of shielding thickness for various angles when for 430 MeV/u carbon ions incident on a 30 cm ICU tissue sphere (Ipe, 2009). Figures 3.11 through 3.13 show similar data for 250 MeV protons. These transmission curves can be used to determine the composite shielding thickness that can be used to replace large concrete thicknesses in the forward direction in the treatment room and thus save space. For example, from Fig. 3.8 it can be observed that 4.65 m of concrete provides about the same attenuation as about 2.6 m of Ledite 293 or 3.3 m of Proshield Ledite or 120 cm of iron plus 165 cm of concrete (total shielding thickness = 2.85 m). Thus, a space savings of 2.05 m is obtained with Ledite 293; 1.65 m is obtained with Proshield Ledite 300; and 1.85 m is obtained with composite shielding of 120 cm of iron plus concrete. From the figures it can also be observed that Ledite 293 is more effective then Ledite 247 and Proshield Ledite 300 in the forward direction, even though Proshield Ledite has a higher density than Ledite 293. Thus, both composition and density of shielding material impact transmission.

2244 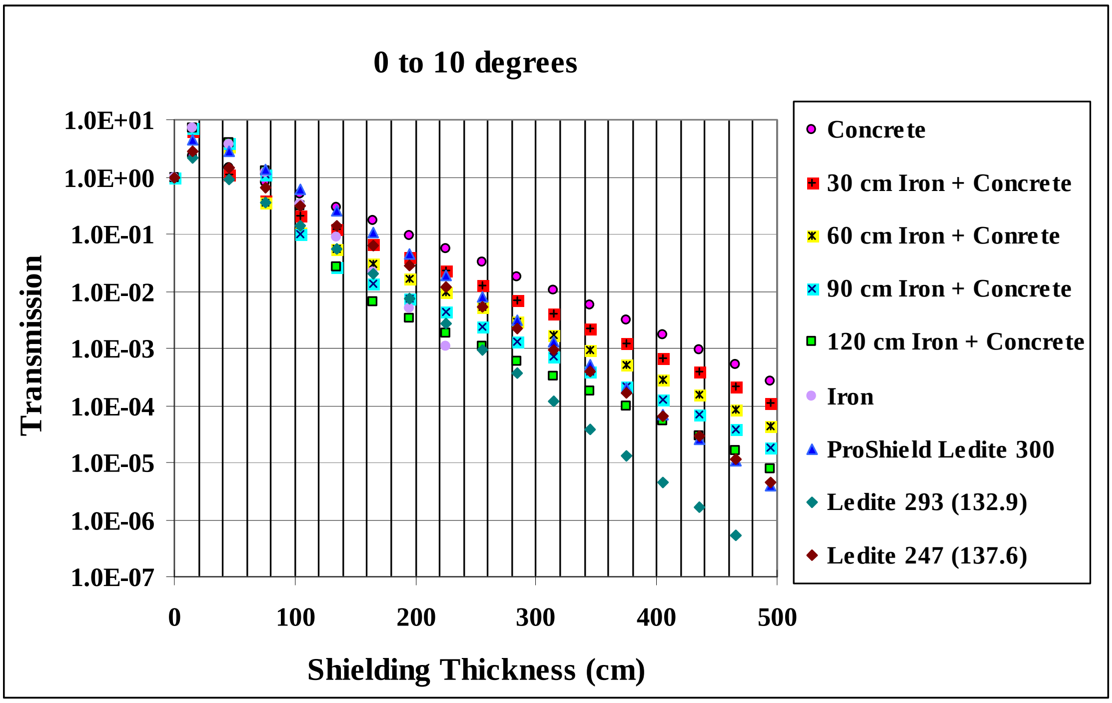

2245 Figure 3.8. Transmission curves for 430 MeV/u carbon incident on 30 cm ICRU sphere (0° to 10°) (Ipe,
2246 2009a) (Copyright 8 September 09 by the American Nuclear Society, La Grange Park, Illinois).

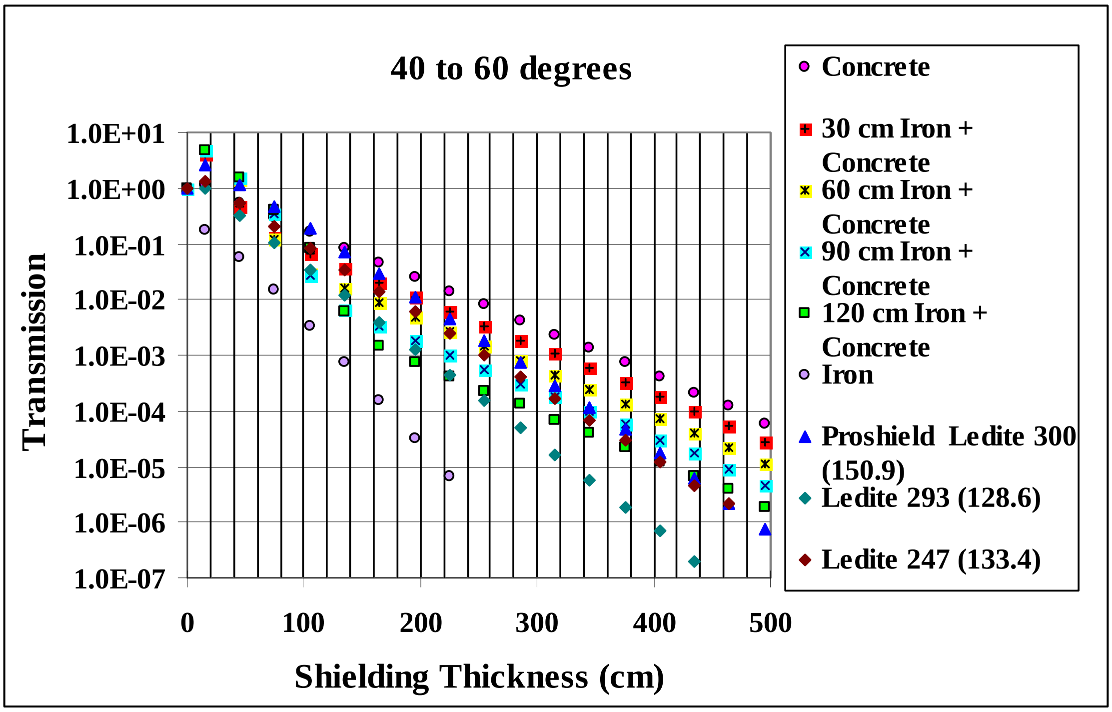

Figure 3.9. Transmission curves for 430 MeV/u carbon incident on ICRU sphere (40° to 60°) (Ipe, 2009a) (Copyright 8 September 09 by the American Nuclear Society, La Grange Park, Illinois).

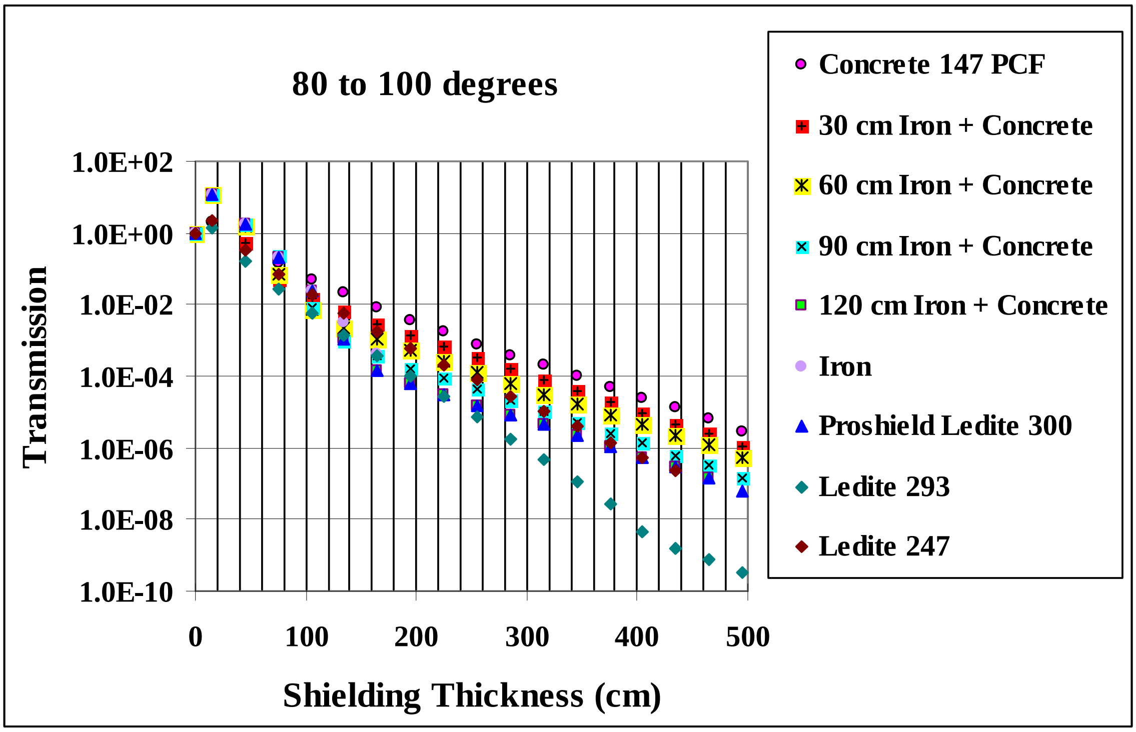

Figure 3.10. Transmission curves for 430 MeV/u carbon incident on ICRU sphere (80° to 90°) (Ipe, 2009b).

2254
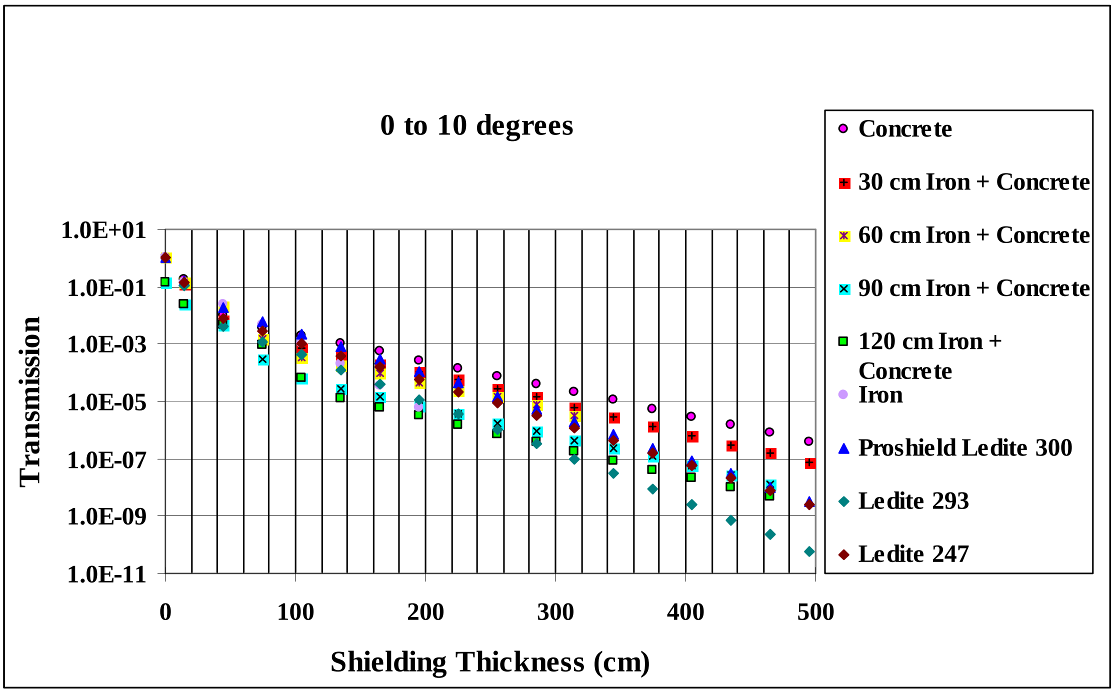

2255 Figure 3.11. Transmission curves for 250 MeV protons incident on ICRU sphere (0° to10°) (Ipe, 2009a)

2256 (Copyright 8 September 09 by the American Nuclear Society, La Grange Park, Illinois.)

2257

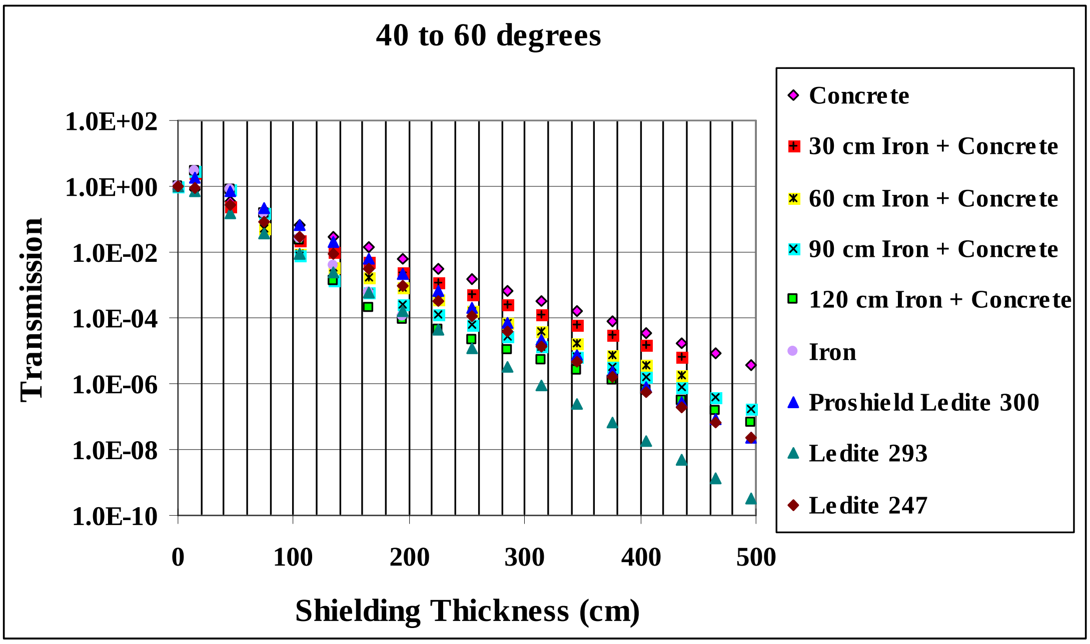

Figure 3.12. Transmission curves for 250 MeV protons incident on ICRU sphere (40° to 60°) (Ipe, 2009a) (Copyright 8 September 09 by the American Nuclear Society, La Grange Park, Illinois).

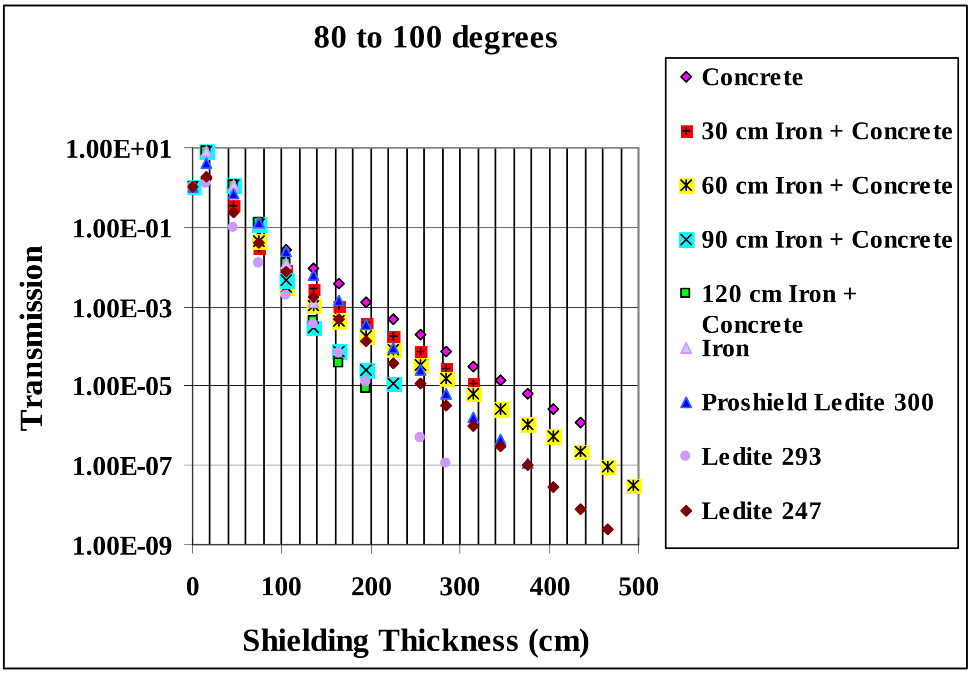

Figure 3.13. Transmission curves for 250 MeV protons incident on ICRU sphere (80° to 100°) (Ipe, 2009b).

3.8.3 Verification of Density and Composition

The transmission of the shielding material depends upon both density and composition. Therefore, it is important to determine density and composition.

3.8.3.1 Density. The density of concrete is a function of mixture proportions, air content, water demand, and the specific density and moisture content of the aggregate (ASTM, 2003). Decrease in density is due to moisture loss that, in turn, is a function of aggregate moisture content, ambient conditions, and the ratio of the surface area to the volume of the concrete member. For most concretes, equilibrium density is approached at about 90 to 180 days. Extensive tests demonstrate that despite variations in the initial moisture content of lightweight aggregate, the equilibrium density will be approximately 0.05 g cm^{-3} (3.0 lb ft^{-3}) greater than the oven-dry density. Therefore, determination of oven-dry density will be the most conservative approach. Because the water in concrete does evaporate with time, the use of “wet” density is not conservative. On-site density testing should be performed.

3.8.3.2 Composition. The composition of concrete is usually determined using x-ray fluorescence (XRF). Fourteen elements can be analyzed (Si, Al, Fe, Ca, Mg, S, Na, K, Ti, P, Mn, Sr, Zn, and Cr). However, this method does not identify elements below sodium, which require combustion tests. The hydrogen content is of great importance in neutron shielding; therefore, additional tests need to be performed. Other tests include the determination of carbon, hydrogen, and nitrogen with the Perkin-Elmer 2400 CHN Elemental Analyzer (ASTM, 2003). Oxygen can be determined with the Carlo Erba 1108 or LECO 932 analyzer. Elements which interfere with oxygen analysis are silicon, boron, and fluorine (high content). Oxygen can also be analyzed with the ICP (inductive coupled plasma) method. Carbon and sulfur can be analyzed using a LECO analyzer. In the XRF test results, the elements are usually reported as oxides. Therefore, a special request must be made up front in order to get the fraction by weight of the raw elements.

3.8.4 Joints, Cracks, and Voids

Joints between the same shielding materials should be staggered to ensure integrity of the shielding. If shielding blocks are used, they should be interlocking. If grout is used, it should have the same density as the shielding material.

For concrete pours, vibration of concrete should be used to ensure that there are no voids in the concrete. Continuous pours are preferred for the concrete walls and ceiling. For non-continuous concrete, appropriate measures (such as sandblasting of poured surface before pouring the next portion, use of keyways, staggered joints, *etc*.) should be in place to ensure that there are no thin spots at the cold joint. For non-continuous pours, the ceiling should be notched into lateral walls.

3.8.5 Rebar and Form Ties

Rebar is made of steel and while its use varies, typically it occupies less than 5 % of the barrier area. The density of steel (7.8 g cm^{-3}) is much higher than concrete (2.35 g cm^{-3}) and its mass attenuation coefficient for photons below ~ 800 keV and above ~ 3 MeV is greater than that of concrete. But because of its higher density, in all cases it is a better photon shield. As stated before, steel followed by concrete is also effective for the shielding of neutrons.

Form ties completely penetrate the shielding, and typically they are heavy double wires or steel rods with a diameter of about 2.5 cm. Thus, the form tie acts as a very long duct, but most of the neutrons will scatter out of the steel. Sometimes cones are used at the end of the form ties. The holes left by the cones should be filled with grout of the same density as the concrete.

3.9 Special Topics

3.9.1 Mazes

Mazes are used to reduce the radiation dose at the entrance to the shielded room so that a massive shielded door is not required. Depending upon the effectiveness of the maze, either no door may be required, or a thin shielded door may be required. The typical approach is to avoid the direct propagation of radiation to the entrance of the maze as shown in Figure 3.14.

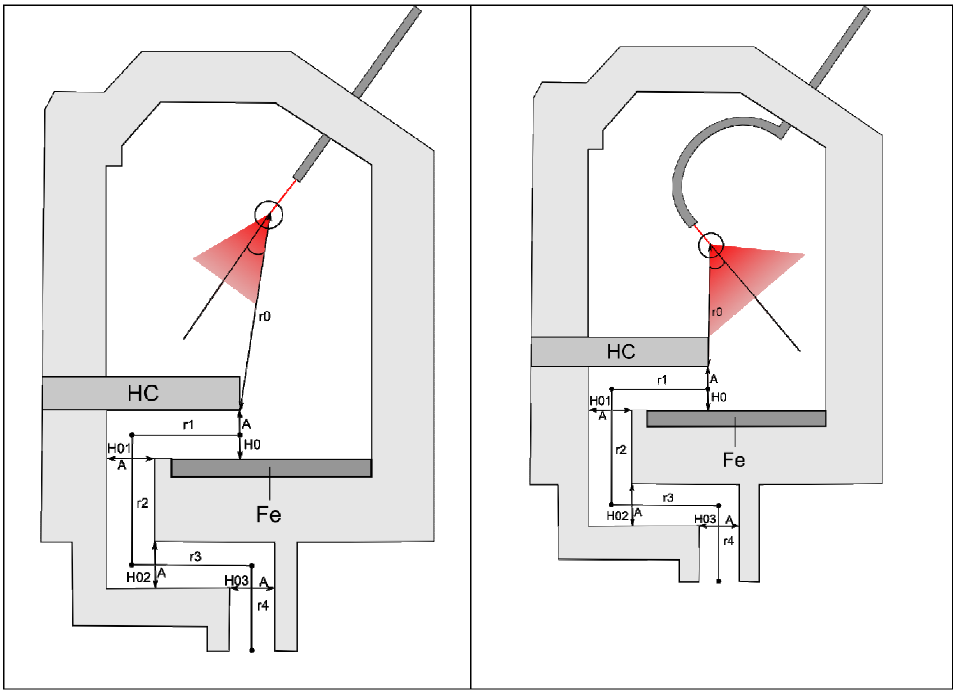

Figure 3.14. Example for the maze of a treatment room with fixed beam geometry (left) and for a gantry geometry with a rotating radiation cone (right). The shielding walls are made of normal concrete, heavy concrete (HC), and concrete reinforced with steel layers (Fe). The maze for the attenuation of secondary radiation has four legs. The legs are most effective when the bends are 90 degrees as shown (Courtesy of G. Fehrenbacher, J. Goetze, T. Knoll, GSI (2009)).

Two basic rules must be considered in the design of a maze: the forward-directed radiation from the target should never be directed toward the maze; and the sum of the thicknesses of each maze wall should be equal to the thickness of the direct-shielded wall. The effectiveness of a maze depends upon the following characteristics:

- As the number of legs increases, the attenuation increases. The legs are normally perpendicular to each other. The effect of the reduction of the radiation levels in the first leg is less pronounced than in the consecutive legs.
- Because the forward-directed radiation does not enter the maze, only the attenuation of scattered radiation, with an energy distribution shifted toward lower energies in comparison to the forward-directed spectrum coming directly from the target, should be considered for the planning of the single maze walls.
- During the propagation of neutron radiation along the maze and the continuous production of thermal neutrons, a permanent source of gamma radiation is present because it is caused by (n,γ) reactions. Therefore, the attenuation of gamma radiation must be taken into account.

Radiation levels inside a maze can be estimated with analytical methods, Monte Carlo calculations, or experimental data. Tesch (1982) provides an approximation that is easy to use and based on experimental data from an Am-Be neutron source and a concrete-lined labyrinth. The equations are defined for the first leg (Equation 3.3) and separately for the second leg and all further legs (Equation 3.4):

$$H(r_1) = 2 \cdot H_0(r_0) \cdot \left(\frac{r_0}{r_1}\right)^2 \text{, for the first leg} \qquad (3.3)$$

$$H(r_i) = \left(\frac{\exp\left(-\frac{r_i}{0.45}\right) + 0.022 \cdot A_i^{1.3} \cdot \exp\left(-\frac{r_i}{2.35}\right)}{1 + 0.022 \cdot A_i^{1.3}} \right) \cdot H_{oi} \text{, for the i}^{\text{th}} \text{ leg (i >1)} \qquad (3.4)$$

where :

H_0 = dose at the first mouth of the maze;

r_0 = distance from the source to the first mouth in the maze (unit in m);

r_1 = center line distance of first leg (m);

r_i = center line distance of i^{th} leg (m);

A_i = cross sectional area of the i^{th} mouth of the i^{th} leg (m^2);

H_{oi} = dose equivalent at the entrance to the i^{th} leg.

The measured dose rates and the corresponding calculated values with Equations 3.3 and 3.4 agree reasonably well. Increasing the length of the maze and decreasing its cross-sectional area increases the attenuation. Other methods can be found in the literature (Dinter, 1993; Göbel *et al.*, 1975; Sullivan, 1992).

3.9.2 Penetrations and Ducts

Ducts and penetrations in the shielding wall are required for the routing of air conditioning, cooling water, electrical conduits, physicist's conduits, *etc*. Direct penetration of the shielded walls must be avoided. Oblique penetrations as shown in Figure 3.15a increase the radiation path length, and hence, the attenuation. However the forward-directed radiation should not point in the direction of the penetration. Another effective method is the introduction of bends and arcs, as shown in Figures 3.15b, 3.15c, and 3.15d. The reduction of the radiation along the duct is accomplished at the bends where the radiation is scattered. In some cases when an oblique penetration of the duct is not feasible, shadow mask shielding such as shown in Figure 3.15d can be used. Usually the cables filling the penetrations provide some minimal shielding.

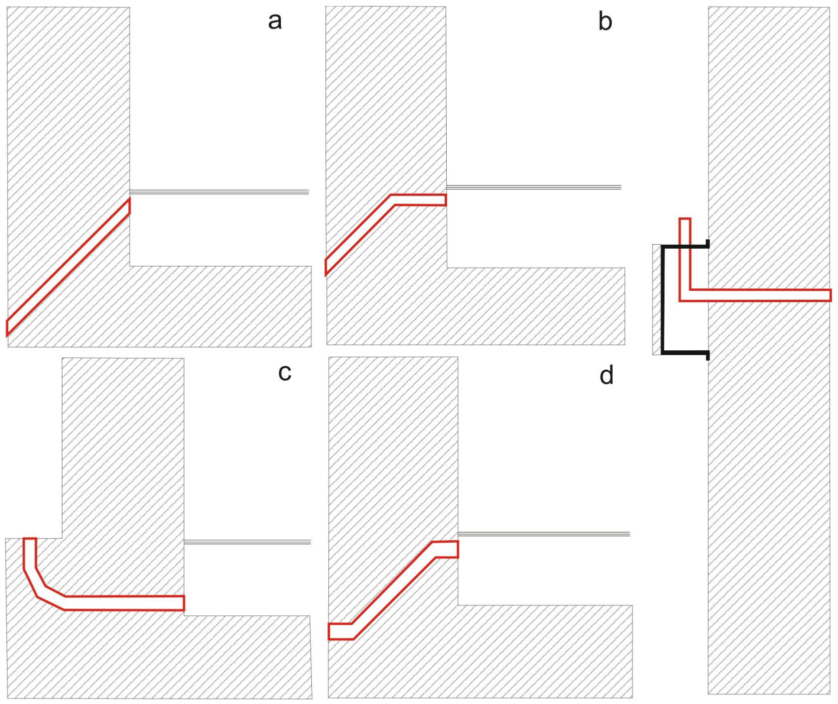

Figure 3.15. Various types of ducts and penetrations with different methods for the reduction of radiation propagation along the duct: a) Extension of the duct length, b) and c) use of a bend, d) use of two bends, and e) covering of the penetration with a shield (Courtesy of G. Fehrenbacher, J. Goetze, T. Knoll, GSI (2009)).

The DUCT III (Tayama *et al*., 2001) code, based upon a semi-empirical method, is suitable for duct calculations (cylindrical, rectangular, annular, and slit) for gamma radiation and neutrons with energies up to 10 MeV and 3 GeV, respectively. The DUCT III code is available through the NEA.

3.9.3 Skyshine and Groundshine

Some facilities may be designed with little shielding in the ceiling above the accelerator or treatment room when the area above the ceiling is not occupied. Secondary radiation may then be scattered down by the atmosphere to the ground level. This is referred to as "skyshine" and illustrated in Figure 3.16. A treatment room is shown with substantial beam depositions in a target, *e.g.*, the tissue of the patient. Similarly, "groundshine" refers to radiation escaping the floor slab, reaching the earth, and scattering upwards.

2403

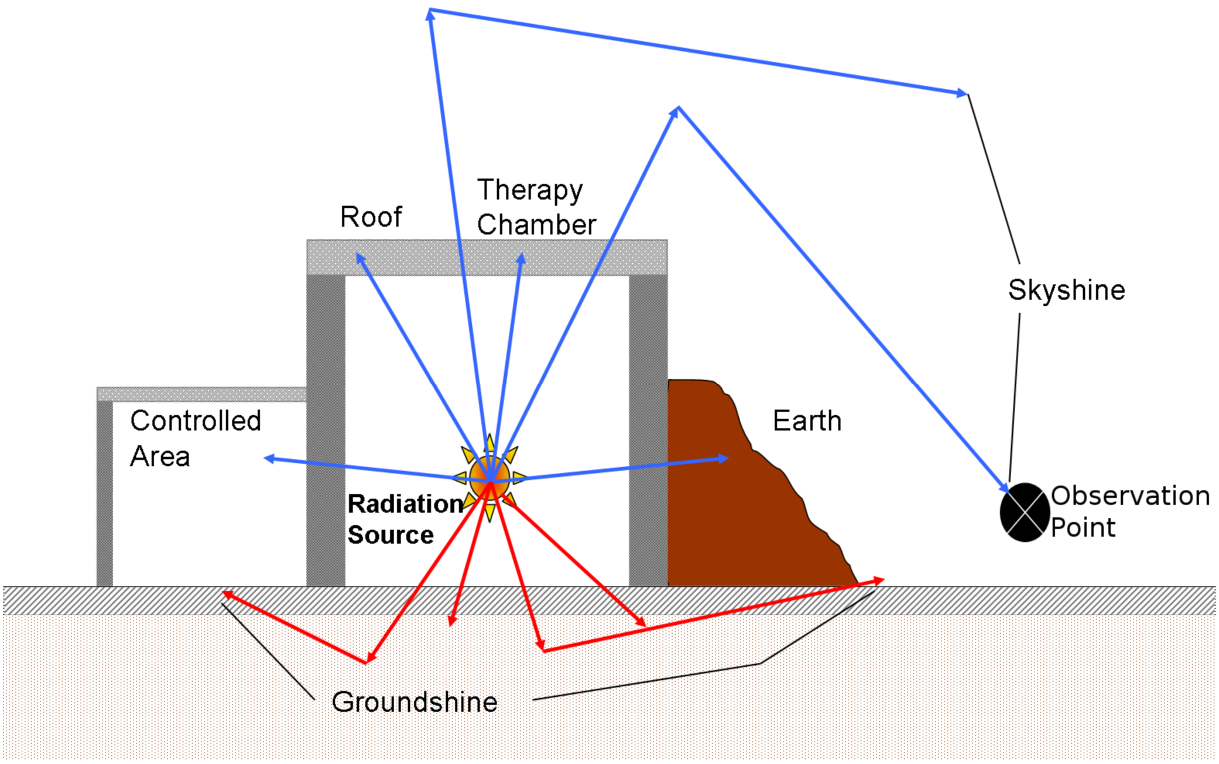

2404

2405 Figure 3.16. Examples of skyshine and groundshine . Secondary radiation produced in a treatment room
2406 can partially escape through the roof (or the floor slab) and cause non negligible dose rates at the
2407 observation point (Courtesy of G. Fehrenbacher, J. Goetze, T. Knoll, GSI (2009)).

Skyshine results from the scattering of lower-energy neutrons (NCRP, 2003). High-energy neutrons that penetrate the ceiling shielding undergo inelastic collisions with the air to generate more low-energy neutrons. Therefore, it is necessary to know the intensities as well as the energy and angular distributions of neutrons entering the sky above the ceiling of the shielded room. Stevenson and Thomas (Stevenson, 1984) developed a method for the calculation of skyshine that are valid at distances of ~ 100 m to 1000 m from the source. The following assumptions and simplifications were made:

- A differential neutron energy spectrum of the form 1/*E* (where *E* is the energy) extending up to a maximum neutron energy (called upper energy of the neutron spectrum) is used. The highly penetrating neutron component is overestimated in this assumption.
- The neutrons are emitted into a cone with a semi-vertical angle of about 75°. This assumption leads to an overestimation of the dose at large distances for neutron emissions with small semi-vertical angles.

The neutron dose equivalent per source neutron escaping the roof shielding is given by:

$$H(r) = \tfrac{\kappa}{r^2} \cdot \exp\left(-\tfrac{r}{\lambda}\right), \qquad (3.5)$$

where *r* is the distance from the source to the observation point (m), κ is a constant with a value between 1.5E-15 Sv·m^2 and 3E-15 Sv·m^2, and λ is the effective absorption length in the air of the maximum neutron energy. The values of λ are given in Figure 3.17 for the energy range from 1 MeV to 10 GeV.

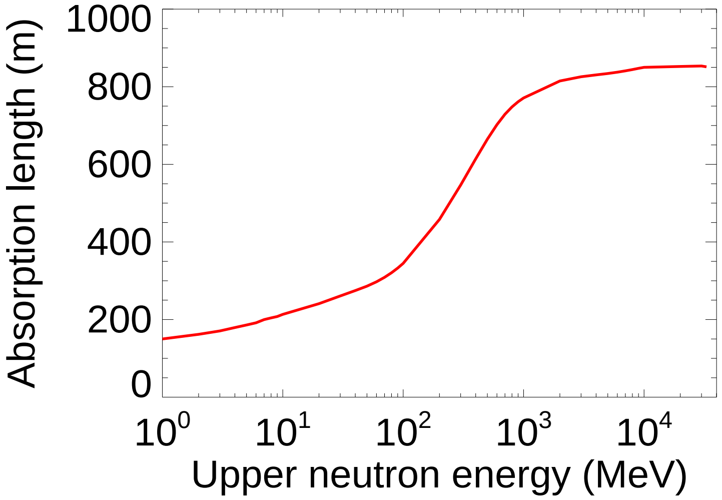

Figure 3.17. Absorption length of neutrons escaping from the ceiling and causing skyshine. Calculated by G. Fehrenbacher based on formula cited in NCRP 144 (NCRP, 2003).

Equation 3.5 was further modified by Stapleton *et al.* (1994) with the introduction of more realistic neutron spectra, the angular dependency of the neutron emission, and weighting of the high-energy neutrons. The modified expression is given by:

$$H(r) = \frac{\kappa'}{(h+r)^2} \cdot \exp\left(-\frac{r}{\lambda}\right) \tag{3.6}$$

where κ' = 2 x 10^{-15} Sv m^2 per neutron and h = 40 m. Equation 3.5 is an empirical summary of experimental and theoretical data, and may used with some constraints.

3.10 Examples for Existing Facilities

This section provides examples of the shielding design of various facilities.

3.10.1 Facilities for Proton Therapy

3.10.1.1 Loma Linda, CA, USA. The Loma Linda University Medical Center (LLUMC) is the first hospital-based proton treatment facility built in the world. Figure 3.18 shows a layout of the facility which is comprised of a 7-m diameter synchrotron (with a 2 MeV RFQ for pre-acceleration), three gantry rooms, and one fixed beam room. The energy range of the synchrotron is 70 MeV to 250 MeV. The design intensity is 10^{11} protons/sec. The beam extraction efficiency is higher than 95 % (Coutrakon, 1990; Scharf, 2001; Slater, 1991). The beam-shaping passive systems include ridge filters, scattering foils, and a wobbler. A total of 1000 to 2000 patients can be treated per year, with a maximum of 150 treatments per day.

Awschalom (1987) collected shielding data for 250 MeV proton beams in preparation for construction planning. The facility was built below ground level, which allowed relatively thin outer walls. The main radiation safety calculations were performed by Hagan *et al.* (1988). Secondary radiation production by protons with energies from 150 MeV to 250 MeV was computed with the Monte Carlo code HETC (Cloth, 1981) for iron and water targets. The subsequent transportation of the produced neutron radiation was performed with the ANISN code (Engle, 1967) for a spherical geometry. Attenuation curves were derived for concrete thicknesses in the range up to 650 cm. An experimental assembly of the synchrotron was set up at the Fermi National Accelerator Laboratory. Holes were drilled in the concrete shielding and TEPC detectors (described in Chapter 4) were positioned outside the holes. Experimental attenuation curves were derived for the angular range from 0° to 90° and served as a benchmark for the theoretical attenuation curves (Siebers, 1990; 1993).

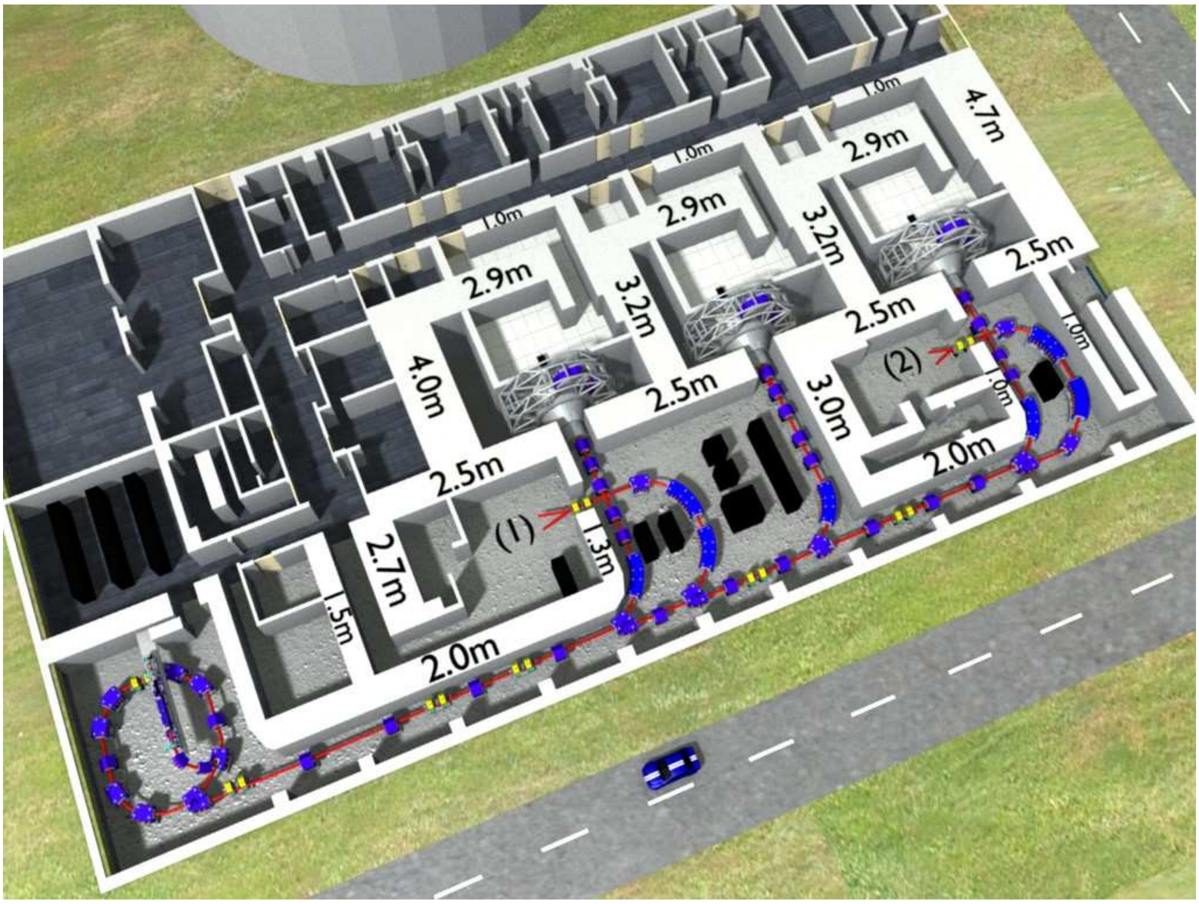

Figure 3.18. Proton therapy facility at the Loma Linda University Medical Center. The installation has a synchrotron, three rooms for treatments with a gantry, and a fixed beam branch with two beam lines (1) and a fixed beam line for calibration measurements (2) (Courtesy of G. Fehrenbacher, J. Goetze, T. Knoll, GSI (2009)).

3.10.1.2 Massachusetts General Hospital (MGH), Boston, MA, USA. Figure 3.19 shows a layout of Massachusetts General Hospital (MGH). The accelerator is an IBA 230 MeV cyclotron. There are two gantry rooms, a horizontal beam line for ocular treatments, and an experimental beam line. The beam-shaping system consists of a passive scattering system and a wobbler. The accelerator and the treatment floor are underground. About 500 patients are treated per year.

The basic layout was designed using analytical models from Tesch for both the bulk shielding (Tesch, 1985) and the mazes (Tesch, 1982). Self-shielding of the beam conducting elements was neglected except for the cyclotron. The facility was built below ground, which allowed relatively thin outer walls. The final design was verified after construction using MCNPX (Newhauser, 2005; Titt, 2005).

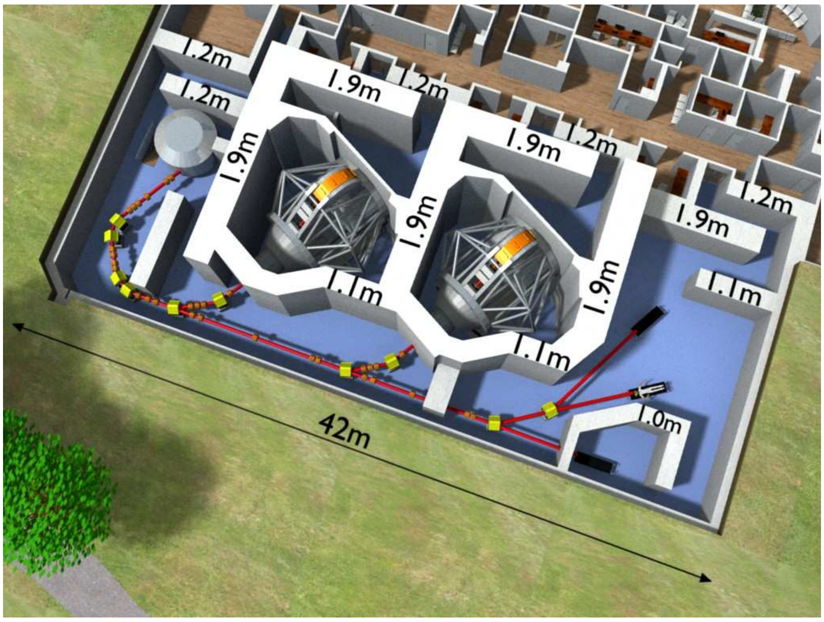

Figure 3.19. Northeast Proton Therapy Center (NPTC) at the Massachusetts General Hospital (MGH) in Boston. The facility is comprised of two gantry rooms, one with a horizontal geometry, and an experimental room (Courtesy of G. Fehrenbacher, J. Goetze, T. Knoll, GSI (2009)).

3.10.1.3 National Cancer Center (NCC), Republic of Korea. Figure 3.20 shows the National Cancer Center (NCC) in Korea. The accelerator is an IBA 230 MeV cyclotron. The facility is comprised of three treatment rooms: two gantry rooms and one fixed beam room. An area is planned for experiments. Initially, the scattering method was used and the wobbling method was expected to be used in the later stages. The raster scan technique will be used in the future.

Shielding calculation were performed initially using Tesch's analytical model (Tesch, 1985) and later using MCNPX. The facility is shielded with concrete of density 2.3 g/cm^3. The assumptions used for shielding calculations are a maximum beam-on time of 30 min per hour, 2 Gy/fraction, and 50 h treatment time per week for 50 weeks per year. The legal dose limits are shown in Table 3.1. It is interesting to note that the maze walls for this facility are 2.9 m thick, compared to the NPTC maze walls which are only 1.9 m thick. As stated previously workloads, usage assumptions, and regulatory requirements vary from facility to facility; therefore, shield designs differ.

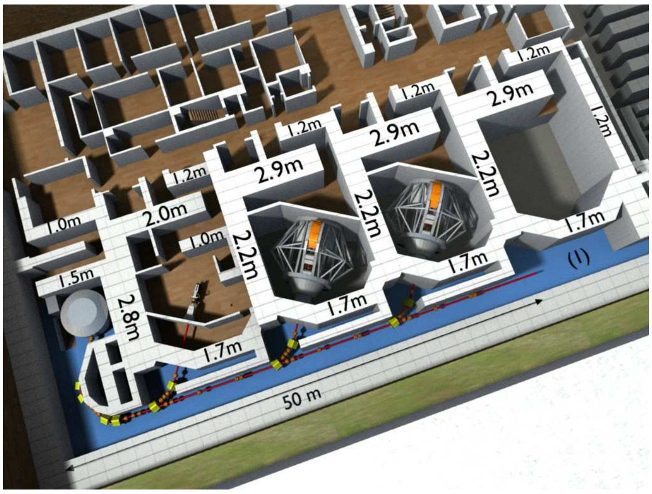

Figure 3.20. Layout of the proton therapy facility in Kyonggi, South Korea. The facility comprises three treatment rooms and an area for experiments (1). The accelerator is a cyclotron from IBA in Belgium. (Courtesy of G. Fehrenbacher, J. Goetze, T. Knoll, GSI (2009)).

3.10.1.4 Rinecker Proton Therapy Center, Munich, Germany. Figure 3.21 shows the Rinecker Proton Therapy Center in Munich. The facility consists of a 250 MeV superconducting cyclotron with a maximum proton current of 500 nA. There are four gantry rooms and one fixed beam room.

Shielding calculations were based on a 250 MeV proton beam incident on a graphite degrader thick enough to reduce the energy to 70 MeV (Hofmann and Dittrich, 2005). Annual dose limits of 5 mSv and 1 mSv were used for occupationally exposed workers and the public, respectively. Ordinary concrete and heavy concrete (mainly for the degrader area) were used for shielding the facility. Shielding calculations were performed with MCNPX. The introduction of variance reduction techniques was necessary to obtain results with comparable statistical errors for all considered regions. Optimization studies for the degrader shielding were performed. Figure 3.21 (right side) shows the isodose curves and the spatial development of the radiation propagation in and around the shielding walls and rooms.

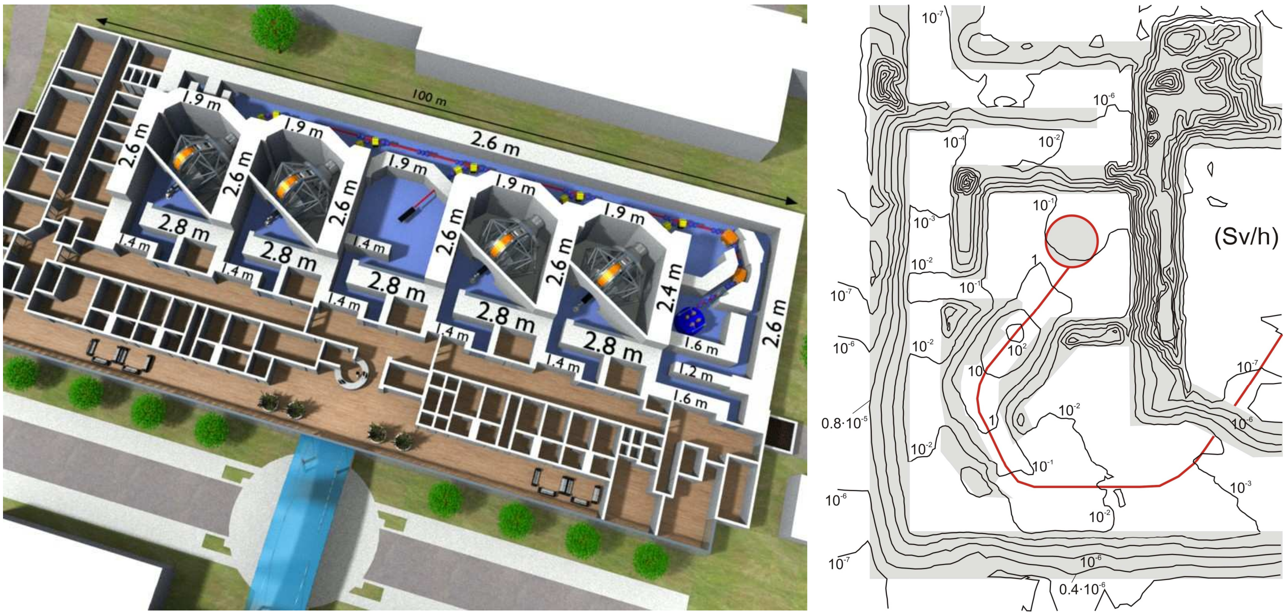

Figure 3.21. Left: Building of the Rinecker Proton Therapy Center in Munich. Right: The dose distribution of the area near the cyclotron and the energy selection system is shown here. The highest dose rates occur in this area (Hofmann and Dittrich, 2005).

3.10.1.5 Paul Scherrer Institute (PSI), Switzerland. Figure 3.22 shows the proton treatment facility at the Paul Scherrer Institute (PSI). The facility is comprised of a 250 MeV ($I_{max} \leq 500$ nA) superconducting cyclotron, two gantry rooms, a fixed beam room, and a research room. The shielding design is essentially based on computational models (Teichmann, 2006). Concrete, heavy concrete, and steel were used for shielding. The design goals were a) dose rates less than 1 µSv/h for lateral walls, b) dose rates less than 10 µSv/h on top of the roof shielding, and c) dose rates less than 1to 10 µSv/h in accessible areas adjacent to the areas with beam. Because existing concrete blocks were used, and due to structural issues, walls are in some cases are thicker than necessary from a shielding point of view. The thickness of the roof of the degrader area is about 3.5 m; of the cyclotron area it is about 2.5 m; and the gantry rooms have a roof of about 1 m.

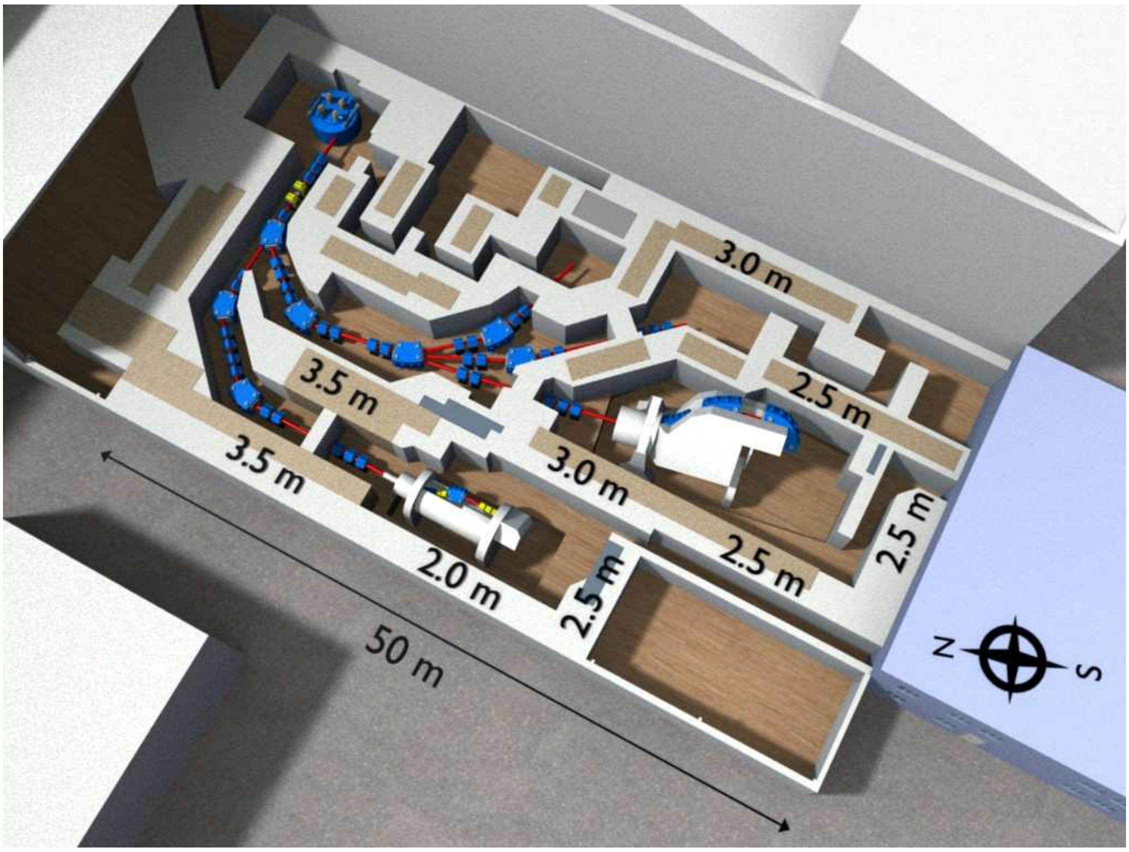

Figure 3.22. Treatment facility at PSI, Switzerland, with two gantry rooms and a fixed beam room (Courtesy of G. Fehrenbacher, J. Goetze, T. Knoll, GSI (2009)).

3.10.1.6 Proton Medical Research Center, Tsukuba, Japan. Figure 3.23 shows the proton medical research center in Tsukuba. The facility is comprised of a 23 m circumference synchrotron, two gantry rooms, and a research room. The injector consists of a Duoplasmatron ion source (30 keV beam energy), a radiofrequency quadrupole RFQ (3.5 MeV), and an Alvarez unit (7 MeV). The synchrotron accelerates protons to energies that range from 70 MeV to 250 MeV. The proton beam intensity is 6.1x 10^{10} particles per second (pps), and the total accelerated charge per week is 258 µC. The shielding design was developed on the basis of experimental data measured at the Los Alamos Meson Physics Facility (Meier, 1990). Double differential distributions for the produced neutron radiation in thick target approximation (carbon, iron, and others) were measured by means of the time-of-flight technique. Proton beams with energy of 256 MeV were used. The angular ranges of the measured neutrons were 30°, 60°, 120° and 150°. The transport of the source neutrons was performed by using the ANISN code (Engle, 1967) in combination with DLC-119B/HILO86R/J3 group constants of the cross sections.

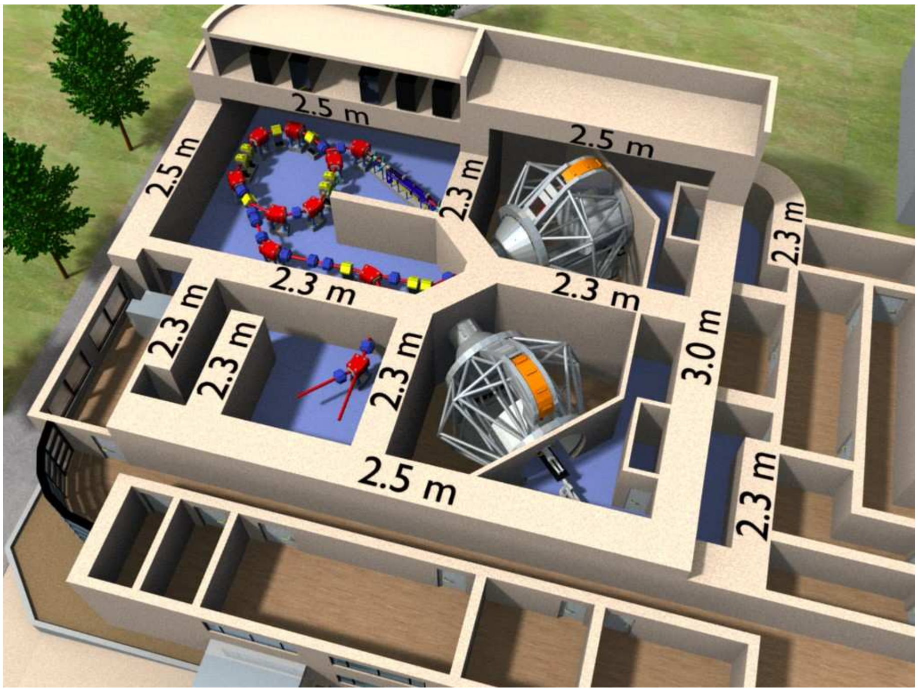

Figure 3.23. Layout of the Proton Medical Research Center at the University of Tsukuba (Courtesy of G. Fehrenbacher, J. Goetze, T. Knoll, GSI (2009)).

3.10.2 Facilities for Proton Therapy and Heavy Ion Therapy

3.10.2.1 Heavy Ion Medical Accelerator in Chiba (HIMAC), Japan. At HIMAC (Hirao *et al.*, 1992) a large variety of ions can be accelerated, such as p, He, C, Ne, Si and Ar ions. However, carbon ions are mainly used for patient treatment. The facility is shown in Figure 3.24 and is comprised of two synchrotrons, one horizontal (H) treatment room, one vertical (V) treatment room, one horizontal and vertical combination treatment room (H&V), a physics and general-purpose irradiation room, a medium energy beam irradiation room, and a room for biological irradiations. The combination treatment room can be operated with two different beams from both synchrotrons (see the red beam lines in Fig. 3.24).

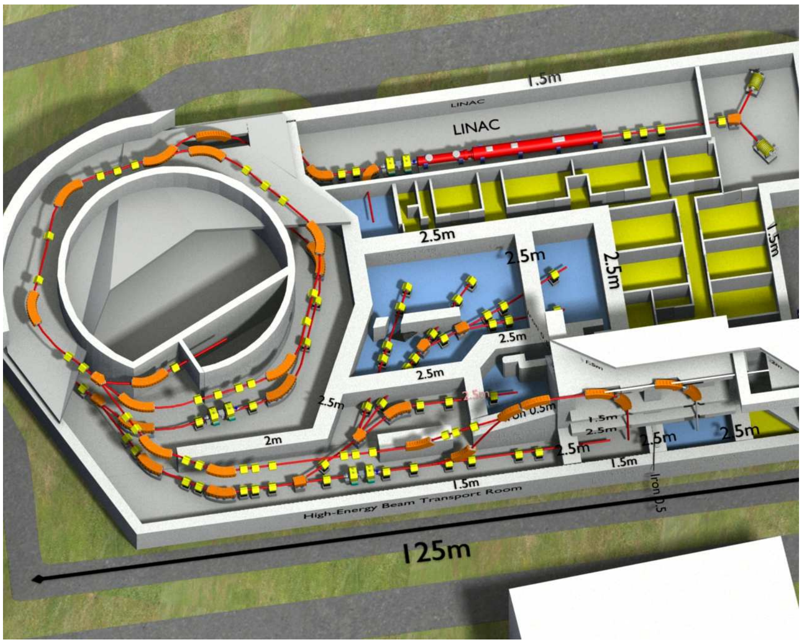

Figure 3.24. Schematic of the HIMAC facility (Courtesy of G. Fehrenbacher, J. Goetze, T. Knoll, GSI (2009)).

The extracted beam intensity for carbon ions from the synchrotron is 2 x 10^8 ions per second (Uwamino, 2007). Beam loss distributions are reported for 500 MeV/u He ions (energy higher than needed for therapy) (Uwamino, 2007). About 5 % beam losses occur during extraction, 10 % beam losses occur during the acceleration along the ring, 15 % beam losses occur at the ring scrapers, and 10 % beam losses at the vertical beam transfer lines. This beam loss data and the estimated time period of weekly operation per week (synchrotron, 108 h/week; treatment rooms, 11to 18 h/week) served as a basis for the shielding calculations. The results of HETC-KFA calculations (Cloth, 1981) were used to develop an approximate formula for the calculation of secondary neutron fluence produced by He ions and other ion types with the capability to compute the neutron fluence as a function of the ion energy (Ban, 1982). The attenuation of the neutron radiation in the bulk shield is calculated and the corresponding dose values are derived (Ban, 1982). The results for the shielding calculations are given in Table 3.7 for some essential areas in HIMAC. The shielding walls are partially augmented by iron. In Table 3.7 (3rd column), the values for the thicknesses of the combined concrete-iron shields are converted into effective values for concrete layers. The thickness of the shielding around the synchrotron is 1.5 m. At the extraction area there is an additional 2.5 m of shielding (Figure 3.24 left). The effective shield thicknesses for the treatment rooms in the forward and lateral direction are 3.2 m and 2.5 m, respectively. Shielding thicknesses for the high-energy beam transfer line, the roof shielding, and the floor shield are also given in Table 3.7.

Table 3.7: Shielding measures of the HIMAC facilities for some areas: synchrotron, therapy A, B, C, roof, floor, HEBT and Linac (Fehrenbacher, 2007).

Area	Shield Thickness (m) Forward Direction /Lateral Direction	Effective Concrete Thickness (m) Forward Direction /Lateral Direction
Synchrotron	1.5 (Additional 2.5 m local shielding inside)	-
A. Horizontal treatment room (H)	2.5 (0.5 Fe) / 2.5	3.22 / 2.5
B. Combination treatment room (H&V)	2.5 (0.5 Fe) / 1.6, Maze 1.6 (0.8 Fe)	3.22 / 1.6 Maze 2.75
C Vertical treatment room V	2.5 / 1.6, Maze 1.2	-
Roof	1.5	-
Floor	2.4	-
HEBT	1.5 – 2.0	-
Linac	1.5	-

3.10.2.2 Gunma University, Japan. Figure 3.25 shows a layout of the Gunma facility, which is comprised of a synchrotron and three treatment rooms (one horizontal beam line, one vertical beam line, and one H&V beam line). A fourth room with a vertical beam line is provided for the development of new irradiation methods (Noda *et al.*, 2006a). The maximum carbon ion energy is 400 MeV/u. About 600 patients are expected to be treated per year.

The desired beam intensity at the irradiation port is 1.2 $\times 10^9$ pps, which yields 3.6 $\times 10^8$ ions per second for patient treatment (Noda *et al.*, 2006a). An overview on beam intensities and beam loss distributions is given in Table 3.8 at different stages of the acceleration process. For the shielding design, it was assumed that unused ion beams are decelerated in the accelerator before being dumped (Noda *et al.*, 2006a) and consequently, the neutron production radiation is reduced. The dose rates are calculated as follows:

- The source distributions of the produced neutron radiation are taken from the Kurosawa measurements (Kurosawa, 1999; Uwamino, 2007).
- The beam loss distributions were determined by Noda *et al.* (2006a) and are listed in Table 3.8.
- The dose rates outside the shielding were computed using the ANISN code (Engle, 1967) and the cross sections from the JAERI (Kotegawa *et al.*, 1993).
- It is also reported that certain areas of the facility are designed using the PHITS-code (Iwase, 2002; Uwamino, 2007) described in Chapter 6.

The shielding thicknesses are shown in Figure 3.25. At some locations, the concrete shielding is augmented by iron shielding. The synchrotron walls are 3 m to 5 m thick. The horizontal treatment rooms are shielded with 3 m thick walls in the forward direction (1.9 m concrete and 1.1 m iron, which results in an effective thickness of 4.6 m concrete) and 1.5 m to 2.5 m in the lateral direction.. The linac walls are 1.0 m to 2.5 m thick. The floor slab has a thickness of 2.5 m. The roof shielding thickness varies from 1.1 m to 2.2 m thickness. The wall thicknesses of the fourth irradiation room (V) range from 1.1 m to 1.7 m, and are obviously reduced in comparison to the other treatment rooms due to shorter estimated irradiation time periods. Table 3.8 summarizes beam loss distributions and absolute beam intensities..

Table 3.8. Beam loss distributions and absolute beam intensities for the Gunma facility, calculated by Noda *et al.* (2006a). Efficiency η gives the ion beam transfer efficiency at different stages of the acceleration and transfer process. The beam intensity is given in the quantity particles per pulse (ppp) or in the quantity particles per sec (pps).

Section	Efficiency η	Beam Intensity
Injection	0.4	2E10 ppp
Synchrotron	0.64	5E9 ppp
Extraction	0.9	1.3E9 pps
HEBT	0.95	1.2E9 pps
Treatment Room	0.3	3.6E8 pps

. 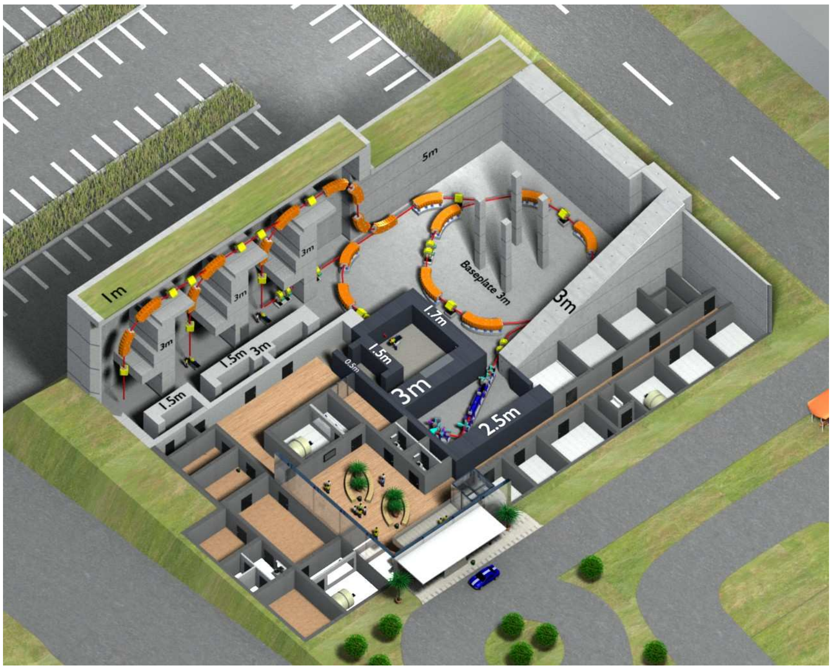

Figure 3.25. Layout of the Gunma ion irradiation facility with the LINAC, the synchrotron (ring accelerator), and the treatment rooms (Courtesy of G. Fehrenbacher, J. Goetze, T. Knoll, GSI (2009)).

3.10.2.3 CNAO, Pavia, Italy. Figure 3.26 shows the first stage of the CNAO facility which is comprised of a synchrotron, two horizontal beam treatment rooms, and one horizontal-vertical combination treatment room. Two gantry rooms will be added in the second stage. The facility is capable of accelerating protons to 250 MeV and carbon ions to 400 MeV. Preliminary shielding studies were performed by Agosteo (1996b). The most recent shielding design was carried by Porta *et al.* (2005) and Ferrarini (2007). The synchrotron is shielded by a 2 m thick concrete wall (for the most part) which is augmented by earth layers (5 m to 7 m for the public area). Inside the synchrotron there are additional local concrete shields. The treatment rooms are shielded such that the adjoining rooms are kept at dose rate levels lower than 0.5 μSv/h (annual dose less than 2 mSv, including the radiation sources from the synchrotron). The lateral shield thicknesses range from 2 m to 3.1 m and the forward shield walls have thicknesses of 4.2 m to 4.8 m with an effective thickness of up to 8 m because of the oblique incidence of the neutrons relative to the shielding walls. The floor shielding is 3.1 m and the roof shielding ranges from 1.1 m to 2 m.

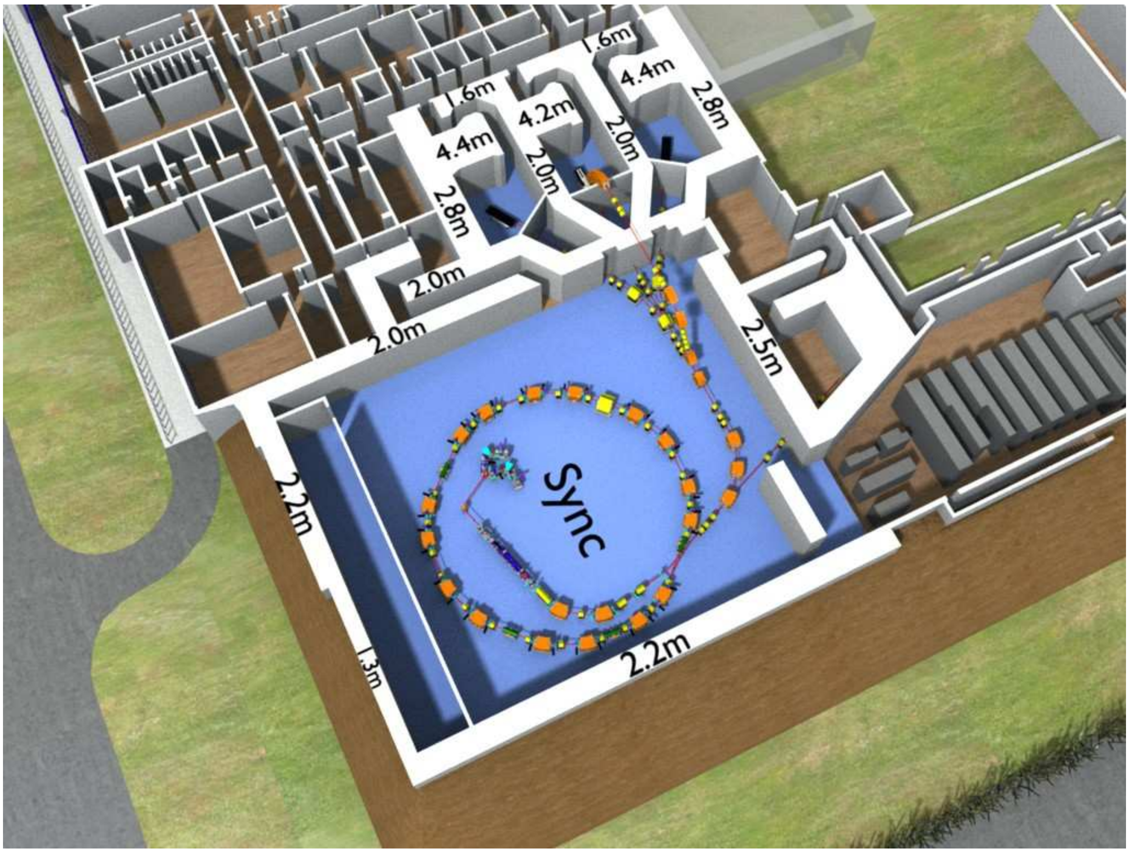

Figure 3.26. Overview of the CNAO facility (Courtesy of G. Fehrenbacher, J. Goetze, T. Knoll, GSI (2009)).

3.10.2.4 HIT, Heidelberg, Germany. Figure 3.27 shows part of the HIT facility which is comprised of a synchrotron, two horizontal treatment rooms (H), a carbon ion gantry room, and a research room. The facility is capable of accelerating protons as well as carbon, oxygen, and helium ions. The energies of the ions are so adapted that the maximum range in water is about 40 cm for protons and helium ions, 30 cm for carbon ions, and 23 cm for oxygen ions. The beam parameters for HIT are 4 x 10^{10} ppp for protons (220 MeV) or 1x 10^{9} ppp for carbon ions (430 MeV/u).

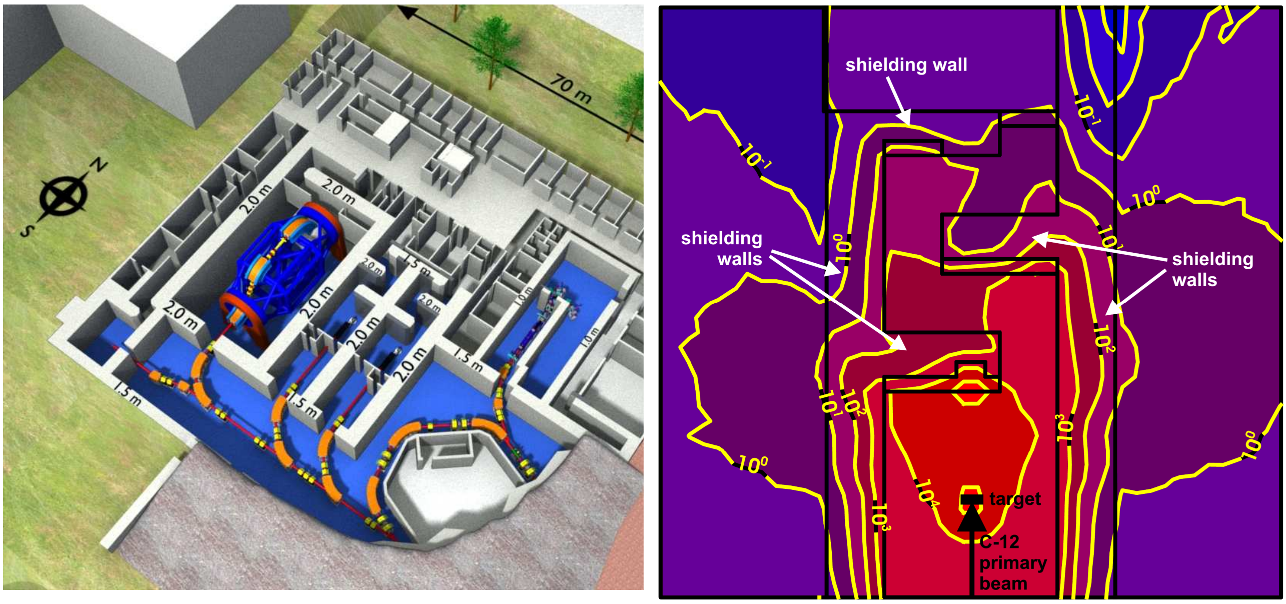

Figure 3.27. Left: Part of the HIT facility in Heidelberg. Right: The dose distribution in the horizontal beam treatment rooms are also shown for carbon ion beams (Fehrenbacher, 2007). The isodose values (yellow) are given in the units of µSv/h. The values range from 10^5 µSv/h (red) over 10^2 µSv/h to 10^{-1} µSv/h (blue) with increments of a factor of 10 (Courtesy of G. Fehrenbacher, J. Goetze, T. Knoll, GSI (2009)).

The shielding design was developed on the basis of the Kurosawa neutron spectra of the 400 MeV/u of carbon ions (Kurosawa *et al.*, 1999). A line-of-sight model was used to determine dose rates of the neutron radiation outside the shield (Fehrenbacher *et al.*, 2001). The model considers the angular dependence of the neutron production (0° to 90°), the angular dependent neutron energy distribution (E_n > 5 MeV), the neutron energy dependent absorption (removal cross section), and the build-up effect of the neutron radiation in matter. For angles greater than 90° relative to the incoming ion beam, the neutron source distribution at 90° was used. Monte Carlo calculations with FLUKA (Fasso *et al.*, 1997) were also performed for the horizontal treatment rooms using the 2000 version of FLUKA and the Kurosawa neutron spectra (Fehrenbacher *et al.*, 2002a; Kurosawa, 1999) as well as for the gantry room (Fehrenbacher *et al.*, 2002b). The results of the treatment room calculations are shown on the right in Figure 3.27 for carbon ion beams with 400 MeV/u and 3x 10^8 ions/sec deposited in a graphite target (Fehrenbacher, 2007). Further specific studies were performed with FLUKA to study the impact of recesses in the floor shielding for the horizontal treatment rooms for the installation of robots. When the heavy ion version of FLUKA (Fasso *et al.*, 2005) was released, a full simulation was performed with FLUKA and the results were compared with the simulation using the Kurosawa neutron source spectra as the input for FLUKA. Reasonable agreement (within 26 %) was obtained for the simulations.

The shielding design is based on the annual dose limits given in the Table 3.1 of Section 3.1.2. An additional dose rate guideline of 3 µSv/h was used outside the interlocked area for 10-min irradiation periods. The shielding design is based on a 10 % beam losses at local (specific) areas, such as the beam extraction point, and a 10 % beam losses in the dipole magnets. Additional local concrete shielding was added in the synchrotron and beam transfer lines because the exact beam loss distribution in these areas was unknown.

For the horizontal beam treatment rooms, the shielding of the three walls in the entrance maze, perpendicular to the beam direction that intercept the 0° beam, is comprised of 1.5 m steel and 5.5 m concrete (total effective concrete thickness of 7.66 m). The lateral concrete thickness is 2 m. The gantry room has a wall thickness of 2 m. For the gantry room calculations, the iron counterweight of 1 m thickness was taken into account, because this attenuates the main neutron cone substantially in the angular range +/- 25° relative to the ion beam line. Application of the use factor for the gantry room reduces the thickness. The roof shielding (2 m) of the horizontal treatment rooms is partially augmented with 0.5 m of steel (total effective concrete thickness of 2.72 m). The synchrotron is shielded by a 1.5 m thick concrete wall and partially by earth on the exterior. Earth (and other bulk materials) covers the concrete roof of the synchrotron and treatment rooms. The floor slab is 1.5 m to 1.8 m thick and reduces the activation of soil and ground water.

3.11 Qualified Expert

In the case of charged particle therapy facilities, a qualified expert is a physicist who has expertise and proven experience in the shielding design and radiological aspects of high-energy particle accelerators, particularly in the shielding of relativistic neutrons. The individual must also be capable of performing Monte Carlo calculations. Various countries may have different requirements for qualified experts. In the U.S., most of the states require that the qualified expert is either registered or licensed in the state.

The qualified expert should be involved in the following phases of the facility design and construction, so that costly mistakes can be prevented and an optimum and cost effective shielding design can be implemented.

3.11.1 Schematic Design

During this phase, the architect organizes the rooms, the layout of the facility is determined, and a preliminary design is generated. The qualified physicist should be invited to attend meetings with the owner and architect. Occupancy factors should be established. Adjacent buildings and multi-storied structures should be identified. The use of space must be evaluated. The highest radiation levels occur near the treatment rooms and the accelerator. Therefore, high occupancy rooms such as nurse's stations, offices, and examination rooms should be located as far away as possible, while low occupancy rooms such as storage areas may be located closer. Typically, control rooms, patient preparation rooms, *etc*. are in the immediate vicinity of the treatment rooms.

Workloads should be established. The owner should provide information on the types of particles to be used, the energies of the particles, the number of treatments per hour, the beam-shaping methods that are to be used, *etc*. If an equipment vendor has been selected, the vendor should provide the information regarding beam losses, locations and targets, and currents for various beam-shaping methods, as well as other information requested by the expert. The concrete composition and density should be provided at this phase so that the physicist can perform Monte Carlo calculations. The architect should provide the expert with scaled drawings including both plans and sections. All dimensions and details must be called out on the drawings. The drawings should show the equipment in place and the location of the isocenter. The qualified expert should work with the owner and architect, suggesting the most cost-effective and space-optimizing design, shielding configurations and materials, and preliminary thicknesses. The preliminary thicknesses will be based on site-specific workload, local regulations, and other assumptions. The architect should incorporate the shielding thicknesses into the drawings, and the revised drawings should be sent to the expert for review. A few iterations may take place. The qualified expert should carefully review the architect's drawings. The qualified expert should write a preliminary shielding report that includes all the assumptions and specifies the required shielding.

3.11.2 Design Development

In this phase, rooms, sizes, and locations will be determined to a greater detail (NCRP, 2005), and the design will be finalized. The mechanical, electrical, and plumbing details will be worked out, and sizes of penetration, conduits, ducts, *etc*. will be determined. The architect should incorporate all the new information into the drawings so that the expert can determine the required shielding for all the penetrations. Once the shielding has been finalized, the expert should write the final shielding report which can be submitted to the pertinent regulatory agency. The report should show doses at all locations and verify regulatory dose compliance. Contents of the report are discussed in Section 3.12.

3.11.3 Construction Documentation

During this phase, all the construction drawings are prepared. Details of the project are finalized in preparation for construction. The shielding in the construction drawings should be identical to that which is shown in the shielding report. The qualified expert should review all drawings and all submittals (drawings and information submitted by subcontractors) related to concrete density and composition, door shielding, penetration shielding, and other special shielding materials. The qualified expert will also respond to request for information (RFI) from the contractor. Prior to construction, the qualified expert should participate in a meeting with the owner, architect, contractor, and all other trades to finalize the shielding items. During this phase there may be changes in shielding configuration due to constructability issues. The qualified expert should review all such changes.

3.11.4 Construction Inspection

During construction, the qualified expert should perform site visits and inspections to ensure that the shielding is implemented as specified in the shielding report. The qualified expert should carefully review the shielding to ensure that there are no cracks or thin spots. The dimensions, materials, and configuration of the room shielding, as well as door and penetration shielding, should be verified. Inspection reports should be provided by the expert. Any instances of noncompliance should be reported and corrected by the contractor or subcontractor.

3.12 Shielding Report

A copy of the shielding report should be maintained by the facility. The shielding report should include but is not limited to:

1. Names and contact information for qualified physicist, architect, and responsible person at the facility
2. Name and address of facility
3. A brief description of accelerator, beam transport lines, treatment rooms
4. Beam parameters, loss scenarios, targets, and location
5. Workload and usage assumptions
6. Occupancy factors
7. Regulatory and design limits
8. Concrete composition and density
9. Drawings, including plans and sections of all shielded rooms with dimensions called out, doors, penetrations, *etc*. and locations at which doses are calculated

10. Dose and dose rate compliance with regulatory limits after application of occupancy and use factors
11. Additional instructions for architects and contractors on shielding, such as concrete pours, the use of keyways, interlocking blocks, site density testing, *etc*.

3.13 Shielding Integrity Radiation Survey

Radiation surveys are performed to verify the integrity of the shielding and dose compliance with design and regulatory limits. Preliminary neutron and photon radiation surveys should be performed as the accelerator is made operational, and when beam is transported to the treatment rooms. A final radiation survey should be performed once the facility is completely operational. Regulatory agencies also typically require shielding integrity radiation surveys during start up. Instruments that can be used for radiation surveys are described in Chapter 4. The survey results should then be used to verify that the doses obtained with the workload assumptions are in compliance with design and regulatory limits. A repetition of the shielding integrity radiation survey must be repeated when there are changes in the shielding (such as dismantling and reassembling) or when there are changes in beam operating parameters. A copy of the survey report should be maintained by the facility. The report should include but is not limited to:

1. Names of individuals performing the survey
2. Name of facility
3. Dates of survey
4. Machine conditions and beam operating parameters
5. Details of phantoms used in treatment room
6. Instruments used, including type, model, serial number, and calibration certificate (calibration must be current)

7. Beam parameters, loss scenarios, targets, and location
8. Workload and usage assumptions
9. Occupancy factors
10. Doses in occupied areas
11. Compliance with design and regulatory limits.

4. Radiation Monitoring

Yoshitomo Uwamino and Georg Fehrenbacher

4.1 Introduction

The different types of radiation which are of concern for individual exposure at a particle therapy facility are prompt radiation during beam operation and residual radiation after the beam is turned off. The prompt radiation is comprised of neutrons and photons behind thick shields of treatment rooms or accelerator vaults, while the residual radiation consists of photons and beta rays from induced radioactivity. Neutron and photon exposure of the patient in the treatment room are also of interest (see Chapter 7).

Many valuable references on the basics and principles of radiation detection are available in the literature (Ahmed, 2007; Knoll, 1999; Leroy and Rancoita, 2005; Tsoulfanidis, 1995). ICRU Report 47 (ICRU, 1992a) provides details on the measurements of photon and electron dose equivalents, while ICRU Report 66 (ICRU, 2001) covers neutron measurements. This chapter provides an overview of radiation monitoring and commercially available instrumentation for particle therapy facilities. Since radiation protection regulations vary from country to country, and in some countries from state to state, each facility must ensure that radiation surveys are performed in compliance with the regulations applicable to their specific facility.

4.1.1 Operational Quantities

The quantities to be measured are ambient dose equivalent at 10 mm depth, $H^*(10)$, for area monitoring, and personal dose equivalent at 10 mm depth, $H_p(10)$, for individual monitoring. The shallow doses $H_p(0.07)$ and $H_p(3)$, at a depths of 0.07 mm, and 3 mm, respectively, are usually not as important at particle therapy facilities when compared to the strongly penetrating radiation which dominates the dose outside the shielding. Figure 4.1 shows the fluence-to-dose-equivalent conversion coefficients (see Section 1.2.2 for details) as a function of particle energy (ICRP, 1996). Also shown are the fluence-to-effective-dose conversion coefficients for Anterior–Posterior irradiation geometry, E(AP), including the recommended data of E(AP) by the Atomic Energy Society of Japan (AESJ, 2004) for high-energy particles. The neutron data provided by the ICRP are limited to energies of 20 MeV and below for $H_p(10)$ and 180 MeV and below for $H^*(10)$, respectively. The photon data is limited to energies of 10 MeV and below. Because the conversion coefficient for $H^*(10)$ for neutrons becomes smaller than that for E(AP) above 50 MeV, measurement of E(AP) may be considered appropriate for high-energy neutrons. $H^*(10)$ is not always a conservative estimate for the effective dose, especially for E(AP). This argument also applies for photons. The results of several studies performed for high-energy neutrons and photons are reported in the literature (Ferrari *et al.*, 1996; 1997; Mares *et al.*, 1997; Sakamoto *et al.*, 2003; Sato *et al.*, 1999; Sutton *et al.*, 2001). The conversion coefficient for E(AP) becomes smaller than that for Posterior-Anterior irradiation geometry, E(PA), at neutron energies above 50 MeV. However, the integrated dose from thermal neutrons to high-energy neutrons is highest for AP geometry, and therefore only E(AP) is considered here.

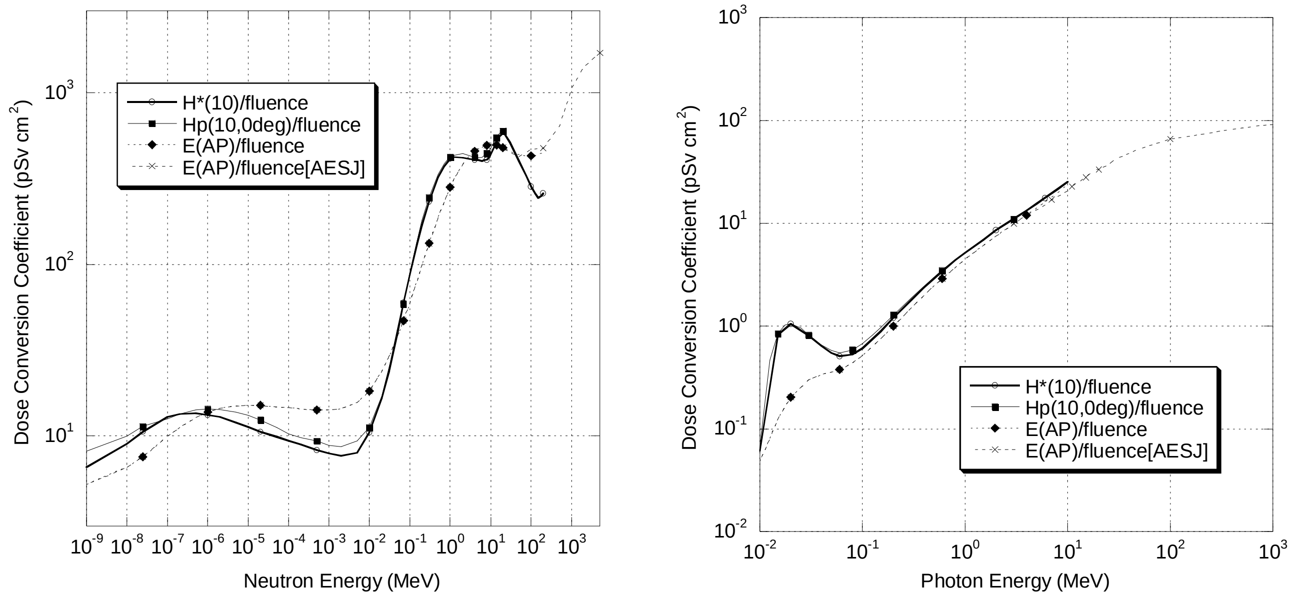

Figure 4.1. Dose conversion coefficients from particle fluence to ambient dose equivalent, $H^*(10)$, personal dose equivalent, $H_p(10)$, and effective dose with AP geometry, $E(AP)$.

4.2 Prompt Radiation Monitoring

4.2.1 Characteristics of Prompt Radiation Field

4.2.1.1 Mixed Field. High-energy protons and ions produce high-energy neutrons and photons through nuclear interactions with the components of the accelerator and the energy selection system, beam delivery nozzle, and the patient tissue. Several kinds of light ions are produced by the fragmentation process of the primary heavy ions, and these light ions also produce neutrons and photons. High-energy neutrons are slowed down by nuclear scattering and are finally absorbed by matter. Photon emissions accompany these nuclear reactions.

Photons produced by primary charged particles are easily absorbed by the thick room shielding; however, high-energy neutrons can penetrate the shielding. These neutrons produce secondary photons during transmission, resulting in neutrons and photons outside of the shielded area. Neutrons having energies lower than several tens of MeV are easily absorbed. Peaks at about 100 MeV and several MeV appear in the neutron energy spectrum at the outer surface of the shielding. Figure 4.2 shows the angular and energy distributions of neutrons produced in a water phantom of 10 cm diameter and 25 cm thickness irradiated by 400 MeV/nucleon ^{12}C ions, and the neutron and photon spectra in the beam direction behind a 2 m thick ordinary concrete shielding.

Figure 4.3 shows the ratio of the cumulative dose as a function of energy to the total dose calculated with the spectra shown in Fig. 4.2. For photons, almost 100 % of the dose can be measured with a detector, which is sensitive up to 10 MeV, and most conventional detectors meet this criterion. For neutrons, however, typical dosimeters, which are sensitive up to about 15 MeV, may give only one third of the true value dose in the forward beam direction outside a thick concrete shield. In the lateral directions, their readings are more reliable.

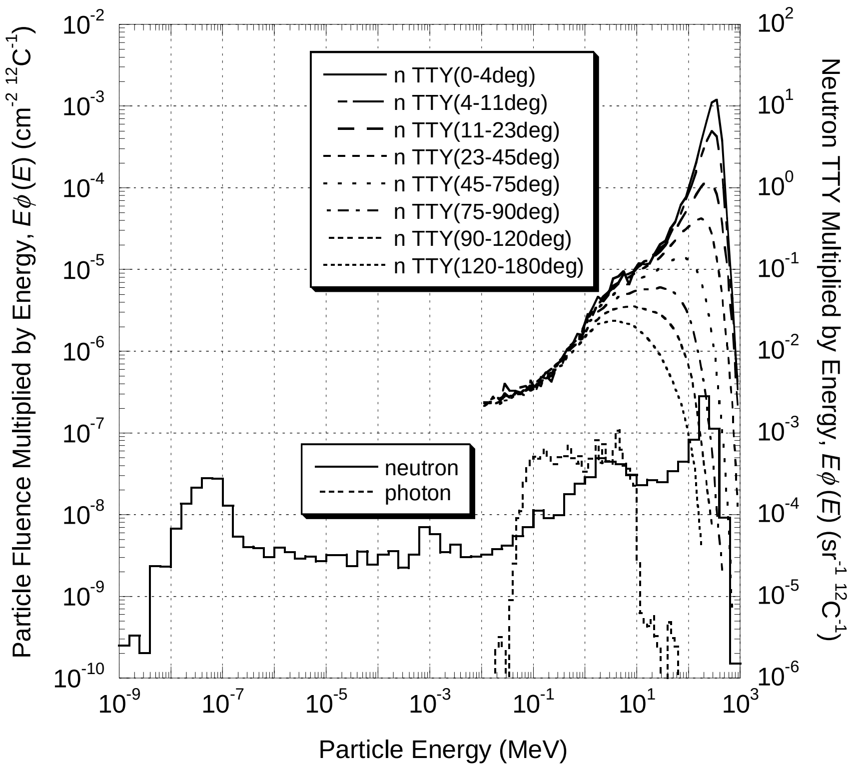

Figure 4.2. Angular and energy distributions of TTY (Thick Target Yield) neutrons from a 10 cm diameter by 25 cm thickness water phantom irradiated by 400 MeV/nucleon ^{12}C ions are shown on the upper right with the right ordinate. Neutron and photon spectra behind a 2 m thick ordinary concrete shield in the beam direction are also shown with the left ordinate. These spectra were calculated using the heavy ion Monte Carlo code, PHITS (Iwase *et al.*, 2002).

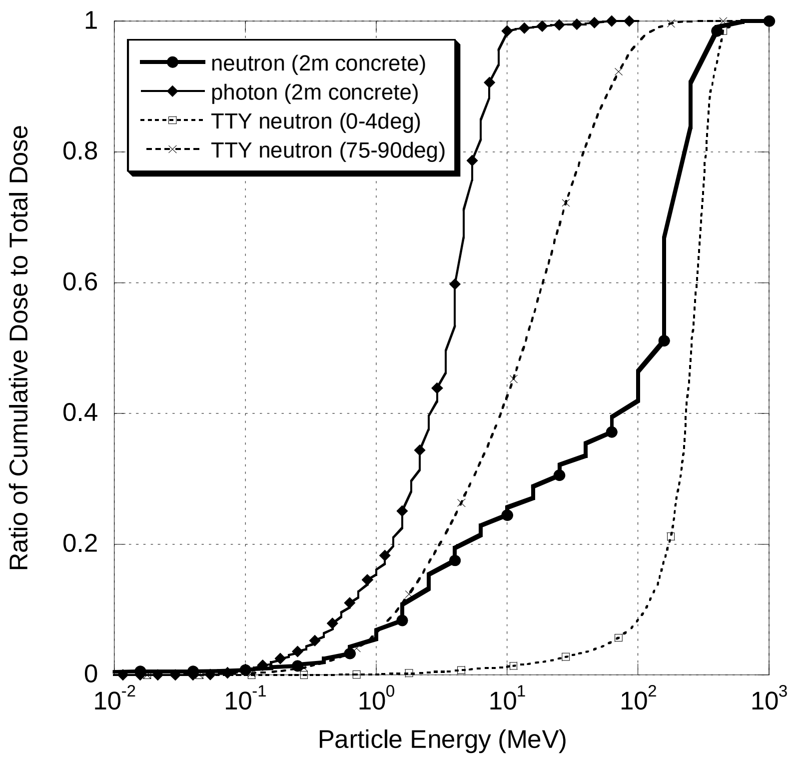

2895

2896 Figure 4.3. The ordinate is $\left(\int_0^E E_\phi(\mathrm{AP})\phi(E)dE \Big/ \int_0^{E\max} E_\phi(\mathrm{AP})\phi(E)dE\right)$ where E is particle energy, E_ϕ(AP) is the

2897 dose conversion coefficients from particle fluence to effective dose for AP geometry (AESJ, 2004), and

2898 $\phi(E)$ is the particle energy fluence shown in Fig. 4.2.

Since a neutron detector, such as a rem meter, has very low sensitivity to photons, it is considered photon insensitive for charged particle therapy facilities. Photon detectors are also somewhat sensitive to neutrons, but the estimation of the neutron contribution is difficult. Because neglecting this contribution results in conservative measurements, the neutron sensitivity is usually ignored for the purpose of radiation protection.

Primary charged particles are stopped in the patient. Heavy ions, however, produce lighter particles such as protons and deuterons through fragmentation reactions before stopping. These lighter particles have longer ranges, and some of them penetrate the patient. When detectors are placed in the vicinity of a phantom to estimate the neutron and photon exposure to a patient, veto counters operated in anticoincidence mode may be necessary to eliminate these lighter particles from being recorded.

4.2.1.2 Pulsed Field. A detector that counts pulsed signals has an insensitive period after counting, and this period is called dead time or resolving time, which usually lies between about 10^{-8} s and 10^{-4} s.

A cyclotron accelerates particles every 10^{-8} s or so, and this acceleration interval is near or shorter than the dead time, and, therefore, the cyclotron beam is considered to be continuous.

The acceleration interval of a synchrotron, on the other hand, is between 10^{-2} s and 10 s, and thus its beam has the characteristics of pulsed radiation. During a pulse, a very large amount of radiation is delivered in a very short time period. Even if several particles of radiation hit a detector within its dead time, the detector produces only one pulsed signal. This counting loss is a serious problem in a pulsed radiation field.

The effect of pulsed field is serious near a radiation source because there is hardly any time delay between the irradiation of primary particles and the detection of secondary neutrons and photons. The time structure of the neutrons outside the shielding, on the other hand, spreads owing to the different time-of-flight, *e.g.*, the time-of-flight for 1 m distance is 8 ns for 100 MeV neutrons and 0.5 ms for thermal neutrons.

If one observes the characteristics of pulsed signals from a detector placed in a pulsed field, on an oscilloscope, it can be determined whether the reading is correct or not. That is, if the pulse repetition rate is coincident with the beam extraction rate, the reading of the detector is not correct. A detector measuring an electric current such as an ionization chamber is not usually affected by the pulsed field. However, saturation effects due to the recombination of the dense electrons and ions at high peaked dose rate may become important.

In a particle therapy synchrotron, however, the accelerated particles are extracted slowly because the irradiation dose must be precisely controlled. The extracted beam, therefore, usually has the characteristics of continuous radiation. For example, at the HIMAC (Heavy Ion Medical Accelerator in Chiba) of the National Institute of Radiological Sciences, the acceleration period is 3.3 s and the duration of extraction is about 2 s.

4.2.1.3 Noise. An accelerator uses high-power, high-frequency voltage for acceleration, which is a very strong source of background noise, thus affecting measurements with active detectors. The signal cables of the detectors should be separated from the accelerator power cables. Wiring in a grounded metal pipe is effective for noise reduction. Use of optical fibers is costly but very reliable for discrimination against noise. Optical fibers, however, are susceptible to mechanical shock and bending, and lose transparency at high radiation exposures.

4.2.1.4 Magnetic Field. Accelerators and beam transport systems use high magnetic fields for bending and focusing the beam. Magnetic fields strongly affect photomultiplier tubes, thus a usual scintillation survey meter cannot be used around the magnetic apparatus. Even if the electric current is switched off, the residual magnetic field due to hysteresis may affect detectors located near magnets. However, a scintillator coupled to a photo diode is hardly affected by a magnetic field. An analog indicator using an ammeter does not respond correctly in a magnetic field. A liquid crystal indicator is much more reliable.

4.2.1.5 Radiations Unrelated to Beam Acceleration. Devices operating under high-radiofrequency power, such as an acceleration cavity and a klystron, emit intense x rays even if the beam is not accelerated. Leakage of radiation occurs at glass windows and bellows, which are made of low atomic number materials or thin metal. X-ray leakage from an Electron Cyclotron Resonance (ECR) ion source is also significant.

4.2.2 Survey Meters

Handheld survey meters are typically used to measure instantaneous dose rates and to map the dose rate distribution outside the shielding. Since the radiation field around a particle therapy facility is comprised of neutrons and photons, the simultaneous use two types of survey meters is required.

4.2.2.1 Neutron Survey Meters

4.2.2.1.1 Rem Meter. A rem meter (or a rem counter) is the most popular neutron dose-equivalent survey meter. It consists of a thermal neutron detector such as a BF_3 (boron trifluoride) or ^3He

(helium) proportional counter or a ^{6}Li (lithium) glass scintillation counter that is surrounded by a specially designed polyethylene neutron moderator. The moderator slows down fast and intermediate energy neutrons, which are then detected by the thermal neutron detector. Because an ordinary rem meter is practically insensitive to neutrons of energies above 15 MeV, it underestimates the result by as much as a factor of 3 when used outside a shield of a particle therapy facility as shown in Fig.4.3. Improved rem meters are also available. These consist of high-atomic number inserts such as lead or tungsten in the polyethylene moderator (Birattari *et al.*, 1990; Olsher *et al.*, 2000). The interaction of high-energy neutrons with this inserted material causes neutron multiplication and energy degrading reactions such as (n, 2n), thus improving the sensitivity to high-energy neutrons. These improved rem meters are too heavy to be handheld, but give reliable results. An example of such a commercially available rem meter, FHT 762 Wendi-2, is shown in Fig. 4.4. This instrument has an excellent energy response from thermal to 5 GeV, and the response function is shown in Fig. 4.5.

Figure 4.4. FHT 762 Wendi-2 rem meter has an improved energy response to high-energy neutrons. (Courtesy of Thermo Scientific[4])

4 Thermo Scientific, 27 Forge Parkway, Franklin, Massachusetts 02038 U.S.A.

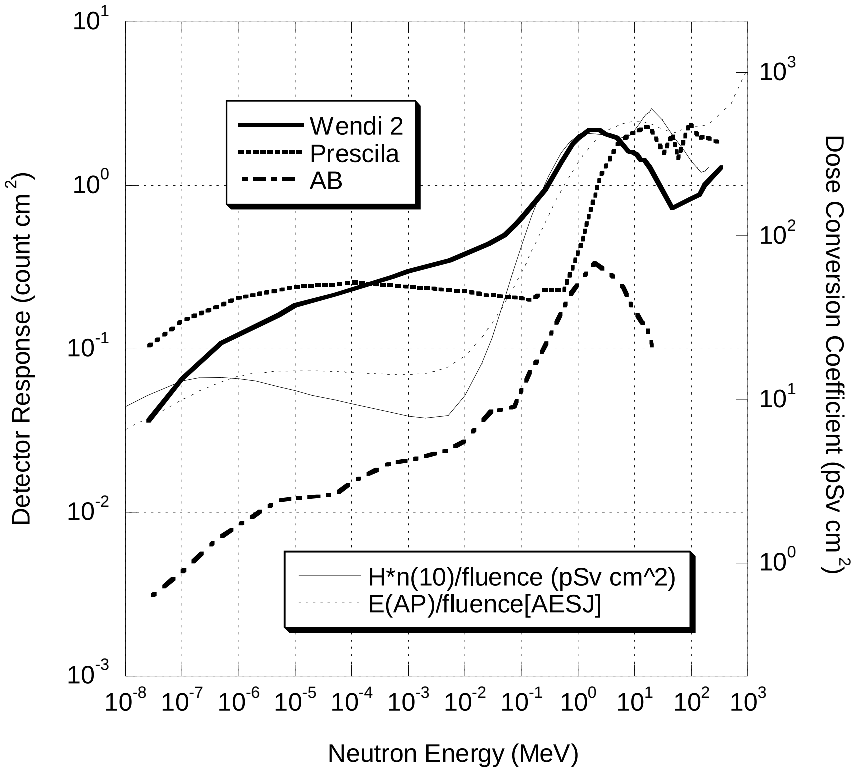

Figure 4.5. The response function of the Wendi-2 rem meter is shown with the left side vertical axis. The response functions of the Prescila rem meter described in Section 4.2.2.1.2 and the conventional Andersson-Braun rem meter (AB) are also shown (Olsher *et al.*, 2000; 2004; courtesy of R.H. Olsher). The dose conversion coefficients of *H**(10) and *E*(AP) are shown for the reference with the right side vertical axis (AESJ, 2004; ICRP, 1996).

4.2.2.1.2 Proton Recoil Scintillation Counter. A complex detector consisting of two types of sensors for fast neutrons and thermal neutrons is available as Prescila rem meter (Olsher *et al.*, 2004). The fast-neutron sensor consists of a mixture of ZnS(Ag) scintillation powder and epoxy glue and a Lucite-sheet light guide. The thermal-neutron sensor is a ^{6}Li+ZnS(Ag) scintillator. By using filters of cadmium and lead, this counter has a response function whose shape is similar to the conversion coefficient for neutron fluence-to-dose equivalent, and is sensitive to neutrons above 20 MeV. Its sensitivity is about 10 times higher than the conventional moderator-based rem meter, and its weight is about 2 kg.

4.2.2.2 Photon Survey Meters

4.2.2.2.1 Ionization Chamber. The ionization chamber is the most useful photon survey meter because it almost energy-independent (usually within ± 10 % of unity) between 30 keV and a few MeV. The lower detection limit is about 1 μSv/h; thus, one cannot measure the dose rates close to the background level. Some types of ionization chambers have removable caps that enable the measurements of very soft x rays. Since the ionization chamber survey meter measures a very weak current of the order of femtoamperes (fA) when placed in a field of several μSv/h, it takes several minutes until the detector becomes stable after being switched on.

4.2.2.2.2 NaI(Tl) Scintillator. Scintillators of high atomic number, such as sodium iodide (NaI) and cesium iodide (CsI), have poor energy response for the measurement of dose equivalent. However, some scintillation survey meters that have compensation circuits show good energy response similar to ionization chambers. Scintillation survey meters are mostly insensitive to photons of energies below 50 keV and not appropriate for low-energy x-ray fields. However, an instrument of NHC5,[5] which is sensitive down to about 8 keV, is currently available.

4.2.3 Spectrometers

4.2.3.1 Photon Spectrometer. High purity germanium (Ge) detectors have an excellent energy resolution and are commonly used for photon spectrometry in research work. Since the Ge detector must be cooled down to liquid-nitrogen temperature, it is not suitable for routine measurements. Handheld scintillation survey meters designed for photon spectral measurements are commercially available, such as InSpector™ 1000[6] and identiFINDER™.[7] Handheld survey meters with cerium-doped lanthanum bromide ($LaBr_3$(Ce)) scintillators are also available. The latter has better energy resolution than the conventional thallium-doped sodium iodide (NaI(Tl)) scintillator. An unfolding process is required for the conversion from the light-output distribution obtained by the detector to the photon energy spectrum.

4.2.3.2 Neutron Spectrometer. Measurements of light-output or time-of-flight distributions are common techniques for obtaining high-energy neutron spectra with good energy resolution. For a simple measurement, a set of neutron detectors with moderators of different thicknesses, the so-called Bonner spheres, can be used (Awschalom and Sanna, 1985; Wiegel and Alevra, 2002). Wiegel and Alevra used copper and lead in the moderators, and their spectrometer, NEMUS,[8] can be used to measure high-energy neutrons up to 10 GeV. Figures 4.6 and 4.7 show the responses of the NEMUS spheres as a function of neutron energy. The difference of the important neutron energies of each sphere gives the spectrum

---

[5] Fuji Electric Systems Co. Ltd., 1-11-2, Osaki, Shinagawa, Tokyo 141-0032 Japan

[6] Canberra Industries, Inc., 800 Research Parkway, Meriden, Connecticut 06450 U.S.A.

[7] ICx Radiation Inc., 100 Midland Road, Oak Ridge, Tennessee 37830 U.S.A.

[8] Centronic Limited, King Henry's Drive, Croydon, Surrey CR9 0BG, UK

information. The set of the results of these detectors is converted to the neutron energy spectrum with an unfolding computer program. An initial assumed spectrum that is properly obtained by calculations or theories is necessary to initiate the unfolding process.

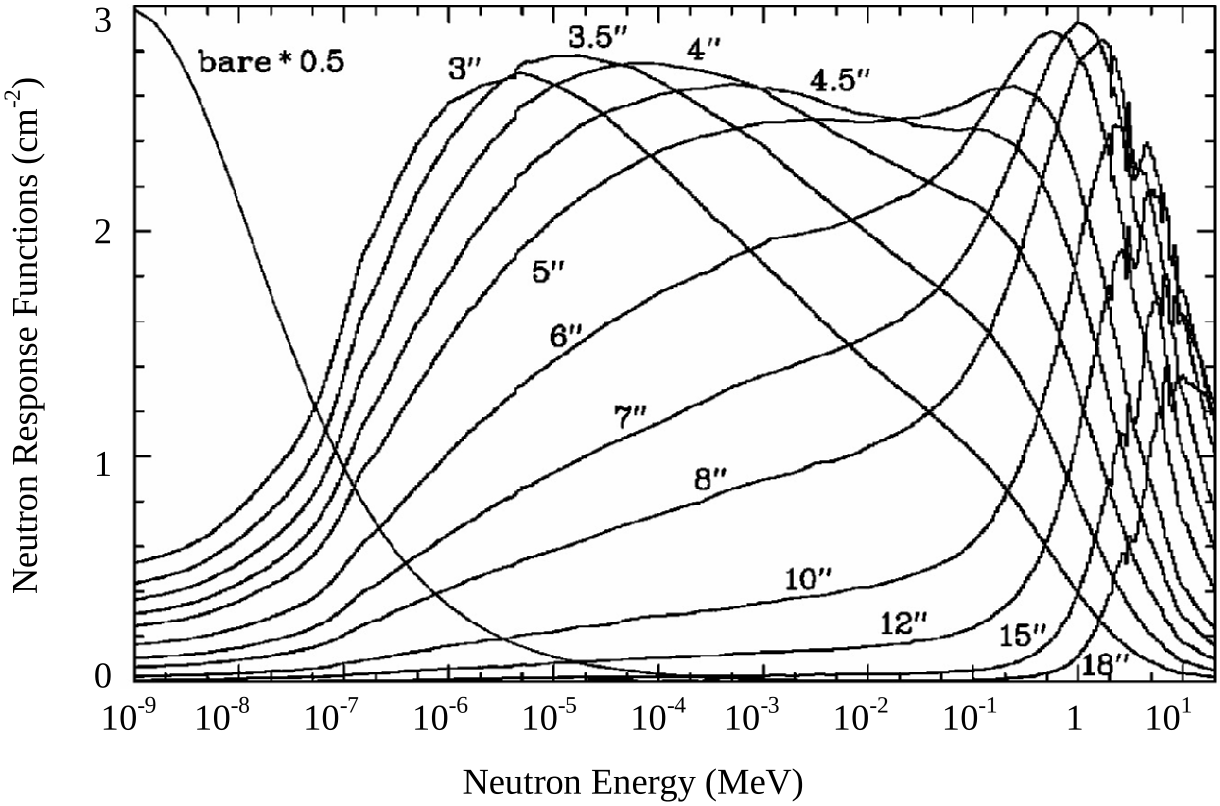

Figure 4.6. Responses of the NEMUS Bonner spheres. The lengths in inches show the diameters of polyethylene moderators (Wiegel and Alevra, 2002).

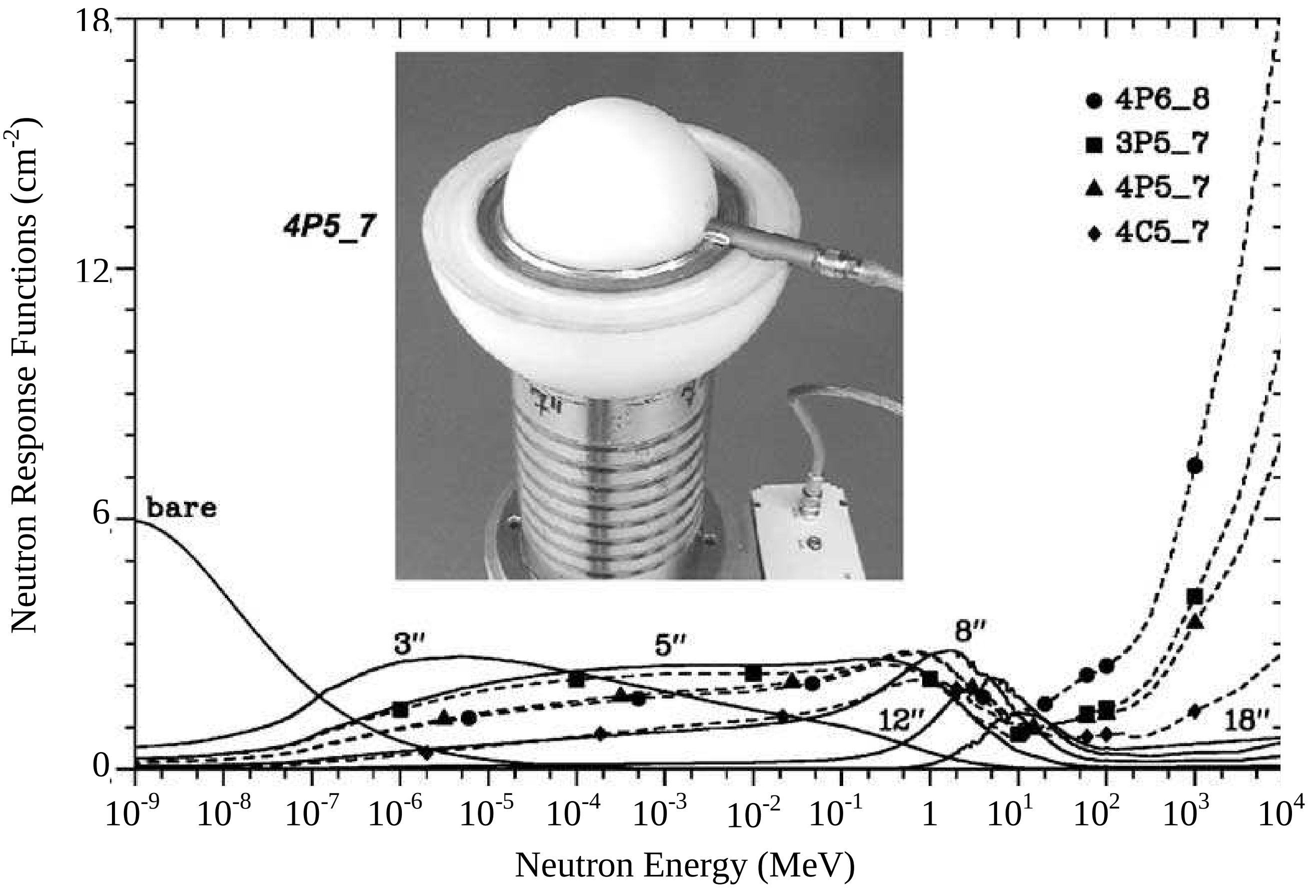

3049

3050 Figure 4.7. Responses of the extended NEMUS Bonner spheres. “4P5_7”, for example, means that the
3051 ^{3}He counter is placed in a 4-inch polyethylene sphere covered by a 0.5-inch-thick Pb shell (the diameter
3052 therefore is 5 in) and all are imbedded in a 7-inch polyethylene sphere. The photo shows the opened
3053 configuration. “4C5_7” means that the inserted shell is of 0.5-inch-thick Cu. Six response functions of
3054 the pure polyethylene moderators are also shown (Wiegel and Alevra, 2002).

4.2.3.3 LET Spectrometer. The tissue-equivalent proportional counter (TEPC) measures an LET (linear energy transfer) spectrum of secondary charged particles produced by neutrons and photons, and the spectrum is converted into dose equivalent or effective dose for both types of radiation. The TEPC is applicable to any type of radiation because of its measurement principle, and the total dose in a mixed field is obtained. Several systems have been developed and used (Alberts, 1989; Mazal *et al.*, 1997). The TEPC, however, has the disadvantage of susceptibility to mechanical shocks, thus preventing its widespread use for routine measurements as a survey meter.

4.2.4 Area Monitors

An area monitoring system consists of pairs of neutron and photon dosimeters and a central control unit. For neutron detection, rem meters are usually used. Ionization chambers, scintillation detectors, or semiconductor detectors are selected for photon detection depending upon the radiation intensities. Stations having local radiation level indicators are also available. The central control unit shows trend graphs of radiation levels of each station, and records data in a server. The system is of high performance and expensive (see Fig. 4.8).

(a) (b)

Figure 4.8. An example of a monitoring station (a) and a central control unit, MSR-3000, (b). The station has a neutron rem meter and a photon detector.(Courtesy of ALOKA[9])

[9] ALOKA Co., Ltd., 6-22-1, Mure, Mitaka,Tokyo 181-8622 Japan

Before determining the monitoring locations, the dose distribution in and around the facility must be thoroughly studied. Monitoring stations are located where high radiation dose rates are expected or where radiation levels are important for safety reasons. However, high dose-rate radiation inside the irradiation room, for example, sometimes causes a breakdown of an intelligent monitoring station.

At accelerator facilities for physics research, area monitors are typically included in safety systems and are interlocked so that they turn the beam off when measured radiation levels outside shielded areas exceed a preset value, either considering instantaneous or integrated values. However, at particle therapy facilities, interruption of the beam is not desirable because the beam is used to treat the patients. Therefore the systems must be designed robustly enough that no false alarms are given. It depends on the local regulations what type of action needs to be performed when an alarm is given.

As the above monitoring system is expensive, it is difficult to distribute many stations. Because the neutron dose is usually dominant around a particle therapy facility, it is possible to place many neutron rem meters, described in Section 4.2.2.1.1, whose analog outputs are read by a programmable logic controller (PLC) of a safety system (Uwamino *et al.*, 2005). When the analog output is logarithmic, the PLC reads the dose rate with a wide dynamic range of more than 5 decades. If the analog output is a voltage signal, it can be converted into a current signal for a reliable transmission.

4.2.5 Passive Monitoring

Passive detectors that were originally developed for individual monitoring, described in Section 4.4.3, can be also used for environmental radiation monitoring. Though real-time results cannot be obtained with passive detectors, they are very useful because of their low cost. They directly give integrated doses over an appropriate time period. Furthermore, passive monitors are hardly influenced by the time structure of a pulsed radiation field, electric noise from lightning, and mechanical shocks.

Since individual monitors are calibrated on a phantom, they cannot be used directly for environmental measurements. The monitors must be calibrated in free air as described in Section 4.5.2.

Hranitzky *et al.* (2002) developed an $H^*(10)$ photon dosimeter with a LiF thermoluminescence dosimeter (TLD) and filters. It showed good energy dependence, with less than 5 % deviation between 30 keV and 2.5 MeV.

For x-ray dose measurements near linacs and ECR ion sources, an $H^*(10)$ dosimeter was developed using LiF TLD chips (Fehrenbacher *et al*., 2008). Each dosimeter has four TLD chips, and two chips are covered with copper filter. The weighted average of readings of these tips gives good responses over the energy range from 10 keV to about 4 MeV; *i.e.*, the deviations of the relative sensitivity from the $H^*(10)$ response are lower than 25 %.

By using a pair of thermoluminescence dosimeters of ^{6}LiF and ^{7}LiF and a specially designed moderator, Fehrenbacher *et al*. (2007b; 2007c) developed an $H^*(10)$ dosimeter for a wide spectrum of neutrons ranging up to several hundreds of MeV.

In high-intensity neutron fields, activation foils are also applicable. Capture reactions of Mn, Co, Ag, In, Dy, and Au are useful for thermal neutron measurement. For fast neutrons, threshold reactions of ^{12}C(n, 2n)^{11}C, ^{27}Al(n, α)^{24}Na, ^{27}Al(n, 2nα)^{22}Na, ^{59}Co(n, α)^{56}Mn, ^{197}Au(n, 2n)^{196}Au, ^{209}Bi(n, xn)$^{210-x}$Bi (x=4 to 12), *etc*. are useful. A combination of these reactions can give a neutron spectrum in the MeV region. Indium activation detectors inserted at the center of spherical polyethylene moderators can be used for neutron spectrometry for the energy range between thermal and 20 MeV (Uwamino and Nakamura, 1985).

4.3 Measurement of Residual Radioactivity

4.3.1 Introduction

Residual radioactivity is sometimes significant at locations where the beam losses are high, such as the beam extraction device, beam dump, energy selection system, components in a passive scattering treatment port, and delivery nozzle that intercept the beam. Measurement of the radiation intensity at locations where maintenance work may be done is important in order to avoid any excess personnel exposure.

Collimators, ridge filters, and range modulators, which are fixed at the treatment port of a passive irradiation facility, are significantly activated. However, the bolus and the patient collimator for each patient are irradiated for a short time, and the residual activities last only for a relatively short period after irradiation because of the short half-lives ($T_{1/2}$) of the induced radioactive isotopes, for example, ^{11}C ($T_{1/2}$ = 20.4 min) in bolus and ^{62m}Co ($T_{1/2}$ = 13.9 min) in collimator (Tujii *et al.*, 2009; Yashima *et al.*, 2003). Thus, the exposure of the treatment staff who handle these patient-specific devices is low (Tujii *et al.*, 2009). However, at most facilities that use passive scattering techniques, these devices are stored for up to 2 to 3 months before they are shipped out of the facility. At a scanning irradiation facility with a synchrotron, activation problems are hardly observed at the treatment port.

Compared to the activation at accelerator laboratories for physics research, the activation situation in particle therapy facilities can be quite different. In patient treatment rooms, the level is usually not very high. In facilities with a cyclotron, however, the strongest activity is in the degraders and the following emittance defining collimators, that is, the energy selection system. Usually this system is located in the beam line directly from the cyclotron and here more than 90 % of the beam intensity is lost in the degrader and on collimators. This system needs to be accessed for maintenance or repairs only and can be shielded properly. In the cyclotron itself several hot spots are present due to beam losses. These can be taken care of by local shielding or removal of the hot components.

Measurement of residual radioactivity is important when the accelerator components, beam delivery nozzle, and patient-specific irradiation devices are classified as “radioactive” or “not radioactive” for waste management.

4.3.2 Ionization Chamber

Ionization chamber survey meters are the most suitable and reliable detectors for the measurement of ambient dose rate due to residual radioactivity. Some detectors have removable windows on the chambers, and they can measure the beta-ray dose that may be important for the estimation of skin dose.

4.3.3 NaI(Tl) Scintillators

NaI(Tl) scintillation survey meters with correction circuits for energy dependency give accurate results of ambient dose rate, similar to an ionization chamber. The lower detection limits are low enough for background measurements and they can also be used for the measurement of radioactive waste.

Handheld photon spectrometers described in Section 4.2.3.1, which function also as dosimeters, may be used for nuclide analysis of residual activity. Because of their limited energy resolution, complicated spectra cannot be resolved. For a precise analysis, high purity germanium (Ge) detectors are recommended.

4.3.4 Geiger-Müller Tube

A Geiger-Müller survey meter with a thin window has almost 100 % sensitivity to the incoming beta rays, and it is very useful in classifying materials as radioactive or not.

A survey meter having an extendable rod with a small Geiger-Müller counter installed at its tip is useful for the measurement of high dose rate from a remote position.

4.3.5 Other Survey Meters for Contamination Measurement

Detectors such as proportional counters, plastic scintillators, and semiconductor detectors are used in survey meters for contamination measurements. These survey meters are also useful in classifying materials as “radioactive” or “not radioactive.” Unlike the Geiger-Müller tube, the properties of these detectors hardly deteriorate with time.

A hand-foot-clothes monitor is useful equipment for contamination tests of a body. Geiger-Müller tubes, proportional counters, and plastic scintillators are often used as sensors. Most sensors are sensitive to beta and gamma rays. Some sensors simultaneously detect alpha-emitter contamination. The monitors are usually placed at the entrances of controlled areas.

4.4 Individual Monitoring

4.4.1 Introduction

Individual personnel exposure is classified as external and internal exposures. Internal exposure is usually important for unsealed-radioisotope handling, and should be considered when highly activated accelerator devices, such as targets and charge-exchange stripper foils, are handled. If a cyclotron-based particle therapy facility using passive irradiation systems has many treatment ports and is operated with high duty factors, this kind of internal exposure may be important. Although internal exposure is usually not important at particle therapy facilities, one should be cautious with removal of dust from some hot spots (*e.g.*, degrader region in a cyclotron facility), cooling water which may have been contaminated by neutron or proton exposure, and activated air in the cyclotron/degrader vault, shortly after switching off the beam.

Dose equivalents, $H_p(10)$ and $H_p(0.07)$, are measured for the estimation of the individual external exposure. The former is important for the effective-dose estimation and the latter is used for the equivalent-dose estimation for skin and eye lenses. Typically, a single personal dosimeter is used, and it is normally worn on the chest for males or on the abdomen for females. If a strong non-uniform exposure is expected, supplementary dosimeters are worn on the extremities such as the finger or head.

If accelerator or energy selection devices having high residual activity require hands-on maintenance, a ring badge worn on a finger is recommended, as the exposure of hands is normally much higher than that of the torso. Because the exposure of the palm is usually higher than that of the back of the hand, wearing a ring badge with the sensitive part facing inside is recommended.

4.4.2 Active Dosimeter

Many types of active personal dosimeters using semiconductor detectors or small Geiger-Müller tubes are available. These detectors usually measure and display the accumulated exposure after being switched on.

Several different types of dosimeters are available. Alarm meters provide an alarm when the accumulated exposure exceeds a preset value. Small survey meters indicate the dose rate. Others make audible clicking sounds with a frequency that corresponds to the dose rate. Some record the trend of the exposure and the data are transmitted to computers for analysis.

Many products are commercially available; for example, DOSICARD,[10] PDM,[11] and Thermo EPD.[12] The last one has all the functions described above. A novel example is PM1208M,[13] which is a wristwatch that includes a gamma-ray dosimeter. NRF30[14] can be connected to the personal access control system, which records the time of entry and exit and the corresponding exposure.

Though small batteries power these dosimeters, many dosimeters work continuously for a week or several months. Radio waves of a cellular phone may affect the responses of some of these dosimeters.

4.4.3 Passive Dosimeter

---

[10] Canberra Industries, Inc., 800 Research Parkway, Meriden, Connecticut 06450 U.S.A.

[11] ALOKA Co., Ltd., 6-22-1, Mure, Mitaka,Tokyo 181-8622 Japan

[12] Thermo Fisher Scientific Inc., Bath Road, Beenham, Reading, Berkshire RG7 5PR, UK

[13] Polimaster Ltd., 51, Skoriny str., Minsk 220141, Republic of Belarus

[14] Fuji Electric Systems Co. Ltd., 1-11-2, Osaki, Shinagawa, Tokyo 141-0032 Japan

Passive dosimeters measure the integrated dose and therefore do not provide any information on the real-time exposure. However, these dosimeters are small, noise-free, and not susceptible to mechanical shock. Their measurements are independent of the time structure of a radiation field in contrast to the active dosimeters, which may give an underestimated value in a strong-pulsed field.

4.4.3.1 Thermoluminescence Dosimeter (TLD). An exposed TLD element, such as calcium sulfate doped with thulium ($CaSO_4$:Tm), emits light when it is heated. The intensity of the light emission is a measure of the exposure. The TLD reader can be placed on a desk, and therefore in-house dosimetry is common. A TLD dosimeter for measuring both photons and beta rays is available. This consists of several elements having different filters, and both $H_p(10)$ and $H_p(0.07)$ can be measured with one dosimeter.

Since the size of TLD is small, it can also be used in a ring badge that measures the exposure to the hands.

4.4.3.2 Optically Stimulated Luminescence (OSL) Dosimeter. An exposed OSL element, such as carbon-doped aluminum oxide (Al_2O_3:C) emits blue light when it is irradiated by a green laser light. A dosimeter badge consisting of an OSL element and filters, which is used for photons and beta rays, is commercially available: LUXCEL OSL.[15] A company[16] provides dosimetry service; that is, the company distributes dosimeter badges consisting of OSL elements, and, after use, it reads and evaluates the exposure. An OSL reader that can be placed on a desk is also available, and thus in-house dosimetry is also possible. The dosimeter is applicable for energies between 5 keV and 10 MeV for photons and

[15] Landauer Inc., 2 Science Road, Glenwood, Illinois 60425-1586 U.S.A.

[16] Landauer Inc., 2 Science Road, Glenwood, Illinois 60425-1586 U.S.A.

between 150 keV and 10 MeV for beta rays. The readable dose ranges between 10 μSv and 10 Sv for photons and 100 μSv and 10 Sv for beta rays.

4.4.3.3 Glass Dosimeter. An exposed chip of silver-doped phosphate glass emits orange light when it is irradiated with ultraviolet laser light. Several glass elements and filters, assembled as a photon and beta-ray dosimeter badge, is commercially available.[17] In-house dosimetry and an external-company service[18] are both available. Reading of the glass element does not reset the dosimeter, and the long-term accumulated dose can be obtained directly. The dosimeter is reset by annealing at high temperatures. Performance of the glass dosimeter is almost the same as the OSL dosimeter.

4.4.3.4 Direct Ion Storage (DIS) Dosimeter. In a DIS dosimeter, a charge stored in a semiconductor is discharged by the current of an ionization chamber. The discharge is read as the change in conductivity. The RADOS DIS-1 dosimeter[19] has a good energy response to photons. The applicable energy range is between 15 keV and 9 MeV for photons, and 60 keV and 0.8 MeV for beta rays. Photon doses between 1 μSv and 40 Sv, and beta-ray doses between 10 μSv and 40 Sv can be read with this dosimeter. In-house dosimetry is common. It can also be used as an active dosimeter by attaching a small reader to the detector.

4.4.3.5 Solid State Nuclear Track Detector. Recoil protons, which are produced in a polyethylene radiator by fast neutrons, create small damage tracks on a plastic chip of Allyl Diglycol Carbonate (ADC or PADC, [Poly]), which is commercially available as CR-39.[20] The damage tracks can

---

[17] Chiyoda Technol Corp., 1-7-12, Yushima, Bunkyo, Tokyo 113-8681 Japan

[18] Chiyoda Technol Corp., 1-7-12, Yushima, Bunkyo, Tokyo 113-8681 Japan

[19] RADOS Technology Oy, PO Box 506, FIN-20101 Turku, Finland

20 PPG Industries, One PPG Place, Pittsburgh, Pennsylvania 15272 USA

be revealed by a suitable etching process (chemical or electrochemical). The tracks can be counted and the track density can be related to the neutron dose equivalent. A boron converter can be used instead of the radiator, to detect thermal neutrons through the $^{10}B(n, \alpha)$ reactions. Commercially available dosimeters include the Landauer Neutrak 144[21] which comprises the fast and thermal options with CR-39. The lower detection limit of the detector is relatively high, which is about 0.1 mSv for thermal neutrons and 0.2 mSv for fast neutrons. The energy range for fast neutrons is 40 keV to 35 MeV. Use of external-company[22] dosimetry services is usual.

4.4.3.6 Film Dosimeter. A film badge dosimeter consists of photographic film and filters. The film is developed after irradiation, and the photographic density is compared with that of the control film, which is kept far from radiation sources. A rough estimate of the photon or beta-ray energy can be obtained by using a combination of filters. Thermal neutron exposure is measured with a cadmium filter. Observation of recoil nuclear tracks with a microscope gives the exposure of fast neutrons. External-company dosimetry services are usually used. In spite of these features, the film badge dosimeter is disappearing quickly because of the following disadvantages: higher detection limit of about 100 μSv for photons and beta rays and of several hundreds of μSv for neutrons; and fading phenomenon that makes the measurement impossible if the dosimeter is left for several months without development after irradiation.

4.5 Calibration

4.5.1 Introduction

[21] Landauer Inc., 2 Science Road, Glenwood, Illinois 60425-1586 U.S.A.

[22] Landauer Inc., 2 Science Road, Glenwood, Illinois 60425-1586 U.S.A.

Calibration involves the comparison between the reading of a dosimeter with the dose rate in a standard radiation field that is traceable to a national standard field, and a description of the relationship between them. Details of the calibration procedure are precisely explained in the ICRU reports for photon dosimeters (ICRU, 1992a) and for neutron dosimeters (ICRU, 2001).

The calibration factor, *N*, is given by:

$$N = H/M \tag{4.1}$$

where *H* is the dose rate of the standard field, and *M* is the reading of the detector after necessary corrections are applied, for example, with atmospheric pressure and with temperature.

There are two kinds of calibration: one is to obtain the detector characteristics of energy, angular and dose-rate dependencies, and the other is to determine the changes in the detector performance with time, such as absolute sensitivity. The manufacturer usually does the former calibration with adherence to national industrial standards. Users do the latter once or twice a year. The latter calibration done by the user is described below.

4.5.2 Calibration of Ambient Dose Monitor

4.5.2.1 Calibration of Photon Monitor. A standard field can be achieved by using a standard gamma-ray source of ^{60}Co or ^{137}Cs. The standard dose rate, *H*, is obtained with the following formula:

$$H = X \cdot f \tag{4.2}$$

where *X* is the given exposure rate at a 1 m distance from the standard source, and *f* is the conversion factor of exposure to ambient dose equivalent, $H^*(10)$, for the gamma-ray energy of the source. If the detector is not placed at 1 m distance from the source, then X should be corrected according to the inverse-square-law of the distance, assuming a point source of radiation.

If a standard exposure dosimeter, which is calibrated in a field having traceability to the national standard field, is used, then the standard dose rate, H is given by:

$$H = N_S \cdot f \cdot M_S \qquad (4.3)$$

where M_S is the reading of the standard dosimeter after necessary corrections are applied, N_S is its calibration factor, and f is the conversion factor of exposure to ambient dose equivalent, $H^*(10)$.

The photons reaching the calibration point after scattering from the walls, floor, and roof are ignored in Equation 4.2. In Equation 4.3, the change of photon energy through the scattering is also ignored. Thus, the detector must not be placed far from the source. On the other hand, if the detector is placed too close to the source, non-uniform irradiation of the detector is caused and a further consequence is a larger relative uncertainty in the distance. Therefore, in order to assume a point source of radiation, the distance should be greater than 5 times the detector diameter, and smaller than 2 m if the source is not collimated. The detector and the source should be located at least 1.2 m away from the floor, and 2 m away from the wall and the roof.

4.5.2.2 Calibration of Neutron Monitor. ^{252}Cf (average energy = 2.2 MeV) and ^{241}Am-Be (average energy = 4.5 MeV) sources are used for calibration. Since scattering significantly affects the dose rate for neutrons, it cannot be reduced to negligible levels. The calibration factor, N, for a standard source with a given neutron emission rate, can be obtained with the following formula:

$$N = \frac{H}{M_F - M_B} \qquad (4.4)$$

where H is the dose rate calculated with the product of the source emission rate and the conversion factor of neutron fluence to dose equivalent, M_F is the reading of the detector irradiated by direct and scattered neutrons, and M_B is the background reading of the detector irradiated only by scattered neutrons, in which case the direct neutrons are shielded by a shadow cone placed between the source and the detector.

Shielding of the direct neutrons needs a massive and costly shadow cone. Instead of using Equation 4.4, the following procedure is also applicable. Since the angular dependence of the neutron detector sensitivity is usually small, the dose rate, H, including the scattered neutrons at the calibration point, can be determined with a standard reference dosimeter. A detector to be calibrated is also irradiated with the direct and scattered neutrons, and the calibration factor, N, is simply obtained with Equation 4.1 and Equation 4.3, where f is unity if the standard reference dosimeter reads ambient dose equivalent.

If the neutron rem meter is of the conventional type and responds to neutrons below 15 MeV, the rem meter calibrated using the above procedure gives a correct value only in a neutron field of energy below 15 MeV. High-energy neutrons are dominant at a particle therapy facility and a conventional rem meter may give only one third of the true dose rate as described in Section 4.2.1.1. To estimate the correct dose rate, the neutron energy fluence, $\phi(E)$, at the field has to be determined. However, the absolute value of $\phi(E)$ is not necessary here. The energy-corrected calibration factor, N_C, is estimated by:

$$N_C = N \frac{\int_0^{E\max} E_\phi(\mathrm{AP})\phi(E)dE}{\int_0^{E\max} R(E)\phi(E)dE} \qquad (4.5)$$

where E is particle energy, E_ϕ(AP) is the dose conversion coefficients from particle fluence to effective dose for AP geometry, and $R(E)$ is the detector response. When the reading of the rem meter, M, is multiplied by N_C, the correct effective dose is obtained.[23] On the other hand, if the rem meter has an improved energy response to high-energy neutrons, it gives also a correct value at high-energy field.

4.5.3 Calibration of Individual Monitors

Individual monitors are worn on and close to the body; thus, the contribution of the scattered photons and neutrons is high. Therefore, the calibration is typically performed with the individual monitor placed on a water phantom of 30 cm width by 30 cm height by 15 cm thickness. The monitor should be placed more than 10 cm away from the edge of the phantom.

The dose rate at the detector position without the phantom, *H*, is calculated using Equation 4.2 with the conversion factor of exposure to the $H_P(10)$ dose rate, *f*. In the case of neutrons, *H* is calculated by the product of the given neutron emission rate of the source and the conversion factor of fluence to the $H_P(10)$ dose rate. The calibration factor, *N*, is obtained using Equation 4.1 with the standard dose rate, *H*, and the reading of the monitor, *M*.

The directional personal 10 mm depth dose equivalent is expressed as $H_P(10, \alpha)$, where α is the angle between the normal direction of the phantom surface and the direction of radiation. The ratio, *R*, of $H_P(10, \alpha)$ to $H_P(10, 0°)$ is close to unity ($0.8 < R < 1$ for $\alpha > 75°$) for photons of energies above 0.4 MeV and for neutrons of energies above 5 MeV. From Fig. 4.3, it can be observed that high-energy particles are the dominant contributors to the doses, and the angular distribution of the radiation does not seriously affect the individual exposure. If the angular dependence of the individual monitor is significantly

[23] Since the $H^*(10)$ dose is much smaller than the effective dose for high-energy neutrons as described in Section 4.1.1, evaluation of the effective dose is discussed. If $H^*(10)$ is estimated, the dose conversion coefficients for $E_\phi(AP)$ are replaced by the dose conversion coefficients for $H^*(10)$.

different from that of $H_P(10, \alpha)$ even at higher energies, the reading of the monitor is not reliable. The calibration factor, N, for angular incidence should also be considered.

5. Activation

Yoshitomo Uwamino

5.1 Introduction

Induced radioactivity produced in an accelerator and its beam-line components may cause exposure of maintenance workers, and makes the disposal of activated components difficult. Further, radioactivity in the vicinity of the treatment port, beam shaping, and delivery systems may result in the exposure of medical staff. This exposure may not be negligible at a facility that does not use a scanning irradiation system. At a cyclotron facility, induced radioactivity of the energy selection system (ESS) is significant.

Accelerated particles exiting the vacuum window interact by nuclear reactions in the air path upstream of the patient, causing activation. The air is also activated by the secondary neutrons that are produced by nuclear reactions of charged particles in the equipment and on the patient. These secondary neutrons also produce radioactivity in equipment cooling water and possibly in groundwater.

Treatment with high-energy charged particles intrinsically activates the diseased part of the patient. Tujii *et al.* (2009) irradiated a phantom with proton and carbon beams at therapy facilities and measured the activation. The estimated exposure of medical staffs and family members of the patient was negligibly small, and the concentration of radioactivity in the excreta of the patient was insignificant when the dilution at a lavatory was taken into account.

A comprehensive book on induced radioactivity was written by Barbier (1969), and useful data was published by the International Atomic Energy Agency (IAEA, 1987). Activation-associated safety aspects of high-energy particle accelerators are discussed in several books (*e.g.*, IAEA, 1988; Sullivan, 1992).

Induced radioactivity and its resulting radiation field can be estimated by using a single Monte Carlo program starting with the primary accelerated particles (Ferrari, 2005). Several Monte Carlo codes calculate the production of residual radioactivity, and post-processing programs follow the decay chain of the radioactivity and calculate the gamma-ray transport and the dose rate. Chapter 6 explains Monte Carlo methods in detail, while in this chapter, calculation and measurement techniques to determine activation of equipment, buildings, water, and air are described.

5.1.1 Activation Reactions

Since neutrons are not affected by the Coulomb barrier of the nuclei, neutrons of any energy react with nuclei. Thermal neutrons mostly interact *via* (n, γ) reactions. However, with some nuclides, such as ^{6}Li, they produce ^{3}H through the (n, α) reaction. Neutrons of energy higher than the excited level of the target nucleus provoke (n, n') reactions. Usually, the excited nucleus immediately transits to its ground state accompanied by gamma-ray emission. When the neutron energy is sufficiently high enough to cause particle emission, many types of activation reactions, such as (n, p), (n, α), (n, 2n), *etc*. occur. Relativistic high-energy neutrons cause spallation reactions that emit any type of nuclide lighter than the target nucleus.

Charged particles with energy lower than the Coulomb barrier do not effectively react with nuclei. Coulomb excitation causes x-ray emission and fission in special cases, such as in uranium. These phenomena, however, can be usually ignored because the x-ray energy is low and not penetrative, and because the fission probability is very small. When the particle energy becomes higher than the Coulomb barrier, particles produce compound nuclei. Depending upon the excitation energy of the compound nuclei, (x, γ) reactions (where x is the incident charged particle), and particle-emitting reactions, such as (x, n), (x, p) and (x, α) reactions, occur and often result in the production of radioactive nuclides. The high-energy charged particles can also cause spallation reactions.

Examples of reaction cross sections are shown in Figs. 5.1 and 5.2. Figure 5.1 is the neutron capture cross section for ^{59}Co. The capture cross sections are generally proportional to 1/v (v is the neutron velocity) or $1/\sqrt{E}$, where E is the energy. They fluctuate at the resonance energy region according to the characteristics of the nuclide. The ^{59}Co(n, γ)^{60}Co reaction is important for the activation of stainless steel by thermal neutrons. The cross sections of threshold activation reactions of ^{27}Al are shown in Fig. 5.2. The threshold energies are 1.9 MeV, 3.2 MeV and 13.5 MeV for the ^{27}Al(n, p)^{27}Mg, ^{27}Al(n, α)^{24}Na, and ^{27}Al(n, 2n)^{26}Al reactions, respectively. In general, cross sections for threshold reactions rapidly increase beyond the threshold energy and have a peak. They decrease beyond the peak energy, since other reaction channels open with the increase of energy.

Figure 5.3 shows the nuclides produced by various reactions of neutrons and protons. The heavy ion reactions are more complex and, therefore, it is difficult to show a similar kind of figure.

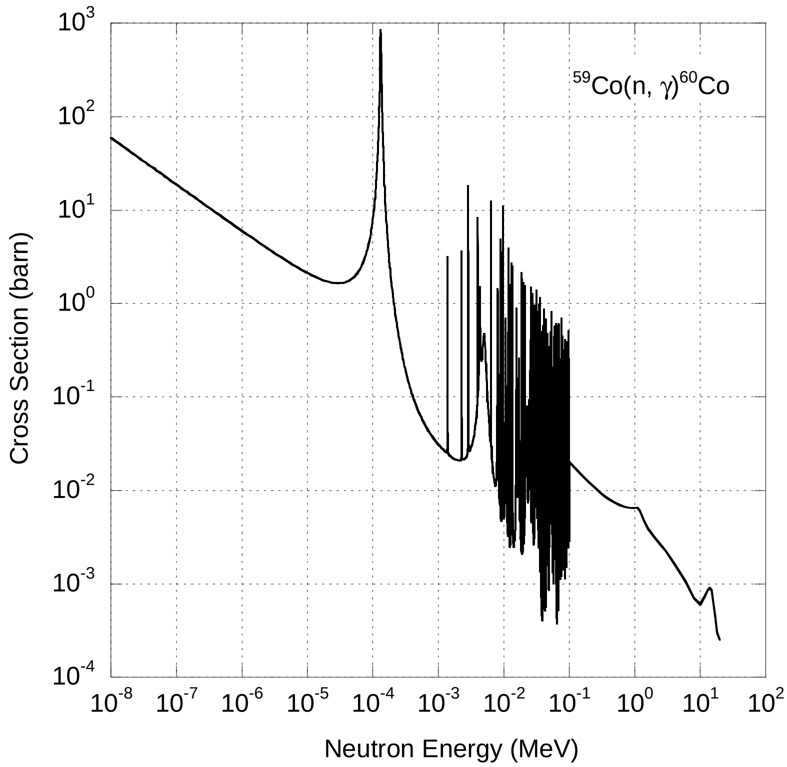

Figure 5.1. Cross section for the ^{59}Co(n, γ)^{60}Co activation reaction as a function of energy (Chadwick *et al.*, 2006).

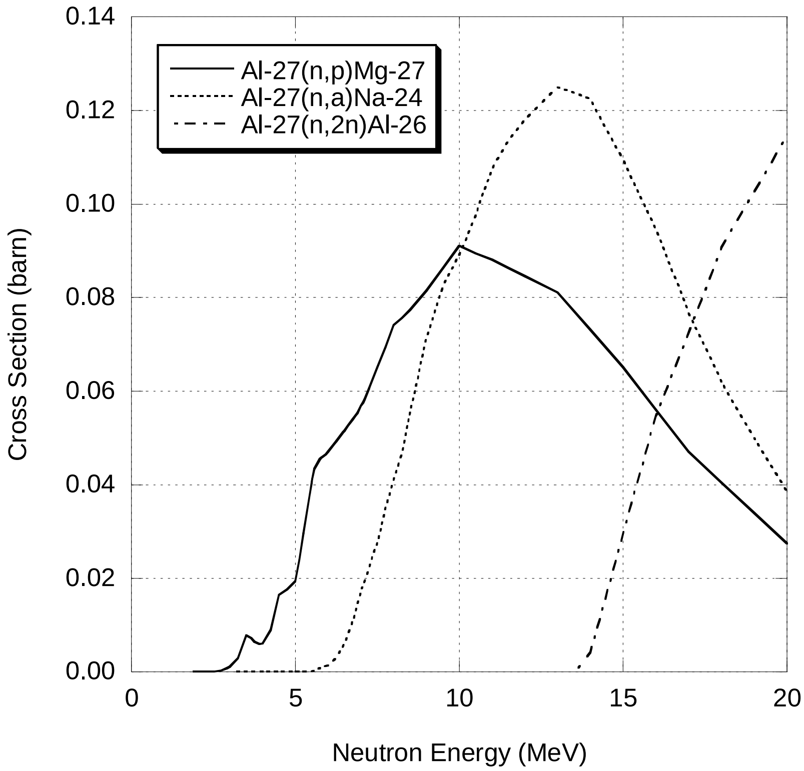

Figure 5.2. Cross sections for the $^{27}Al(n, p)^{27}Mg$, $^{27}Al(n, \alpha)^{24}Na$, and $^{27}Al(n, 2n)^{26}Al$ activation reactions as a function of energy (Chadwick *et al.*, 2006).

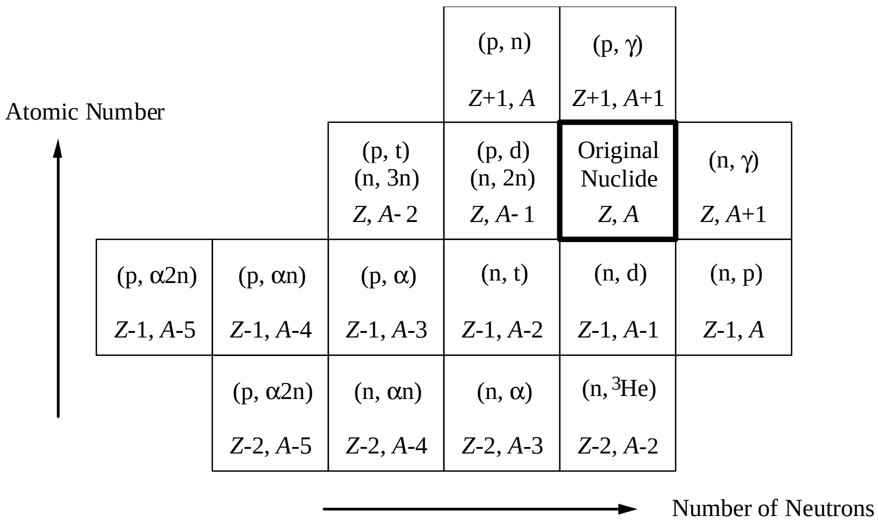

Figure 5.3. Nuclides produced by various nuclear reactions. (n, d) reaction includes (n, pn) reaction, and (n, t) reaction includes (n, dn) and (n, p2n) reactions, and so on.

5.1.2 Activation and Decay

The production rate of a radioactive nuclide, R (s^{-1}), is calculated by the following formula:

$$R = \phi \sigma N_{\mathrm{F}} V \tag{5.1}$$

where ϕ (cm^{-2} s^{-1}) is the radiation fluence rate averaged over the irradiation field, σ (cm^{2}) is the activation cross section averaged over the radiation energy, N_F (cm^{-3}) is the atomic density of the nuclide to be activated, and V (cm^{3}) is the volume of the irradiation field.

The radioactivity, $A(T_R)$ (Bq), immediately after an irradiation time period of T_R (s) is given by the following formula:

$$A(T_{\mathrm{R}}) = R(1 - e^{-\lambda T_{\mathrm{R}}}) \tag{5.2}$$

where λ (s^{-1}) is the decay constant of the radioactive nuclide. R is the saturation activity. If T_R is much longer than the half-life, $T_{1/2}$ (= ln2/λ), $A(T_R)$ becomes equal to R.

The radioactivity after T_D seconds have elapsed after the irradiation end, $A(T_R + T_D)$ (Bq), is given by the following formula:

$$A(T_{\mathrm{R}} + T_{\mathrm{D}}) = R(1 - e^{-\lambda T_{\mathrm{R}}}) e^{-\lambda T_{\mathrm{D}}} \tag{5.3}$$

Equation 5.3 is shown in Fig. 5.4 with the thick solid line.

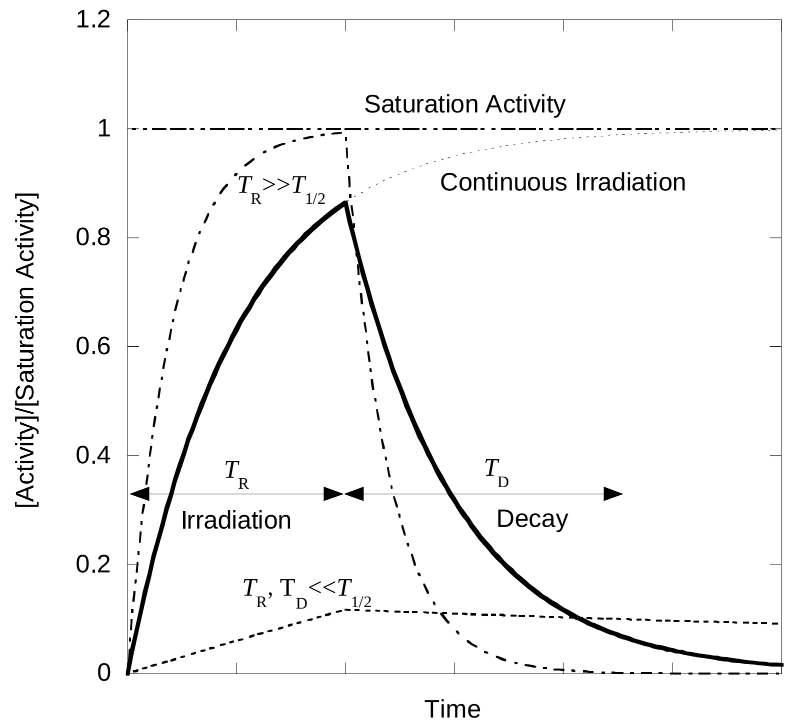

Figure 5.4. Change of radioactivity during irradiation and decay. The thick solid line shows the general case, the dotted and dashed line shows the case of short half-life ($T_R >> T_{1/2}$), and the dashed line shows the case of long half-life ($T_R << T_{1/2}$ and $T_D << T_{1/2}$).

If T_R is much longer than the half-life, $T_R >> T_{1/2}$, the radioactivity is saturated at the end of irradiation, and the radioactivity after the irradiation is approximated by the following formula:

$$A(T_R + T_D) \approx R e^{-\lambda T_D} \quad (5.4)$$

The radioactivity reaches a maximum (saturation activity), and decays in a short time after the irradiation. This is shown by the dotted and dashed line in Fig. 5.4.

If T_R and T_D are much shorter than the half-life, the produced radioactivity accumulates almost without any disintegration. The amount of radioactivity is much smaller than the saturation value. This is shown by the dashed line in Fig. 5.4.

$$A(T_R + T_D) \approx \lambda R T_R \quad (5.5)$$

Compared with the high-energy, high-intensity accelerators used for physics research, the beam intensity of the particle therapy facility is low, and therefore, saturation radioactivity is also low. Moreover, the irradiation time is short at a therapy facility, and the cumulated radioactivity of long-half-life nuclides is usually low. Therefore, the exposure of maintenance workers and medical staff is not usually of major concern at a facility dedicated to charged particle therapy. However, the activation of air may become significant level in a treatment room and in an enclosure of equipment where high beam loss occurs.

5.2 Accelerator Components

5.2.1 Residual Activity Induced by Primary Particles

Radioactive nuclides are mostly produced by primary beams in the accelerator and beam-line components, including beam shaping and delivery devices, and the energy selection system (ESS). The accelerator and beam-line components are mainly made of aluminum, stainless steel (nickel, chromium and iron), iron, and copper. Residual activities are induced by spallation reactions occurring between these materials and the projectile particles.

Because of high melting point and high density, tungsten and tantalum are often used in accelerators, *e.g.* at an extraction septum of a cyclotron and at beam stoppers. They are not only activated, but also have a tendency to evaporate and to contaminate the surfaces of the surrounding materials.

5.2.1.1 Residual Activities in Al, Cr, Fe, Ni, Cu. Various radionuclides are produced from spallation reactions. Reaction cross sections of nuclides produced in Cu, Ni, Fe, Cr, and Al for 400 MeV/nucleon ^{12}C ion irradiation were measured at HIMAC and shown in Fig. 5.5. In Fig. 5.5, a strong target mass number dependency is not observed, but there is a wider distribution of the produced nuclides with increasing target mass number.

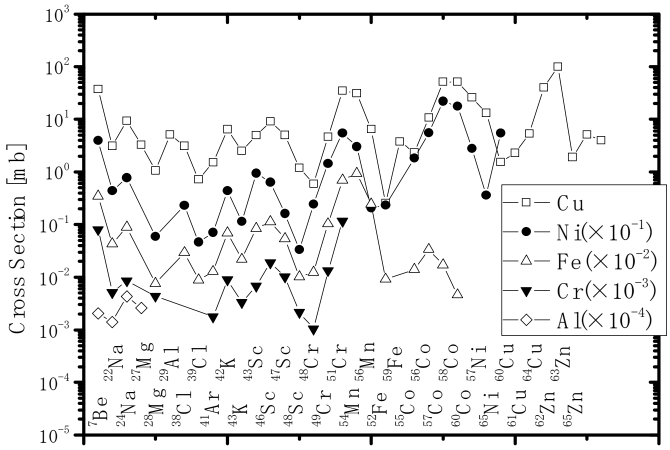

Figure 5.5. Reaction cross sections of nuclides produced in Cu, Ni, Fe, Cr, and Al for 400MeV/nucleon ^{12}C ion irradiation (Yashima *et al*., 2004a).

5.2.1.2 Mass-Yield Distribution of Residual Activities in Cu. The mass-yield (isobaric-yield) distributions of nuclides produced in Cu for various projectiles and energies are shown in Fig. 5.6. The product nuclides can be divided into the three groups of (I) to (III) as shown in Fig. 5.6; (I) target fragmentation occurring from a reaction of small impact parameter or projectile fragmentation of a heavy projectile, (III) target fragmentation occurring from a reaction in which the impact parameter is almost equal to the sum of projectile radius and the target radius, (II) target fragmentation occurring from a reaction in which the impact parameter lies between (I) and (III).

It is evident from Fig. 5.6 that the cross sections of isobaric yields initially decrease with increasing mass number difference between Cu and the product nuclide. However, the production cross sections increase for light nuclides of group (I), since light nuclides like ^{7}Be are produced not only by heavy disintegrations of the target nuclei through small-impact-parameter reactions, but also as smaller fragments of light disintegrations. These light nuclides are also produced by projectile fragmentations of heavy particles.

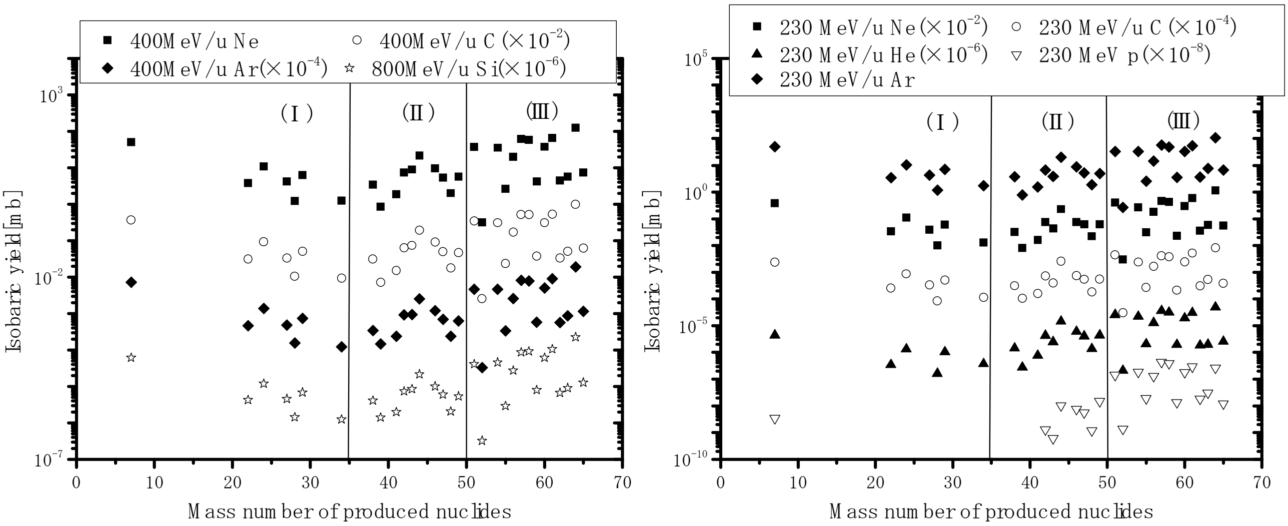

Figure 5.6. Mass-yield (isobaric-yield) distributions of nuclides produced in Cu for various projectile particles and energies. The distributions are divided into three groups as explained in the text (Yashima *et al*., 2002; 2004a).

5.2.1.3 Spatial Distribution of Residual Activities with Cu Target Depth. The spatial distributions of residual activities of ^{7}Be, ^{22}Na, ^{38}Cl, ^{49}Cr, ^{56}Mn, and ^{61}Cu induced in Cu are shown in Fig. 5.7(a) to (f) , where the target depth is expressed in units of the projectile range. In this Section and the following two Sections (5.2.1.4 and 5.2.1.5), the residual activities produced in the vicinity of the primary ion trajectory are discussed. Whereas the activities are mostly produced by the primary ions, they include the productions of secondary charged particles and neutrons. Figures 5.7(a) to (f) can be understood and summarized as follows. When the mass number difference between Cu and the produced nuclide is large, *i.e.*, the produced nuclide belongs to group (I) in Fig. 5.6, the nuclides are produced dominantly by the primary projectile reaction. Most of the reaction cross sections therefore slowly decrease with target depth, according to the attenuation of projectile flux through the target. When the mass number difference between Cu and the produced nuclide is small, *i.e.*, the nuclides produced belonging to group (II) or (III) in Fig. 5.6, the fraction of nuclides produced by reactions with secondary particles is large. With increasing mass number of the produced nuclides and the projectile energy, the residual activity increases with the depth of the Cu target due to the increasing contribution of secondary particle reactions. In Fig. 5.7(a), 5.7(b), and 5.7(c), the residual activity increases steeply near the projectile range in some cases; for example, ^{7}Be production by 100 MeV/nucleon ^{12}C, ^{22}Na production by 800 MeV/nucleon ^{28}Si, and ^{38}Cl production by 230 MeV/nucleon ^{40}Ar. This is attributed to the projectile fragmentation during flight. Since a projectile fragment has the similar velocity and direction to the projectile ion, the projectile fragment stops at a slightly deeper point than the projectile range. Similar phenomenon are expected in ^{11}C production by ^{12}C irradiation.

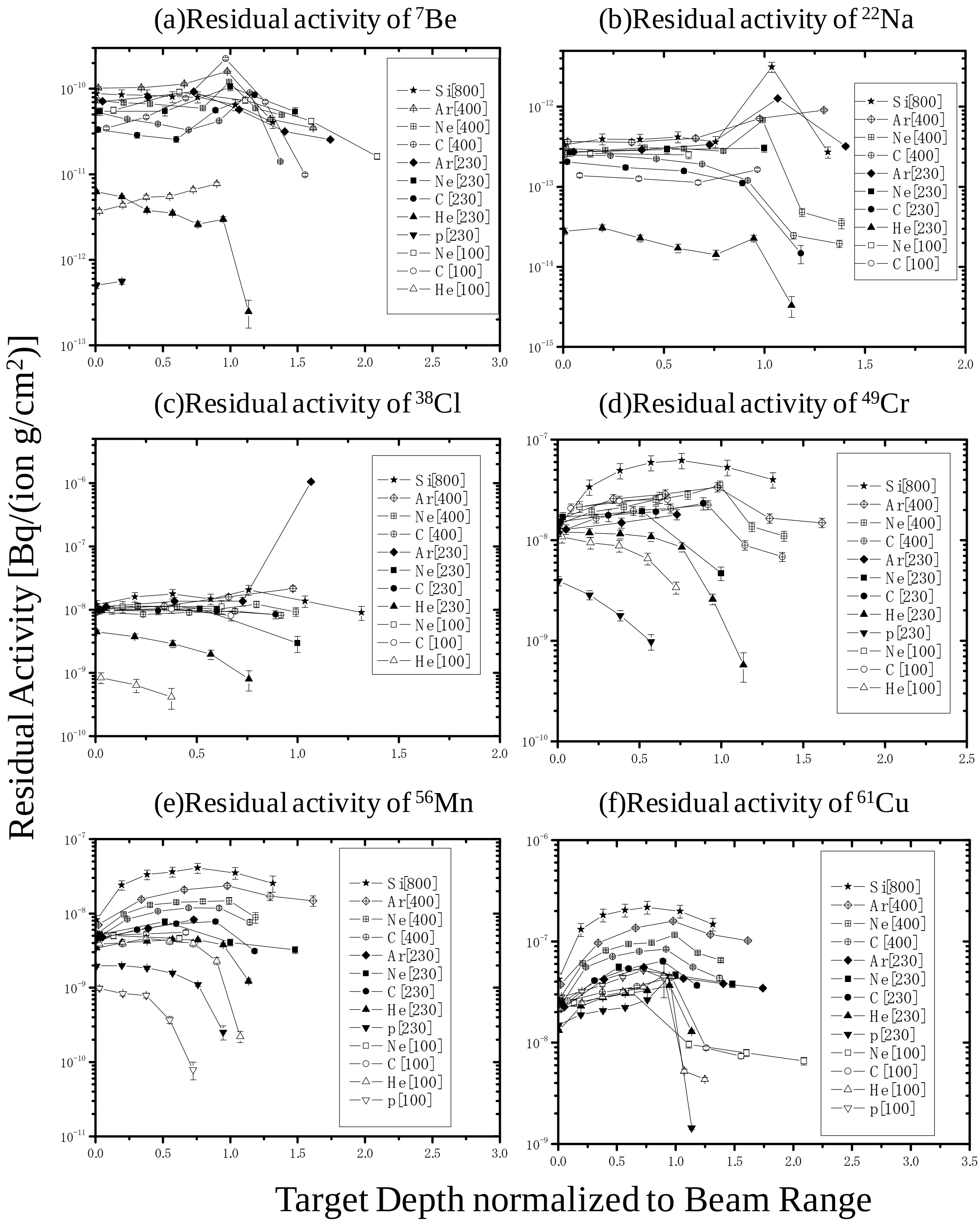

Figure 5.7. Spatial distribution of residual activities with Cu target depth for various projectile types and energies (Yashima *et al*., 2004b).

5.2.1.4 Total Residual Activity Estimation Induced in Cu Target. Cooling down of the total residual activity induced in Cu target, which was estimated from the above-mentioned measured spatial distribution, is shown in Fig. 5.8 (a) and 5.8(b) for a short irradiation time and a long irradiation time (10 months and 30 years, respectively) under the condition of 6.2 x 10^{12} particles/sec, *i.e.*, 1 particle μA (1 pμA) beam intensity. Notice that the x-axis unit is second for Fig. 5.8(a), and day for Fig. 5.8(b).

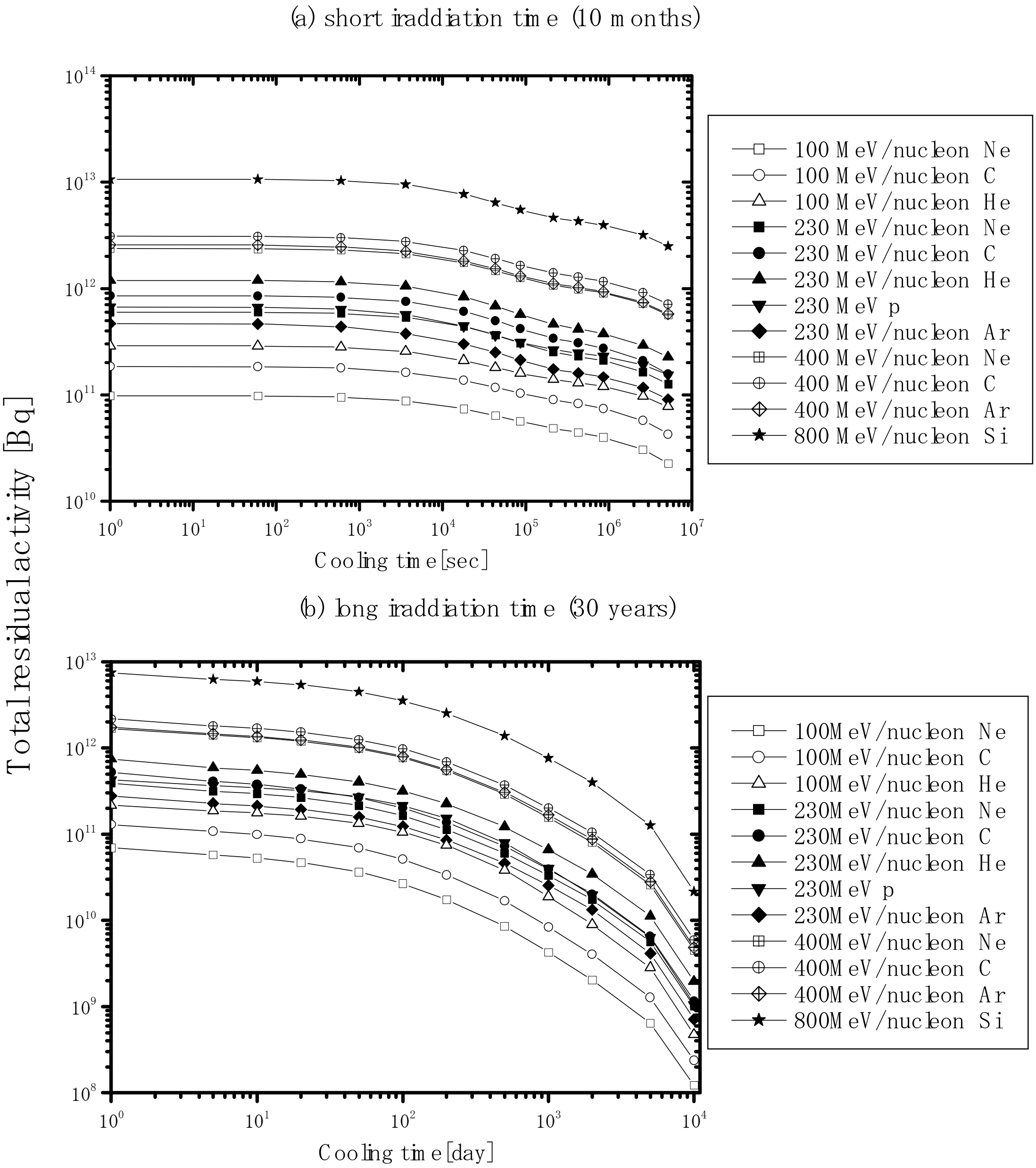

Figure 5.8. Total residual activity induced in Cu target irradiated by 1-pμA ions (Yashima *et al.*, 2004b).

The total residual activity produced in a thick target at the end of irradiation is shown as a function of the total projectile energy in Fig. 5.9(a). The projectile particles are same as those of Fig. 5.8. The total activity for the same projectile energy per nucleon decreases with increasing projectile mass number except for 230 MeV proton irradiation. This can be explained as follows. Because the production cross sections of these nuclides do not depend strongly on the projectile mass number having the same energy per nucleon (Yashima *et al*., 2002; 2004a), the residual activities are larger with lighter projectiles, which have longer ranges. 230 MeV protons have the same range as 230 MeV/nucleon He and have smaller cross sections as shown in Fig. 5.6. Therefore, the total activity produced by protons is smaller than that by He. When the total activity produced by a specific particle is compared, it increases with increasing projectile energy per nucleon.

The majority of the residual activities is dominated by ^{61,64}Cu, ^{57,58}Co, ^{52}Mn, ^{51}Cr, and ^{7}Be at the end of irradiation; ^{65}Zn, ^{56,57,58}Co, ^{54}Mn, and ^{51}Cr at a cooling time of two months; and ^{60}Co and ^{44}Ti after 30 years of cooling, respectively. The fraction of these nuclides produced by reactions with secondary particles is also large. The residual activities are therefore larger with higher energy projectiles, which produce more secondary particles. The specific residual activity per unit mass of Cu target is shown as a function of total projectile energy in Fig. 5.9(b). The target is a Cu cylinder having a cross section of 1 cm^2 and a length equal to the projectile range. In Fig. 5.9(b), the specific residual activity increases with increasing the total projectile energy.

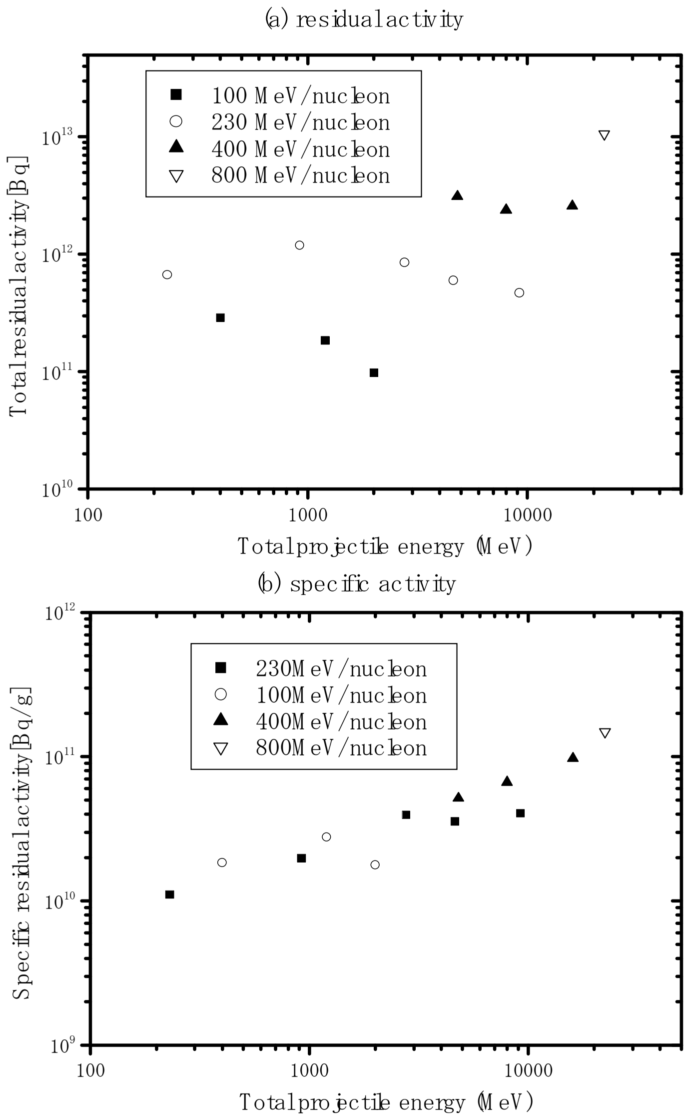

Figure 5.9. Projectile energy dependence of total residual activity and specific residual activity induced in Cu target immediately after the 10 month 1-pμA irradiation (Yashima *et al.*, 2004b).

5.2.1.5 Gamma-Ray Dose Estimation from Residual Activity in Cu Target. The decay of the gamma-ray effective-dose rate at the point located 1 m distant from the Cu target is shown in Fig. 5.10(a) and (b) for a short irradiation time and a long irradiation time (10 months and 30 years, respectively). The contribution of annihilation photons is included in the dose rate. The dose rate at the end of irradiation is shown as a function of total projectile energy in Fig. 5.11. The energy and projectile dependence of gamma-ray dose is similar to that of residual activity.

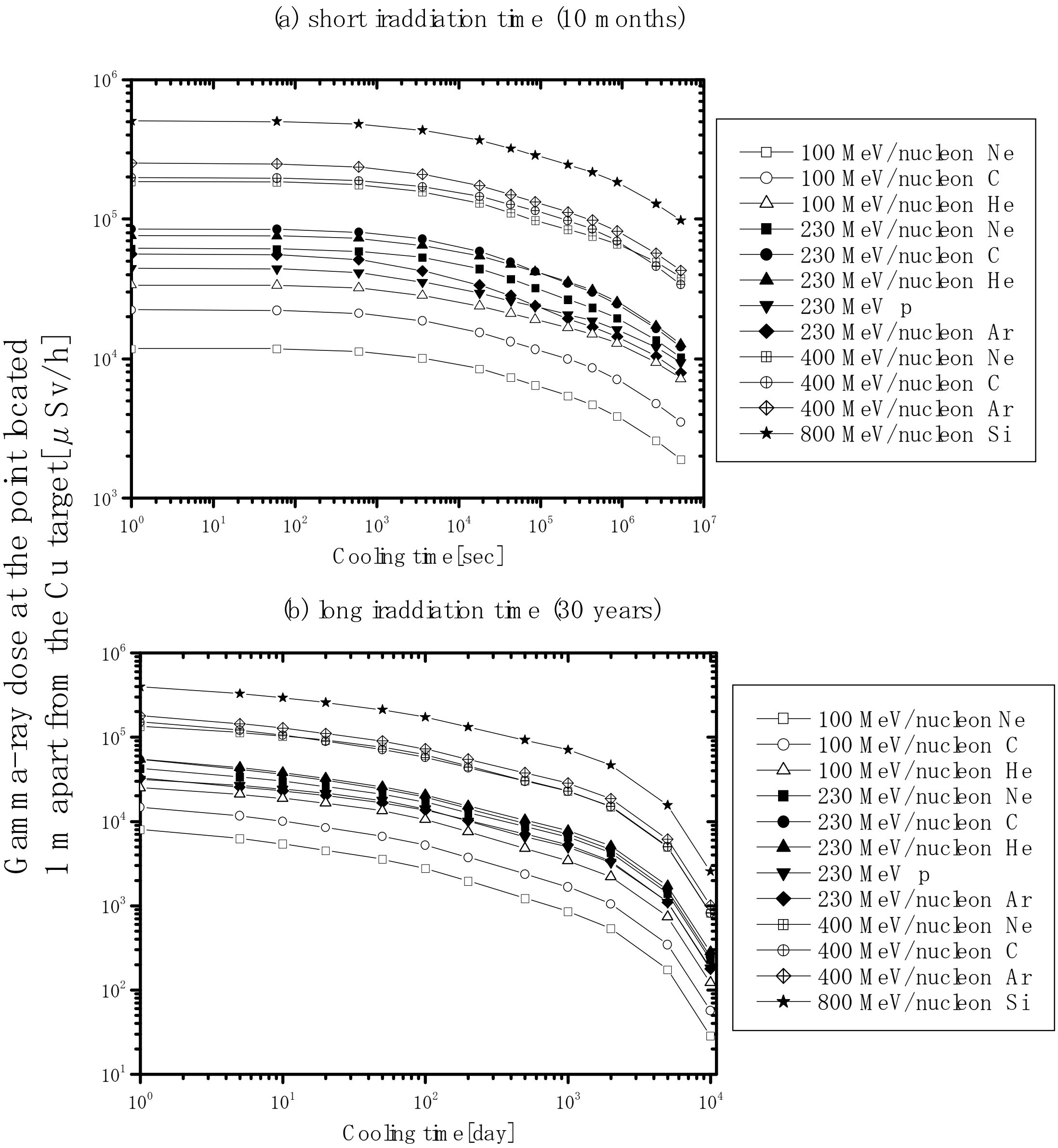

3638

3639 Figure 5.10. Gamma-ray dose from total residual activities induced in Cu target irradiated by 1-pμA ions

3640 (Yashima *et al*., 2004b).

3641 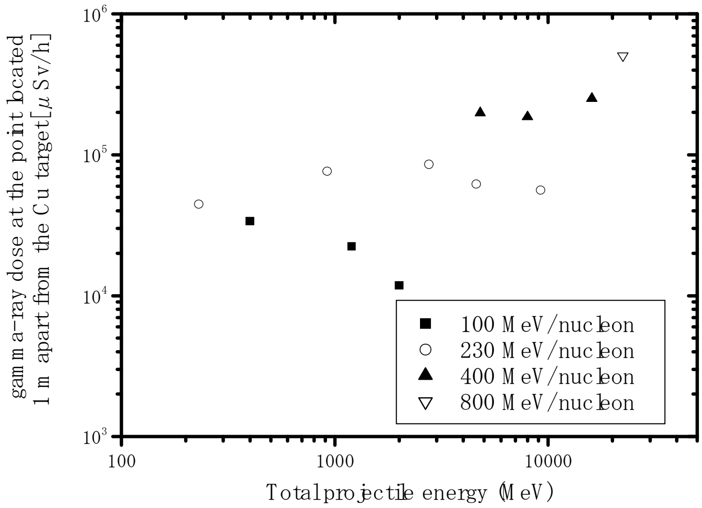

3642 Figure 5.11. Projectile dependence of gamma-ray effective dose from total residual activity induced in

3643 Cu target immediately after the 10 month 1-pμA irradiation (Yashima *et al*., 2004b).

5.2.2 Residual Activities Induced by Secondary Neutrons

Radioactive nuclides are also induced by secondary neutrons, the energies of which extend up to the primary proton energy, and in the case of heavy ions, up to about double the primary particle energy per nucleon.

Because of high permeability, neutron activation is widely distributed, while the activation by charged particles is limited to within the particle range. The intensity of secondary high-energy neutrons is strongly forward-peaked along the primary-particle direction, and decreases with the inverse square of the distance from the effective source.

Neutron-induced reaction cross section data are very scarce above 20 MeV. It is often assumed that the cross sections have the same value as proton-induced cross sections above 100 MeV. As an example, a comparison of cross sections of $^{nat}Cu(n, x)^{58}Co$ and $^{nat}Cu(p, x)^{58}Co$ reactions is shown in Fig. 5.12. In Fig. 5.12, neutron-induced reaction cross sections are slightly larger than proton-induced reaction cross sections above 80 MeV.

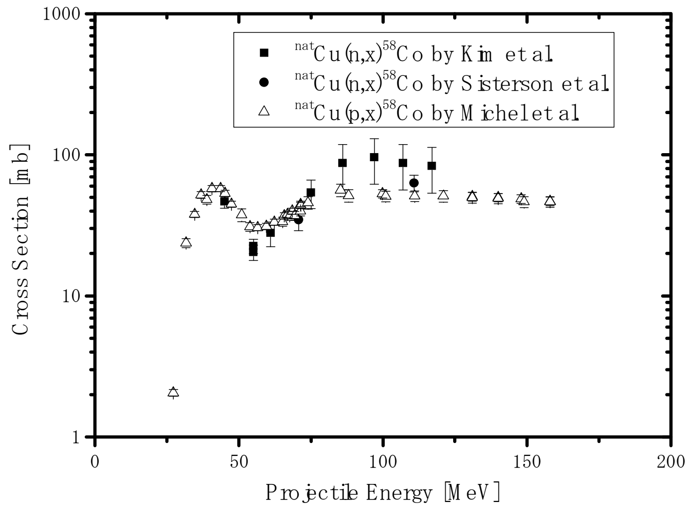

Figure 5.12. Cross sections of the ^{nat}Cu(n, x)^{58}Co and the ^{nat}Cu(p, x)^{58}Co reactions (Kim *et al*., 1999; Michel *et al*., 1997; Sisterson *et al*., 2005).

Thermal neutrons are almost uniformly distributed inside an accelerator enclosure. The fluence ϕ_{th} at places further than 2 m from the neutron production point can be estimated by the following simple formula (Ishikawa, 1991):

$$\phi_{\text{th}} = \frac{CQ}{S} \tag{5.6}$$

where C is a constant estimated to be 4, Q is the number of total produced neutrons, and S is the total inside surface area of an enclosure, including the walls, the floor, and the roof.

Table 5.1 shows the characteristic radionuclides produced in metals by thermal neutrons. Mn and Co are impurities in iron and stainless steel. ^{56}Mn is also produced by fast neutrons in the ^{56}Fe(n, p) reaction. Brass is an alloy of Cu and Zn. Lead bricks sometimes contain Sb to improve the mechanical characteristics.

Table 5.1 Characteristic radionuclides produced in metals by thermal-neutron capture. Gamma rays of which emission probabilities are larger than 1 % are listed (Firestone, 1999; Sullivan 1992).

Radionuclide	Half-life	Decay mode	γ-ray (emission)	Fertile nuclide, abundance, and capture cross section
^{56}Mn	2.58 hour	β^-: 100%	847 keV (98.9%) 1811 keV (27.2%) 2113 keV (14.3%)	^{55}Mn, 100%, 13.3b
^{60}Co	5.27 year	β^-: 100%	1173 keV (100%) 1332 keV (100%)	^{59}Co, 100%, 37.2b
^{64}Cu	12.7 hour	EC: 43.6% β^+: 17.4% β^-: 39.0%	511 keV (β^+)	^{63}Cu, 69.2%, 4.5b
^{65}Zn	244.3 day	EC: 98.6% β^+: 1.4%	1116 keV (50.6%) 511 keV (β^+)	^{64}Zn, 48.6%, 0.76b
^{69m}Zn	13.8 hour	IT: 100%	439 keV (94.8%)	^{68}Zn, 18.8%, 0.07b
^{122}Sb	2.72 day	β^-: 97.6% EC: 2.4%	564 keV (70.7%) 693 keV (3.9%)	^{121}Sb, 57.4%, 5.9b
^{124}Sb	60.2 day	β^-: 100%	603 keV (98.0%) 646 keV (7.3%) 723 keV (11.3%) 1691 keV (48.5%) 2091 keV (5.7%)	^{123}Sb, 42.6%, 4.1b
			etc.	

5.3 Concrete

The amount of induced radioactivity and activity concentration in concrete used for shielding is smaller than that in the accelerator components that are directly irradiated by the primary accelerator beams. After accelerator operation has ceased, workers inside the shielded room are exposed by gamma rays from ^{24}Na (half-life = 15 hours) in the concrete. After accelerator decommissioning, the shielding barriers are also dismantled. In this case, special care must be taken because of long-lived residual radioactivity.

Measured and calculated secondary neutron spectra in thick shields are shown in Fig. 5.13. Neutron spectra do not change much, and high-energy reactions are still important at locations deep within the shields. Radioactivity decreases exponentially with concrete depth.

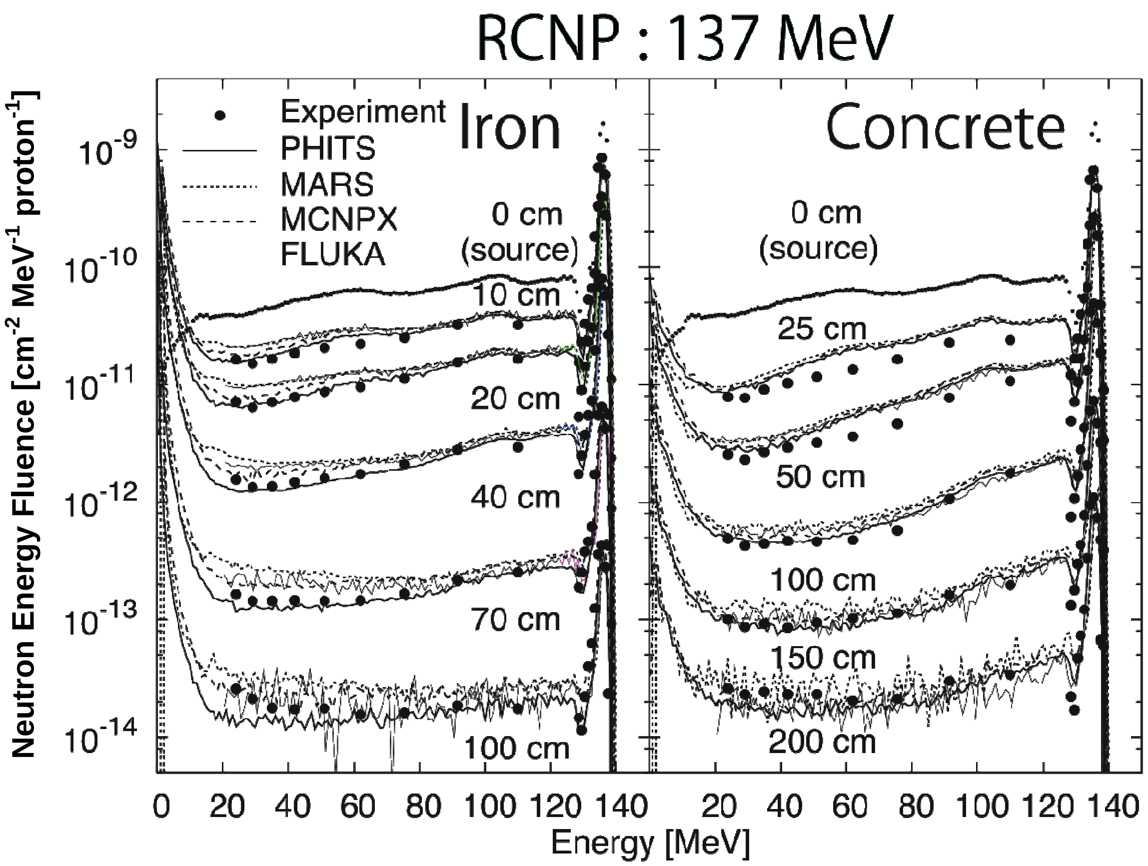

Figure 5.13. Measured and calculated secondary neutron spectra in thick concrete or iron shields irradiated by 140 MeV p-Li neutron source at RCNP (Kirihara *et al.*, 2008).

Several measurements were made in 4 m thick concrete shields of a neutron irradiation facility using a 500 MeV proton synchrotron (Oishi *et al.*, 2005), in 0.5 m thick shields of several proton cyclotrons (Masumoto *et al.*, 2008; Wang *et al.*, 2004), and in 6 m thick 12 GeV proton synchrotron shields (Kinoshita *et al.*, 2008). Typical radionuclides present in concrete are ^{22}Na, ^{7}Be, ^{3}H, ^{46}Sc, ^{54}Mn, ^{60}Co, ^{134}Cs, and ^{152}Eu. When concrete comes into contact with groundwater, ^{22}Na and ^{3}H are dissolved in the water, though the amount of radioactivity in the water is usually very small.

The most important long-lived radioactive nuclides of concern in decommissioning are ^{22}Na, ^{60}Co, and ^{152}Eu. ^{60}Co and ^{152}Eu are produced by thermal neutron capture reactions with Co and Eu impurities in the concrete. The amounts of these impurities are small, but the ^{59}Co(n, γ) and ^{151}Eu(n, γ) cross sections are large. However, ^{22}Na is produced by nuclear spallation reactions of high-energy neutrons. Exemption concentration levels (IAEA, 1996) are 10 Bq g^{-1} for these nuclides. ^{60}Co activities in iron reinforcing rods in concrete are important because ^{59}Co impurities are large in iron.

Because the amounts of impurities of ^{59}Co and ^{151}Eu depend upon the concrete composition, it is difficult to estimate the activities. Typically, the activity of ^{3}H is about ten times higher than that of ^{60}Co and ^{152}Eu (Masumoto *et al.*, 2008), although the exemption level for ^{3}H is much larger, 10^{6} Bq g^{-1}. ^{3}H are produced by both nuclear spallation reactions and thermal-neutron capture.

The depth profile of activity in the concrete shields of a 12 GeV proton synchrotron facility (Fig. 5.14) were measured. Samples of concrete cores were obtained by boring holes up to depths of 4 m to 6 m in the walls. Gamma activity was measured using germanium detectors, and ^{22}Na, ^{54}Mn, ^{60}Co, and ^{152}Eu γ-rays were identified. The concrete sample was heated, and tritium was collected in a cold trap. Beta activity was measured using liquid scintillation counters. The results are shown in Fig. 5.15. The radioactivity of nuclides produced by high-energy reactions, such as ^{22}Na, decrease exponentially as the penetration depth in the shield increases. The activity of radionuclides produced by neutron capture reactions, such as ^{60}Co and ^{152}Eu, increase from the inner surface up to the depth of about 20 cm, then decrease with increasing the depth (Kinoshita *et al.*, 2008).

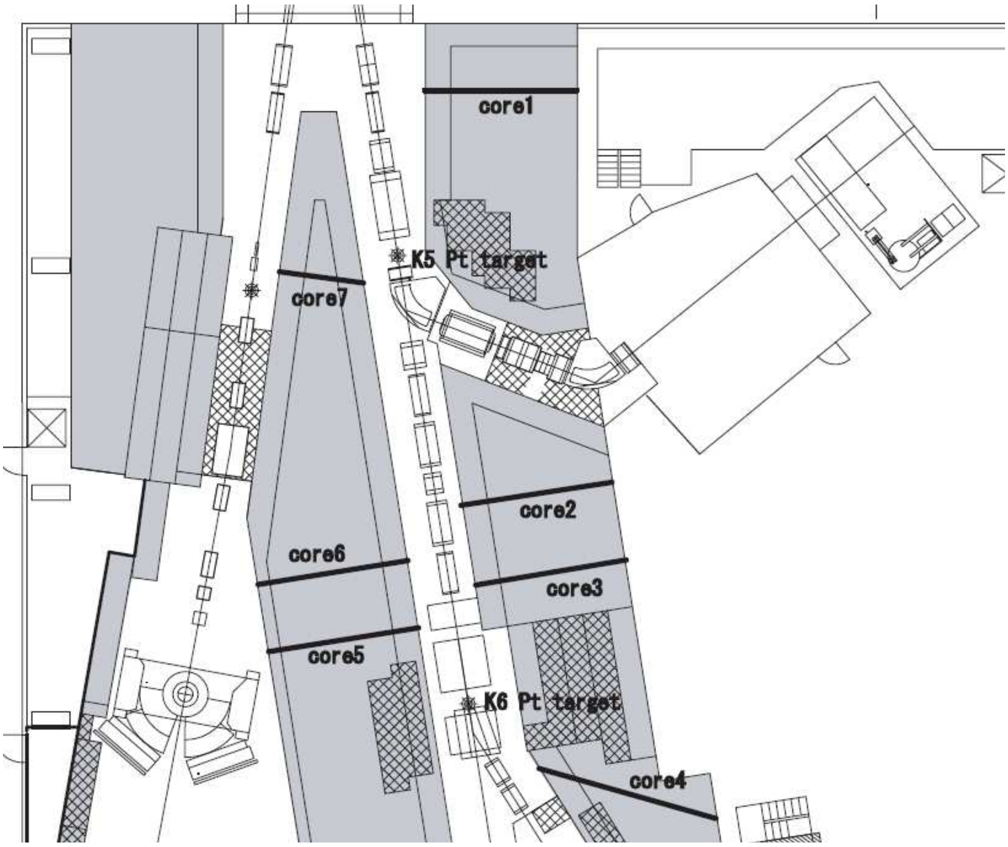

Figure 5.14. Plan view of concrete shields near the Pt targets in a 12 GeV proton synchrotron facility (Kinoshita *et al.*, 2008). Sampling locations of radioactivity are shown at core 1 to 7.

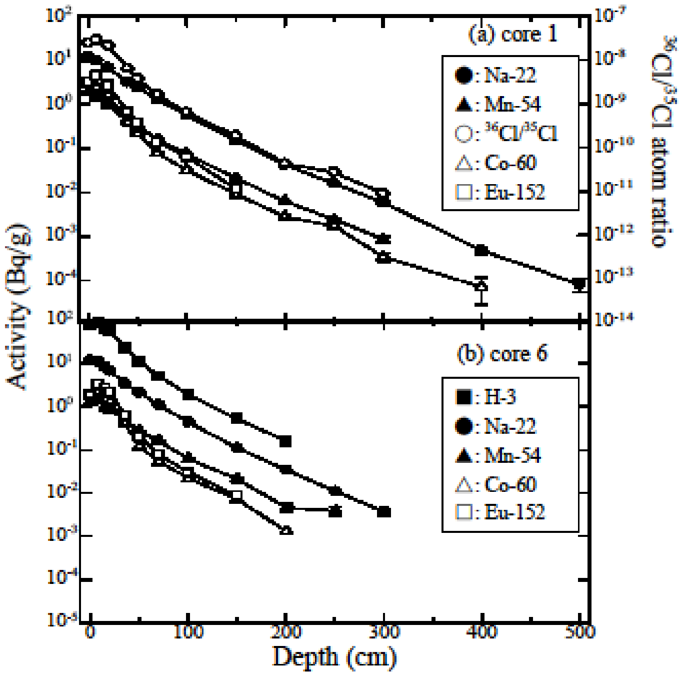

Figure 5.15. Depth profile of radioactivity in 6 m thick concrete shields near the platinum targets irradiated in a 12 GeV proton synchrotron facility shown in Fig. 5.14 (Kinoshita *et al.*, 2008).

It is easier if the concentration of radioactivity can be estimated from the measured surface dose rates. Dose rates from concrete were calculated with an assumption that the activity is uniformly distributed in several sizes of rectangular parallelepipeds. With a dose rate of 1 μSv/h at 10 cm distance from the surface, the total amount and concentration of radioactivity were calculated and the results are shown in Fig. 5.16 (Ban *et al.*, 2004). Both the concentration and total quantity of activity do not exceed IAEA exemption levels (IAEA, 1996) at the same time. The activity concentration and the total activity of the exemption levels are 10 Bq/g and 1 x 10^6 Bq for ^{22}Na, 10 Bq/g and 1 x 10^5 Bq for ^{60}Co, and 10 Bq/g and 1 x 10^6 Bq for ^{152}Eu.

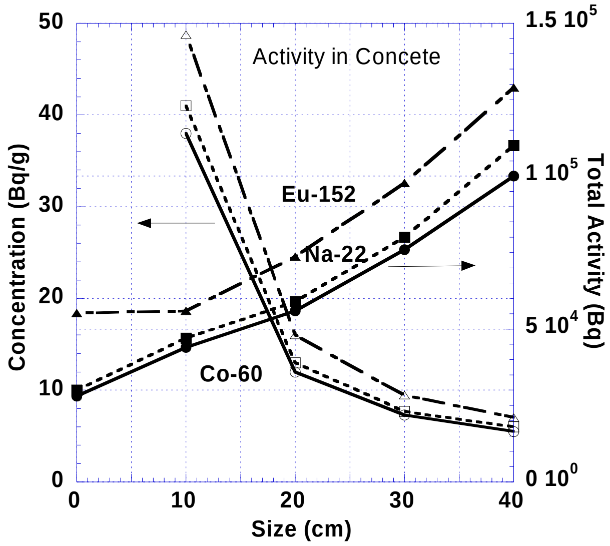

Figure 5.16. Total activity and concentration in 5 cm thick rectangular parallelepiped made of concrete when the ambient dose equivalent $H^*(10\ \mathrm{mm})$ rate at 10 cm distant is 1 μSv/h. Activity is uniformly distributed in concrete (Ban *et al.*, 2004).

Usually it is difficult to calculate radioactivity in concrete shields because irradiation conditions and the composition of the concrete are not well known. Benchmark calculations were done at the KENS spallation neutron source facility (Oishi *et al.*, 2005). Source neutrons from a tungsten target bombarded by 500 MeV protons were calculated using the NMTC/JAM code (Niita, 2001). Neutron-induced activities in 4 m thick concrete were calculated using the NMTC/JAM code at neutron energies above 20 MeV, and using the MCNP5 code below 20 MeV. Good agreement to within factors of 2 to 5 were obtained for the nuclides that were not produced mainly by the spallation reactions, though there were large differences for ^{28}Mg, ^{52}Mn, ^{7}Be, and ^{56}Co.

5.4 Cooling and Groundwater

5.4.1 Activation Cross Sections

Cooling water for magnets, slits and stoppers in the beam transport line, and the energy selection system (ESS), *etc*. is activated by secondary neutrons produced by beam losses of the accelerated particles. However, at slits and stoppers and at the extraction deflector of a cyclotron, the accelerated particles may directly hit and activate the cooling water. High-energy secondary neutrons produced by beam losses and treatment irradiations may penetrate the shielding and activate the groundwater.

High-energy neutrons produce ^{14}O, ^{15}O, ^{13}N, ^{11}C, ^{7}Be, and ^{3}H through spallation reactions of oxygen. These production cross sections are shown in Table 5.2 (Sullivan, 1992). The cross sections shown are for neutrons above 20 MeV.

The activation cross sections of protons that pass through the cooling water are thought to be equal to those of neutrons, and Table 5.2 is applicable to the proton reactions. Natural oxygen contains 0.205

% of ^{18}O. If protons hit water, positron-emitting ^{18}F, with a half-life of 1.83 hours, is produced by the ^{18}O(p, n) reaction. These reaction cross sections are shown in Fig. 5.17.

On the other hand, since the mass number of ^{12}C is large, the reaction cross sections of ^{12}C are also large. If the geometrical cross section is considered, the cross section of the ^{16}O+^{12}C reaction is assumed to be 1.87 times larger than that of ^{16}O+p reaction. The ^{12}C cross sections thus obtained are also shown in Table 5.2.

Table 5.2. Water activation cross sections for neutrons and protons. The parenthesized values are for ^{12}C ions. (Firestone, 1999; Sullivan, 1992)

Nuclide	Half-life	Decay Mode, γ-ray Energy and Emission Probability	Cross Section	
			Oxygen (mb [a])	Water (cm^{-1}) [b]
^{3}H	12.3 year	β^-	30 (56)	1.0×10^{-3} (1.9×10^{-3})
^{7}Be	53.3 day	EC, 0.478MeV γ 10.5%	5 (9)	1.7×10^{-4} (3.1×10^{-4})
^{11}C	20.4 min	β^+	5 (9)	1.7×10^{-4} (3.1×10^{-4})
^{13}N	9.97 min	β^+	9 (17)	3.0×10^{-4} (5.6×10^{-4})
^{14}O	1.18 min	β^+, 2.3MeV γ 99.4%	1 (2)	3.3×10^{-5} (6.2×10^{-5})
^{15}O	2.04 min	β^+	40 (75)	1.3×10^{-3} (2.5×10^{-3})

[a] $1\ mb = 1 \times 10^{-3} b = 1 \times 10^{-27}\ cm^2$

[b] Atomic densities are H: $6.67 \times 10^{22}\ cm^{-3}$, O: $3.34 \times 10^{22}\ cm^{-3}$.

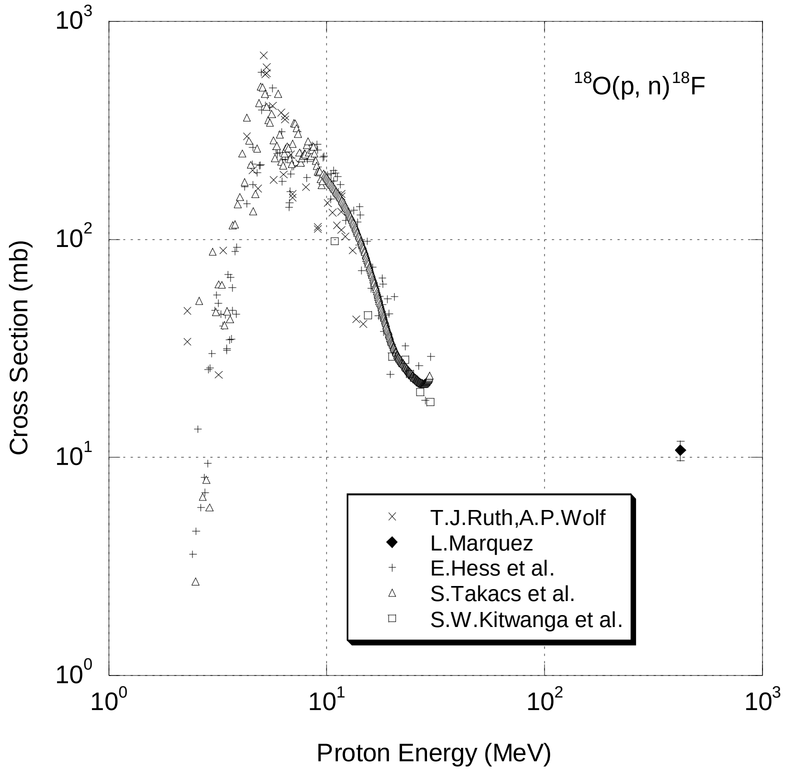

Figure 5.17. Cross sections of $^{18}O(p, n)^{18}F$ activation reaction (Hess *et al.*, 2001; Kitwanga *et al.*, 1990; Marquez, 1952; Ruth and Wolf, 1979; Takacs *et al.*, 2003).

5.4.2 Effects of Water Activation

The radioactivity of ^{14}O, ^{15}O, ^{13}N ,and ^{11}C, all of which have short half-lives, reaches saturation in a short irradiation time. The annihilation photons produced by these positron-emitting nuclides increase the dose rate around cooling-water pipes and ion-exchange resin tanks. The dose rate around a cooling-water pipe of infinite length is given by the following formula, when the self-absorption of photons by the water and the pipe wall is ignored:

$$E = \frac{\pi^2 \gamma_E r^2 c}{d} \quad (\mu\text{Sv/h}) \tag{5.7}$$

where

E is the effective dose rate (μSv/h);

γ_E is the effective dose rate factor (0.00144 μSv/h Bq^{-1} cm^{-2} for positron-emitting nuclide);

r is the radius of the cooling-water pipe (cm);

c is the concentration of positron-emitting nuclides in water (Bq cm^{-3}); and

d is the distance between the cooling-water pipe and the point of interest (cm).

The radioactivity of ^{14}O, ^{15}O, ^{13}N, and ^{11}C rapidly decreases after the end of irradiation, and the dose rate also decreases. However, the accumulated ^{18}F and ^{7}Be in the ion-exchange resin result in measurable dose rates. If the proton beam directly penetrates the water, the dose rate due to ^{18}F may be significant for about a day. ^{7}Be should be taken care of when the ion-exchange resin is replaced. Its half-life, however, is 53 days, and ^{7}Be disappears after 2 or 3 years. ^{3}H (T) stays in water in the form of HTO, and accumulates because of its long half-life (12.3 years). The concentration should be measured periodically. However, the beam intensity at a particle therapy facility is low, and the concentration is usually much lower than the limit for disposal into the sewer system.

The groundwater may be used for drinking purposes, and therefore, the activation must be kept low. Radioactivity produced in the ground can transfer to the water. Unless there is a well close to the accelerator facility, the activated water is not immediately used for drinking purposes, but can enter drinking water supplies after it migrates in the ground. Therefore, radionuclides of short half-life, such as ^{14}O, ^{15}O, ^{13}N, and ^{11}C, and those of small mobility, such as ^{7}Be, usually do not affect the groundwater, while ^{3}H may affect it. The groundwater activation should be considered at the design stage. If the water concentration of radioactivity outside the shield is not negligible, the concentration at the well or at the site boundary should be estimated. If the speed of groundwater is high, the accumulation of long half-life nuclides is low. If the speed is low, decay of the nuclides is significant. Considering these phenomena, the concentration can be estimated with the following formula:

$$C = C_0 (1 - e^{-\lambda \frac{L_1}{v}}) e^{-\lambda \frac{L_2}{v}} \quad (\text{Bq cm}^{-3}) \tag{5.8}$$

where

C is the concentration at the given point (Bq cm^{-3});

C_0 is the saturated concentration at the irradiation area (Bq cm^{-3});

λ is the decay constant of the nuclide (s^{-1});

L_1 is the length of the irradiation area outside the shield (cm);

v is the velocity of the groundwater (cm s^{-1}); and

L_2 is the distance between the irradiation area and the considering point (cm).

5.5 Air

5.5.1 Activation Cross Sections

Activation of air is caused by the secondary neutrons at a particle therapy facility; however, it is also caused by the primary particles in the air path between the accelerator vacuum system and the patient position.

A detailed estimation of the air activation can be done with Monte Carlo codes as shown in Chapter 6. At most particle therapy facilities, however, the air activation is much lower than the regulation levels, and a rough estimation is usually enough, as is is explained in the following text. If the estimated value is close to the regulation level, a detailed estimation should be done.

The airborne radionuclides produced by high-energy neutrons are mainly ^{3}H, ^{7}Be, ^{11}C, ^{13}N, ^{14}O, and ^{15}O. Thermal neutrons produce ^{41}Ar. The production cross sections of these nuclides are listed in Table 5.3 (Sullivan, 1992). Cross sections shown for N and O are for neutrons above 20 MeV.

The cross sections of N and O for protons can be considered equal to those for neutrons, and Table 5.3 is applicable to protons. The geometrical cross section of $^{14}N+^{12}C$ is 1.90 times larger than that of $^{14}N+p$, and that of $^{16}O+^{12}C$ is 1.87 times larger than that of $^{16}O+p$. The cross sections for ^{12}C ions obtained using the previously mentioned ratios are also shown in Table 5.3 in parentheses.

Table 5.3. Air activation cross sections for neutrons and protons. The parenthesized values are for ^{12}C ions. (Firestone, 1999; Sullivan, 1992)

Nuclide	Half-life	Emission of beta, gamma	Cross Section		
			Nitrogen (mb [a])	Oxygen (mb [a])	Air (cm^{-1}) [b]
^{3}H	12.3 year	β^-	30 (57)	30 (56)	$1.5x10^{-6}$ ($2.8x10^{-6}$)
^{7}Be	53.3 day	EC, 0.478MeV γ 10.5%	10 (19)	5 (9)	$4.4x10^{-7}$ ($8.4x10^{-7}$)
^{11}C	20.4 min	β^+	10 (19)	5 (9)	$4.4x10^{-7}$ ($8.4x10^{-7}$)
^{13}N	9.97 min	β^+	10 (19)	9 (17)	$4.9x10^{-7}$ ($9.2x10^{-7}$)
^{14}O	1.18 min	β^+, 2.3MeV γ 99.4%	0 (0)	1 (2)	$1.1x10^{-8}$ ($2.0x10^{-8}$)
^{15}O	2.04 min	β^+	0 (0)	40 (75)	$4.2x10^{-7}$ ($7.8x10^{-7}$)
^{41}Ar	1.82 hour	β^-, 1.3MeV γ 99.1%	610 (for ^{40}Ar)		$1.42x10^{-7}$

[a] 1 mb = 1×10^{-3}b = 1×10^{-27} cm^2

[b] Atomic densities are N: $3.91x10^{19}$ cm^{-3}; O: $1.05x10^{19}$ cm^{-3}; ^{40}Ar:$2.32x10^{17}$ cm^{-3}.

5.5.2 Estimation of Concentration of Air Activation

Several formulae for the estimation of radionuclide concentration in the air are shown below (RIBF, 2005). The air in a room is assumed to be uniformly mixed.

Explanatory notes for the symbols are as follows:

- A_0: saturated activity (Bq) produced in a room, which is equal to R of Eq. (5.1)
- λ : decay constant (s^{-1})
- V: volume of the room (cm^3)
- v: ventilation speed of the room ($cm^3\ s^{-1}$)
- v_A: ventilation speed at the stack of the facility ($cm^3\ s^{-1}$)
- ε : penetration rate of the filter if a purification system is installed (1.0 except for ^7Be)
- T_R: irradiation time (s)
- T_D: decay time between the end of irradiation and the start of ventilation (s)
- T_E: working time of persons in the room (s)
- T_W: time between the end of irradiation and the start of the next irradiation (s)

The air concentrations in the room and at the stack should be estimated at the planning stage of the facility and compared with the regulatory limits. Then the required ventilation can be determined.

5.5.2.1 Radionuclide Concentrations of Exhaust Air. Case 1: Average concentration at the stack during one irradiation cycle, *i.e.*, between the start of the first and second irradiations, under the condition of continuous ventilation; C_1

$$C_1 = \frac{\varepsilon v \lambda A_0}{v_A V(\lambda + \frac{v}{V})(T_R + T_W)}\left[T_R - \frac{1}{\lambda + \frac{v}{V}}\{1 - e^{-(\lambda+\frac{v}{V})T_R}\}e^{-(\lambda+\frac{v}{V})T_W}\right] \qquad (5.9)$$

Case 2: Average concentration at the stack during one irradiation cycle under the condition that the ventilation is stopped during the irradiation and started at time T_D after the irradiation is stopped; C_2 (Average value during the ventilating time of T_W-T_D)

$$C_2 = \frac{\varepsilon v A_0}{v_A V(\lambda + \frac{v}{V})(T_W - T_D)}(1 - e^{-\lambda T_R})e^{-\lambda T_D}\{1 - e^{-(\lambda + \frac{v}{V})(T_W - T_D)}\} \quad (5.10)$$

5.5.2.2. Radionuclide Concentrations of Room Air. Case 3: Air concentration of the continuously ventilated treatment room at the time the irradiation is stopped; C_3

$$C_3 = \frac{\lambda A_0}{V(\lambda + \frac{v}{V})}\{1 - e^{-(\lambda + \frac{v}{V})T_R}\} \quad (5.11)$$

Case 4: Average air concentration in a room during the working time of T_E under the condition that work and the ventilation are started simultaneously at a time T_D after the irradiation was stopped; C_4

$$C_4 = \frac{A_0}{V(\lambda + \frac{v}{V})T_E}(1 - e^{-\lambda T_R})e^{-\lambda T_D}\{1 - e^{-(\lambda + \frac{v}{V})T_E}\} \quad (5.12)$$

This condition can be applied to an accelerator enclosure, for example, where persons enter only at maintenance time.

6. Monte Carlo Codes for Particle Therapy

Stefan Roesler

6.1 General-Purpose Codes

Nowadays the use of general-purpose particle interaction and transport Monte Carlo codes is often the most accurate and efficient choice to design particle therapy facilities. Due to the widespread use of such codes in all areas of particle physics and the associated extensive benchmarking with experimental data, the modeling has reached an unprecedented level of accuracy. Furthermore, most codes allow the user to simulate all aspects of a high-energy particle cascade in one and the same run: from the first interaction of a TeV nucleus over the transport and re-interactions (hadronic and electromagnetic) of the secondaries produced, to detailed nuclear fragmentation, the calculation of radioactive decays, and even of the electromagnetic shower caused by the radiation from such decays. Consequently, there is no longer any need for time-consuming multi-step calculations employing different Monte Carlo codes that significantly increases the consistency of the results and greatly reduces the uncertainties related to the subsequent use of different codes.

At the same time, computing power has increased exponentially, allowing one to perform complex simulations with low statistical uncertainty in a few hours or days. Often the time spent to set up a simulation and to post-process its results significantly exceeds the actual computation time, despite the fact that many general-purpose codes now come with user-friendly graphical interfaces that have significantly reduced the preparation and post-processing phases as well. It follows that it is often more economical to invest resources in a careful study optimizing the facility shielding than in conservative shielding and infrastructure that compensate for less accurate estimates.

The following general-purpose Monte Carlo codes are commonly used for radiation transport simulations and will be described further below: FLUKA (Ferrari, 2005; Battistoni *et al*., 2007), GEANT4 (Agostinelli *et al*., 2003; Allison *et al*., 2006), MARS15 (Mokhov, 1995; Mokhov and Striganov, 2007; Mokhov, 2009), MCNPX (Pelowitz, 2005; McKinney *et al*., 2006), PHITS (Iwase, 2002; Niita, 2006), and SHIELD/SHIELD-HIT (Geithner *et al*., 2006; Gudowska *et al*., 2004).

6.2 Areas of Application

6.2.1 Shielding Studies and Secondary Doses to the Patient

The areas of application of Monte Carlo codes include all radiation protection aspects of the facility design. The most prominent application is shielding design where only Monte Carlo codes allow a careful optimization of complex access mazes, ducts, wall materials, and wall thicknesses that would be impossible to describe with analytical methods. The risks to personnel and patients due to secondary whole-body irradiation are typically calculated by folding fluence spectra with energy-dependent conversion coefficients that have also been obtained with detailed Monte Carlo simulations, *e.g.*, employing complex voxel phantoms of the human body (Pelliccioni, 2000). Numerous shielding studies done especially for particle research accelerators and, more recently, for therapy facilities have used Monte Carlo codes. Examples can be found in Agosteo *et al*. (1996b; 1996c), Brandl *et al*. (2005), Fan *et al*. (2007), Newhauser *et al.* (2005a), Polf *et al*. (2005), Popova (2005), Schneider *et al*. (2002), Titt *et al*. (2005), and Zheng *et al*. (2008). Some aspects of secondary radiation production in the beam-line elements are discussed in Chapter 7.

Monte Carlo simulations can also assess secondary doses to the patient, directly through the calculation of energy deposition in individual organs by using phantoms of the human body (see Chapter 7).

6.2.2 Activation Studies

The Monte Carlo simulation of all aspects of activation has grown significantly over the past years due to the availability and increasing quality of both microscopic models for the production of individual nuclides and experimental benchmark data. While an uncertainty factor of 2 to 5 in such predictions was considered reasonable in the past, modern codes are now able to predict individual isotopes often with a 30 % or better accuracy (Brugger *et al.,* 2006). In addition to the production of radionuclides, some codes also allow (in the same simulation) the computation of radioactive decay and the transport of the decay radiation and, thus, of residual doses (Brugger *et al.,* 2005). Consequently, the material choice and design of shielding and accelerator components can be optimized in this regard during the design stage, thus reducing costs at a later stage that result from precautionary measures such as unnecessary accelerator down-times to allow for "cool-down" of components or temporary protection.

The capability of accurately predicting radioactive nuclide production and distributions with Monte Carlo methods has now even entered the field of particle therapy quality assurance (*e.g.*, positron emission tomography, PET; see, for example, Parodi *et al.*, 2007 and Pshenichnov *et al*., 2007). This field is, however, outside of the scope of this review. Air and water activation are also typically estimated with Monte Carlo simulations, although in this case the direct calculation of nuclide production is usually replaced by off-line folding of particle fluence spectra with evaluated cross section data due to the low density of the media and the associated inefficient nuclide production during a simulation.

6.3 Requirements

The requirements can be subdivided into two categories: those related to physics modeling and those associated with the user-friendliness of the code. While details on different Monte Carlo codes are given further below, this Chapter provides some guidance as to which code might best fulfill the various requirements.

6.3.1 Shielding Studies

A code to be used for shielding design at a particle therapy facility should be able to describe interactions of hadrons and nuclei with energies up to a few hundred MeV/u in arbitrary materials. Because exposures behind shielding are typically caused by neutrons, an accurate description of double differential distributions of neutrons and light fragments emitted in an interaction, as well as their transport through the shield down to thermal energies, is vital. For ion beams and shielding in the forward (beam) direction, a detailed treatment of projectile fragmentation by the respective code is of equal importance. A folding with energy-dependent dose equivalent conversion coefficients (for example, those summarized in Pelliccioni, 2000) and direct scoring of the latter quantity is usually most convenient for the user, and the code should offer this option. The contribution to the total dose behind shielding due to electromagnetic cascades is usually small (~ 20 %) as compared to the contribution by neutrons. Still, a coupled simulation of both hadronic and electromagnetic showers through the shield is necessary for benchmarking the calculations with measurements (the radiation monitors may have an enhanced response to electromagnetic particles), and for establishing so-called field calibration factors.

The availability of variance reduction (biasing) techniques is a 'must' in order for a Monte Carlo code to be used for the design of thick shielding (one meter or more) and complex access mazes. In contrast to an analog Monte Carlo simulation, in which physics processes are sampled from actual phase space distributions, a biased simulation samples from artificial distributions with the aim of achieving a faster convergence of the calculated quantities to the true values (*i.e.*, a faster reduction of the variance) in the phase space regions of interest, *e.g.*, behind thick layers of shielding. Note that a biased simulation predicts average quantities but not their higher moments and can, therefore, not reproduce correlations and fluctuations. A rigorous mathematical treatment of variance reduction techniques can be found in several textbooks; see for instance Lux and Koblinger (1991) and Carter and Cashwell (1975).

There exist several variance reduction methods. The choice of the most appropriate method depends on the actual problem, with a combination of different techniques often being the most effective approach. The so-called "region importance biasing" is the easiest method to apply and safest to use. The shield is split into layers that are assigned importance factors. The values of the factors increase towards the outside of the shield, with the relative value of the factors of two adjacent layers equal to the inverse of the dose attenuation in that layer.

FLUKA (Ferrari, 2005; Battistoni *et al*., 2007) and MCNPX (Pelowitz, 2005; McKinney *et al*., 2006) are two general-purpose codes that include powerful variance reduction techniques and have therefore been used widely in shielding studies.

6.3.2 Activation Studies

A reliable description of inelastic interactions by microscopic models is indispensable for activation studies of beam-line and shielding components. Only activation by low-energy neutrons constitutes an exception where evaluated experimental data on nuclide production are typically available in the respective neutron transport library. Activation of accelerator components is often dominated by spallation reactions. An accurate simulation of these reactions requires a generalized intra-nuclear cascade model with pre-equilibrium emission, as well as models for evaporation, fission, and fragmentation. The description of the break-up of a highly excited heavy residual (so-called multi-fragmentation), which can be very complex and too time-consuming during a shower simulation, is often approximated by a generalized evaporation of nuclides with mass numbers of up to 20 or more. Predictions for the production of individual nuclides are non-trivial and depend on the quality of many different physics models, not only for the inelastic interaction and nuclear break-up but also for particle transport and shower propagation. Thus, detailed benchmark exercises to assess the reliability of the results are of utmost importance. Typically, the longer the cooling time, the less nuclides contribute to the total activation, and therefore, details of the production of individual nuclides become more important. At short cooling times (up to a few days) over- and underestimations of the nuclide production tend to cancel each other so that integral quantities such as total activity or residual doses are much less affected by model uncertainties. Both MARS15 and MCNPX can use the Cascade-Exciton Model (CEM) and Los Alamos Quark Gluon String Model (LAQGSM) for hadronic interactions that have been shown in extensive benchmark experiments to provide reliable predictions for nuclide production (Mashnik, 2009). The FLUKA code also includes detailed microscopic models for nuclide productions which have been proven to give very accurate results (Brugger *et al*., 2006). In this case, the models are fully integrated into the code, providing a high level of quality assurance that is often needed in safety-related applications.

In the past, residual dose rates were often estimated by means of so-called omega factors that relate the density of inelastic interactions in a solid material to contact dose-equivalent rates caused by radioactive nuclides in the material. At present, more and more codes include a description of radioactive decay and the transport of decay radiation, and allow one to avoid approximations inherent to omega factors. A code capable of a direct simulation of radioactive decay should be preferred for this type of study because handling of activated components is an important cost factor due to decreasing dose limits and also due to the increasing importance of the optimization principle during the design stage. At present, the FLUKA Monte Carlo code gives the most consistent and reliable single-step prediction of residual dose rates (Ferrari, 2005; Battistoni *et al*., 2007; Brugger *et al*., 2005). Other general purpose codes make use of omega factors (MARS15) or require a separate calculation of the radioactive decay with a different code (MCNPX).

6.3.3 Secondary Doses to Patients

Monte Carlo simulations have been used extensively to study secondary doses in patients (see Chapter 7). Such simulations obviously require an accurate modeling of the transport, interaction, and fragmentation (for ion beams) of the primary beam in tissue-equivalent material, as well as a fully coupled hadronic and electromagnetic shower simulation. The capability of the transport code to use voxel phantoms usually increases the reliability of the predictions due to the great detail in which the human body can be modeled with such phantoms. GEANT4 (Agostinelli *et al*., 2003; Allison *et al*., 2006; Rogers *et al*., 2007) and FLUKA (Ferrari, 2005; Battistoni *et al*., 2007; Battistoni *et al*., 2008) are two examples of codes that support voxel geometries.

6.3.4 User-Friendliness

In addition to physics modeling, the user-friendliness of a code can be of significant importance. As mentioned earlier, increasing computing power greatly reduces the time actually spent for the calculation such that, in many cases, the time necessary to set up a simulation and process its results becomes a dominating factor. To address this problem, graphical user interfaces that also take over a basic check of input options exist for many codes. A few examples can be found in Vlachoudis, 2009; Theis *et al.*, 2006; and Schwarz, 2008. The check of input options is vital as increasing user-friendliness is associated with increasing usage of the code as a "black-box," and one risks having simulation artefacts being taken into account undetected. Furthermore, it is observed that the acceptance of the results, *e.g.*, by authorities, can depend a great deal on the way the results are presented. In this regard, three-dimensional geometry visualization, the overlay of results onto the geometry, and the use of color contour plots can be of importance. Finally, it should be noted that despite the enormous advantages of graphical user interfaces, a minimum knowledge on the available physical models is indispensible in order to judge on the accuracy of the obtained results.

6.4 Overview of the Most Commonly Used Codes

6.4.1 FLUKA

FLUKA is a general-purpose particle interaction and transport code with roots in radiation protection studies at high energy accelerators (Ferrari, 2005; Battistoni *et al.*, 2007). It therefore comprises all features needed in this area of application, such as detailed hadronic and nuclear interaction models, full coupling between hadronic and electromagnetic processes, and numerous variance reduction options.

The module for hadronic interactions is called PEANUT and consists of a phenomenological description (Dual Parton Model-based Glauber Gribov cascade) of high-energy interactions (up to 20 TeV), a generalized intra-nuclear cascade, and pre-equilibrium emission models, as well as models for evaporation, fragmentation, fission, and de-excitation by gamma emission. Interactions of ions are simulated through interfaces with different codes based on models applicable in certain ranges of energy (DPMJET3 above 5 GeV/nucleon, rQMD-2.4 between 0.1 and 5 GeV/nucleon, Boltzmann Master Equation below 0.1 GeV/nucleon; see Battistoni, 2007 and references therein).

The transport of neutrons with energies below 20 MeV is performed by a multi-group algorithm based on evaluated cross section data (ENDF/B, JEF, JENDL, *etc*.) binned into 260 energy groups, 31 of which are in the thermal energy region. For a few isotopes (^{1}H, ^{6}Li, ^{10}B, ^{14}N), pointwise cross sections can be optionally used during transport. The detailed implementation of electromagnetic processes in the energy range between 1 keV and 1 PeV is fully coupled with the models for hadronic interactions.

Many variance reduction techniques are available in FLUKA, including weight windows, region importance biasing, and leading particle, interaction, and decay length biasing (among others). The capabilities of FLUKA are unique for studies of induced radioactivity, especially with regard to nuclide production, decay, and transport of residual radiation. In particular, particle cascades by prompt and residual radiation are simulated in parallel based on the microscopic models for nuclide production and a solution of the Bateman equations for activity built-up and decay.

FLUKA is written in Fortran77 and runs on most Linux and Unix platforms on which the compiler g77 is installed. The code is distributed in binary form, with the addition of the source code for user routines and common blocks (http://www.fluka.org). The complete FLUKA source code is available by request after an additional registration procedure (see http://www.fluka.org/fluka.php for details). No programming experience is required unless user routines are needed for specific applications.

6.4.2 GEANT4

GEANT4 is an object-oriented toolkit originally designed to simulate detector responses of modern particle and nuclear physics experiments (Agostinelli *et al*., 2003; Allison *et al*., 2006). It consists of a kernel that provides the framework for particle transport, including tracking, geometry description, material specifications, management of events, and interfaces to external graphics systems.

The kernel also provides interfaces to physics processes. In this regard, the flexibility of GEANT4 is unique as it allows the user to freely select the physics models that best serve the particular application needs. Implementations of interaction models exist over an extended range of energies, from optical photons and thermal neutrons to high-energy interactions required for the simulation of accelerator and cosmic ray experiments. In many cases, complementary or alternative modeling approaches are offered from which the user can choose.

Descriptions of intra-nuclear cascades include implementations of the Binary and the Bertini cascade models. Both are valid for interactions of nucleons and charged mesons, the former for energies below 3 GeV, and the latter for energies below 10 GeV. At higher energies (up to 10 TeV), three models are available: a high-energy parameterized model (using fits to experimental data), a quark-gluon string model, and the Fritiof fragmentation model, with both the quark-gluon string model and the Fritiof fragmentation model based on string excitations and decay into hadrons. Nuclear de-excitation models include abrasion-ablation and Fermi-breakup models. Furthermore, heavy-ion interactions can also be simulated if the appropriate packages are linked.

The package for electromagnetic physics comprises the standard physics processes as well as extensions to energies below 1 keV, including emissions of x rays, optical photon transport, *etc.*

To facilitate the use of variance reduction techniques, general-purpose biasing methods such as importance biasing, weight windows, and a weight cut-off method have been introduced directly into the toolkit. Other variance reduction methods, such as leading particle biasing for hadronic processes, come with the respective physics packages,.

GEANT4 is written in C++ and runs on most Linux and Unix platforms as well as under Windows with CygWin Tools. The code and documentation can be downloaded from the GEANT4 website at http://cern.ch/geant4. Experience in C++ programming is indispensable for using the code.

6.4.3 MARS15

The MARS15 code system (Mokhov, 1995; Mokhov and Striganov, 2007; Mokhov, 2009) is a set of Monte Carlo programs for the simulation of hadronic and electromagnetic cascades that is used for shielding, accelerator design, and detector studies. Correspondingly, it covers a wide energy range: 1 keV to100 TeV for muons, charged hadrons, heavy ions and electromagnetic showers; and 0.00215 eV to 100 TeV for neutrons.

Hadronic interactions above 5 GeV can be simulated with either an inclusive or an exclusive event generator. While the former is CPU-efficient (especially at high energy) and based on a wealth of experimental data on inclusive interaction spectra, the latter provides final states on a single interaction level and preserves correlations. In the exclusive mode, the cascade-exciton model CEM03.03 describes hadron-nucleus and photo-nucleus interactions below 5 GeV, the Quark-Gluon String Model code LAQGSM03.03 simulates nuclear interactions of hadrons and photons up to 800 GeV and of heavy ions up to 800 GeV/nucleon, and the DPMJET3 code treats the interactions at higher energies. The exclusive mode also includes models for a detailed calculation of nuclide production *via* evaporation, fission, and fragmentation processes.

MARS15 is also coupled to the MCNP4C code that handles all interactions of neutrons with energies below 14 MeV. Produced secondaries other than neutrons are directed back to the MARS15 modules for further transport.

Different variance reduction techniques, such as inclusive particle production, weight windows, particle splitting, and Russian roulette, are available in MARS15. A tagging module allows one to tag the origin of a given signal for source term or sensitivity analyses. Further features of MARS15 include a MAD-MARS Beam-Line Builder for a convenient creation of accelerator models.

MARS15 modules are written in Fortran77 and C. The code runs on any Linux or Unix platform in both single- and multi-processor modes. A powerful user-friendly graphical user interface provides various visualization capabilities. The code must be installed by the author on request (for details see Mokhov, 2009).

6.4.4 MCNPX

MCNPX originates from the Monte Carlo N-Particle transport (MCNP) family of neutron interaction and transport codes and, therefore, features one of the most comprehensive and detailed descriptions of the related physical processes (Pelowitz, 2005; McKinney *et al*., 2006). Later it was extended to other particle types, including ions and electromagnetic particles. This allowed an expansion of the areas of application from those purely neutronics-related to accelerator shielding design, medical physics, and space radiation, among others.

The neutron interaction and transport modules use standard evaluated data libraries mixed with physics models where such libraries are not available. The transport is continuous in energy and includes all features necessary for reactor simulations, including burn-up, depletion, and transmutation. Different generalized intra-nuclear cascade codes can be linked to explore different physics implementations, such as CEM2K, INCL4 and ISABEL (see McKinney *et al*., 2006 and references therein). They either contain fission-evaporation models or can be coupled to such models (*i.e*., ABLA), allowing detailed predictions for radionuclide production. While the intra-nuclear cascade codes are limited to interaction energies below a few GeV, a link to the Quark-Gluon String Model code LAQGSM03 extends this energy range to about 800 GeV. The latter code also allows the simulation of ion interactions. Electromagnetic interactions are simulated in MCNPX by the ITS 3.0 code.

MCNPX contains one of the most powerful implementations of variance reduction techniques. Spherical mesh weight windows can be created by a generator in order to focus the simulation time on certain spatial regions of interest. In addition, a more generalized phase space biasing is also possible through energy- and time-dependent weight windows. Other biasing options include pulse-height tallies with variance reduction and criticality source convergence acceleration.

MCNPX is written in Fortran90 and runs on PC Windows, Linux, and Unix platforms. The code (source code, executables, data) is available to nearly everyone (subject to export controls on sensitive countries) from the Radiation Safety Information Computational Center (http://www-rsicc.ornl.gov) in Oak Ridge, TN, U.S.A. Experience in programming is not required for many applications.

6.4.5 PHITS

The Particle and Heavy-Ion Transport code System PHITS (see Iwase, 2002; Niita, 2006 and references therein) was among the first general-purpose codes to simulate the transport and interactions of heavy ions in a wide energy range, from 10 MeV/nucleon to 100 GeV/nucleon. It is based on the high-energy hadron transport code NMTC/JAM that was extended to heavy ions by incorporating the JAERI Quantum Molecular Dynamics code JQMD.

Below energies of a few GeV, hadron-nucleus interactions in PHITS are described through the production and decay of resonances, while at higher energies (up to 200 GeV) inelastic hadron-nucleus collisions proceed *via* the formation and decay of so-called strings that eventually hadronize through the creation of (di)quark-anti(di)quark pairs. Both are embedded into an intra-nuclear cascade calculation. Nucleus-nucleus interactions are simulated within a molecular dynamics framework based on effective interactions between nucleons.

The generalized evaporation model GEM treats the fragmentation and de-excitation of the spectator nuclei and includes 66 different ejectiles (up to Mg) and fission processes. The production of radioactive nuclides, both from projectile and target nuclei, thus follows directly from the mentioned microscopic interaction models.

The transport of low-energy neutrons employs cross sections from evaluated nuclear data libraries such as ENDF and JENDL below 20 MeV and LA150 up to 150 MeV. Electromagnetic interactions are simulated based on the ITS code in the energy range between 1 keV and 1 GeV. Several variance reduction techniques, including weight windows and region importance biasing, are available in.PHITS.

Due to its capability to transport nuclei, PHITS is frequently applied in ion-therapy and space radiation studies. The code is also used for general radiation transport simulations, such as in the design of spallation neutron sources.

The PHITS code is available for download from its Web site, http://phits.jaea.go.jp/

6.4.6 SHIELD/SHIELD-HIT

The SHIELD Monte Carlo code (Sobolevsky, 2008; Dementyev and Sobolevsky, 1999) simulates the interactions of hadrons and atomic nuclei of arbitrary charge and mass number with complex extended targets in the energy range from 1 MeV/nucleon to 1 TeV/nucleon, and down to thermal energies for neutrons.

Inelastic nuclear interactions are described by the so-called multi-stage dynamical model (MSDM). The name refers to the different stages through which a hadronic interaction proceeds in SHIELD: fast cascade stage, pre-equilibrium emission of nucleons and light nuclei, and a nuclear fragmentation and de-excitation stage. Interactions above 1 GeV are simulated by the quark-gluon string model (QGSM), while the Dubna Cascade Model (DCM) handles intra-nuclear cascades at lower energies. The models implemented for the equilibrium de-excitation of a residual nucleus cover all aspects of this stage, such as evaporation, fission, Fermi break-up of light nuclei, and multi-fragmentation. In the latter case, the disintegration of highly excited nuclei into several excited fragments is described according to the statistical models of multi-fragmentation (SMM). Neutron transport below 14.5 MeV is simulated by the LOENT (Low Energy Neutron Transport) code based on 28 energy groups and using the data system ABBN.

The code SHIELD-HIT (Gudowska *et al*., 2004; Geithner *et al*., 2006), a spin-off of SHIELD, specializes in the precision simulation of interaction of therapeutic beams with biological tissue and tissue-like materials. Improvements in SHIELD-HIT, relevant for light-ion therapy, comprise ionization energy-loss straggling and multiple Coulomb scattering effects of heavy charged particles. Further aspects of particle transport that were modified when compared to SHIELD include updated stopping power tables, an improved Fermi break-up model, and an improved calculation of hadronic cross sections.

The code can be obtained from the authors by request (for further information, see http://www.inr.ru/shield).

7. Patient Dose from Secondary Radiation

Harald Paganetti and Irena Gudowska

When charged particles such as protons and carbon ions are used in cancer therapy, secondary particles such as neutrons, protons, pions, and heavy charged ions are produced through nuclear inelastic reactions of the primary ions with the beam-line components and the patients themselves. These particles may possess very high energies (up to several hundred MeV) and undergo a variety of cascade events during their transport through the patient, which generate new series of secondary particles. An extensive part of the patient body may be exposed to the complex radiation field. Secondary radiation produced in the beam-line components and that reaches the patient can be regarded as external radiation. On the other hand, secondary particles produced in the patient represent an internal radiation source.

The number of review articles in the literature shows the increased awareness regarding health risks due to secondary radiation for patients undergoing radiation therapy (Palm and Johansson, 2007; Suit *et al.*, 2007; Xu *et al.*, 2008). Numerous experimental and theoretical studies have been done and many results have been published. There are quite a few uncertainties leading to controversies among experts in the field (Brenner and Hall, 2008b; Chung *et al.*, 2008; Gottschalk, 2006; Hall, 2006; Paganetti *et al.*, 2006). In this chapter, the secondary doses (both absorbed doses and equivalent doses delivered to the tissue) produced in proton and carbon ion beams of different energies are discussed. Concepts of equivalent dose or dose equivalent applied to secondary radiation in ion therapy are explained. We summarize the main issues with regard to cancer risk due to secondary radiation (*i.e.*, neutrons) in heavy charged particle radiation therapy. Given the amount of material published by several groups, this chapter cannot be comprehensive and we discuss only a subset of the available data.

7.1 Sources of Secondary Radiation

7.1.1 Secondary Particles Produced in the Beam-Line Elements

Secondary particles like neutrons, protons, and light charged ions (^{2}H, ^{3}H, ^{3}He, ^{4}He, *etc*.) are produced when primary ion beams interact through nuclear reactions with beam-line components or in patients. As far as the dose outside the main radiation field is concerned, proton beams deposit secondary dose mostly *via* secondary neutrons. For light-ion radiation therapy, heavier by-products might occur. However, such contributions are likely to be stopped in the multiple collimators or scatterers. The production of neutrons outside the patient depends on the material (type and dimensions) in the beam path and, hence, depends on the design of the beam line.

For protons and carbon-ion beams delivered by cyclotrons with a fixed energy, a significant amount of secondary radiation is produced in the energy selection systems, which include energy degraders of variable thickness and energy-defining slits. These degraders are usually outside the treatment room (in the accelerator vault) and thus do not cause secondary dose exposure of the patient. However, special care must be taken where the degradation is done, at least partially, directly upstream of the patient position. This is the case, for example, in beam lines devoted to ophthalmic applications, using small fields (*e.g.*, < 3 cm diameter) and low energies (< 70 MeV) but with high dose rates (*e.g.*, 15 to 20 Gy/min).

Neutrons and protons produced in the nozzle can undergo tertiary interactions in the beam-line elements, which result in the cascade of high-energy secondaries. Depending on the beam focusing and scattering components, certain fractions of these high-energy secondaries, mainly neutrons, reach the patient. High-energy neutrons (of energies greater than 10 MeV) and high-energy protons produced by an intra-nuclear cascade process, are mainly forward-peaked. Neutrons of energies below 10 MeV are produced by an evaporation process and are emitted fairly isotropically around each source in the treatment head. In general, high-*Z* materials generate more neutrons per incoming proton than low-*Z* materials. However, it is not practical to manufacture most treatment head devices with, for example, low-*Z* and high-density plastic materials. Some of the materials typically used in treatment heads are brass, steel, carbon, or nickel.

Design of proton therapy beam delivery systems and treatment heads can have considerable variations when comparing different facilities. In addition, the beam and treatment-head configuration is dependent on the treatment field size. Broad-beam, energy-modulated (or passively scattered) proton therapy needs various scatterers, beam-flattening devices, collimators, and energy-modulation devices to produce the spread-out Bragg peaks. Additionally, for each treatment field, individual apertures and range compensators are generally used. Consequently, the neutron fluence and energy spectrum produced in the treatment head of a proton therapy machine used for broad-beam energy-modulated treatments depends on several factors. These include the characteristics of the beam entering the treatment head (energy, angular spread); the material in the double-scattering system and range modulator; and the field size upstream of the final patient-specific aperture (Mesoloras *et al.*, 2006). Depending on the field size incident on the aperture, the latter can cause neutron dose variations up to one order of magnitude. The complexity of field delivery, specifically for passive-scattering techniques, causes considerable variations in neutron doses and prevents us from defining a ‘typical’ neutron background representing proton therapy in general (Gottschalk, 2006; Hall, 2006; Paganetti *et al.*, 2006; Zacharatou Jarlskog and Paganetti, 2008b).

In proton therapy, generally only neutrons and protons of high energies, especially those produced in the final target-shaped collimators located close to the patient, are of concern for undesired exposures in the patient. In addition, most proton therapy delivery systems allow the delivery of only a few fixed-field sizes impinging on the final patient specific aperture. Consequently, the efficiency of most proton therapy treatment heads is quite low (below 30% and even as low as 10% for typical field sizes). This implies that the neutron yield from such treatment heads typically increases with decreasing field size for passive-scattering proton beam treatments, as has been demonstrated in experiments (Mesoloras *et al.*, 2006) and Monte Carlo simulations (Zacharatou Jarlskog *et al.*, 2008).

For beam scanning, a proton pencil beam is magnetically scanned throughout the target volume without the need for scattering, flattening, or compensating devices. Therefore, for scanned beams the intensity of secondary radiation is much lower than for passive systems because there is little material in the beam path (typically only monitor ionization chambers or beam position monitors).

In passive-scattering systems where patient-specific collimators are routinely used, the patient is also exposed to out-scattered primary particles from the edges of the collimator. This process is especially important in proton therapy beams, where the edge-scattered protons influence the lateral out-of-field dose distribution in a patient. Note that this radiation is referred to as scattered radiation as compared to secondary radiation consisting of secondary particles and is not discussed in this chapter.

7.1.2 Secondary Particles Produced in the Patient

Secondary radiation is also produced in the patient. In proton therapy, the most significant (in terms of dose) secondary particles from nuclear interactions are either protons or neutrons. Those protons that originate from a primary proton have a lower energy than the primary proton and typically contribute to the dose in the main radiation field, *e.g.,* in the entrance region of the Bragg curve (Paganetti, 2002). Secondary neutrons, however, can deposit dose at large distances from the target in the patient. They deposit most of their dose *via* protons generated in neutron-nucleus interactions. Thus, these protons can be produced anywhere in the human body.

The difference in neutron dose between scanned beams and passively scattered beams is mainly determined by the ratio of internal (generated in the patients) and external (generated in the treatment head) neutrons. This ratio depends heavily on the organ and its distance to the treatment target volume (Jiang *et al*., 2005). It was concluded that the ratio of neutron dose generated by treatment-head neutrons to patient-generated neutrons could be as much as one order of magnitude, which depends mainly on the design of the treatment head and on the field size (Jiang *et al*., 2005). Typically, neutron absorbed dose generated by neutrons from the treatment head dominates, which implies that proton beam scanning substantially reduces neutron dose to patients.

The neutron yield and the neutron dose due to neutrons generated in the patient depends on the range of the beam (Zheng *et al*., 2007). The greater the penetration of the beam, the greater is the overall likelihood of a nuclear interaction producing neutrons. In addition, the neutron yield depends on the irradiated volume simply because a bigger volume requires more primary protons in order to deposit the prescribed dose in the target. Thus, in contrast to external neutrons, internal neutron yields typically increase with increasing treatment volume.

The situation is far more complex in light-ion therapy than it is in proton therapy. With light-ion beams, the primary ions are fragmented due to nuclear inelastic collisions with the atomic nuclei in the tissue. This process results in beam-produced secondary ions and attenuation of the primary beam intensity. Also the target nuclei can undergo nuclear fragmentation that results in the production of secondary ions that are generally of low energies and a deposit local energy close to the ion track. Neutrons and secondary ions with atomic masses lower than that of the primary ions are produced, *e.g.*, hydrogen, helium, lithium, beryllium, boron, carbon. These lighter fragments can have longer ranges and wider energy distributions than the primary ions and give rise to a characteristic undesirable dose tail beyond the Bragg peak and broadening of the transverse dose profiles along the beam path.

In the same way as the incident particle, the beam-produced fragments will undergo elastic scattering with the target nuclei. Heavier beam fragments with atomic number $Z > 2$ generally scatter through small angles, whereas the scattering of lighter beam fragments of $Z \leq 2$ results in larger angle scattering which broadens the beam and contributes to the dose outside the treatment field. Fast beam-produced secondaries are focused mainly in the forward direction, but can also have a noticeable angular spread. Target-produced secondaries on the other hand, have a much wider angular distribution, but as they generally have low energies they are transported only short distances. Beam-produced fragments, especially neutrons and secondary protons, may possess high energies (Gudowska and Sobolevsky, 2005; Gunzert-Marx *et al.*, 2008; Porta *et al.*, 2008), causing dose deposition at larger distances outside the treated volume. Simultaneously, as they traverse the patient they undergo nuclear interactions with the tissue elements that result in the generation of high-energy secondaries, produced in the cascade of events.

7.2 Out of Treatment Field Absorbed Dose to Patients (Secondary Dose)

7.2.1 Experimental Methods

A variety of theoretical and experimental studies have been conducted to determine the distributions of secondary particles produced in water and tissue-equivalent materials when irradiated with ion beams at energies of therapeutic interest. These studies concern both the depth dependence and spatial distributions of the charged secondaries produced in the water, carbon, PMMA, and different tissue-equivalent phantoms, as well as the energy spectra of particles leaving the irradiated phantoms or the patient. A large fraction of the published data addresses the production of fast neutrons, neutron energy spectra, and neutron angular distributions by stopping ion beams of different energies in thick tissue-equivalent targets.

In addition, various groups from radiation therapy facilities have performed experiments to assess secondary doses. In proton therapy, measurements have been primarily concentrated on the use of Bonner spheres (Mesoloras *et al.*, 2006; Schneider *et al.*, 2002; Yan *et al.*, 2002). Thermoluminescence dosimetry has been applied as well (Francois *et al.*, 1988a; Reft *et al.*, 2006). CR-39 plastic nuclear track detectors were used in the studies by Schneider *et al.* (2002) and Moyers *et al*. (2008), whereas a bubble detector was used by Mesoloras *et al*. (2006). An improved neutron rem-counter, WENDI, was applied for neutron dose measurement in carbon beams in the energy range 100 to 250 MeV/u (Iwase *et al.*, 2007). Microdosimetric detector systems are very promising in terms of providing reliable dose estimates. Microdosimetric distributions of secondary neutrons produced by 290 MeV/nucleon carbon beams have been measured by using a tissue-equivalent proportional counter (Endo *et al.*, 2007). Silicon-based microdosimetry provided information on the depth and lateral distance dependence of the dose equivalent for a passively scattered proton beam (Wroe *et al.*, 2007; Wroe *et al.*, 2009). In other areas of radiation protection and radiation therapy, microdosimetric concepts have been shown to be powerful tools for relative comparisons of treatment field characteristics in terms of lineal energy (Hall *et al.*, 1978; Loncol *et al.*, 1994; Morstin and Olko, 1994; Paganetti *et al.*, 1997).

7.2.2 Calculation Methods (Monte Carlo Techniques)

Secondary doses, in particular neutron doses, are difficult to measure. Neutrons are indirectly ionizing and interact sparsely causing only low absorbed doses. Although this makes Monte Carlo methods very valuable, even Monte Carlo codes have considerable uncertainties when it comes to simulating secondary particle production because the underlying physics is not known with sufficient accuracy. Firstly, there is insufficient experimental data of inelastic nuclear cross sections in the energy region of interest in heavy charged particle radiation therapy. Secondly, neutron and secondary charged particle emissions from nuclear interactions can be the result of very complex interactions. There are uncertainties in the physics of pre-equilibrium and fragmentation as well as the intra-nuclear cascade mechanisms, the latter being based in parameterized models for Monte Carlo transport calculations. Several codes have been used to study low doses in radiation therapy, in particular neutron doses generated in proton and ion therapy. The Monte Carlo code MCNPX (Pelowitz, 2005) was used to assess neutron and photon doses in proton beams (Fontenot *et al.*, 2008; Moyers *et al.*, 2008; Perez-Andujar *et al.*, 2009; Polf and Newhauser, 2005; Taddei *et al.*, 2008; Zheng *et al.*, 2007; Zheng *et al.*, 2008). Further, FLUKA (Battistoni *et al.*, 2007; Ferrari *et al.*, 2005) and GEANT4 (Agostinelli *et al.*, 2003; Allison *et al.*, 2006) were applied to assess secondary doses in proton beams (in Agosteo *et al.*, (1998) and Jiang *et al.*, (2005), and Zacharatou Jarlskog *et al.*, (2008), respectively). Other codes used for ions are SHIELD-HIT (Dementyev and Sobolevsky, 1999; Gudowska *et al.*, 2004) and PHITS (Iwase *et al.*, 2002; Niita *et al.*, 2006). For light ion beams, studies of secondary neutron doses were done with FLUKA (Porta *et al.*, 2008), PHITS (Gunzert-Marx *et al.*, 2008; Iwase *et al.*, 2007), GEANT4 (Pshenichnov *et al.*, 2005), and SHIELD-HIT (Gudowska *et al.*, 2002; Gudowska *et al.*, 2004; Gudowska *et al.*, 2007; Gudowska and Sobolevsky, 2005; Iwase *et al.*, 2007). A review of Monte Carlo codes used in radiation protection is presented in Chapter 6 of this report.

In order to describe the radiation field incident on the patient, the treatment head needs to be simulated. Monte Carlo simulations of treatment heads have been extensively reported for protons (Newhauser *et al.*, 2005b; Paganetti, 1998; 2006; Paganetti *et al.*, 2004). The characterization of the beam entering the treatment head is typically based on parameterizations obtained from measurements (Cho *et al.*, 2005; Fix *et al.*, 2005; Janssen *et al.*, 2001; Keall *et al.*, 2003; Paganetti *et al.*, 2004).

Simulating secondary dose in the patient geometry can, in principle, be done in a similar fashion as calculating primary dose using Monte Carlo simulations (Paganetti *et al.*, 2008). The difference is that the quantity of interest is not the absorbed dose but the equivalent dose, which is a parameterization of radiation effects. Thus, calculations of the secondary equivalent doses to patients require particle and particle energy-dependent radiation weighting factors in order to consider the biological effectiveness (see section on equivalent dose below). There are different ways to determine equivalent doses using Monte Carlo simulations, as discussed by the ICRU (1998). One possible strategy is to calculate the average absorbed dose for the organ under consideration and scale the dose with an average radiation weighting factor. Another approach frequently used (Polf and Newhauser, 2005; Zheng *et al.*, 2007) is to calculate the particle fluences at the surface of a region of interest (organ) and then use energy dependent fluence-to-equivalent dose conversion coefficients (Alghamdi *et al.*, 2005; Boag, 1975; Bozkurt *et al.*, 2000; 2001; Chao *et al.*, 2001a; 2001b; Chen, 2006; NCRP, 1971). In this case, dose deposition events are not explicitly simulated. Using this method, Sato *et al.* (2009) have calculated organ-dose-equivalent conversion coefficients for neutron and proton monoenergetic beams in adult male and adult female reference phantoms using the PHITS code.

When dealing with neutrons, Monte Carlo simulations are typically quite time consuming (in order to achieve a reasonable statistical accuracy) when based on the dose actually deposited *via* neutrons. However, it is presumably more accurate to score each energy deposition event (*i.e.*, without using fluence-to-dose conversion). Fast neutrons lose most of their kinetic energy in the initial relatively small number of interactions. In the low/thermal energy region, there is a decreasing probability for neutrons to slow down and cause a large number of elastic scatterings in soft tissues, causing the neutron energy distributions in the patient to be dominated by low-energy neutrons (Jiang *et al.*, 2005).

An explicit simulation applying radiation weighting factors on a step-by-step basis considering particle type, particle history, and particle energy has been done to assess organ-specific neutron equivalent doses in proton-beam therapy (Zacharatou Jarlskog *et al.*, 2008). If a neutron was in the interaction history of the dose depositing particle, the dose deposition was considered to be due to a neutron and a neutron radiation weighting factor was then assigned. Similarly, if a proton from a proton chain deposited the absorbed dose, the dose depositions would be classified as proton induced. For each interaction chain history. a division into different groups was done depending on particle energy in order to apply energy-dependent quality factors.

Different dose-scoring methods were compared by Zacharatou Jarlskog and Paganetti (2008a). For neutron equivalent doses in proton beam therapy, it was found that using average weighting factors can underestimate the neutron equivalent dose in comparison to those calculated on a step-by-step basis. The difference was found to be around 25% depending on organ and field specifications.

In the approach applied by Pshenichnov *et al.* (2005) and Gudowska *et al.* (2007) the neutron absorbed doses delivered to tissue-equivalent phantoms by proton and carbon-ion beams were determined by two sets of calculations. First, Monte Carlo simulation was performed with the full hadronic cascade and transport of all secondary particles, whereas in the second simulation the secondary neutrons were produced at the point of interaction but excluded from further transport through the phantom. By comparison of the energy deposited in the phantom in these two calculations, the absorbed dose due to secondary neutrons was determined.

7.2.3 Human Phantoms

Measurements or simulations of secondary doses in simple geometries are useful in understanding the relative differences between treatment modalities or beam conditions. However, a more meaningful assessment has to be based on actual patient geometries. Because of the concern of excessive radiation with most imaging techniques, whole-body scans are rarely available. In order to perform Monte Carlo simulations considering organs not imaged for treatment planning, the use of computational phantoms is a valuable option.

Interestingly, these kinds of simulations could potentially provide dosimetric information to improve risk models based on long-term follow up of radiation therapy patients and the knowledge of the organ doses they received during the course of their treatment for the primary cancer.

The simpler the geometry, the faster a Monte Carlo simulation typically is. Consequently, simulations were based initially on stylized phantoms (Snyder *et al.*, 1969), including male and female adult versions (Kramer *et al.*, 1982; Stabin *et al.*, 1995). Cristy and Eckerman (1987) introduced a series of stylized pediatric and adult phantoms based on anthropological reference data (ICRP, 1975). Such phantoms are based on simple geometrical shapes, *e.g.*, an elliptical cylinder representing the arm, torso, and hips, a truncated elliptical cone representing the legs and feet, and an elliptical cylinder representing the head and neck. In terms of media, a distinction is drawn only between bone, soft tissue, and lung. Stylized models have been used for a variety of simulations for radiation protection, nuclear medicine, and medical imaging (ICRP, 1975; 1991; 1998; ICRU, 1992a; 1992b; NCRP, 1996). Work has been done on organ doses from medical exposures using stylized models (Stovall *et al.*, 1989; Stovall *et al.*, 2004) and to derive dose-response relationships for patients in epidemiological studies. Because human anatomy is much more complex than that modeled with stylized models, results based on such model calculations are controversial and uncertainties may be significant (Lim *et al.*, 1997; Ron, 1997). Simulated organ and marrow doses based on stylized models have not produced strong correlations with radiotoxicity (Lim *et al.*, 1997).

A more realistic representation of the human body can be achieved using voxel phantoms. Each voxel is identified in terms of tissue type (soft tissue, hard bone, *etc.*) and organ identification (lungs, skin, *etc.*) (Zaidi and Xu, 2007). Lee *et al.* (2006a) analyzed the differences between the use of stylized phantoms and the use of voxel phantoms and found dosimetric differences of up to 150% in some organs. Other similar studies showed differences in organ doses as high as 100% (Chao *et al.*, 2001a; Jones, 1998; Lee *et al.*, 2006a; Petoussi-Henss *et al.*, 2002). The discrepancies were explained by the geometrical considerations in the stylized phantom, *i.e.*, relative positions of organs and organ shapes.

Many different voxel phantoms have been created. One of the first was used to compute dose from dental radiography (Gibbs *et al.*, 1984). This was followed by developments of Zubal and Harell (1992) of a head-torso phantom used to estimate absorbed doses using Monte Carlo simulations (Stabin *et al.*, 1999). Kramer *et al*. (2003; 2006) developed male and female adult voxel models. Recently, a voxel-based adult male phantom was introduced with the aim of using it for Monte Carlo modeling of radiological dosimetry (Zhang *et al.*, 2008). Models of pregnant patients have been introduced (Shi and Xu, 2004; Shi *et al.*, 2004; Xu *et al.*, 2007). Realistic models of the pregnant patient representing three-, six-, and nine-month gestational stages were constructed by Bednarz and Xu (2008). The many different types and properties of voxel phantoms have been reviewed by Zaidi and Xu (2007).

A popular voxel phantom is the adult male model, VIP-Man (Xu *et al.*, 2000; 2005), developed from anatomical color images of the Visible Man from the Visible Human Project by the National Library of Medicine (Spitzer and Whitlock, 1998). Part of it is shown in Figure 7.1 and distinguishes adrenal glands, bladder, esophagus, gall bladder, stomach mucosa, heart muscle, kidneys, large intestine, liver, lungs, pancreas, prostate, skeletal components, skin, small intestine, spleen, stomach, testes, thymus, thyroid, gray matter, white matter, teeth, skull CSF, male breast, eye lenses, and red bone marrow (Spitzer and Whitlock, 1998; Xu *et al.*, 2000). It has a resolution of $0.33 \times 0.33 \times 1$ mm^3. The composition of VIP-Man tissues/materials was done according to ICRU specifications (ICRU, 1989).

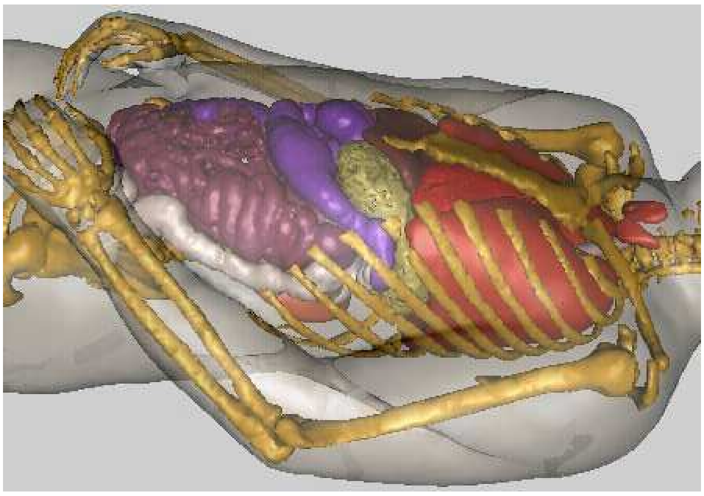

Figure 7.1. Torso of the whole-body adult male model, VIP-Man (Xu *et al.*, 2000), developed from anatomical color images of the Visible Man from the Visible Human Project by the National Library of Medicine (Spitzer and Whitlock, 1998).

It has been recognized that secondary doses in radiology and radiation therapy are of particular concern for pediatric patients. Thus, there was a need for pediatric studies (Francois *et al.*, 1988b). Quite a few pediatric phantoms have been designed (Caon *et al.*, 1999; Lee and Bolch, 2003; Nipper *et al.*, 2002; Staton *et al.*, 2003; Zankl *et al.*, 1988). Such phantoms cannot be generated by scaling an adult phantom because of the differences in relative organ position, relative organ sizes, and even organ composition as a function of a person's age. A series of five computational phantoms of different ages were constructed from CT images of live patients for use in medical dosimetry (Lee and Bolch, 2003; Lee *et al.*, 2005; Lee *et al.*, 2006b; Lee *et al.*, 2007a; Lee *et al.*, 2007b; Lee *et al.*, 2008). The phantoms approximate the bodies of a 9-month-old, 4-year-old, 8-year-old, 11-year-old, and 14-year-old child with resolutions between $0.43 \times 0.43 \times 3.0$ mm^3 and $0.625 \times 0.625 \times 6.0$ mm^3. Age-interpolated reference body masses, body heights, sitting heights, and internal organ masses as well as changes in geometry and material composition as a function of age and gender were assigned according to ICRP references (2003a). For the lungs, effective densities were assigned so that the total lung mass would match its interpolated reference mass (inclusive of pulmonary blood). Later, a newborn phantom was added to this series (Nipper *et al.*, 2002). Initially these phantoms did not have arms and legs. Extremities are relevant when computing doses for risk estimations because of their active bone marrow. Thus, a set of truly whole-body voxel phantoms of pediatric patients were developed through the attachment of arms and legs (Lee *et al.*, 2006b).

Comparative organ dosimetry between stylized and tomographic pediatric phantoms proved that stylized phantoms are inadequate for secondary dose estimations (Lee *et al.*, 2005). Here, a series of photon beams were used to 'irradiate' a stylized 10-year-old child phantom, a stylized 15-year-old child phantom, and a more realistic 11-year-old male child phantom within MCNPX. For example, dose coefficients for the thyroid were significantly lower in the UF 11-year-old child phantom, particularly under the lateral irradiation geometries, than seen in the stylized model.

Voxel phantoms are largely based on CT images and manually segmented organ contours. Uncertainties are introduced because of image noise and because some representations of mobile organs may be blurred. Further, in order to match a particular patient as closely as possible, one might have to interpolate between two different phantoms of a specific age. Organ dimensions can only be modified by changing the voxel resolution, which generally limits the modification to uniform scaling. Creating a non-50th percentile individual from a reference 50th-percentile cannot be done realistically for a number of reasons (for example, because of the difference in the distribution of subcutaneous fat).

To overcome these limitations, voxel data can be combined with surface equations to design hybrid models. In these phantoms, the boundary of each organ can be adjusted to the desired shape and volume using patient-specific images and deformable image registration. A series of reference (*i.e.*, 50th height/weight percentile) pediatric hybrid phantoms based on NURBS (non-uniform B-spline fits;see Piegl, 1991) surfaces has been developed (Lee *et al.*, 2007a). A similar hybrid approach to phantom construction has been made in nuclear imaging (Tsui *et al.*, 1994). Segars *et al.* (Garrity *et al.*, 2003; Segars *et al.*, 1999; Segars, 2001) developed the 4D NURBS-based Cardiac-Torso model that is used as a deformable model to simulate SPECT images and respiratory motion (Segars and Tsui, 2002). Initially, phantoms have been used in combination with analytical dose models. Diallo *et al.* (1996) estimated the dose to areas volumes outside the target volume using a whole-body phantom. However, Monte Carlo methods are typically the method of choice. In order to use whole-body computational voxel phantoms with Monte Carlo codes, these either have to be able to handle voxelized geometries, *i.e.*, a large amount of individual voxels, or to incorporate contoured organ shapes *via* surface equations.

For dose calculations involving real patient data, the information stored for each CT voxel is a Hounsfield number, which reflects the attenuation coefficient of tissues to diagnostic x rays. In contrast, for phantom simulations each voxel is usually tagged with a specific material composition and density. Many of the phantoms listed above have been implemented in Monte Carlo codes. Using Monte Carlo simulations, two mathematical models of a patient were used to assess the clinical relevance of computational phantoms (Rijkee *et al.*, 2006). The VIP-Man was implemented in four Monte Carlo codes: EGS4 (Chao *et al.*, 2001a; 2001b; Chao and Xu, 2001), MCNP (Bozkurt *et al.*, 2000), MCNPX (Bozkurt *et al.*, 2001), and GEANT4 (Jiang *et al.*, 2005; Zacharatou Jarlskog *et al.*, 2008), to calculate organ doses for internal electrons (Chao and Xu, 2001), external photons (Chao *et al.*, 2001a), external electrons (Chao *et al.*, 2001b), external neutrons (Bozkurt *et al.*, 2000; 2001), and external protons (Jiang *et al.*, 2005; Zacharatou Jarlskog *et al.*, 2008). Pediatric voxel models have been used within GEANT4 to assess organ-specific doses in proton therapy (Zacharatou Jarlskog *et al.*, 2008). Xu *et al.* (2007) implemented a pregnant female model based on voxelization of a boundary representation in the Monte Carlo codes EGS4 and MCNPX. The same group then implemented anatomically realistic models of the pregnant patient representing three-, six-, and nine-month gestational stages into MCNPX (Bednarz and Xu, 2008). Further, studies involving parts of a patient's geometry have been done using phantoms, *e.g.*, with a high-resolution eye model (Alghamdi *et al.*, 2007).

7.3 Results of Measurements of Secondary Doses in Particle Therapy

Secondary radiation from therapeutic proton beams has been measured by several groups (see *e.g.*, Agosteo *et al.*, 1998; Binns and Hough, 1997; Mesoloras *et al.*, 2006; Newhauser *et al.*, 2005b; Polf and Newhauser, 2005; Roy and Sandison, 2004; Schneider *et al.*, 2002; Tayama *et al.*, 2006; Wroe *et al.*, 2007; Yan *et al.*, 2002). The secondary dose due to neutrons, protons, and photons was studied by Agosteo *et al.* (1998). The dose due to secondary and scattered photons and neutrons varied from 0.07 to

0.15 milligray per treatment gray (mGy/Gy) at different depths and distances to the field edge. Secondary doses for proton beam delivery using passive scattered beams of 160 MeV and 200 MeV were measured by Yan *et al.* (2002) and Binns and Hough (1997), respectively. Neutron equivalent doses of up to 15 millisievert per treatment gray (mSv/Gy) were deduced. Polf and Newhauser (2005) studied the neutron dose in a passive-scattering delivery system. The neutron dose decreased from 6.3 to 0.6 mSv/Gy with increasing distance to isocenter and increased as the range modulation increased. Tayama *et al.* (2006) measured neutron equivalent doses up to 2 mSv/Gy outside of the field in a 200 MeV proton beam.

Measurements were also done using anthropomorphic phantoms and microdosimetric detectors (Wroe *et al.*, 2007). Equivalent doses from 3.9 to 0.18 mSv/Gy were measured when moving from 2.5 cm to 60 cm distance from the field edge. The dose and dose equivalent delivered to a large phantom patient outside a primary proton field were determined experimentally using silver halide film, ionization chambers, rem meters, and CR-39 plastic nuclear track detectors by Moyers *et al.* (2008). The purpose of another investigation using etch-track detectors was to measure the impact of Ti-alloy prostheses on the neutron dose during proton and photon radiotherapy (Schneider *et al.*, 2004). Roy and Sandison (2004) irradiated an anthropomorphic phantom and found secondary neutron doses between 0.1 and 0.26 mSv/Gy for a passive-scattering system with a beam energy of 198 MeV. Secondary neutron dose equivalent decreased rapidly with lateral distance from the field edge. Subsequently, a systematic study on secondary neutron dose equivalent using anthropomorphic phantoms was done (Mesoloras *et al.*, 2006). The neutron dose decreased with increasing aperture size and air gap, implying that the brass collimator contributes significantly to the neutron dose. The contribution by neutrons generated in the patient increased with field size. Due to the reduced area available for interaction with the patient collimator, as aperture size increases, externally generated neutrons decrease with field size. The neutron dose varied from 0.03 to 0.87 mSv/Gy for large fields.

The results from all these studies vary significantly with details of the beam-delivery system and because the neutron doses decrease rapidly with lateral distance from the proton field, making them heavily dependent on the precise point of measurement. For a scanning system, measurements of the secondary neutron dose were performed using a Bonner sphere and CR39 etch detectors by Schneider *et al.* (2002). The measured neutron equivalent doses varied between 2 and 5 mSv/Gy for target volumes of 211 cm^3 (sacral chordoma) and 1253 cm^3 (rhabdomyosarcoma), respectively, and 0.002 to 8 mSv/Gy for lateral distances of 100 cm to 7 cm from the isocenter. In the region of the Bragg peak, the neutron equivalent dose for a medium-sized target volume reached ~ 1 % of the treatment dose. They concluded that a beam line using the passive-scattering technique shows at least a ten-fold secondary neutron dose disadvantage as compared with the spot-scanning technique.

Using Bonner spheres for measurements in carbon as well as in proton beams, it was found that the neutron ambient dose equivalent in passive-particle radiotherapy is equal to or less than that in photon radiotherapy with 6 MV beams (Yonai *et al.*, 2008). Microdosimetric data have been obtained in carbon beams as well (Endo *et al.*, 2007). Downstream of the Bragg peak, the ratio of the neutron dose to the carbon dose at the Bragg peak was found to be $< 1.4 \times 10^{-4}$ and the ratio of neutron dose to the carbon dose was $< 3.0 \times 10^{-7}$ on a lateral face of a phantom. The neutron contamination in therapeutic ^{12}C beams has been studied experimentally (Gunzert-Marx *et al.*, 2004; Gunzert-Marx *et al.*, 2008; Iwase *et al.*, 2007; Schardt *et al.*, 2006). The yield, energy spectra, and angular distribution of fast neutrons and secondary charged particles were measured for 200 MeV/u carbon ions impinging on a water-equivalent phantom (Gunzert-Marx *et al.*, 2004; Gunzert-Marx *et al.*, 2008). It was found that the neutrons were mainly emitted in the forward direction. The reported neutron dose of 8 mGy per treatment Gy was less than 1 % of the treatment dose, whereas the absorbed dose due to secondary charged particles was about 94 mGy per treatment Gy. From the resulting yield of 0.54 neutrons with energies above 20 MeV per primary ion, a neutron dose of 5.4 mSv per treatment gray equivalent (GyE) delivered to the target was estimated. Schardt *et al.* (2006) compared neutron doses in proton and carbon-ion therapy using beam scanning techniques. The secondary neutron absorbed doses per treatment dose were found to be similar. Although the cross sections for neutron production are much higher for therapeutic carbon- ion beams compared to proton beams, the neutron absorbed dose is expected to be similar (albeit with a different neutron energy distribution). Due to the higher LET of carbon ions, fewer particles are needed to deliver the same target dose compared to protons, approximately compensating for the higher neutron production per primary particle.

Other than in proton therapy, the depth-dose curves of light-ion beams show a fragmentation tail beyond the Bragg peak (Matsufuji *et al.*, 2003; Schimmerling *et al.*, 1989). Neutron production by fragmentation of light ions in water and graphite was investigated by Cecil *et al.* (1980) and by Kurosawa *et al.* (1999), respectively. Using ^{12}C beams of 200 and 400 MeV/u kinetic energy, the production of secondary fragments from nuclear reactions in water was investigated at GSI, Darmstadt, Germany (Gunzert-Marx *et al.*, 2004; Gunzert-Marx *et al.*, 2008; Haettner *et al.*, 2006). Fast neutrons and energetic charged particles (p-, d-, t-, α-particles) emitted in forward direction were detected by a BaF2/plastic scintillation-detector telescope and neutron energy spectra were recorded using time-of-flight techniques.

7.4 Results for Calculated Secondary Doses to Patients

Monte Carlo simulations have been used in several studies of secondary doses. Agosteo *et al.* (1998) analyzed the neutron dose for a passive-beam delivery system with a beam energy of 65 MeV. The absorbed dose due to neutrons varied between 3.7×10^{-7} and 1.1×10^{-4} Gy per treatment Gy depending on the distance from the field. For a high-energy proton beam, the secondary dose due to photons and neutrons varied from 0.146 to 7.1×10^{-2} mGy per treatment Gy for depths ranging from 1 to

8 cm and distances to the field edge ranging from 9 to 15 cm. Polf and Newhauser (2005) found in their MCNPX calculations that the neutron dose decreased from 6.3 to 0.63 mSv/Gy as the distance from the field center was increased from 50 to 150 cm. In a subsequent study this group has reported equivalent doses up to 20 mSv/Gy (Zheng *et al.*, 2007). The dose increased as the modulation extent was increased. The neutron dose equivalent per therapeutic proton absorbed dose was estimated for passively spread treatment fields using Monte Carlo simulations by Polf *et al*. (2005). For a beam with 16 cm range and a 5×5 cm^2 field size, the results show an equivalent dose of 0.35 mSv/Gy at 100 cm from the isocenter. Further, Monte Carlo calculations for a passive-scattering proton therapy treatment nozzle were done for various settings of the range modulator wheel (Polf and Newhauser, 2005). Zheng *et al*. (2007) also analyzed secondary radiation for a passive-scattering proton therapy system using Monte Carlo simulations. The whole-body effective dose from secondary radiation was estimated for a passively scattered proton treatment beam incident on an anthropomorphic phantom (Taddei *et al.*, 2008). The results show a dose equivalent of 567 mSv, of which 320 mSv was attributed to leakage from the treatment head. Using the MCNPX code it was shown that the range modulation wheel is the most intense neutron source of any of the beam-modifying devices within the treatment head (Perez-Andujar *et al.*, 2009). Simulations by Moyers *et al.* (2008) illustrated that most of the neutrons entering the patient are produced in the final patient-specific aperture and pre-collimator just upstream of the aperture, not in the scattering system. Additionally, Monte Carlo simulations were performed using the FLUKA code for a 177 MeV scanned proton beam by Schneider *et al*. (2002). For the proton-beam scanning system, neutron equivalent doses between 2 and 5 mSv/Gy were measured for target volumes of 211 cm^3 (sacral chordoma) and 1253 cm^3 (rhabdomyosarcoma), respectively, and 0.002 to 8 mSv/Gy for lateral distances of 100 cm to 7 cm from the isocenter (Schneider *et al.*, 2002).

Secondary particle production in tissue-like and shielding materials for light and heavy ions was done using the Monte Carlo code SHIELD-HIT (Gudowska *et al.*, 2002; Gudowska *et al.*, 2004). For ion beams, simulations of secondary particle production and absorbed dose to tissue were done by Gudowska and Sobolevsky (Gudowska *et al.*, 2007; Gudowska and Sobolevsky, 2005). For a 200 MeV proton beam, these authors reported the neutron absorbed dose delivered to the water and A-150 phantoms of about 0.6 % and 0.65 % of the total dose, respectively. The calculated absorbed dose due to secondary neutrons produced by a 390 MeV/u ^{12}C beam in the water and A-150 phantoms were 1.0% and 1.2% of the total dose, respectively.

Further, simulations using a Monte Carlo model for light-ion therapy (MCHIT) based on the GEANT4 toolkit were done by Pchenichnov *et al*. (2005). The energy deposition due to secondary neutrons produced by ^{12}C beams in water was estimated to be 1 % to 2 % of the total dose, *i.e.*, slightly above the neutron contribution (~ 1 %) induced by a 200 MeV proton beam. Morone *et al*. (2008) studied the neutron contamination in an energy modulated carbon-ion beam using the FLUKA Monte Carlo.

The mathematical anthropomorphic phantoms EVA-HIT and ADAM-HIT have been used in the Monte Carlo code SHIELD-HIT07 for simulations of lung and prostate tumors irradiated with light ions (Hultqvist and Gudowska, 2008). Calculations were performed for ^{1}H, ^{7}Li, and ^{12}C beams in the energy range 80 to 330 MeV/u. The secondary doses to organs due to scattered primary ions and secondary particles produced in the phantoms were studied, taking into account the contribution from secondary neutrons, secondary protons, pions, and heavier fragments from helium to calcium. The calculated doses to organs per dose to target (tumor) were of the order of 10^{-6} to 10^{-1} mGy/Gy and generally decrease with increasing distance from the target.

Figure 7.2 summarizes some of the experimental and theoretical results of neutron doses as a function of lateral distance from the field edge for various proton-beam facilities and beam parameters.

These data share a very similar trend although the values show significant variations associated with different beams and field parameters.

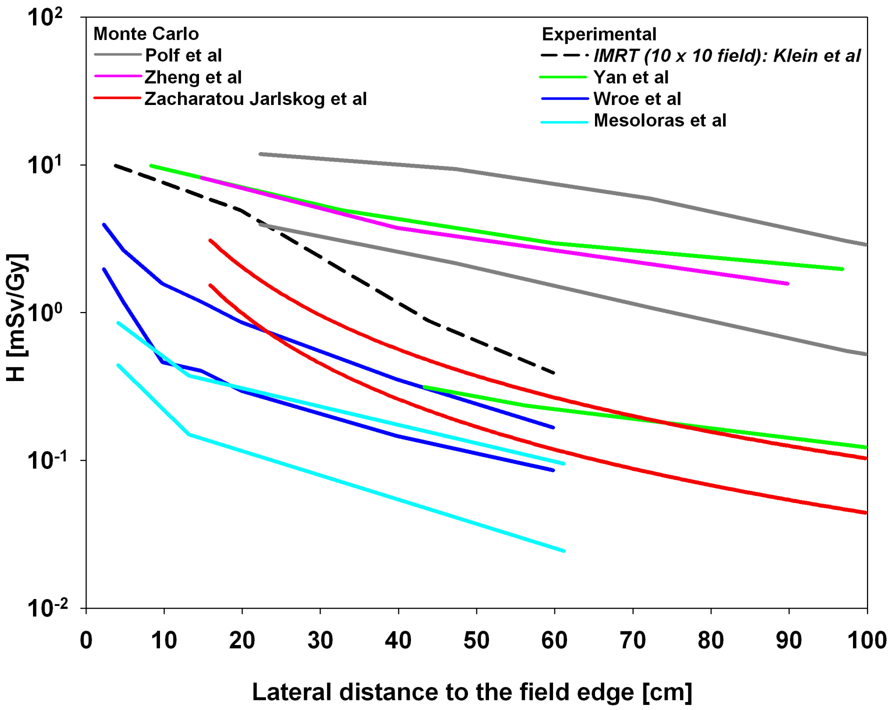

Figure 7.2. Equivalent doses as a function of distance to the field edge for therapeutic proton beams using passive-scattering techniques. Shown are data from experiments (Mesoloras *et al.*, 2006; Wroe *et al.*, 2007; Yan *et al.*, 2002) and calculations (Polf and Newhauser, 2005; Zacharatou Jarlskog and Paganetti, 2008a; Zheng *et al.*, 2007). In most cases, several beam parameters were considered and we plot two curves, the maximum and minimum findings. Also shown is the scattered photon dose for an intensity-modulated x-radiation therapy (IMRT) case assuming a 10 cm × 10 cm field (Klein *et al.*, 2006).

While the data shown in Figure 7.2 help to understand differences among different beam-delivery conditions, epidemiological studies require the use of organ-specific doses for proper risk analysis. To this end, a number of recent studies have used whole-body patient phantoms and Monte Carlo simulations to calculate organ doses for different proton treatment conditions.

Organ doses out of the target (tumor) volume in the whole-body VIP-Man model for proton therapy treatments have been studied by Jiang *et al.* (2005) assuming treatments of a tumor in the head and neck region and a tumor in the lung. The simulations were based on the GEANT4 Monte Carlo code. The treatment head simulation incorporated the different settings (combinations of scatterers, variable jaws, *etc.*) necessary to simulate hardware configurations for each treatment field. The average neutron dose equivalent for organs of the abdomen region was 1.9 and 0.2 mSv/Gy for a lung tumor and paranasal sinus treatment plans, respectively. The dose in the red bone marrow was found to be 3 to 4 orders of magnitude lower than the prescribed dose to the tumor volume. However, the dose distribution is highly non-uniform. The yield, the quality factors, and the absorbed doses from neutrons produced internally in the patient's body and externally in the treatment nozzle were analyzed for each organ. Internal neutrons include the neutrons produced in the patient *via* interactions of primary protons and the later generation of neutrons originating from them. In contrast, external neutrons are those generated in the treatment nozzle and also the next generation of neutrons generated by them in the patient. Jiang *et al.* (2005) reported, for internal and external neutrons, the equivalent doses for individual organs. The simulations confirmed that the externally produced neutrons dominate the secondary neutron dose.

Using a Monte Carlo model of a proton therapy treatment head and a computerized anthropomorphic phantom, Fontenot *et al.* (2008) determined that the effective dose from secondary radiation per therapeutic dose for a typical prostate patient was ~ 5.5 mSv/Gy. The secondary dose decreased with distance from the isocenter, with a maximum of 12 mSv/Gy for the bladder. The specific aim of the study by Taddei *et al*. (2009) was to simulate secondary doses to organs following cranio-spinal irradiation with proton therapy. A passive-scattering proton treatment unit was simulated using Monte Carlo simulations methods and a voxelized phantom to represented the pediatric patient. For a treatment using delivering 30.6 Gy to the target plus a boost of 23.4 Gy, the predicted effective dose from secondary radiation was 418 mSv, of which 344 mSv were from neutrons originating outside the patient. Monte Carlo simulations of secondary radiation for passively scattered and scanned-beam proton irradiation of cranio-spinal lesions were also done using a male phantom (Newhauser *et al.*, 2009). Zacharatou Jarlskog *et al.* (2008) simulated proton beam therapy for pediatric patients and considered several proton fields of varying field size, beam range and modulation width for the treatment of tumors in the intracranial region. To simulate age- and organ-specific equivalent doses, one adult phantom and five pediatric phantoms (a 9-month old, a 4-year old, an 8-year old, an 11-year old, and a 14-year old) were considered. Organ doses were presented as a function of organ index for up to 48 different organs and structures. The organ-specific neutron equivalent doses varied as a function of field parameters. Further, variations in dose between different organs was caused by differences in volume, in their distance to the target, and in their elemental composition. For example, a greater range in tissue requires a higher beam energy and thus more material (tissue) is needed to reduce the penetration of the proton beam. Consequently, simulations based on the voxel phantom of a 4-year-old resulted in neutron equivalent doses of about 1.3 mSv/Gy in the lungs for short-range fields and about 2.7 mSv/Gy for long-range fields. Neutron equivalent doses to organs increased with treatment volume because the number of protons necessary to deposit the prescription dose in the target had to increase. The neutron equivalent dose due to external neutrons typically increases with decreasing field size (Gottschalk, 2006; Paganetti *et al.*, 2006). It was found that for a small target volume, the contribution of neutrons from the treatment head can be close to 99 % of the total neutron contribution, while for a large target volume it can go down to ~ 60 %. The neutron equivalent dose was as high as 10 mSv/Gy in organs located near the target but decreased rapidly with distance (Zacharatou Jarlskog *et al.*, 2008). Figure 7.3 shows how the thyroid, esophagus and liver equivalent doses vary significantly with patient age (Zacharatou Jarlskog *et al.*, 2008). Younger patients are exposed to a higher neutron contribution from the treatment head because of their smaller bodies. With increasing distance from the target, doses vary more significantly with patient age. For example, simulation based on the phantom of a 9-month old showed ~ 50 % higher dose to the thyroid compared to simulations based on an adult phantom. In the case of esophagus, the ratio of the dose to the phantoms of the adult to the 9-month old child was roughly a factor of 4. Simulations showed that the maximum neutron equivalent dose delivered to an organ was ~ 10 mSv/Gy (Zacharatou Jarlskog *et al.*, 2008). Organs at larger distances from the target will show higher dependency on the patient age; *e.g.*, for the same field, the factor of dose increase for liver is approximately 20.

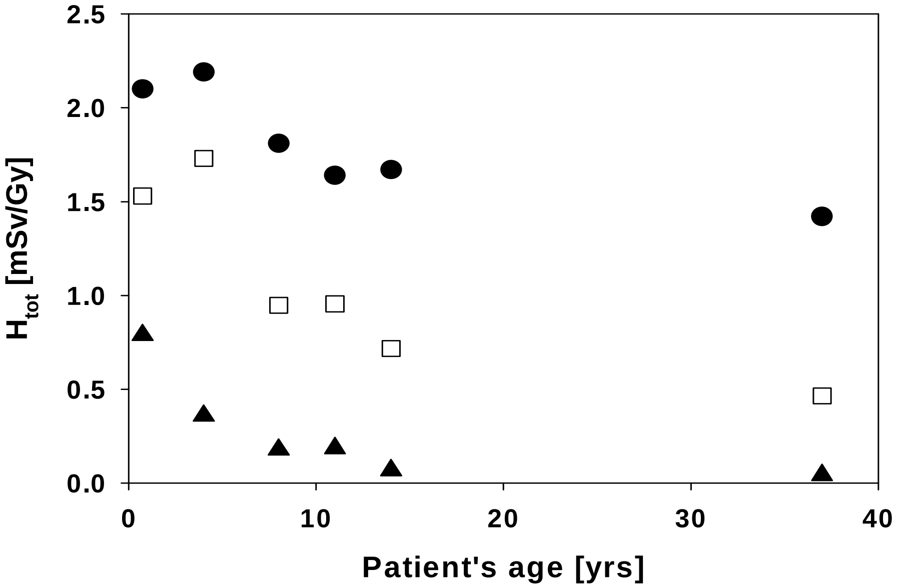

Figure 7.3. Organ equivalent dose in the thyroid (circles), esophagus (squares) and liver (triangles) as a function of patient age averaged over six different cranial treatment fields. (Zacharatou Jarlskog *et al.*, 2008)

Table 7.1 shows, averaged over eight proton therapy fields used in the head and neck region (Zacharatou Jarlskog *et al.*, 2008), how the equivalent doses compare with doses from chest CT scans. Apparently, for young patients it could correspond to on average of about 25 additional CT scans for the fields considered. A similar analysis was done by Moyers *et al.* (2008). In their study, the total dose equivalent outside of the field was similar to that received by patients undergoing IMRT. At the center of a patient, the dose equivalent for a full course of treatment was comparable to that delivered by a single whole-body CT scan.

Table 7.1. Equivalent doses (in mSv) for thyroid and lung due to secondary neutron radiation for a 70 Gy treatment of a brain lesion (averaged over eight treatment fields). The values are compared to the radiation to be expected from a chest CT scan as a function of patient's age. (Zacharatou Jarlskog *et al.*, 2008)

	4-year old	11-year old	14-year old	Average
H to thyroid from proton therapy	195.4	166.0	155.1	
H to thyroid from chest CT scan	9.0	5.2	6.9	
Therapy / CT scan (thyroid)	21.6	31.8	22.4	25.3
H to lung from proton therapy	128.2	54.7	34.7	
H to lung from chest CT scan	13.9	12.0	12.6	
Therapy / CT scan (lung)	9.3	4.5	2.8	5.5

In order to apply the appropriate energy-dependent radiation weighting factor for neutrons, the energy of the neutrons causing dose deposition in organs needs to be determined. Figure 7.4 shows the energy distribution of neutrons at the surface of several organs (Jiang *et al.*, 2005). Fast neutrons lose most of their kinetic energy in the initial relatively small number of scatterings. In the low/thermal energy region, there is a decreasing probability for neutrons to slow down, causing a large number of elastic scatterings in soft tissues with a prevailing field of low-energy neutrons in the patient. However, the dose deposition events (and thus the determination of the radiation weighting factor) are mainly due to higher energy neutrons (> 10 MeV). Zheng *et al.* (2008) calculated the neutron spectral fluence using Monte Carlo simulations

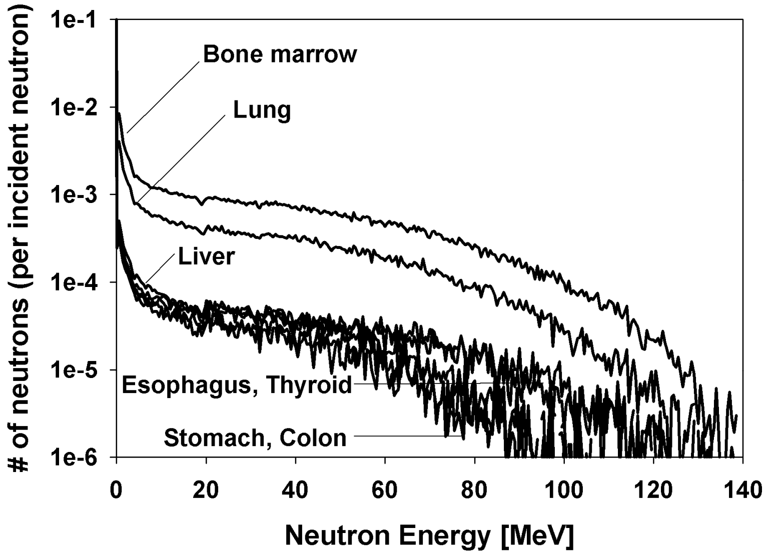

Figure 7.4. Energy distribution of external neutrons (per incident neutron entering the patient) arriving at the outer surface of some major organs lateral to the field edge under a head and neck tumor plan. (Jiang *et al.*, 2005)

7.5 Biological Effects of Secondary Particles (Low- and High-LET Particles, Low Doses)

The radiation quality of particles is often classified by their linear energy transfer (LET). Although there is not a direct relationship between LET and biological effect, higher linear energy transfer radiations in most situations cause more severe damage to tissue. The parameter often used to compare the biological effect of different radiations in radiation therapy is the relative biological effectiveness (RBE). The RBE is defined as the ratio of the doses required by two different types of radiation to cause the same level of effect for a specified end point. The RBE depends on dose, dose rate, overall treatment time, fractionation, tissue, and endpoint. It is only defined with respect to a reference radiation. To understand the effect of scattered or secondary radiation in ion therapy one has to examine low-dose radiation effects. Because the RBE is defined for a given level of effect and increases with decreasing dose (neglecting the potential effect of low-dose hypersensitivity and threshold effects), one has to consider RBE_{max}, *i.e.*, the RBE extrapolated to the zero dose level on the survival curves for a specified radiation such as neutrons and the reference radiation.

The dose deposited by secondary neutron radiation is typically quite low. While it may be straightforward with simple laboratory cell systems to extrapolate high- or medium-level dose-response data to low doses, it is very difficult to extrapolate to low doses with complex systems. This is due to competing effects influencing in particular the low dose region. The biological effectiveness of radiation depends on many different physical factors (*e.g.*, dose, dose rate, track structure) and biological factors (*e.g.*, tissue type, endpoint, repair capacity, and intrinsic radiosensitivity).

The biological effect of neutrons is a complex matter because neutrons are indirectly ionizing. At very low energies (below 1 MeV) neutrons contribute to absorbed dose by elastic scattering processes (protons); by protons produced in neutron capture in nitrogen; by recoil of carbon, oxygen, nitrogen atoms; and partly by γ-rays from thermal neutron capture processes in hydrogen. For higher energy neutrons (around 1 to 20 MeV) a substantial amount of dose is deposited *via* recoil protons.

To assess the risk of developing a second tumor from radiation therapy, the parameter of interest is fractionated low-dose delivery leading to carcinogenesis. Such data are sparse, in particular at doses below 0.1 Gy. Furthermore, the data on carcinogenesis in animal models based on fission neutrons reveal that the dose-response relationship is non-linear (except for the initial portion), making extrapolation to low doses very difficult and unreliable. As discussed by Edwards (1999), it is very difficult, and associated with big uncertainties, to fit the correct initial slopes to neutron and reference radiations because of the significant experimental uncertainties.

The vast majority of data on neutron RBE has been obtained using fission neutrons. Fission neutrons typically have energies between (on average) 1 and 1.5 MeV. It has been shown (Shellabarger *et al.*, 1980) that even single doses of 1 mGy of 0.43 MeV neutrons have the potential to increase the tumor induction rate for fibroadenomas in rats. Broerse *et al.* (1986) have shown for the incidence of benign mammary tumors in rats that 0.5 MeV neutrons are significantly more effective than 15 MeV neutrons. Others have studied this as well (Fry, 1981). Because of the lack of high-energy neutron carcinogenesis data, extrapolations have been made of the energy dependence of the measured neutron (RBE_{max}) values up to much higher neutron energies (ICRP, 1991; 2003b; 2008; ICRU, 1986; NCRP, 1990; 1991).

Based on the human data from neutron dose estimates to Japanese atomic bomb survivors (Egbert *et al.*, 2007; Nolte *et al.*, 2006), two independent groups have estimated the most likely RBE_{max} for neutron-induced carcinogenesis in humans to be 100 for solid-cancer mortality (Kellerer *et al.*, 2006) and

63 for overall cancer incidence (Little, 1997), respectively. The radiation field to which the atomic bomb survivors were exposed is of course much different from the conditions in radiation therapy.

As has been discussed, for example, in the review by Kocher *et al*. (2005) and by Brenner and Hall (2008b), considerable uncertainties exist for neutron RBE values because of the paucity of data on RBEs at energies outside the range of about 0.1 to 2 MeV; *i.e.*, the energies of most fission neutrons. Reviews by the NCRP (1990) and Edwards (1999) did not include data for neutrons above 20 MeV.

7.6 Concept of Equivalent Dose to Patient Due to Secondary Particles

7.6.1 Radiation Weighting Factors

In the low-dose region of secondary radiation, the use of the term "radiation weighting factor" instead of RBE emphasizes the fact that the quality or weighting factor is typically not endpoint- or dose-dependent. The radiation weighting factor superseded the quantity "quality factor" (ICRP, 1991). The conservative radiation weighting factors (w_R) as defined, for example, by the ICRP (2003b; 2008), can be associated with RBE_{max}. Thus, for radiation protection involving relatively low dose levels, the radiation weighting factor is defined as a conservative and simplified measure of the RBE. For radiation protection purposes one is interested in defining a parameter that is largely independent of dose and biological endpoint (*e.g.*, a maximum RBE). There are three main reasons for this: first, dose levels of interest in radiation protection are typically low; second, recommendations for the general public should be easy to understand; and third, a radiation protection recommendation does not aim at accuracy but provides a conservative guideline.

For γ rays, fast electrons, and x rays, a radiation weighting factor of 1 can be assumed (ICRP, 1991) (although there is evidence based on chromosomal aberration data and on biophysical considerations that, at low doses, the biological effectiveness per unit absorbed dose of standard x rays may be about twice that of high-energy photons). The ICRP recommends for photons and electrons a radiation weighting factor of 1, for protons a weighting factor of 2, and for alpha particles a weighting factor of 20 (ICRP, 2008).

For neutrons, the ICRP defines an energy dependent bell-shaped curve with a maximum weighting factor of 20 at around 1 MeV (ICRP, 1991; 2003b; 2008). Ambiguities in weighting factor assignments exist for uncharged particles. For example, fast neutrons deposit their energy mostly *via* secondary protons. Nevertheless, the maximum radiation weighting factor recommendation for neutrons is 20, while the factor for protons has a constant value of 2.

One has to keep in mind that radiation weighting was recommended for radioprotection purposes and the applicability to secondary radiation produced in the patient is questionable. The weighting factors are given for external radiation and could be applied to the secondary radiation produced in the beam-line components. However, the secondary radiation produced in the patient can be regarded as an internal radiation source and the use of weighting factors in this case is problematic. The quality factor is defined as a function of the unrestricted linear energy transfer, whereas the radiation weighting factor is defined as a function of particle and particle energy. Both concepts should result in similar outcomes. However, in particular for indirectly ionizing radiation like neutrons, some inconsistencies exist with these concepts as was discussed in section 7.2.2.

7.6.2 Equivalent Dose

The ICRP also defines a radiation protection quantity, equivalent dose, as the average absorbed dose in an organ or tissue multiplied by the radiation weighting factor for the type, and sometimes the energy, of the radiation (ICRP, 2003b). The radiation weighting factor converts the absorbed dose in gray (Gy) to sievert (Sv). Another radiation protection quantity is “effective dose” which normalizes partial-body exposures in terms of whole-body stochastic risk (ICRP, 2003b). The ICRP developed the concept of effective dose in order to recommend an occupational dose limit for radiation protection. However, effective dose is not measurable or additive, and it depends on the so-called tissue weighting factors that are subject to revision. The ICRP has stated that, for situations involving high doses, doses should be evaluated in terms of absorbed dose and, where high-LET radiations (*e.g.*, neutrons or alpha particles) are involved, an absorbed dose weighted with an appropriate RBE should be used. Further, the ICRP (1991) states that the effective dose concept should not be used to indicate risk for specific individuals.

When estimating equivalent doses under various conditions, *e.g.*, in the case of a patient treated with radiation therapy, the dose rate (fractionation) has to be taken into account. Radiation therapy is typically delivered in multiple fractions, *e.g.*, on 30 consecutive days (typically excluding weekends). Most risk models are valid for a single irradiation. The difference in effect between a single fraction and a multiple fraction irradiation with the same dose is due to the difference in repair capacity of the tissues. In order to account for this effect, a dose and dose-rate effectiveness factor (DDREF) has to be applied. DDREF is 1 for neutrons due to their high LET nature (Kocher *et al.*, 2005). DDREF is applied for doses below 0.2 Gy and for chronic exposure. The Biological Effects of Ionizing Radiation (BEIR) committee (BEIR, 2006) recommends the use of an average correction factor of 1.5 to take into account fractionation when using dosimetric data for risk analysis for solid tumors and linear dose-response relationships. While this is appropriate for photon radiation, equivalent doses from high-LET radiation, like neutrons, should not be scaled using DDREF when dealing with low dose exposure because of the different biological mechanisms with which neutrons interact with tissues (Kocher *et al.*, 2005). There can even be an inverse dose-rate effect describing a situation where the biological effectiveness of high-LET radiation increases with decreasing dose rate. However, this effect is typically not seen at lower doses.

7.7 Early and Late Effects

Volumes in the patient receiving dose can be separated into three regions: 1) the target (tumor), characterized by the planning target volume (PTV) treated with the therapeutic dose; 2) organs at risk typically defined in the tumor vicinity (these may intersect with the beam path and are allowed to receive low to intermediate doses); and 3) the rest of the patient body, which may receive low doses.

Dose delivered to healthy tissues can lead to severe side effects, *e.g.*, affecting the functionality of organs (see *e.g.*, Nishimura *et al.*, 2003) or even causing a second cancer. In the tumor and along the path of the therapeutic radiation beam, one may have to accept a risk for developing even significant side effects because of the therapeutic benefit. A significant number of second tumors is found in the margins of the target volume (Dorr and Herrmann, 2002). Such effects are not necessarily proportional to dose. For example, if the dose is prescribed with the aim of killing tumor cells without leaving behind cells with the potential for mutation, the risk of radiation-induced cancer within the target volume might be smaller than the risk in the surrounding tissues receiving intermediate doses.

Organs that are part of the patient volume imaged for treatment planning are considered in the treatment planning process by using dose constraints. They typically receive medium doses (> 1 % of the prescribed target dose). The dose is due to scattering of the particle beam and due to the fact that these organs lie within the primary beam path. The total dose delivered is termed integral dose. Other organs are further away from the target volume and receive low doses (< 1 % of the prescribed target dose). These organs are typically not imaged or outlined for treatment planning. The dose is a result of radiation being scattered at large angles in the treatment head, radiation leakage through the treatment head, and secondary radiation, *i.e.*, radiation generated by interactions of the primary radiation with material in the treatment head or the patient. Some treatment techniques, while aiming at highly conformal dose to the target, do not necessarily deliver lower doses to areas distant from the target. Several authors have cautioned that compared with conventional radiotherapy, the use of IMRT or proton therapy could result in a higher incidence of radiation-induced second cancers (Hall, 2006; Hall and Wuu, 2003; Kry *et al.*, 2005; Paganetti *et al.*, 2006). Because doses are low, the main concerns are late effects and, in particular, second cancers.

Treatment-related cancers are a well-recognized side effect in radiation oncology (Schottenfeld and Beebe-Dimmer, 2006; Tubiana, 2009; van Leeuwen and Travis, 2005). The likelihood of developing a second cancer depends on both the entire irradiated volume and on the volume of the high-dose region. With respect to radiation-induced sarcoma, the main concern is not primarily the dose far away from the beam edge, but the dose delivered directly in the beam path. The second malignancy rates in children from incidental normal tissue dose are of the order of 2 to 10 % 15 to 20 years after radiotherapy (Broniscer *et al.*, 2004; Jenkinson *et al.*, 2004; Kuttesch Jr. *et al.*, 1996). Others have estimated the cumulative risk for the development of second cancers over a 25-year follow-up interval as ranging from 5 to 12 % (de Vathaire *et al.*, 1989; Hawkins *et al.*, 1987; Olsen *et al.*, 1993; Tucker *et al.*, 1984) with conventional radiation therapy as a predisposing factor (de Vathaire *et al.*, 1989; Potish *et al.*, 1985; Strong *et al.*, 1979; Tucker *et al.*, 1987). Radiation can cause intracranial tumors after therapeutic cranial irradiation for leukemia (Neglia *et al.*, 1991), tinea capitis (Ron *et al.*, 1988; Sadetzki *et al.*, 2002), and intracranial tumors (Kaschten *et al.*, 1995; Liwnicz *et al.*, 1985; Simmons and Laws, 1998). The median latency of second cancers has been reported as 7.6 years in one group of patients (Kuttesch Jr. *et al.*, 1996). In patients with pituitary adenoma a cumulative risk of secondary brain tumors of 1.9 to 2.4 % at ~ 20 years after radiotherapy and a latency period for tumor occurrence of 6 to 21 years was reported (Brada *et al.*, 1992; Minniti *et al.*, 2005). Brenner *et al.* (2000) examined second cancers from prostate radiotherapy and found that the absolute risk was 1.4 % for patients surviving longer than 10 years. The relative risk of developing a second cancer is less in patients with smaller treatment volumes (Kaido *et al.*, 2001; Loeffler *et al.*, 2003; Shamisa *et al.*, 2001; Shin *et al.*, 2002; Yu *et al.*, 2000). Data on radiation-induced cancer and mortality after exposure to low doses data have been summarized in the BEIR VII (Biological Effects of Ionizing Radiation) report for various organs (BEIR, 2006).

The relative risk of irradiated versus non-irradiated population for fatal solid cancer for persons 30 years of age for 1 Sv of whole-body irradiation was estimated to be 1.42 (Preston *et al.*, 2004). Pierce *et al.* (1996) estimated lifetime excess risks of radiation-associated solid cancer death rates and lifetime excess risks for leukemia as a function of age, gender, and dose. The risk was higher for those exposed at younger ages (Imaizumi *et al.*, 2006). High rates of late (50 years after exposure) second cancers are pertinent to risk estimates based on patient follow-up data extending to only 10 to 20 years. Thus, estimates of radiation-induced cancer risk in radiation treated patients must be considered to be less than the actual lifetime risk.

Often the highest incidence of radiation-associated second tumors occurs at field peripheries and not at the field center (Epstein *et al.*, 1997; Foss Abrahamsen *et al.*, 2002). However, even doses delivered far outside the main field have been associated with second tumors. Decades ago, the scalps of children in Israel were irradiated to induce alopecia for the purpose of aiding the topical treatment of tinea capitis (Ron *et al.*, 1988). Mean doses to the neural tissue were ~ 1.5 Gy. The relative risk of tumor formation at 30 years compared with the general population was 18.8 for schwannomas, 9.5 for meningiomas, and 2.6 for gliomas with a mean interval for tumor occurrence of 15, 21, and 14 years, respectively. Sadetzki *et al.* (2002) report on the development of meningiomas after radiation for tinea capitis with a time from exposure to meningioma diagnosis of 36 years. A recent study has concluded that, even 40 years after initial radiation treatment of cervical cancer, survivors remain at an increased risk of second cancers (Chaturvedi *et al.*, 2007).

Second cancers are late effects and thus of particular importance in the treatment of childhood cancers. For childhood cancers, the relative five-year survival rate has risen from 56 % for children diagnosed between 1974 to 1976 to 79 % for those diagnosed in the period 1995 to 2001 (Jemal *et al.*, 2006); the current ten-year survival rate is ~ 75 % (Ries *et al.*, 2006). Although the majority of children with cancer can expect a long life post-treatment, a second cancer will occur in some pediatric cancer patients following successful treatment of the original disease (Ron, 2006). Most published data are based on the Childhood Cancer Survivor Study, an ongoing multi-institutional retrospective study of over 14,000 cases (Bassal *et al.*, 2006; Kenney *et al.*, 2004; Neglia *et al.*, 2001; Sigurdson *et al.*, 2005).

7.8 Models

7.8.1 Model Concepts

Cancer risk is specified as either the risk for incidence or the risk for mortality. Dose-response relationships are typically defined as a function of age, gender, and site. The cancer incidence rate at a given point in time is defined as the ratio of number of diagnosed individuals in a time interval divided by the interval duration and the total number of unaffected individuals at the beginning of this interval. Cancer risk, on the other hand, is defined as the probability for disease occurrence in the population under observation, *i.e.*, risk equals the ratio of number of diagnosed to total number of individuals in the given time interval. The baseline risk refers to the incidence of cancer observed in a group without a specific risk factor (*e.g.*, the un-irradiated reference population). In order to obtain a measure of the relation between the incidence rate in the exposed population and the incidence rate in the unexposed population, one can use either their difference or their ratio.

Quite often, risk estimates are performed using whole-body effective doses and organ weighting factors (EPA, 1994; 1999; ICRP, 1991; 2003b; NCRP, 1993). The NCRP defines probabilities of fatal cancer for bladder, bone marrow, bone surface, breast, esophagus, colon, liver, lung, ovary, skin, stomach, thyroid, and remainder of the body (NCRP, 1993). The ICRP defines a whole-body effective dose with organ-specific weighting factors (ICRP, 2003b). The methodology was originally designed for setting radiation protection limits by making sure the radiation exposures to workers are controlled to a level that is considered to be safe (ICRP, 1991; 2003b). Tissue weighting factors employed by the NCRP and ICRP for the effective dose are gender- and age-averaged values applying a radiation independent dose-rate correction. Thus, these models are rough approximations which yield a nominal risk value of 5 x 10^{-2}/Sv. Effective doses are suited for radiation protection studies but it has to be stated clearly that they are not suited for risk models for secondary cancer, which are site specific. The ICRP has advised against the use of effective dose for the risk of a single patient and of a site-specific tumor. Epidemiological risk assessments should be based on organ-specific equivalent doses. The BEIR report (2006) provides formalisms to calculate organ-specific risks of cancer incidence and mortality. Dose-response relationships are typically defined as a function of age, gender, and site.

Relative risk (RR) is the rate of disease among groups with a specific risk factor (*e.g.*, having received some radiation) divided by the rate among a group without that specific risk factor. Excess relative risk (ERR) is defined as the rate of an effect (*e.g.*, cancer incidence or mortality) in an exposed population divided by the rate of the effect in an unexposed population minus 1, or RR-1. In risk models using ERR, the excess risk is expressed relative to the background risk. Absolute risk is the rate of a disease among a population, *e.g.*, cancer cases per capita per year. Excess absolute risk (EAR) is the rate of an effect (*e.g.*, cancer incidence or mortality) in an exposed population minus the rate of the effect in an unexposed population. Thus, in risk models using EAR, the excess risk is expressed as the difference in the total risk and the background risk. The latter depends on the area in which the person lives, their age, sex, and date of birth (Ries *et al*., 2003). When modeling a dose-response relationship for a specific disease, one can either use the concept of ERR or the concept of EAR. In general, estimates based on ERR can have less statistical uncertainties and thus are more meaningful for small risks. On the other hand, EAR is often used to describe the impact of a disease on the population. The excess risk can be calculated as a function of attained age of the individual, age at exposure, dose received, sex index, and an index denoting population characteristics. The lifetime attributable risk (LAR) is the probability that an irradiated individual will develop a radiation-induced cancer in their lifetime (Kellerer *et al.*, 2001). It includes cancers that would develop without exposure but which occur sooner in life due to radiation. The LAR can be estimated as an integral of excess risk over all attained ages using either ERR or EAR (BEIR, 2006).

The models presented in BEIR report (2006) define the relation between the incidence rate in the exposed population and the incidence rate in the unexposed population. The excess risk can be calculated as a function of attained age of the individual: a, age at exposure, e; dose received, D; sex index, s; and time since exposure, t. One assumes a linear (solid cancers) or quadratic (leukemia) function of dose. The BEIR committee suggests that ERR for solid cancers (except for breast and thyroid) depend on age only for exposures under age 30. Specific parameterizations are given for estimation of breast cancer risk, thyroid cancer risk, and leukemia.

Schneider and Kaser-Hotz (2005) proposed the concept of "organ equivalent dose" (OED), in which any dose distribution in an organ is equivalent and corresponds to the same OED if it causes the same radiation-induced cancer incidence. For low doses, the OED is simply the average organ dose. At high doses the OED is different, because cell killing becomes important. The basis for the OED model is the dose-response relationship for radiation-induced cancer for different organs. The model is a linear-exponential dose-response model that takes into account cell-killing effects by an exponential function that depends on the dose and the organ-specific cell sterilization factor that is determined by Hodgkin's disease data. The dose distributions used to determine the organ-specific cell sterilization factor were calculated in individual organs for which cancer incidence data were available. Kry *et al.* (2005) pointed out that developing concepts like the OED model suffers from major deficiencies, such as single specific irradiated populations. However, the OED approach has the advantage compared to the BEIR model that it is able also to estimate cancer risk from medium to high dose exposures, *i.e.*, in the vicinity of the target (Schneider *et al.*, 2006; Schneider *et al.*, 2007).

By developing models based on the atomic bomb data, differences in the radiation exposure compared to radiation treatments need to be considered. Even though most bomb survivors were exposed to low doses (< 0.1 Gy), some were exposed to doses exceeding 0.5 Gy, thus influencing the risk estimation. The risk is also dose-rate dependent. Grahn *et al.* (1972) observed reduction in leukemia incidence by a factor of ~ 5 with reduction of dose to 0.2 to 0.3 Gy/day. Ullrich *et al.* (Ullrich, 1980; Ullrich *et al.*, 1987) reported on dose-rate dependencies for the incidence of lung adenocarcinoma in mice. Maisin *et al.* (1991) found that ten fractions of 0.6 Gy yielded more cancers than a dose of 6 Gy in mice following whole-body irradiation. Brenner and Hall (1992) discussed this inverse effect of dose protraction for cancer induction. Dose rate effects are well understood for therapeutic dose levels with low-LET radiation (Paganetti, 2005). Most risk models account for dose rate effects by introducing scaling factors. However, the effect of dose protraction may be different in low dose regions in particular for neutron irradiation. While a positive "dose and dose-rate effect factor" (DDREF) is established for scattered photon doses, there is evidence for no dose-rate effect or even a reverse dose-rate effect for low doses of neutron radiation. This effect is a well-known phenomenon for high-LET radiation (Kocher *et al.*, 2005).

To establish a more precise dose-response relationship for second cancers as a function of modality, treatment site, beam characteristics, and patient population, progressively larger epidemiological studies are required to quantify the risk to a useful degree of precision in the low dose regions (Brenner *et al.*, 2003). In order to facilitate the evaluation of dose-response relationships as defined in epidemiological models, organ-specific dosimetry is needed. In fact, one of the reasons for considerable uncertainties in the current risk models is that actual second cancer incidences from radiation therapy patients are difficult to interpret due to the lack of accurate organ-specific dosimetric information. Further, simple dose-response relationships can be misleading. Dose-rate effects certainly play a role (Gregoire and Cleland, 2006).

7.8.2 Dose-Response Relationships

Various low-dose response relationships for second cancer induction have been discussed (Brenner *et al.*, 2003). Studies on leukemia suggest that the carcinogenic effect of radiation decreases at high doses because cell killing starts to dominate mutation (Upton, 2001). Patients treated with radiation for cervical cancer showed an increased risk of developing leukemia with doses up to ~ 4 Gy, which decreased at higher doses (Blettner and Boice, 1991; Boice *et al.*, 1987). Sigurdson *et al.* (2005) found that the risk for developing a second thyroid cancer after childhood cancer increased with doses up to ~ 29 Gy and then decreased. There is other evidence that the risk of solid tumors might level off at 4 to 8 Gy (Curtis *et al.*, 1997; Tucker *et al.*, 1987). For pediatric patients, Ron *et al.* (1995) showed that a linear dose-response relationship best described the radiation response down to 0.1 Gy. In general, a linear dose-response curve is assumed for solid cancers (Little, 2000; 2001; Little and Muirhead, 2000).

It has been shown that even a single particle can cause mutations in a single-cell irradiation process. This is an indication of a linear dose-response relationship (Barcellos-Hoff, 2001), at least down to about 0.1 Gy (Frankenberg *et al.*, 2002; Han and Elkind, 1979; Heyes and Mill, 2004; NCRP, 2001). For even lower doses a small decrease in transformation has been reported (Ko *et al.*, 2004) while some data suggest a non-linear dose-response curve (Sasaki and Fukuda, 1999). Others have suggested a protective effect (Calabrese and Baldwin, 2000; 2003; Feinendegen, 2005; Hall, 2004; Upton, 2001). Results of whole-body irradiation (WBI) of primates with a follow-up of 24 years show no increase in cancer for 0.25 to 2.8 Gy (Wood, 1991).

Most currently used risk models are based on these data. Both the BEIR VII Committee (2006) and the ICRP (1991) recommend, for doses below 0.1 Gy, a “linear no-threshold” (LNT) model. This concept has been challenged by recent data (Tubiana *et al.*, 2009).

Assumptions about dose-response relationships for tumor induction are largely based on the atomic bomb survivor data. These are consistent with linearity up to ~ 2.5 Sv with a risk of ~ 10 %/Sv (Pierce *et al.*, 1996; Preston *et al.*, 2003). However, some analyses show a linear dose response for cancer incidence between 0.005 and 0.1 Sv (Pierce and Preston, 2000), some indicate a deviation from linearity (Preston *et al.*, 2004), and some find no increased cancer rate at doses less than 0.2 Sv (Heidenreich *et al.*, 1997). There is even some evidence for a decreasing slope for cancer mortality and incidence. This may be caused by the existence of small subpopulations of individuals showing hypersensitivity (ICRP, 1999). There might also be reduced radioresistance in which a small dose decreases the radiosensitivity, as has been reported for carcinogenesis (Bhattacharjee and Ito, 2001), cellular inactivation (Joiner *et al.*, 2001), mutation induction (Ueno *et al.*, 1996), chromosome aberration formation (Wolff, 1998), and *in vitro* oncogenic transformation (Azzam *et al.*, 1994). Further, linearity would not necessarily hold if multiple radiation-damaged cells influenced each other (Ballarini *et al.*, 2002; Little, 2000; Little and Muirhead, 2000; Nasagawa and Little, 1999; Ullrich and Davis, 1999). An increasing slope seems to fit dose-effect relations for radiation-induced leukemia (Preston *et al.*, 2003), while a threshold in dose seems to be present for radiation-induced sarcoma (White *et al.*, 1993). Also, animal data have not shown significant cancer excess for doses below 100 mSv (Tubiana, 2005). The lack of evidence of a carcinogenic effect for low doses could be because the carcinogenic effect is too small to be detected by statistical analysis or because there is a threshold.

7.9 Risks of Radiation-Induced Secondary Cancers in Particle Therapy

Second malignancies are a major source of morbidity and mortality in pediatric cancer survivors. Although IMRT provides highly conformal dose to the target volume at high doses, due to the increased volume of tissue receiving lower doses it may nearly double the risk of second malignancy compared with 3D conformal techniques (Hall and Wuu, 2003). Protons reduce the integral dose by a factor of 2 to 3 compared to photon techniques and can thus be expected to decrease second cancer risk.

Recently, the comparative risk for developing second malignancies from scattered photon dose in IMRT and secondary neutron dose in proton therapy has been assessed by analyzing clinical data (Chung *et al.*, 2008). The study matched 503 patients treated with proton radiation therapy from 1974 to 2001 at the Harvard Cyclotron Laboratory and 1591 photon patients from the Surveillance, Epidemiology, and End Results (SEER) cancer registry. Patients were matched by age at radiation treatment, year of treatment, cancer histology, and site of treatment. The median age in both groups was comparable. It was found that 6.4 % of proton patients developed a second malignancy as compared to 12.8 % of photon patients The median follow-up was 7.7 years in the proton cohort and 6.1 years in the photon cohort.

After adjusting for gender and the age at treatment, the results indicated that the use of proton radiation therapy is associated with a lower risk of a second malignancy compared to photon radiation therapy.

Because we can assume (for passive-scattering techniques) that the majority of the neutrons in the patient are generated in the treatment head, we can infer that proton beam scanning reduces the neutron dose exposure significantly, in particular for small treatment fields (*i.e.*, small apertures in scattering systems). In fact, it has been demonstrated that scanned proton beams result in a lower second cancer risk than passive-scattered protons or photons (Miralbell *et al.*, 2002; Schneider *et al.*, 2002). Miralbell *et al.* (2002) assessed the potential influence of improved dose distribution with proton beams compared to photon beams on the incidence of treatment-induced second cancers in pediatric oncology. Two children, one with a parameningeal rhabdomyosarcoma (RMS) and a second with a medulloblastoma, were considered. They showed that proton beams have the potential to reduce the incidence of radiation-induced second cancers for the RMS patient by a factor of > 2 and for the medulloblastoma case by a factor of 15 when compared with IMRT (Table 7.2). These data for scanned proton beams do not include any secondary neutron component. Thus the improvement is simply due to a smaller irradiated high-dose volume.

Table 7.2. Estimated absolute yearly rate of second cancer incidence after treating a medulloblastoma case with either conventional x ray, IMRT, or scanned proton beams. <u>(Miralbell *et al.*, 2002)</u>

Tumor site	X-rays (%)	IM X-rays (%)	Protons (%)
Stomach and esophagus	0.15	0.11	0.00
Colon	0.15	0.07	0.00
Breast	0.00	0.00	0.00
Lung	0.07	0.07	0.01
Thyroid	0.18	0.06	0.00
Bone and connective tissue	0.03	0.02	0.01
Leukemia	0.07	0.05	0.03
All secondary cancers	0.75	0.43	0.05
Relative risk compared to standard X-ray plan	1	0.6	0.07

The magnitude of second cancer risk in patients treated with passive and scanned proton radiation has also been estimated utilizing computer simulations of organ doses using computational phantoms (Brenner and Hall, 2008b; Jiang *et al.*, 2005; Newhauser *et al.*, 2009; Taddei *et al.*, 2009; Zacharatou Jarlskog and Paganetti, 2008b). Based on dosimetric data on organ doses given by Jiang *et al.* (2005), Brenner and Hall (2008a) estimated second cancer risks for various organs assuming a neutron RBE value of 25. They reported that lifetime cancer risk due to external neutrons in passive-scattered proton therapy is 4.7 % and 11.1 % for a cured 15-year-old male and female, respectively. The estimations were based on a proton treatment for lung cancer. The risk decreased to 2 % and 3 %, respectively, for an adult patient.

Based on Monte Carlo simulations using a treatment head model and a voxelized phantom, Taddei *et al.* (2009) estimated the second cancer risk from secondary radiation following cranio-spinal irradiation with proton therapy. An effective dose corresponding to an attributable lifetime risk of a fatal second cancer of 3.4 % was determined. The equivalent doses that predominated the effective dose from secondary radiation were in the lungs, stomach, and colon. Further, cranio-spinal irradiation of a male phantom was calculated for passively scattered and scanned-beam proton treatment units (Newhauser *et al.*, 2009). The total lifetime risk of second cancer due exclusively to secondary radiation was 1.5 % for the passively scattered treatment versus 0.8 % for the scanned proton-beam treatment.

Based on the data on organ neutron equivalent doses using five pediatric computational phantoms, risk estimations based on BEIR risk models have been done (Zacharatou Jarlskog and Paganetti, 2008b). For eight proton fields to treat brain tumors, the risk for developing second cancer in various organs was calculated. Figure 7.5 shows the lifetime attributable risk (LAR) for some of the organs. It was found that young patients are subject to significantly higher risks than adult patients due to geometric differences and age-dependency of risk models. In particular, a comparison of the lifetime risks showed that breast cancer should be the main concern for females, whereas for males, risks for lung cancer, leukemia, and thyroid cancer were more significant. Other than for pediatric patients, leukemia was the leading risk for an adult. Most of the calculated lifetime risks were below 1 % for the 70 Gy treatment considered. The only exceptions were breast, thyroid, and lung for females. For female thyroid cancer the treatment risk can exceed the baseline risk. The patient’s age at the time of treatment plays a major role (Zacharatou Jarlskog and Paganetti, 2008b).

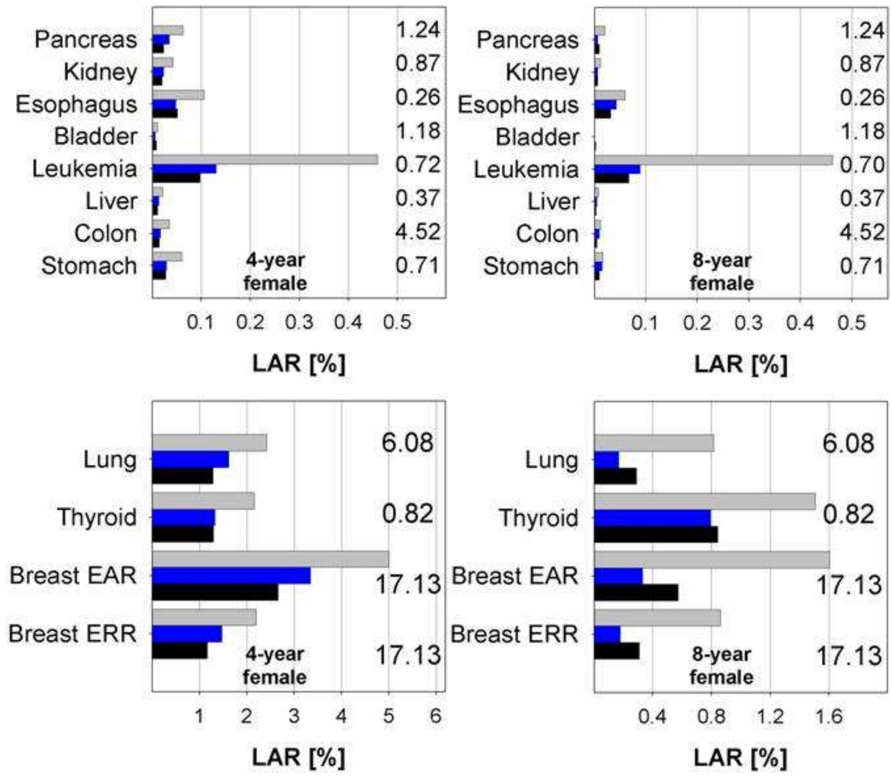

Figure 7.5. Lifetime attributable risk [%] based on a 70 Gy treatment for various second cancers for 4-year-old and 8-year-old brain tumor patients. The three colors refer to three different treatment fields. The numbers on the right represent the baseline risks for these cancers. (Zacharatou Jarlskog and Paganetti, 2008b)

Although strictly speaking it is a radiation protection quantity, the whole-body dose equivalent was used to estimate the risk by a few groups (Followill *et al.*, 1997; Kry *et al.*, 2005; Verellen and Vanhavere, 1999). In this approach, the whole-body dose equivalent was determined for a point in the patient, usually 40 to 50 cm from the edge of the treatment field. This value is then multiplied by a whole-body risk coefficient. Followill *et al.* (1997) measured whole-body dose equivalent for neutrons and photons at a point 50 cm from the isocenter. The radiation weighting factor of 20 for neutrons was used. As the beam energy increased, the neutron contribution increased dramatically. For each treatment modality, the whole-body dose equivalent for 25 MV beams was found to be eight times greater than that for the 6 MV beams. For a given energy, the whole-body dose equivalent was the highest for serial tomotherapy, and lowest for 3D-CRT procedures. The risk of any fatal second cancer associated with the scattered dose from the 6 MV unwedged conventional treatment technique was estimated by the authors to be 0.4 %. The risk for an assumed 25 MV tomotherapy treatment was estimated to be 24.4 %. The increased risks were associated with the increase in total number of monitor units used for each treatment technique. Another series of calculations of whole-body dose equivalents for 3D-CRT and IMRT prostate treatments were carried out by Kry *et al.* (2005). The authors reported major differences between using this method and organ-specific risk calculations.

7.10 Uncertainties and Limitations of Risks Estimations

Neutron radiation weighting factors are subject to significant uncertainties that can affect risk estimations, in particular at low doses (Brenner and Hall, 2008a; Hall, 2007; Kocher *et al.*, 2005). The ICRP radiation weighting factors may not be very accurate for extremely low doses (Kellerer, 2000). Energy-averaged neutron radiation weighting factors in the human body based on the ICRP curve are typically between 2 and 11 (Jiang *et al.*, 2005; Wroe *et al.*, 2007; Yan *et al.*, 2002). However, much higher neutron RBE values have been found for various endpoints both *in vivo* and *in vitro* (Dennis, 1987; Edwards, 1999; NCRP, 1990). The NCRP has shown neutron radiation weighting factors of more than 80 for fission neutrons considering several radiation endpoints in the energy range of 1 to 2 MeV, where the ICRP recommendation assumes a weighting factor of 20 (NCRP, 1990). Dennis (1987) has reviewed experimental neutron RBE data and found maximum *in vivo* values at low doses of up to 71.

There are insufficient data to define the radiation effectiveness of neutrons for epidemiological endpoints. The radiation weighting factor recommendation by the ICRP may not reflect reality as it does focus on radiation protection rather than radiation epidemiology. The ICRP explicitly states that the term effective dose is a quantity for use in radiation protection and not in epidemiology. These limitations have to be considered when analyzing secondary doses.

There are many different contributions that provide uncertainties in absolute risk estimates that have been given in the literature. Kry *et al.* (2007) examined the uncertainty in absolute risk estimates and in the ratio of risk estimates between different treatment modalities using the NCRP/ICRP risk model and a risk model suggested by the U.S. Environmental Protection Agency (EPA, 1994; 1999). They found that the absolute risk estimates of fatal second cancers were associated with very large uncertainties, thus making it difficult to distinguish between risks associated with the different treatment modalities considered.

Several risk models have been proposed and used to estimate the risk of second malignancies induced by radiation treatment. The models in use today are largely based on the atomic bomb survival data. Both the BEIR VII Committee (2006) and the ICRP (1991) recommend, for doses below 0.1 Gy, a linear dose-response relationship without a low-dose threshold based on the epidemiological data obtained from Japanese atomic bomb survivors. This population was exposed to a single equivalent dose fraction of between 0.1 and 2.5 Sv. The radiation field, dose, and dose rate were certainly much different from the radiation fields in radiation therapy. However, extracting dose-response relationships from patient data is associated with large statistical uncertainties (Suit *et al.*, 2007).

At low doses, none of the epidemiological data are sufficient to establish the shape of the dose-response relationship and more extensive studies are required to quantify the risk to a useful degree of precision (Brenner *et al.*, 2003). One reason for the considerable uncertainties in risk models is the fact that actual second cancer incidences are difficult to interpret because of the lack of accurate dosimetric information. For example, in estimating the baseline risk for lungs from the atomic bomb survivors, a significant fraction in the cohort were smokers. The lung cancer risk associated with smoking is additive with the secondary cancer risk in lungs from the radiation. There is a large ambiguity in what fraction of the cohort in the atomic bomb survivors were smokers. Consequently, the estimated baseline risk for lung cancers for both genders is over estimated.

7.11 Summary and Conclusion

The issue of secondary radiation to patients undergoing proton beam therapy has become an important topic among medical physics researchers and clinicians alike. A large amount of data has been published on this subject particularly within the last few years. To some extent this shows the success of radiation therapy. Due to early cancer diagnosis and long life expectancy post treatment, second cancer induction could be a significant late effect.

Although dosimetric data, experimental as well as theoretical, are known by now to a sufficient degree of accuracy, the actual cancer risk associated with the absorbed doses is not well known at all. This is due to huge uncertainties in the biological effectiveness of neutrons at low doses and due to huge uncertainties in current epidemiological risk models.

Clinical data are difficult to interpret because of inter-patient variability and lack of dosimetric information in the low dose region. However, improved dosimetric data in combination with long-term patient follow-up might eventually lead to improved risk models.

8. Safety Systems and Interlocks

Jacobus Maarten Schippers

8.1 Introduction

The purpose of safety systems and interlocks (particle-beam interruption systems) in a particle therapy facility is threefold:

1. to protect personnel, patients, and visitors from inadvertent exposure to overly excessive radiation doses;
2. to protect patients from receiving an incorrect dose or a dose in an incorrect volume; and
3. to protect equipment and environment against heat, radiation damage, or activation.

How these goals are implemented depends strongly on the local radiation protection legislation, the specific requirements and traditions of the institute concerned, and the standards to which the company delivering the equipment adheres. In this chapter several methods and relevant parts of either planned or actually installed safety systems are discussed, with the sole purpose of showing the underlying philosophy and how one could implement such systems in practice. Therefore, the description of the systems is by no means complete and is sometimes simplified. Most examples of the systems discussed in this chapter refer to the situation at the Center for Proton Therapy at the Paul Scherrer Institute (PSI) in Switzerland as they existed or were planned at the time of writing this chapter. Other methods will be applicable to other treatment facilities or when other irradiation techniques are applied. Due to the differences and continuing developments in legislation, it is up to the reader to decide which ideas or systems could be of use in one's own country or facility. The purpose of this chapter is to inform the reader about the different aspects of safety systems that need to be addressed; to give a potential user enough background information and some suggestions to define one's own list of criteria for a safety system in order to have relevant and thorough discussions with the vendors; and to provide information to help users understand, judge, and eventually criticize a vendor's proposal and to check compliance with local requirements and regulations.

Figure 8.1 shows the facility at PSI, which has been built and designed in-house. Within a research collaboration with the supplier of the cyclotron, PSI has contributed to the development of the accelerator, its interfaces, and control system. The experience obtained since the start of particle therapy at PSI in 1980 has evolved in the current design of the control and safety systems. Until 2005, the therapy program ran parallel with the physics program at PSI by using a fraction of the high intensity proton beam (Pedroni *et al.*, 1995). This type of operation imposed special constraints on the design of the safety systems, such as the rigorous separation of patient safety functions from the machine control system. This philosophy has been used again in the newly built stand-alone proton therapy facility that has been in use since 2007. This therapy facility (Schippers *et al.*, 2007) consists of a cyclotron, energy degrader and beam analysis system, two rotating gantries (Gantry 1 and Gantry 2, the latter of which is not yet operational at the time of writing), an eye treatment room (OPTIS2), and a room for experimental measurements.

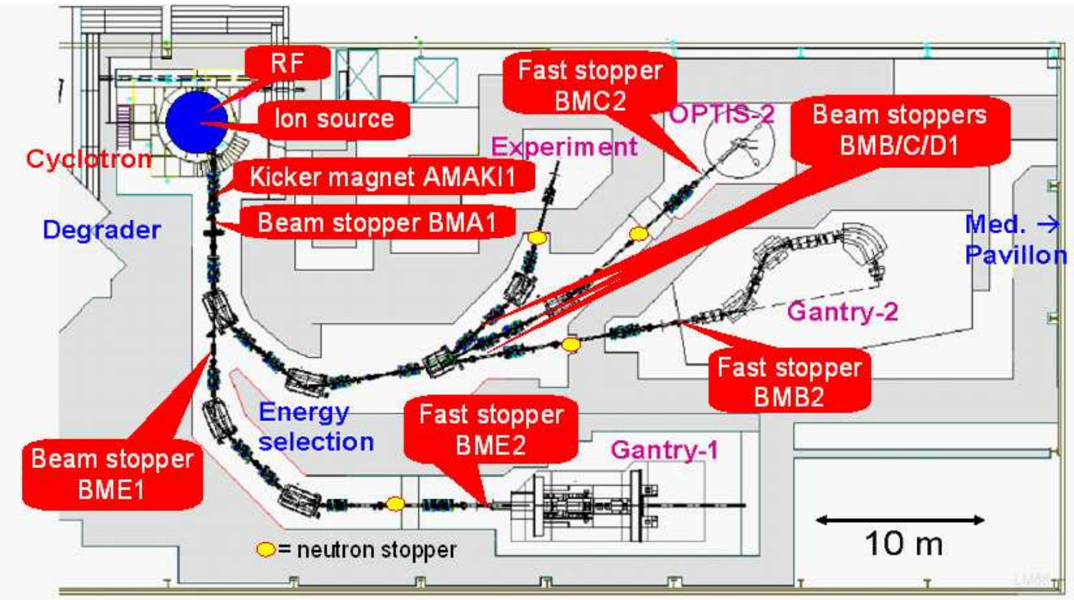

Figure 8.1. Floor plan of the proton therapy facility at PSI, indicating the actuators that can be used to stop or intercept the beam. (Courtesy of PSI)

At PSI the three safety functions mentioned above are controlled by three separate systems: a Personnel Safety System (PSS); a Patient Safety System (PaSS); and a Run Permit System (RPS). The PSS and PaSS operate separately from the control system of the machine (cyclotron and beam lines). The separation of functions reduces the risks and complexity that might occur in the case of a system in which the design is based on one combined operation and safety system in which "everything is connected to everything else." Of course, well-designed systems with a global function approach to the facility can be conceived without this separation, but the separated function approach leaves more freedom for further technical developments. The control system architecture at PSI allows explicit visibility of these functions in the system architecture.

In the case of an undesired input signal or status, each of the three safety systems has the capability to "trip": it sends a signal that switches the beam off or prevents the beam from being switched on. The event of changing into a state which is not "OK" is usually referred to as "a trip" or "an interlock trip." Each safety system has its own sensor systems, actuators, switches, and computer systems. Although actuators that can switch off the beam (Fig. 8.1) can be activated by more than one safety system, they have separate inputs/outputs for the signals from/to each of these safety systems. In many cases, dedicated diagnostic signals are also used to determine if the actuator is working properly. Apart from the statuses "OK" and "not OK," the other possible states of an actuator might be "NC" (not connected) and "err" (short circuit). This defines the fail-safe nature of the signals.

The displays in the control room indicate which system causes the interception or interruption of the beam and allow a detailed in-depth analysis in order to find out the cause of such an error status. All events are logged with time reference stamps.

In this chapter, these three safety systems and their implementation will be described. Although some issues are specific to PSI (*e.g.*, the spot scanning technique; see Pedroni *et al.*, 1995) or to the use of a cyclotron, the concepts are applicable to any facility. The most important aspect of the safety concept used at PSI is the complete and rigorous separation of the three systems. By this, a very flexible arrangement has been created. Some general issues on safety systems are discussed in Sec. 8.1, followed by information on the beam-intercepting devices in Sec. 8.2, with Sec. 8.3 describing the relevant aspects of the control system at PSI, and Sec. 8.4, 8.5, and 8.6 providing a detailed description of the three safety systems.

8.1.1 Safety Requirements

The risk limitation and reduction required by various authorities depends upon local laws and administration rules, and is in steady development. An FDA approval (U.S.A.), CE conformity procedure (E.U.), or similar authorization by equivalent bodies in other countries of the facility could be required. When the research and development of the equipment and software was started a long time ago, or when it is not thought that the system will be put on the market, an adaptation of the project into a more regulated form is generally not possible without substantial effort. For these special cases, special regulations might exist.

However, for proton/ion therapy, the practical implementation of existing regulations might sometimes not be evident or applicable. Then one has to negotiate with the appropriate authorities, *e.g.*, regarding how the documentation and test procedures should be designed in order to obtain approval for treatments. In any case, a state-of-the-art approach would at least consist of a report with a thorough description of the safety systems, a risk analysis, operating instructions, and a list of tests to be done with a specified frequency of these tests. In general, the results of initial and periodic tests must be available for the appropriate authorities.

8.1.2 Safety Standards

To the best of the author's knowledge, there are no existing specific norms or widely applicable safety guidelines specifically for proton and ion therapy facilities at this time. However, in some countries authorities follow or adapt applicable existing recommendations or guidelines for linear accelerators for photon or electron therapy, and regulations for particle therapy facilities are being developed. The current recommendations and guidelines present generally accepted safety standards for radiation therapy, many of which are also applicable to proton and ion therapy. One could, for instance, use the applicable parts of the standards for medical electron linear accelerators, as given in the International Electrotechnical Commission's Publication 60601-2-1 (1998). As an example, in proton or ion therapy, it would then also require two dose monitors in the treatment nozzle, one giving a stop signal at 100 % and the second monitor giving a stop signal at approximately 110 % of the prescribed dose. Also, useful guidelines can be found in the recently issued new IEC Publication 62304 (2006), which deals with software for medical applications.

Criteria for accidental exposures in radiotherapy are listed in ICRP Publication 86 (2000). An overdose due to a failure in procedure or in equipment is classified as a "Class I hazard," when the extra dose could cause death or serious injury. Within this class, two types of hazards are distinguished: type A, which can likely be responsible for life-threatening complications (25 % overdose or more of the total prescribed treatment dose); and type B (5 to 25 % dose excess over the total treatment dose), which increases the probability of an unacceptable treatment outcome (complications or lack of tumor control).

One of the goals of a patient safety system could thus be defined as preventing an excess dose that is due to an error in dose delivery and exceeds 5 % of the treatment dose, which is typically ~ 3 Gy.

8.1.3 Risk Analysis

The requirements for and extent of a risk analysis for medical devices differ from country to country and are in steady development, so a general rule cannot be given. Furthermore, there is no unique way of performing a risk analysis, but one can obtain good working structures from existing norms and recommendations on medical devices. Note, however, that whether and under which conditions proton or ion therapy equipment and its accessories fall under the definition of “a medical device” can differ from country to country (although, in the EU it is the same for all members).

In ISO 14971 (2007), the general process of how risk management could be applied to medical devices is given. On the ISO Web site mentioned in the above standard, a list of member countries that have recognized ISO 14971 is given. This ISO norm presents an organizational structure of activities related to risk management. One can typically distinguish the following steps in a risk management process:

- *Risk analysis*: identification of hazardous situations and risk quantification, *e.g.*, by analyzing fault trees;
- *Risk evaluation*: decide upon need for risk reduction;
- *Risk control*: describe measures (definition, implementation, and verification) to reduce risk;
- *Residual risk evaluation*: what is the risk after implementing the measures;

- *(Post) production information*: review the actual implementation and observe how these implementations perform in real practice. This gives the process the capability to update the risk analysis and to react to observed problems after production.

For an estimation of the amount of needed safety measures, one could use a process in analogy to the one given in IEC Publication 61508 (2005) as a guideline. In Part 5 of this international standard for the functional safety of electrical, electronic, and programmable electronic equipment, many examples are given to categorize hazardous events in a "hazard severity matrix" by means of their impact and their probability of occurrence. When the combination of severity and occurrence (*i.e.*, the risk) exceeds a certain threshold, a measure must be taken. The robustness of such a measure (the Safety Integrity Level, or SIL) must increase with the risk. One way to increase the robustness of a measure is to add redundancy, *i.e.*, to increase the number of independent safety related systems that comprise the measure taken. Specialized companies have developed software tools as an aid to make such a risk analysis.

8.1.4 Interlock Analysis and Reset

An interlock trip occurs when a device, component, measurement, or signal under the control of a specific safety system is found in an undesirable state with respect to specified tolerances. It is important to reset the interlock signals and restore the machine setting to their normal operating states as soon as possible after the machine state is "OK" again. This is necessary in order to limit waiting time, but also to prevent loss of extra time for retuning of the machine to its normal operating state due, *e.g.*, to temperature drifts. This applies especially to interlock trips that were caused by a condition that was not met for only a short time interval, but which was not caused by a malfunctioning device. For example, one could think of an interlock trip caused by a transient state in which not all components are in an

"OK" status. It could also occur due to a short occurrence of a too high beam current, which might happen when the intensity (signal) is noisy.

In order to recognize the cause of an interlock trip, a clear indication of the signals and an error logging with time stamps of the underlying process and relevant events are essential tools for the diagnosis and repair of problems. Figure 8.2 shows the PSI user interface in the control room as an example.

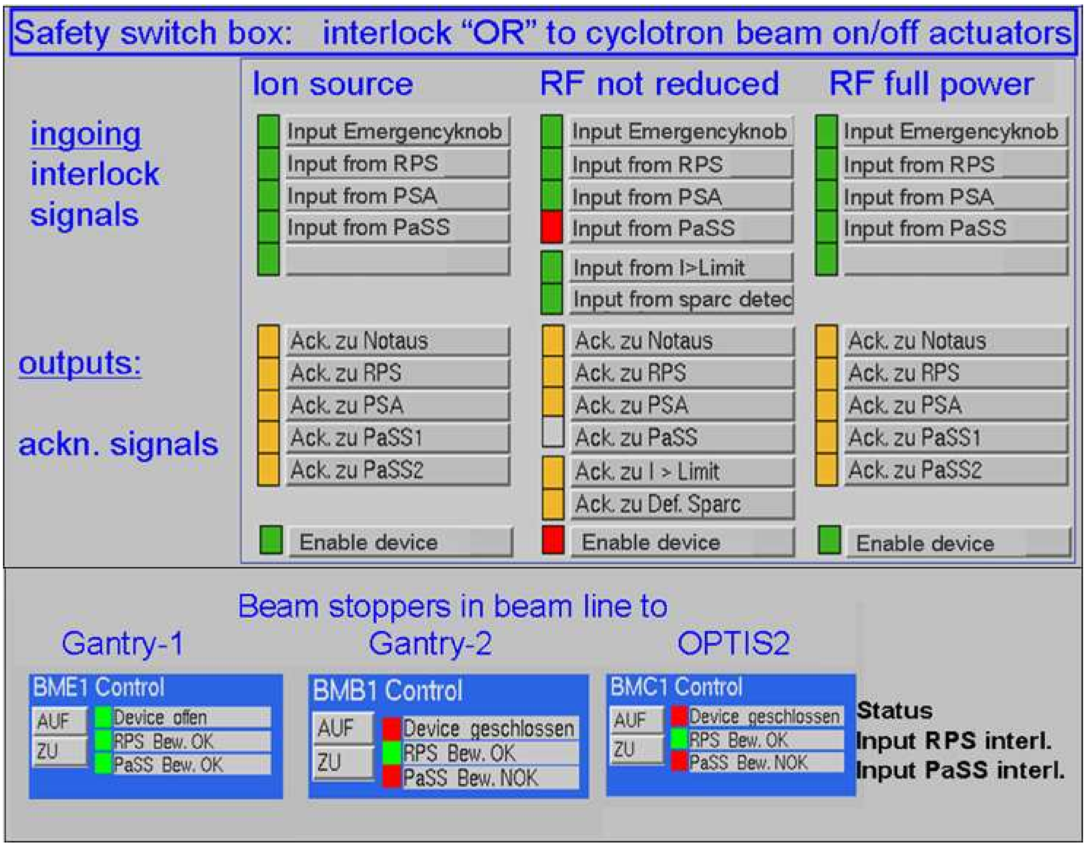

Figure 8.2. The user interface of PSI's control system showing the status of beam-intercepting actuators in the cyclotron (controlled *via* a Safety Switch Box) and area-specific beam stoppers "BMx1." ("Offen" means "open"; "geschlossen" means "closed.") (Courtesy of PSI)

The programs displaying the interlock status and bypasses ("bridges") must be capable of giving easy and quick access to such data. Data from deeper levels that cannot be displayed on the main screen, or more detailed information on the status of specific beam-line sections or devices, can be found by clicking on the components of interest or on a details field in the main screen. Depending on the failure scenario, the continuation of the therapy has to be forbidden or disabled and a comprehensive evaluation of the machine status and the dose already delivered to the patient must be carried out. An easily interpreted interlock analysis program to inform the (therapy) operator can save a lot of time.

After resetting an interlock, the beam should not be automatically switched on again. For safety reasons, a dedicated manual action should be required to switch the beam on again.

8.1.5 Quality Assurance

Although rigorous tests of interlock systems must be done in theory, in practice it is impossible to test all conceivable situations (control system configurations). However, a set of tests can be done to verify that the entire system is working properly. For this purpose one can design tests during the commissioning of the system (which could be part of the acceptance tests) as well as tests during the operational phase of the facility. The combination of such tests should then exclude (or reveal) all errors that one could think of. When a commercial therapy system is obtained, the possibilities for end user testing are limited; however, a vendor should be able to state what type of tests have been done.

During the commissioning of any proton or ion therapy facility, certified or not, several quality assurance tests can be done by generating specific fault conditions. Sometimes the system needs to be "fooled" in order to reach a faulty state for the test. Some possible testing scenarios include a sudden increase of beam current; detuning of magnets; setting the energy degrader or collimator in the wrong position; placing a radioactive source in front of a dosimeter; pressing emergency buttons; or bypassing the limit switches on mechanical beam stoppers. Some of these tests are also incorporated in a quality control program of periodic tests.

All modifications or substantial repairs of the therapy equipment or control systems need to be documented and followed by an "end-to-end test," described in the quality control program of the facility. Similar to standard radiation therapy, in a partial simulation of a treatment, a dose distribution is delivered to a phantom in a treatment room. Measurements are made of the dose and proton range within the phantom, and specified functions of the Patient Safety System are tested.

8.2 Methods of Turning off the Beam

In a particle accelerator and beam transport system there are many mechanisms for turning the beam off. The action of each actuator (method or device) has its own specific reaction time, varying from a few microseconds to fractions of a second. Also the time and effort to switch the beam on again depends on the actuator. In case of severe risk (determined by a risk analysis; see Sec. 8.1.3), several actuators must switch the beam off at the same time (redundancy). In case of low risk or routine switch-off, only one actuator will work, but if the beam does not stop in time, the action of more actuators will follow. When a cyclotron is used as the accelerator, one might consider keeping the beam on, but only allow the beam to be transported to a certain element in the beam line, *e.g.*, by using an inserted mechanical beam stopper. In case of a synchrotron, one might decide to stop the slow extraction and store the beam in the synchrotron. In this case, an additional fast kicker magnet in the beam line to the treatment areas can be used to suppress protons that "leak out" of the synchrotron. For cyclotrons, one should limit the duration of this type of interruption to avoid unnecessary accumulation of radioactivity in and around the beam stopper. In case of a synchrotron, one might completely decelerate the beam in the synchrotron and, in some cases, dump the low-energy beam on a beam dump when the waiting time would be so long that beam losses would start to activate the machine.

Most of the beam interrupting components can receive a “beam off” command from different systems. At PSI these systems are the machine control system (see Sec. 8.3) and the safety systems PSS, RPS and PaSS.

Beam interrupting components implemented at PSI as well as those used in commercial facilities are devices typical for cyclotron/synchrotron laboratories. When using external ion sources (*e.g.*, ECR electron cyclotron resonance ion source) in ion therapy facilities, or staged accelerator systems (*e.g.*, an injector followed by a synchrotron), beam interruption can be done with similar methods. With a synchrotron, however, one should realize that an interruption in the injection line or at the ion source is decoupled from the beam to the treatment room. In this section an overview of components that turn off the beam will be given. This is followed by a discussion of their use and the implications for the time and actions that are needed after an interruption to get the beam back in the treatment room again.

8.2.1 Beam Interrupting Components

When a synchrotron is used, there are different options to stop the beam before it enters the beam transport system. One could stop the radio frequency (RF) kicker that performs the slow extraction process, and thus reduce the extracted intensity. One could also use a fast kicker magnet in the ring to dump the stored particles on a beam dump. This can be done immediately in case of a severe emergency, or after deceleration to reduce the amount of radioactivity in the beam dump. The method (or methods) used depends on the type of synchrotron and the manufacturer. In addition, one can shut off the ion source. In general, more than one of these actions can be used to achieve safety redundancy.

In a cyclotron facility, the devices that can turn the beam off include fast and normal mechanical beam stoppers, and fast deflection magnets in the beam line. In addition, one can switch off the RF acceleration voltage of the cyclotron or the ion source arc current, or use a fast electrostatic deflector in the center of the cyclotron. Below, some details of the beam interrupting devices used at PSI are listed as examples, starting from the center of the cyclotron.

As in all proton cyclotrons, the ion source is located at the center of the cyclotron and at PSI it is of the "cold cathode" type (Forringer *et al.*, 2001). The performance of such a source is compromised when it undergoes a fast switch-off (within < 1 min). Moreover, because the beam intensity decay is slow when the source is switched off, taking several fractions of a second, the source should only be switched off in severe cases. In general, some instability after switching on again might be expected in any type of ion source.

The next beam interruption device is a set of parallel plates, mounted near the center of the cyclotron. Between these plates an electric field in the vertical direction can be generated. This field deflects the protons, which still have low energy, in the vertical direction, so that they are stopped on a collimator that limits the vertical aperture. This very fast (40 μs) system stops the protons before they are accelerated to energies at which they can produce radioactivity.

The RF of the cyclotron offers two options to switch the beam off: a reduced power mode (in which a fraction of the nominal RF-power is applied), or switching the RF completely off. The reduced mode also prevents the beam from being accelerated. This mode is used for non-severe reasons to switch off the beam, thus allowing a fast return of the beam. The reaction time is less than 50 μs.

After extraction from the cyclotron, the first beam-intercepting device is a fast kicker magnet, AMAKI. When the current in this magnet is switched on, it deflects the beam within 50 μs onto a beam dump next to the beam axis. This kicker magnet is the main “beam on-off switch” used during therapy. It plays an essential role in the spot-scanning technique used at PSI. The magnet is equipped with an independent magnet current verification device as well as with magnetic field switches to measure whether the magnet has reacted within an appropriate time.

The mechanical beam stopper, BMA1 (reaction time < 1 s), is located downstream of AMAKI. This stopper is only opened when beam is allowed downstream. When closed, the cyclotron can be ramped up and the extracted beam can be measured and prepared independently of the status of the other beam lines or treatment rooms (see Fig. 8.3).

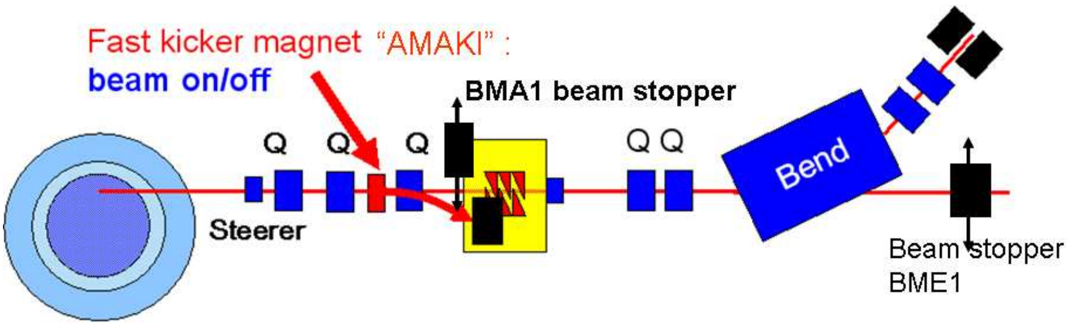

Figure 8.3. The first beam line section with a fast kicker magnet serving as main beam "on/off" switch. (Courtesy of PSI)

A mechanical stopper, BMx1, is located at the start of each beam line section specific for a treatment room (“x” indicates beam line/treatment room B, C, D or E). This stopper must be closed in order to allow persons to enter a treatment room. Only one of the BMx1s can be open at a time to prevent the beam from entering the wrong room due to a magnet failure.

In the beam line leading to each treatment room an additional fast mechanical stopper, BMx2 (reaction time < 60 ms), is inserted for longer beam interruptions and when a PaSS interlock trip occurs. The beam stoppers are also used to stop the beam in normal operation and to measure the beam current. Furthermore, a moveable neutron stopper (a block of iron) is mounted just upstream of the hole in the wall through which the beam line enters the treatment room. The neutron stoppers are not allowed to be struck directly by the proton beam and can therefore only be inserted when the preceding BMx1 stopper is closed. Otherwise an interlock trip will be generated.

8.2.2 Use of the Different Beam Interrupting Components

When the beam is stopped for normal operation reasons, the appropriate actuator is selected to minimize the activation and radiation load as well as to minimize the time to get back to stable operation. For beam interruptions up to a few minutes, the fast kicker magnet AMAKI is used. For longer interruptions, the goal is to stop the beam at low proton energy in the cyclotron with the vertical deflector.

In case of a detected error state, the beam is switched off by one of the safety systems. Table 8.1 lists the various beam-intercepting actuators and when they are used by the three safety systems. The major factor that determines which device is to be used is the reaction time. The combination of reaction time and dose rate determines the extra dose received by the patient when the beam is shut down during treatment due to an error condition. The goal of the Patient Safety System is to limit the extra dose in such cases. This goal is discussed more specifically in Sec. 8.5.1, where two types of errors are described. The first is an extra dose due to an error in the dose application, but dealt with by, for example, the dual monitor system. The extra unintended dose must be lower than 10 % of the fraction dose (IEC, 1998). At PSI, we aim for less than 2 % of the fraction dose, *i.e.*, typically 4 cGy for Gantry-1. The second dose error is more serious and falls under the "radiation incident" category. In case of a radiation incident, the goal of the Patient Safety System is to prevent an unintended extra dose larger than 3 Gy (see Sec. 8.1.2 and 8.5.1).

Table 8.1. Beam-Intercepting Actuators and their Use In PSS, PaSS, and RPS. (Courtesy of PSI)

Beam turn-off method used[a]	**Personnel Safety System PSS**	**Patient Safety System PaSS**	**Run Permit System RPS**
kicker magn.AMAKI		ALOK [b]	ILK [d] from beam line
Fast stopper BMx2		ALOK	
RF cyclotron "reduced"		ATOT [c]	ILK from beam line
RF cyclotron "off"	alarm	ETOT: Emergency off	ILK from cyclotron
Ion source off	alarm	ETOT: Emergency off	ILK from cyclotron
Beam stopper BMA1		ATOT	ILK from beam line
Beam stopper BMx1	when alarm in x, otherwise status check only	ATOT	
Neutron stopper x	when alarm in x, otherwise status check only		when BMx1 closes

---

[a] The first column indicates which of the Beam-off switches is used when one of the three safety systems (PSS, PaSS and RPS) generates a signal listed in column 2, 3 and 4 respectively.

[b] "ALOK" indicates a local PaSS alarm, caused by a device within a treatment room.

[c] A more serious alarm, "ATOT" indicates a global alarm from the PaSS, which requires general beam off.

[d] "ILK" means "interlock signal," and "x" represents a given beam line toward a specific treatment room (B,C,D, *etc*.).

Table 8.2 shows the list of switching devices with the response times of the actuators and the approximate response time of the beam detectors and processing electronics. The calculated extra dose deposition includes the complete system response time. With the regular beam setting for Gantry-1, which has 100 nA extracted from the cyclotron, the dose rate of the pencil beam in the Bragg peak (*i.e.*, a volume of < 1 cm^3) is approximately 6 Gy/s. When the Patient Safety System detects an error, *e.g.*, the beam has not been switched off on time, it will switch off the RF. The extra dose is then 0.09 cGy, which is far below the maximum error of 4 cGy.

Table 8.2. Response times for beam interruption by the different beam stop methods and estimated extra dose deposition at Gantry 1 at PSI for two cases with different extracted beam intensities Ip.[a] (Courtesy of PSI)

Device	**Response time** Device, sensor &electronics	**Dose** with 6 Gy/s (*Ip*=100 nA) nominal case	**Dose** with max. intensity (*Ip*=1000 nA) worst case
Kicker magn. AMAKI	50 µs 100 µs	0.09 cGy	0.9 cGy
RF cyclotron “off” RF cyclotron “reduced”	50 µs 100 µs	0.09 cGy	0.9 cGy
Ion source	20 ms 100 µs	12 cGy	120 cGy
Fast Beam stop. BME2	60 ms 100 µs	36 cGy	360 cGy
Beam stopper BME1	< 1 s	<6 Gy	<60 Gy
Beam stopper BMA1	< 1 s	<6 Gy	<60 Gy

[a] Note that the maximum possible current extracted from the cyclotron in normal operation conditions is only a factor 10 larger than the normal current during Gantry-1 operation.

When using a cyclotron, an unintended increase of the beam intensity can occur. In a synchrotron this might also happen due to extraction instabilities; however, the number of protons is limited to those stored in the ring. In a cyclotron an unintended increase of the beam intensity might happen due to, for example, a sudden crack in the aperture of the ion source. To limit the beam intensity, fixed collimators in the central region of the cyclotron are provided. These are designed such that they intercept most of the unwanted additional intensity because protons originating from such an event are not well-focused. When the intensity becomes higher than allowed (this limit depends on the application; for eye treatments at PSI, it is a few times higher than for treatments at the gantry), it will be detected by the permanently installed beam-intensity monitors at the exit of the cyclotron. These monitors will cause an alarm signal and the two fast-switching devices (AMAKI and RF) will stop the beam. Even though there will be a time delay in the signaling and the operation of the devices, the extra dose will stay below 3 Gy, as specified in Sec. 8.1.2 and 8.5.1. To prevent the extremely unlikely event that these fast and redundant systems fail, mechanical beam stoppers are also inserted into the beam line to stop the beam. Due to their longer reaction time a higher excess dose will be given to the patient, but only in case both fast systems fail (see Table 8.2).

8.3 Control Systems, Mastership, and Facility Mode

The operation of the accelerator and beam lines (*e.g.*, setting the current of a power supply, inserting a beam monitor, measuring the beam intensity) is done by means of a control system. The safety systems must work independently of the control system. The only interactions between the safety systems and the control system are receiving and sending status information. Because the concept of the control system architecture is related to the goals and the design of the safety systems, some essential aspects are discussed in this section. Questions such as who is in control in case of having multiple treatment rooms (mastership), who can do what (machine access control) and when (facility mode), and how is a separation of (safety) systems guaranteed, need to be considered in any design. In this section these aspects will be elucidated by discussing the concepts used at PSI.

8.3.1 Control Concept

At PSI, a rigorous separation has been achieved between the responsibilities of cyclotron and beam transport lines and those related to the treatment equipment. This decouples the tasks and responsibilities of the machine as a beam delivery system and a user who decides whether the beam is accepted or not for a treatment.

This separation is reflected in the control system architecture (see Fig. 8.4). A Machine Control System (MCS) controls the accelerator and beam lines and it only controls the machine performance itself. Each treatment area has its own Therapy Control System (TCS). Each TCS communicates with the MCS *via* a Beam Allocator (BAL), a software package that grants the TCS of the requesting area exclusive access (the Master status) to the corresponding beam line up to the accelerator. Also, it grants the Master TCS a selected set of actions. This includes control of the degrader, beam line magnets and kicker, and the right to give beam on/off commands. The Master TCS will ask the MCS *via* the BAL to set the beam line according a predefined setting list. Independently of the MCS, the Master TCS will start, verify, use, and stop the beam.

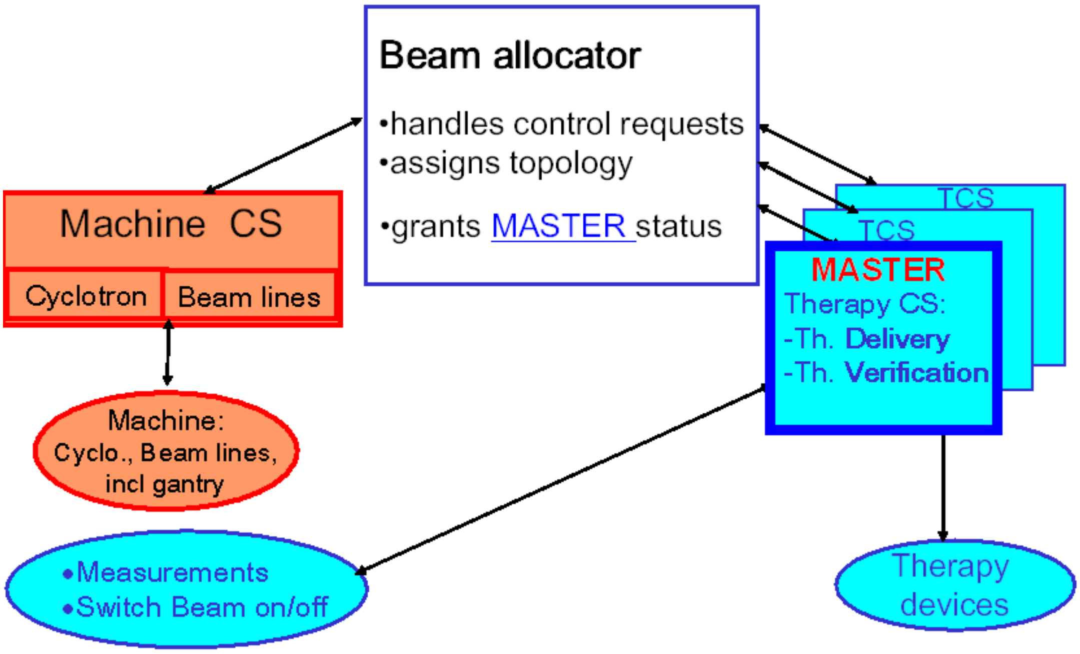

Figure 8.4. Concept of the different control systems. Only one of the Therapy Control Systems (TCS, right side) has mastership over the facility and can set beam line components *via* the Beam Allocator (BAL). Necessary measurements and beam on/off is done directly by the Master TCS. (Courtesy of PSI)

8.3.2 Separation of Systems

The separation of the safety systems as well as the control systems extends to the cabling of the hardware, and if possible to the hardware itself (*e.g.*, ion chambers). Each system has its own signal cables and limit switches. As can be seen in Figure 8.5, the closed (“in”) position of a mechanical beam blocker is equipped with three limit switches, one for each safety system.

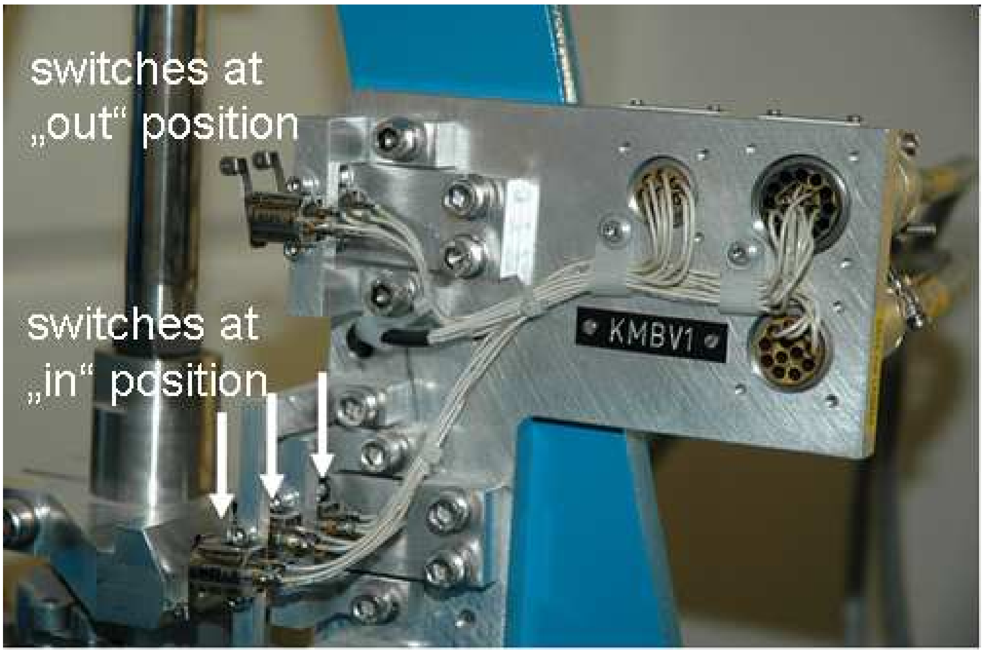

Figure 8.5. Partial view of a mechanical actuator of a stopper. Each safety system (for machine, personnel, and patients) has its own signal, resulting in three limit switches on this stopper. (Courtesy of PSI)

8.3.3 Facility Modes

In order to organize when certain operator actions are allowed, three different facility modes have been defined. The Therapy Mode is used for patient treatment. The Diagnostic Mode is used for tuning a beam line which is allocated to an area with Master status. Normally no patient treatment is allowed. However, in case of a minor problem (*e.g.*, bridging a RPS interlock signal due to a problem with a vacuum pump), this mode can be used to finish a treatment. Special rules apply in this case (see Sec. 8.6.1). The facility can only be in Therapy Mode or Diagnostic Mode when requested by the control system of a treatment room. The Machine Mode is used for the daily setup of the machine and allows beam tests to be made with the accelerator and the energy degrader. In Machine Mode, the facility safety system is set to a virtual user area "accelerator"; opening of all the beam stoppers BMx1 is disabled and beam cannot be directed to the user areas.

Only the operator of the treatment area that has obtained mastership is able to set the facility mode to Therapy Mode or Diagnostic Mode and use the beam. Switching from an area which is in Diagnostic Mode to an area in Therapy Mode requires a procedure which first forces the beam line and current setting into a safe state.

8.3.4 Treatment Procedure and Typical Operator Actions

The way a facility is operated is strongly site dependent. At PSI there is an operator crew in a main control room (24hrs/day, 7 days/week) and there are local radiation therapists (or therapy operators) at every treatment room. The task of the operator in the main control room is to prepare and check the accelerator and beam lines early in the morning and to store specific machine parameters for several standard beam intensities for the day. When these activities have been completed, the mastership is handed over to the first treatment area, where QA checks are to be performed. This QA comprises the set-up and check of the scanning parameters, dose delivery, and interlock system.

During the day, until the last patient has been treated, the radiation therapists are responsible for setting the machine and safety systems in the mode that allows patient treatment or switching of treatment areas. Changing facility mode is done *via* a well defined procedure that validates the integrity of the system.

When a particular room is ready to receive beam for a patient treatment, the radiation therapist in that treatment room requests mastership from the Beam Allocator application (BAL; see Sec. 8.3.1) to be able to start therapy operation. Mastership is granted when not possessed by another treatment room. For efficient use of the beam time, the radiation therapist of each treatment room needs to be informed of the status and progress of the treatments in the other rooms. Although not yet implemented at PSI, one could imagine a screen showing the expected time left until mastership is released by the current Master treatment room. In most commercial systems, the control system has an application which provides information about the treatment status and patient flow in each treatment room and proposes or alerts the next treatment room in the queue to get mastership.

When mastership has been obtained and the patient is ready for treatment, the radiation therapist selects the steering file and presses the “GO” button. This starts the computer program on the Therapy Control System (TCS) that executes the treatment. The TCS executes the sequence of commands listed in the steering file for this treatment that was generated by the treatment planning system. This file contains all necessary parameters and the appropriate order of actions to perform the treatment. After the treatment has reached a normal end, the kicker magnet AMAKI deflects the beam automatically to stop the beam and, in addition, beam stopper BMx2 is inserted automatically. When mastership is released (treatment is completed) or the room is to be entered by the therapist, beam stoppers BMA1 and BMx1 are also inserted as well as the neutron stopper.

In case of an interlock trip during treatment, the radiation therapist who has mastership determines the cause by checking the displays of the interlock system and the error log. When the problem is transient or can be solved, the system is reset by the radiation therapist and the spot scanning continues where it had stopped. If the treatment cannot be resumed within a few minutes (depending on the patient), the partial treatment is logged and documented and the patient is taken from the gantry to the preparation room. On the other hand, when an interlock occurs, the mastership can be given to the main control room so that the problem can be solved by a machine operator. When the problem has been solved, the patient will be brought back to the gantry and repositioned. After getting back the mastership, the procedure for restarting an interrupted treatment is performed and then the treatment will continue at the spot number (and its corresponding position) where the treatment had stopped. The TCS always keeps track of the spot number and the monitor units applied using a power fail safe procedure.

8.3.5 Hardware

In the sections dealing with the respective safety systems, details of the hardware are given. In general, one should try to use well-proven components and systems. Aspects to consider when selecting hardware are: robustness; fail-safe design; which transient states are possible; what if the device is switched off or cables not connected; robustness and signaling of overflow or signal saturation; time response (speed as well as reproducibility); possible SIL level; and certification by manufacturer. Programmable Logic Controllers (PLCs) can be used for user interface applications and general control functions. In general, however, PLCs are not allowed to be used in safety systems. Therefore, some companies have developed dedicated and certified safety PLCs. To reach the required level of safety, special concepts (*e.g.*, redundancy) have been integrated into the PLC design. One part of these concepts is a rigorous test program that is to be performed after any small change in a program of the PLC.

When speed or a reproducible time response is an issue (*e.g.*, in switch-off systems) advanced logic components and/or Digital Signal Processors (DSPs) are preferred.

8.4 Personnel Safety System

A Personnel Safety System (PSS) needs to be robust to prevent irradiation of staff or other persons; however, it needs a certain flexibility to ensure reliable beam operation and both fast and easy access to areas where patients are treated. Considerable experience exists with such systems in accelerator laboratories and radiation therapy departments, although there are different constraints in these applications. In a proton or ion therapy facility, the philosophies of an accelerator laboratory and a radiation therapy department must be combined. The PSS used at PSI is based on the philosophy of an accelerator laboratory, but for the application in the treatment rooms it has implemented an extension dedicated to patient treatment. The accelerator laboratory type of system that is normally installed at the PSI accelerator complex is applied to the access control of the room for experimental measurements and to the cyclotron/beam-line vaults. Access to these areas is controlled (*via* PSS) by the operators in the permanently manned control room for all accelerators at PSI. The necessary communication with these operators when entering these areas is usually organized differently in a hospital-based facility. On the other hand, the system used for the therapy rooms at PSI is not much different from the system used in a hospital-based proton or ion therapy facility.

8.4.1 Purpose

The purpose of a PSS is to prevent people from reaching areas where beam can be delivered, which can eventually result in an accidental exposure due to particle or photon irradiation. Specifically, a PSS has to ensure that no beam can be transferred into an area accessible to personnel. On the other hand, personnel access has to be inhibited if beam operation is possible in that area. Furthermore, PSS signals can be used to monitor radiation levels in accessible controlled areas for which the beam is blocked. The radiation dose in an accessible area could be too high due to uncontrolled beam losses in a neighboring area. A PSS must generate an interlock trip when an event occurs (*e.g.*, a limit switch opens) or when a critical situation develops that does not concur with the actual PSS access conditions, *i.e.*, an excessive dose rate in an accessible controlled area.

The designation of different areas according to their radiological risk and the associated accessibility concepts are applied in different way in different countries. For example, areas can be designated as “forbidden,” “locked,” “controlled,” “surveyed,” “public,” “staff only,” *etc*. Sometimes one uses indications of radioactivity levels (“red,” “yellow,” “green”), or lamps indicating “beam on” or “beam off.” These assignments should be associated with a risk evaluation that determines the area classification and the access rules. Apart from the goal to protect persons, it is also of utmost importance that the access rules are easy to understand and maintain. When access is “forbidden,” it should not be possible to enter accidentally.

In most countries, areas with an enhanced radiological risk must be designated as “controlled areas” or the equivalent. For such areas, access restrictions must exist as prescribed by local rules. The most common requirement is the wearing of individual dose meters applicable to the potential type of radiation occurring (*i.e.*, neutron radiation or γ radiation) in order to detect the radiation exposure of people. Frequently, a level classification is assigned to the controlled areas. This level classification is related to the level of contamination risk (leading to an adapted dress code), possible dose rate (potentially resulting in restricted occupation time), or possible presence of the proton beam. The accessibility depends on the area type (level) and status of the PSS, and can be designated "free" or "limited" access areas for authorized personnel.

8.4.2 Modes of Operation

At PSI the access status of an area is set by the PSS and is displayed at a panel near the entrance of the area (see Sec. 8.4.5.1).

It can have the following modes:

- "free": doors can be open.
- "limited": the door is unlocked remotely by the control room operator and each person must take a key from the key bank at the door.
- "locked": the door is locked. It is possible that there is beam present in the area or that the dose rate in the area is above a specified limit.
- "alarm": Beam is switched off and the door of the area is released.

Treatment rooms can only be "free" or "locked." When the area has the status "locked," either a door is locked or a light barrier will detect a person entering the room and initiate an alarm; see below.

When a treatment room "x" is accessible, one must ensure that no beam can be sent into the room. This is guaranteed by inserting the beam stopper BMx1 and a neutron stopper just upstream of the hole in the wall where the beam line enters this room. When the accessible area is a beam-line vault or the cyclotron vault, the cyclotron RF as well as the ion source must be switched off.

Table 8.3 summarizes the different conditions and actions related to the PSS access control. In order to switch the mode of an area from “free” to “limited” or “locked,” a search for persons in the room is mandatory. The search is made by the last person leaving the area, who must push several buttons at different locations in the area, to ensure the complete search has been made. Also, an audio signal warns people to leave the area (except in treatment rooms). When a person wants to enter the cyclotron/beam-line vaults or the experimental vault again, this can be done in “limited” access mode. In this mode, each person entering the area must take a key from the key bank near the door. In order to switch the access mode of an area from “limited” to “locked,” no search is needed, but all keys must be in the key bank at the entrance door of the area before that vault’s status can be switched back to “locked.” Only when the area is “locked” can BMx1 and its neutron stopper can be removed from the beam line, or the cyclotron RF and ion source can be switched on again.

Table 8.3. Status and actions of beam intercepting components for area access.

Reason for beam off by Personnel Safety System	**Beam interrupting components**				**Other constraints**
	RF	Ion source	BMx1	Neutron stopper x	
allowed access to user area x			must be in	must be in	Area dose monitor being checked (prevents access or evokes alarm signal when dose rate too high)
allowed access in cyclotron/beam-line vault, when the area is (limited) accessible	must be off	must be off			Lead shield must be at degrader Area dose monitor being checked (prevents access or evokes alarm signal when dose rate too high)
Emergency off request / Alarm signal in cyclotron/beam-line vault e.g: -emergency button pressed -failure in safety relevant element -local dose monitor above limit	Switch off	Switch off			
Emergency off request / Alarm signal in user area x e.g: -emergency button pressed -failure in safety relevant element -local dose monitor above limit	Switch off	Switch off	insert	insert	

The entry of all vaults and rooms is through a maze. A polyethylene door is mounted at the exit of the mazes to the patient treatment rooms. It is not closed during patient treatment in order to allow fast access to a patient by the therapist. In the maze, a light barrier that detects a person who enters the corridor is used in Therapy Mode. The light barrier will trigger an alarm that stops the RF and the ion source, and inserts BMx1 and corresponding neutron stopper x. The polyethylene door must be closed for non-therapy operation in a treatment room (*e.g.*, QA, calibrations, *etc.*).

At PSI, the access status of the cyclotron vault and experimental room can only be changed remotely by an operator in the control room. The treatment rooms, however, have a local control panel near the door by which the medical staff can set the access status themselves (“free” or “locked”).

Emergency-off buttons are mounted in each area and in each vault to initiate an alarm by a person who is still in the room. This alarm switches the RF and ion source off, inserts BMx1, and unlocks the area entrance doors.

8.4.3 Rules of Beam Turn-Off

Because the PSS basically only gives permission to turn the RF and ion source on after checking if all conditions are met, it is, in effect, passive with respect to beam control. During beam operation, if one of the conditions is not met anymore, permission will be removed and the beam (RF and ion source) turned off. It is important that the beam does not automatically switch on after it has been switched off due to an interlock trip and reset again. Beam must always be turned on deliberately by the operator.

8.4.4 Functional Implementation

The PSS system runs on a dedicated safety PLC that is certified for safety functions. It is constructed of fail-safe components and is completely separated from other systems. This system has its own dedicated actuator supervision sensors (*e.g.*, limit switches or end switches) to register the status of connected actuators such as beam stoppers. When the PSS causes an interlock trip, beam and neutron stoppers will "fall" into their closed position. At PSI, the motion of mechanical stoppers is controlled by compressed air in addition to gravity (fail-safe). In the event of such a trip, several devices (mechanical stoppers but also RF) will act at the same time to intercept the beam.

A separate PSS input is present in the control boxes of the RF and ion source. A fail-safe signal must be present to allow "RF on" or "ion source on." If a cable is disconnected the signal is absent.

8.4.5 Components

The PSS is only one part of a system ensuring personnel safety. Several devices, with different functions, are connected to this system; some of them will be discussed here.

8.4.5.1 Area Access Control. The implementation of access control in a hospital-based proton or ion therapy facility can be organized quite similarly to a conventional radiation therapy facility. The way it is implemented might also depend on the distance and visual contact situation between the control desk of the radiation therapist and the door to the treatment room.

At PSI, dedicated cabinets for area access control are installed near the entrance door of each area (Fig. 8.6). The cabinets at the therapy areas are equipped with touch panels that guide the user through a menu of required sequential actions to allow access or to allow beam into the area. The panels and key banks at the beam-line vault are installed next to a dedicated PSS door. The access status is visible on the panel and a direct intercom connection to the control room is used if one wants to change the access status or enter the vault in “limited” access mode. At PSI, no “beam on” type of signal is displayed at the door. The access status only forbids or permits beam in the area, but whether beam is actually sent to the area is up to the user.

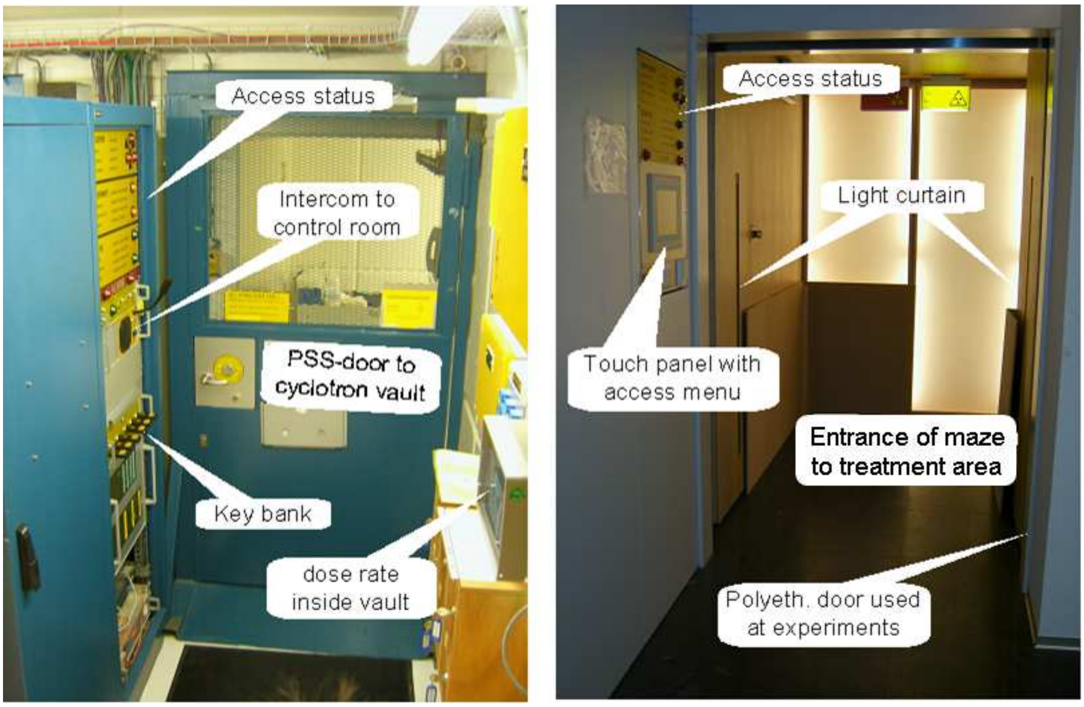

Figure 8.6. Personnel Safety System units at vault entrance and treatment room entrance (Courtesy of PSI)

For radiation shielding purposes, the cyclotron vault has an additional concrete door at the maze entrance from the vault. Inside the vaults, warning lights and audio signals provide warning before the access mode is changed to “locked.” In order to prevent patient confusion, this is not done inside the patient treatment rooms at PSI. However, local regulations might impose that beam on/off warning lights must also be installed or used in the treatment rooms.

8.4.5.2 Detectors. Monitors are mounted in the vaults, controlled areas, and patient treatment rooms to protect personnel against radiation. The extension for proton or ion therapy is that monitors must be installed for gamma rays as well as for neutrons (see Chapter 4). They must trigger an alarm that leads to an interlock trip when the area is in “free” or in “limited” access mode and a dose rate above a preset threshold is detected. At the exits of the cyclotron/beam-line vault and the experimental area at PSI, hand/foot monitors are installed. These are not connected to the interlocks.

8.5 Patient Safety System

The purpose of the Patient Safety System (PaSS) is to guarantee a safe treatment of the patient. This has led to the rigorous separation of the functionality and safety systems, and it enabled PSI to build a dedicated patient safety system that can be understood by all users and is well documented. The design of the PSI system is based on general safety concepts and safety functions, which can in principle be applied in any particle therapy system. In this section, the concepts of the system will be discussed first, followed by a more detailed description of the components with the purpose of illustrating how the concepts can be realized in practice. As a consequence, a simplified description is given, which is by no means complete. Finally, the PSI-specific situation with respect to spot scanning will be addressed, followed by the rules applied by the Patient Safety System to turn the beam off, and some remarks on quality assurance.

8.5.1 Purpose

The task of any Patient Safety System (PaSS) is to comply with established requirements in order to reach the essential safety goals for patient protection. These goals can be formulated as such:

Goal 1: No serious radiation accidents can occur.

The most serious accident is the delivery of an unintended high dose to the patient. The first and most important safety aim is to prevent an unintentional additional dose delivery greater than 3 Gy (5 % of the total treatment dose) in case of a serious radiation accident. This is in correspondence with the claim to prevent all Class I hazards of type A and B, following the classification for accidental exposures published in ICRP Publication 86 (2000). The main concerns here are the monitoring and beam switch-off systems.

Goal 2: To apply the correct and known radiation dose.

Any error in the total treatment dose delivered can adversely increase the probability of an unacceptable treatment outcome (lack of tumor control or increased complications). Therefore, the second safety goal is to prevent the occurrence of such errors during therapy, *e.g.*, by using a redundant dose monitoring system in the nozzle of the beam delivery system, and to limit the unintended extra dose due to such errors (IEC, 1998). This extra unintended dose must be lower than 10 % of the fraction dose (IEC, 1998). At PSI, we aim for less than 2 % of the fraction dose, *i.e.*, 4 cGy for Gantry 1.

Goal 3: To apply the dose to the correct position in the patient.

The main concerns here are the control of the position (checked by means of a position sensitive ionization chamber in the nozzle of the beam delivery system) and energy of the beam (checked by means of a dedicated position signal from the degrader and dedicated reading of bending magnet settings), and the position of the patient (by prior CT scout views, x rays, cameras).

Goal 4: Applied dose and dose position must be known at all times.

If the irradiation is interrupted at any time, the dose already given and the beam position of the last irradiated spot must be known.

8.5.2 Functional Requirements

The amount of the dose and the position of applied dose are monitored by the therapy control and therapy monitoring systems (see Sec. 8.5.4.4). The major requirement of the Patient Safety System is to cause an interlock trip when the tolerance limits in this monitoring system or in other devices that monitor the status of crucial beam line and accelerator components are exceeded. In general, this is in analogy with the usual practice in radiation therapy to record and verify all the parameters being used during the treatment and interrupting treatment in case of lack of agreement between planned and real values. This could be done, *e.g.*, by using commercially available "Record and Verify" systems. Due to the high degree of complexity of a proton or ion therapy system, the number of available parameters is too large to deal with for this purpose. Furthermore, many parameters have no relevance for the safety of the patient. Therefore, in every proton or ion therapy facility, a selection of the relevant parameters or components must be made. The most important components selected for this purpose at PSI are described in 8.5.4.4. Further, to avoid severe radiation accidents and to switch off the beam with high reliability after each interlock trip, a redundant system is needed with multiple independent systems to switch the beam off.

In a system with multiple treatment areas, a secure patient treatment in a pre-selected area must be guaranteed, and interferences from other parts of the treatment facility are not allowed. It is usually required to be able to sequentially treat patients in different areas with a switching time of less than one minute.

An important specification is the independence of the treatment delivery and patient safety system from the rest of the facility, including the control systems. Signals from beam-line devices that are crucial for safe operation are directly sent to the PaSS and the PaSS also has direct access to selected components to switch off the beam. It has no other control functionality than switching off the beam (or preventing the switching on of the beam) through these devices when an anomaly has been detected.

When a patient is being treated, all parameter values, patient-specific or field-specific devices, and machine settings must be read from the steering file generated by the treatment planning system. One important task of a Patient Safety System is to ensure that the correct devices are installed and that parameters are set appropriately.

At PSI, the irradiation of the patient is fully automated, which minimizes human errors. Before the treatment starts, the TCS reads all instructions, all settings of the machine, and dose limits from the steering file. The PaSS also obtains the steering file information and makes an independent check of the settings of selected critical devices, and watches relevant measurements. When the treatment is started, the TCS starts the actions listed in the steering file and the PaSS verifies online if the treatment proceeds as it should.

8.5.3 Description of System

During a treatment the (Master) TCS sends instructions to the machine control system (MCS; see Sec. 8.3). In the scanning technique employed at PSI, the beam-line settings vary during the treatment because the energy is also a beam-line parameter. For each beam energy the MCS will use a predefined setting of the beam line (a “tune”). During treatment, a sequence of tunes is used as given in the steering file. For every tune to be set, the TCS sends the tune information to the MCS, which sets the degrader and the magnets, *etc.* accordingly. The TCS automatically verifies whether the beam characteristics satisfy the user’s needs by means of dedicated beam diagnostics at the checkpoints, and dedicated signals from energy-defining elements. The Patient Safety System automatically checks the results of these verifications (Jirousek *et al.*, 2003). Note that all these readout systems are exclusively used by PaSS (the blue boxes in Figure 8.7).

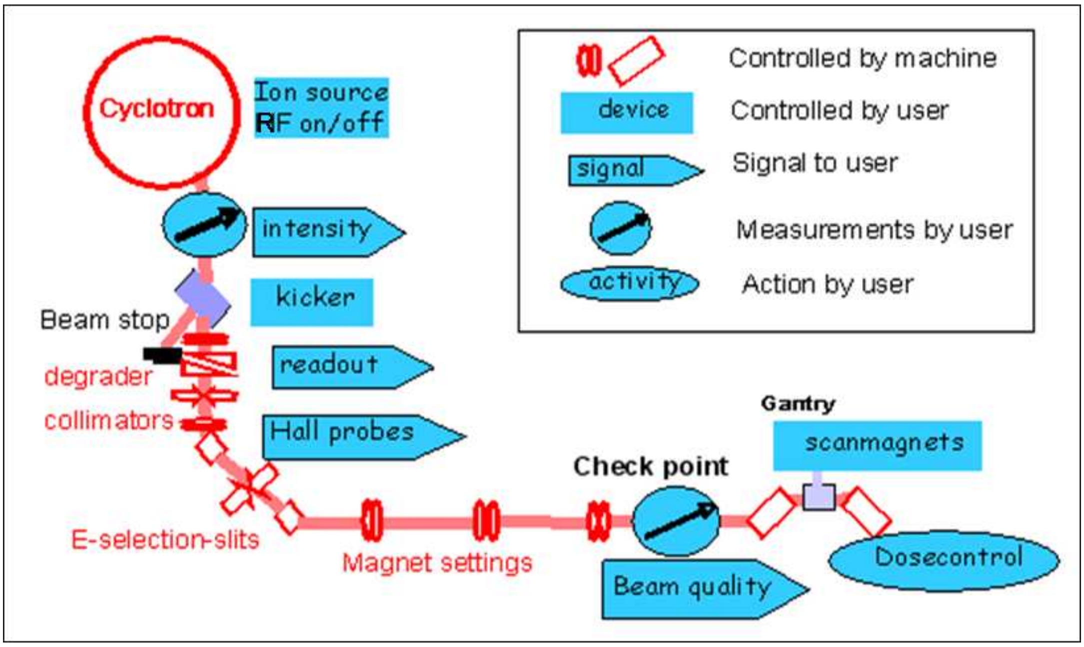

Figure 8.7. Signals to the Therapy Control System (TCS) of Gantry-1 are indicated with arrow-boxes. Components controlled by TCS or PaSS are in rectangular boxes and the oval boxes indicate actions by TCS or PaSS. (Courtesy of PSI)

8.5.4 Components of the Patient Safety System (PaSS)

The main components of the PaSS are:

- *Main Patient Safety Switch and Controller (MPSSC)*: a central system that controls and supervises a unique beam line and area allocation to only one user or treatment room (the Master treatment room) at a time and transfers or triggers interlock signals.
- *Local PaSS*: the local patient safety system of a treatment room. It monitors all the signals (interlocks, warnings, and "beam ready") connected to the Therapy Control System of this room and can generate and send interlock to the local and remote actuators.
- *Emergency OR module*: a logic unit that generates a global emergency beam switch-off signal when either one of the input signals (permanent hardwired connections to each room) is not OK. Being an independent device, it also acts as a redundant safety switch-off for the MPSSC.
- *Detectors and sensors*: these devices are wired to the PaSS.
- *Beam-interrupting devices*: The actuators are activated by the local PaSS or the MPSSC. For details, see Sec. 8.2.

In addition, there are modules that read out, digitize, process, and distribute the signals observed by the PaSS. These modules perform simple tasks that are implemented in the low-level software or firmware and they operate independently of the control system (except for being informed of the currently requested beam tune).

In the following subsections, the function of the main components will be described in more detail. The organization of these components and the interlock signals are schematically displayed in Figure 8.8.

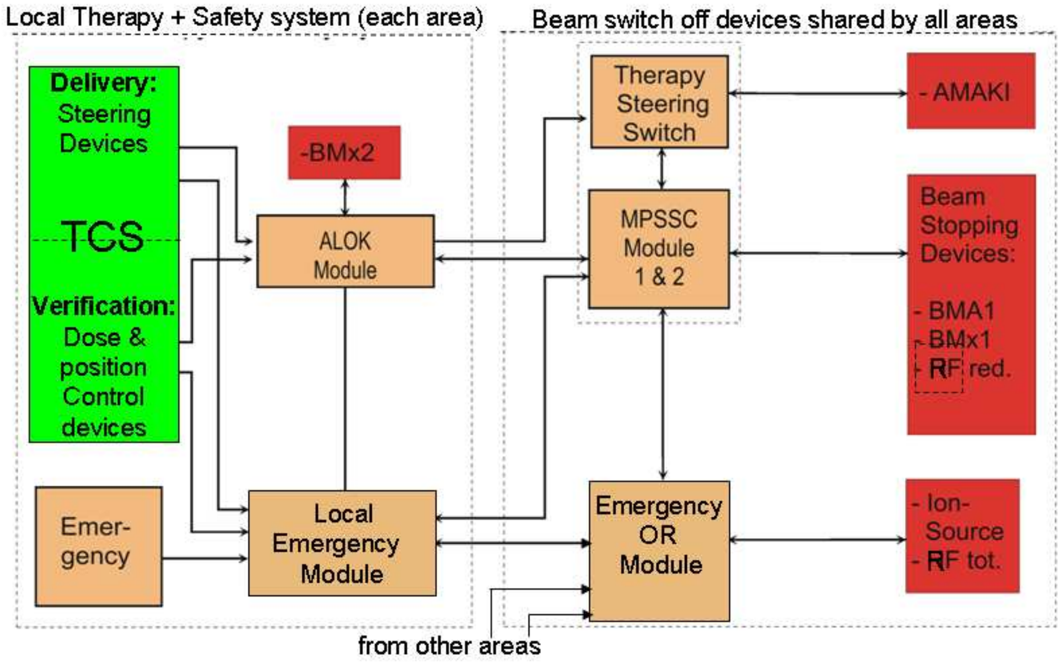

Figure 8.8. The connection between the Local Patient Safety System (Local PaSS) of each area, MPSSC (Main Patient Safety Switch and Controller), Emergency OR module, and the major beam on/off actuators. The Emergency OR can generate a redundant switch-off signal, hard wired to the RF and ion source. (Courtesy of PSI)

8.5.4.1 Main Patient Safety Switch and Controller (MPSSC). A topology control must be implemented because there are multiple areas for treatments or experiments in the facility. Therefore an important part of the PaSS is a central system that controls and supervises a unique beam line and area allocation to only one user or treatment room (the Master treatment room) at a time. This system, the Main Patient Safety Switch and Controller (MPSSC) monitors the interlocks and status of all areas. It controls and supervises a unique beam line and area allocation, then sets its operation mode according to a defined sequence including the following steps: disable the beam stoppers in all areas, and enable the beam stopper BMx1 in the Master area. The exclusivity of the granting of the Master status will be checked. It enables the Master user to switch on the beam with the fast kicker magnet AMAKI and monitors its interlock status. Further, it monitors the operation of the beam interrupting elements and verifies the consistency of the ready signal returned from the RPS and the reservation signal from the Master area's TCS.

The MPSSC will generate an interlock trip when one of the above mentioned supervising functions indicates an error or an inconsistency. In case of a failure within the MPSSC and its beam actuators, the MPSSC will generate a emergency interlock (ETOT). The MPSSC has been built in a redundant configuration.

8.5.4.2 Local PaSS. Each area has a local PaSS that is embedded in the TCS of that area and that monitors all the signals connected to that TCS (interlocks, warnings, and "beam ready"). It generates and monitors the pre-programmed AMAKI on/off signals for the spot scanning and monitors the remaining beam intensity in case of a local interlock ("ALOK"). The local PaSS can stop the beam independently of the MPSSC status. In that case, it uses BMx2, a beam blocker controlled solely by the local PaSS.

8.5.4.3 Emergency OR Module. The Emergency OR module is a logic unit with permanent hardwired input signals from each area. It generates a global emergency switch-off signal “ETOT” when there is an alarm signal on one of the input signals. The electronic module has no processors and acts as a simple logic “OR” function to pass the alarm signal on to the RF and ion source. As can be seen in Fig. 8.8, the system is independent of the MPSSC and user status. The independence guarantees that the beam can be turned off by two redundant systems, each using a separate set of beam stopping actuators.

8.5.4.4 Detectors and Safety-Relevant Signals from Various Components. The signals from the beam line leading to an interlock trip from the Patient Safety System come from:

- dedicated beam-intensity monitors (ionization chambers and a measurement of the secondary electron emission from a foil, which does not saturate at high intensities);
- dedicated reading of the degrader position to verify the set beam energy;
- dedicated magnetic switch in the AMAKI kicker magnet, to verify the action of the kicker;
- dedicated Hall probes in each dipole magnet to verify the set beam energy;
- beam-intensity monitors at the check points (specific locations along the beam line); and
- monitors in the beam nozzle upstream of the patient, which encompass, *e.g.*, the plane parallel-plate ionization chambers “Monitor 1” and “Monitor 2” in Gantry 1 (the latter of which has a larger gap to provide diversity in sensor design; see Sec. 8.5.5). “Monitor 3” is an ionization chamber to measure dose as well, but equipped with a grid to have a faster response. In addition, multi-strip ion chambers are used to measure the position of the pencil beam during the delivery of each spot.

8.5.4.5 Electronics, Hardware, and Firmware. The hardware platform used in the PaSS is an Industry Pack (IP) carrier board with a Digital Signal Processor (DSP). The logic to switch the beam off is embedded in IP modules mounted on the carrier boards.

Several methods are used to enhance reliability. Redundant paths were implemented between the subsystems to avoid single points of failure. Further , diagnostic coverage in the system has been increased. At the same time, care has been taken to use diversity, such as the use of different types of sensors, but also the supervision of actuators as well as the direct detection of the beam status.

8.5.5 Implementation of the PaSS for Dose Application and Spot Scanning

The use of the spot-scanning technique at PSI has specific implications for the design details of the patient safety system. In Gantry-1 of PSI, the dose is applied by discrete spot scanning. The eye treatment in OPTIS2 is performed with a scattered beam that is applied as a sequence of single spots from the control system point of view. The application of the spot sequence is the most critical phase in terms of patient safety. The dose is delivered as a sequence of static dose deliveries ("discrete spot scanning"). The dose of each spot is checked online during the spot application. The dose delivery is based on the signal of Monitor 1 in the treatment nozzle. For the dose verification, two other monitors, Monitor 2 and Monitor 3, are used.

The radiation beam is switched off by the fast kicker magnet AMAKI between each spot delivery. The Monitor 2 preset value is always programmed with a built-in safety margin added to the prescribed dose. If Monitor 1 fails, then the beam is switched off by the Monitor 2 preset counter. The spot overdose resulting from this delay is estimated to be at maximum 0.04 Gy, which is 2 % of the fraction dose (PaSS Safety Goal 2). This corresponds to a fault situation and therefore an interlock signal will be generated (beam switch-off with interruption of the treatment). If no interlock signals were generated and if all the measuring systems show that the spot deposition has been carried out correctly, the TCS sets the actuators, verifies actuators, and applies the next dose spot. The maximum dose per spot that can be planned or given is limited by the maximum value that is allowed to be stored in the register of the preset counter.

A fixed upper limit for the maximum dose and dwell time of a spot is defined within the hardware. These limits are checked by watchdogs (also called backup timers) in the PaSS. These are separate electronic counters measuring the spot dose and the spot dwell time. If a defined value is exceeded (counter overflow), then an error signal will be produced automatically. Each watchdog is set back to zero at the end of the irradiation and approval of the spot dose. If the beam remains switched on unintentionally, the watchdogs will prevent a patient overdose greater than the maximum defined spot dose.

8.5.6 Rules for Turning the Beam Off

The layout of the safety system for beam switch-off with the interconnections between local interlock modules and the shared beam switch devices is drawn schematically in Fig. 8.8. Here one can see the central role of the MPSSC. It checks the interlock status of all areas, enables the main user to switch the kicker AMAKI, and controls its interlock status. It controls the commands of the Master user and the operation of specific beam-interrupting elements (reduced RF and the mechanical beam stoppers BMA1 and BMx1).

The PaSS can generate beam-off signals with different consequences and for different reasons. The signals and their causes are listed in Table 8.4. Their interlock level (hierarchy) and the switch-off action are listed in Table 8.5.

Table 8.4. The interlock signals of the Patient Safety System and examples of their causes.

PaSS interlock signal	**General cause**	**Examples of specific causes**
ALOK	error detected within the local therapy control system	• Functional errors in a local device of TCS • Crossing of dose or position limits checked in the steering software.
ATOT	severe error detected in the allocated user safety system or error in the shared safety system that might lead to an uncontrolled deposition of dose or injury of a person	• Error in the allocated user safety system • AMAKI error, area reservation error • Watchdog error in any TCS which is in Therapy Mode • Error in any of the beam switch-off devices BMA1, BME1, RF red. • Error in MPSSC boards and firmware
ETOT	emergency signal generated in any user safety system or error detected in ATOT generation	• Emergency button pushed in any user safety system • Beam detected and ATOT interlock present • Error in the beam switch-off devices, RF off, or ion source • Error in the local supervision of emergency status.

Table 8.5. The hierarchy of the interlock signals from the Patient Safety System and the components that will switch off the beam.

<table>
<tr><th colspan="4">Interlock Level /
Beam Switch-Off Control Function</th><th>Measures for Beam-Off</th></tr>
<tr><td rowspan="7">ETOT</td><td rowspan="5">ATOT</td><td rowspan="2">ALOK</td><td>Beam Off command</td><td>Send current through kicker magnet AMAKI</td></tr>
<tr><td></td><td>Close local beam stopper BMx2</td></tr>
<tr><td colspan="2" rowspan="3"></td><td>Close beam stopper BMx1</td></tr>
<tr><td>Close beam stopper BMA1</td></tr>
<tr><td>Reduce RF power to 80%</td></tr>
<tr><td colspan="3" rowspan="2"></td><td>Switch off RF power</td></tr>
<tr><td>Switch off ion-source power supply</td></tr>
</table>

During treatment, all relevant safety checks are performed for each spot. If there is any discrepancy between the prescribed and measured values of dose (Monitor 1, 2) or spot position (multi-strip monitor in the nozzle of the gantry, or a segmented ion chamber in the nozzle of OPTIS2), or in the case of a technical fault, the result is always an immediate interruption of the treatment and the generation of a local interlock trip “ALOK.”

The watchdogs that check fixed upper limits for the maximum dose and dwell time of a spot will automatically produce a global interlock “ATOT” if a defined value is exceeded (counter overflow). Figure 8.8 also shows that, through the separate connection to the Emergency OR module, the local system has the redundant capability of generating a global switch-off signal (“ETOT”), independent of the beam-line Master. The ETOT controls the switch-off of the ion source and the RF system.

8.5.7 Quality Assurance

As described in Sec. 8.1.5, frequent checks are performed of the Patient Safety System and each treatment area. The checks are described in a QA manual, which also prescribes the frequency of the tests (daily, weekly, monthly, yearly, *etc.*).

During the building phase of the facility, a rigorous quality test program has been undertaken. Not all possible configurations of a complete system can be checked; therefore, a procedure has been developed for performing separate bench tests during the production phase of the electronic components that are used in the Patient Safety System. With a simulation program that generates many initial conditions for the electronic circuit boards under test, the boards have been tested and automatic test reports have been generated.

8.6 Machine Safety: Run Permit System

A machine safety interlock system should be used in every accelerator system. The tasks of this interlock system are protection of the machine and its subsystems from damage due to wrong actions or faulty devices, and to prevent unwanted high beam intensities. In the following sections, the system will be described in more detail.

8.6.1 Purpose

The machine interlock system at PSI is called the Run Permit System (RPS). It checks the status of signals from all beam lines and cyclotron devices and compares these signals with the requested topology (beam-line sections that will be used). The beam can only be switched on when the RPS allows this; *i.e.*, when its "beam-off" signal is "false." This is done when a topology has been reserved and when all devices in this topology have been set to their values and return an "OK" status. After the beam-off status has been set to false, it sends a "machine ready" signal to the (Master) TCS, which then can actually switch on the beam (with the kicker magnet AMAKI).

The task of the RPS is to prevent the machine from being damaged, to prevent unnecessary activation, and to prevent higher beam intensities than those allowed by the authorities. It does not check beam optics, or whether the calculated settings of magnets are correct. However, from beam diagnostics, several signals are observed online and bending magnet currents should be within intervals corresponding with the used beam lines. Furthermore, the RPS will switch the beam-off to "true" when fatal device faults are registered, such as an excessive temperature in a power supply or excessive pressure in the vacuum system.

A bridge can be set to ignore these signals in the case of non-severe failure signals. In Therapy Mode, however, no bridge is allowed. A protocol, signed by designated persons, must be used for cases when one has to run with a bridged signal ("degraded mode"). Running in Therapy Mode with a bridged signal is only allowed when an approval procedure by qualified persons is carried out, and only for a limited time (*e.g.*, one day).

Some functions of the RPS are redundantly implemented in the PaSS for therapy purposes (*e.g.*, a limit on the maximum allowed beam intensity). The "responsibilities" of RPS and PaSS, however, are strictly separated and the systems do not rely on each other.

8.6.2 Functional Requirements

The RPS is not intended to be used for personnel or patient safety; therefore, the requirements with respect to redundancy and "fail-safe" are less critical. However, for the RPS, general design rules (*e.g.*, cabling, where a failed connection invokes a safe state) apply that result in a high safety standard. An important requirement that applies specially for a proton therapy facility is that the RPS must be able to quickly change its settings, as the operational requirements change quickly. Because an important requirement for a proton therapy facility is a high uptime and high availability for the treatments, this requires special precautions against false alarms and the implementation of a user interface with clear data logging, failure recognition, and easy retrieval of the sequences that can lead to an interlock trip.

Most of the auxiliary devices possess their own device-safety system that checks the proper working of the devices. From these devices only status signals and, when available, detailed error information are sent to the RPS inputs. These are sent over fail-safe connections. Connections to the actuators as well as the end switches of beam stopping devices are separate from the ones of PaSS and PSS.

8.6.3 Description of System

Before turning the beam on, the topology and operation mode (Therapy, Diagnostic or Machine) are sent to a computer program that generates the unique logic configurations and defines the beam switch-off chain. Unlike the switch-off chain, which is hardwired to the various components that can switch off the beam; the data acquisition and element control are performed by software in VME computers.

The user interface (Fig. 8.9) indicates the RPS status by coloring the cyclotron and beam line sections. Green indicates that the section is ready for beam; red that it is not ready for beam; and yellow that it is ready, but with “bridges” applied. When an interlock trip from the RPS occurs, the cause of the sequences is logged and listed with time stamps in a message window. When clicking with the mouse on a beam line section, a screen with the status of all its components will show up for further analysis.

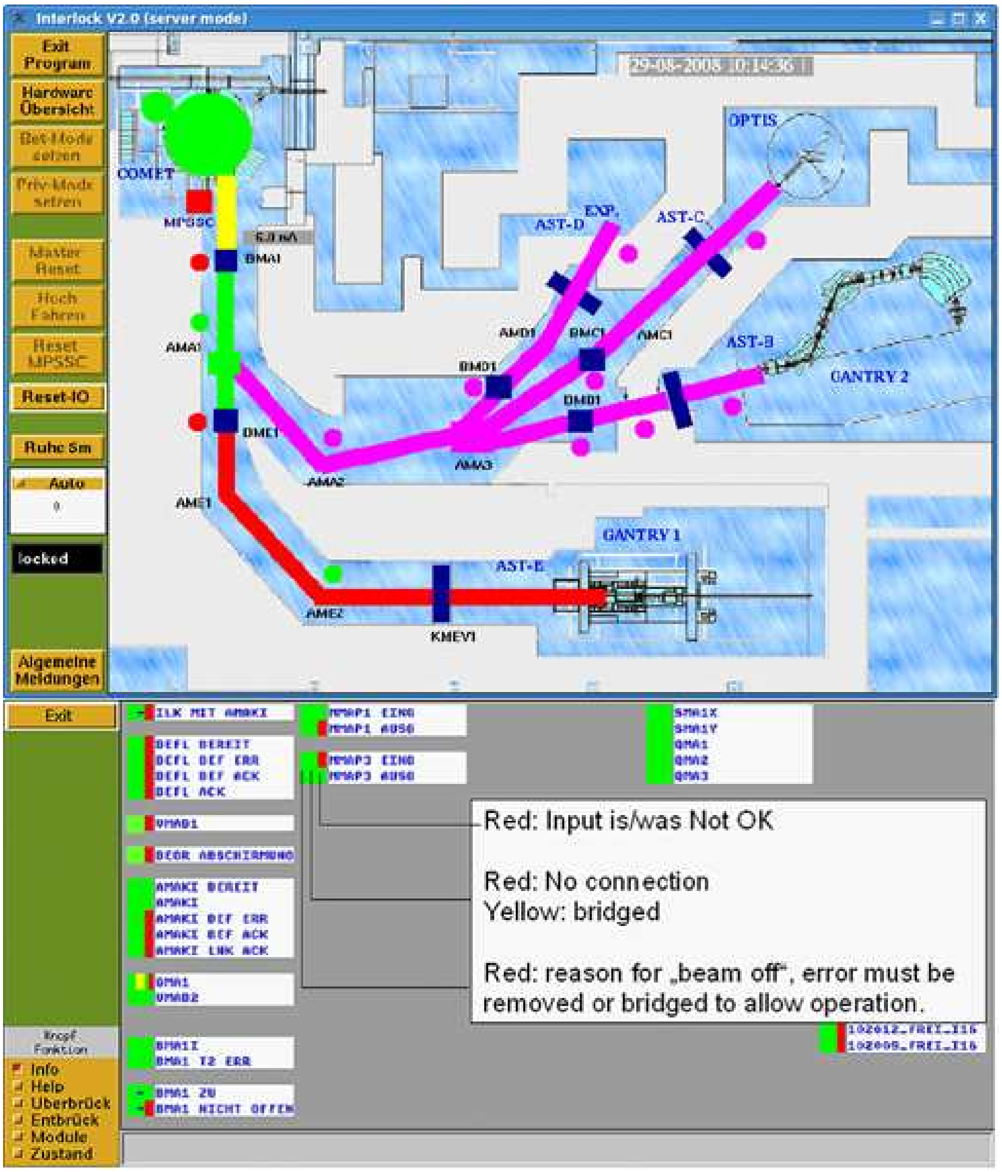

Figure 8.9. Overview of the machine interlock (RPS) status. In the top figure, the beam line colors indicate the status of the corresponding beam line section. The bottom figure shows the status of individual components in the "bridged" first beam line section. (Courtesy of PSI)

8.6.4 Components and Conditions That Are Checked

Inputs that cause the logic to generate a switched-off signal are deduced from the status of the following component groups:

a) Active devices: power supplies of bending magnets, quadrupole magnets, and steering magnets belonging to the selected topology. The status signals yield information on the cooling, the ready signal (actual current = requested current), and a few general signals of the power supply.
b) Devices with a verification/guarding role: beam current monitors (also ratios between monitors), slit and collimator currents, beam currents from beam stoppers, temperature measurements, water flow controls, *etc*.
c) Configuration (topology) dependent parameters: magnet current intervals, positions of the neutron stoppers, beam stoppers, vacuum valves in the beam line, *etc*.

Many of the interlock trips will be caused by a device error, sent by a device that is part of the active topology. When an error occurs, it usually has an effect on the beam characteristics and beam losses. Some changes in beam losses can also lead to interlock trips. This intrinsic redundancy is very useful and, with the aid of proper logging with time stamps, helps in a quick diagnosis of a problem consisting of a chain of events.

8.6.5 High-Reliability Components and Fail-Safe Design

The Run Permit System is built of dedicated modules (Run Permit System module, RPSM), each having multiple I/O channels. Up to 4 RPSMs are mounted on a VME Basis plate. The direction of the signal flow is programmed in firmware (XILINX). The logic that determines whether to switch off or not is part of this program. Therefore, this logic is independent of the machine control system. The control system communicates with the RPSMs *via* I/O-Computers (IOCs) to obtain the switch-off diagnostics and information for the visualization programs, or to perform periodic tests.

The following security measures are incorporated in each RPSM:

a) The inputs and outputs are equipped with three-wire connections, so that disconnections or shorts are recognized and the module changes its state into “NC” (not connected) or “err” (short).
b) Every RPSM is characterized by an individual ID number.
c) The consistency of the internal firmware program is checkable by means of Check Sums.
d) The Machine Control System must use an encrypted communication procedure to write into the control register or the bypass/bridging register. The new content of these registers must be identified with the ID number of the RPSM in which has been written.
e) The data read from an RPSM must be signed with its ID number.
f) The RPSMs have a dedicated input which can be used by the Machine Control System to enforce a beam-off command for test purposes. The time interval between this command and the actual beam off is logged and can be read by the Machine Control System.

8.6.6 Rules for Turning the Beam Off

Beam turn-off is implemented by the Run Permit System with a three-fold redundancy:

a) fast kicker magnet AMAKI;
b) RF at reduced power so that particles are not accelerated. This is done if the fast kicker magnet does not react within 50 to 100 μsec, or when the integrated charge on BMA1 increases by a certain value within a preset time. This last error condition has been implemented to avoid unnecessary activation;
c) Switch-off the ion source when the RF does not react in time.

8.6.7 Tests and Quality Assurance (QA)

The frequency of component periodic tests depends on their relative importance in terms of machine security.

Several tests are performed online: cross checks with PaSS signals; checks of cable connections between RPS modules and those of the input signals; and check-sum verification of the XILINX contents.

In the Machine Control System, several test procedures are built-in and are typically run every week:

a) test switch-off *via* primary switch-off channels and analysis of switch-off times;
b) checks of contacts of limit switches of moveable components (*e.g.*, beam stoppers);
c) checks of interlocks on the allowed topology-dependent current interval of magnet currents.

Additional tests are done after maintenance or repair. These tests are of course related to the components involved in the maintenance or repair.

Glossary

absorbed dose (*D*): The quotient of $D = \frac{d\bar{\varepsilon}}{dm}$ where $d\bar{\varepsilon}$ is the mean energy imparted by ionizing radiation to matter of mass dm. The unit is J kg^{-1} .The special name for the unit of absorbed dose is the gray (Gy).

activation: The process of inducing radioactivity by irradiation.

ALOK: Local interlock signal from PaSS

AMAKI: Fast magnetic kicker used at PSI

ambient dose equivalent (*H*(d)*): The dose equivalent at a point in a radiation field that would be produced by the corresponding expanded and aligned field in the ICRU sphere (diameter = 30 cm, 76.2 % O, 10.1 % H, 11.1 % C, and 2.6 % N) at a depth, *d*, on the radius opposing the direction of the aligned field (ICRU, 1993). The ambient dose equivalent is measured in Sv.

attenuation length (λ): The penetration distance in which the intensity of the radiation is attenuated by a factor of e.

BAL: Beam allocation system

BMxi: Mechanical beam stopper number i, in beam line x at PSI

bridge: The bypass of a system, irrespective its status.

compound nucleus: A metastable nucleus that exists during the time between the fusion of a target nucleus *X* and a impinging particle *p* and the separation into a residual nucleus *Y* and a outgoing particle *q*. Niels Bohr introduced this concept in 1936.

computational human phantom: Computer representation of the human body

conversion coefficients: The quotient of the dose equivalent under specified conditions and the associated field quantity (for example, fluence).

Coulomb barrier: The repulsive Coulomb force between the target nucleus and the charged particle that an impinging charged particle does not have enough velocity to overcome ; hence, the collision does not take place. The Coulomb barrier lowers the probability of nuclear reactions of charged particles.

degrader: A system to slow down the particles to a chosen energy.

directional dose equivalent *H'(d, Ω)*: The dose equivalent at a point in a radiation field that would be produced by the corresponding expanded field in the ICRU sphere at a depth, *d*, on the radius in a specified direction, Ω (ICRU, 1993). The directional dose equivalent is measured in Sv.

dose equivalent (*H*): The product of *Q* and *D* at a point in tissue, where *D* is the absorbed dose and *Q* is the quality factor at that point. Thus, $H = Q\,D$. The unit of dose equivalent in the SI system of units is joules per kilogram (J kg^{-1}) and its special name is the sievert (Sv).

DSP: Digital Signal Processor

ECR source: An ion source often used for heavy ions, applying ionization by electron cyclotron resonance.

effective dose: Weighted sum of various organ or tissue doses using organ weighting factors

Emergency OR module: A logic "OR" unit used for an emergency-off.

equivalent dose (H_T): A quantity in a tissue or organ that is used for radiation protection purposes and takes into account the different probability of effects which occur with the same absorbed dose delivered by radiation with different radiation weighting factors (w_R). It is given by $H_{\mathrm{T}} = \sum_R w_R D_{T,R}$, where $D_{T,R}$ is the mean absorbed dose in the tissue or organ, T, due to radiation R, and w_R is the corresponding radiation weighting factor. The unit of equivalent dose is the sievert (Sv).

ETOT: Global emergency switch-off signal from PaSS

excess absolute risk (EAR): Rate of an effect in an exposed population minus the rate of the effect in an unexposed population

excess relative risk (ERR): Rate of an effect in an exposed population divided by the rate of the effect in an unexposed population minus 1

exemption: The determination by a regulatory body that a radioactive source need not be subject to regulatory control on the basis that the exposure due to the source is too small.

external radiation: Secondary radiation produced in the treatment head

fluence (*Φ*): The quotient of $d\underline{N}$ *by* $d\underline{a}$ where $d\underline{N}$ is the number of particles incident on a sphere of cross-sectional area $d\underline{a}$. The unit is m^{-2} or cm^{-2}.

generalized intra-nuclear cascade: Description of nuclear interactions at energies up to a few GeV which is based on a cascade of elastic and inelastic collisions between hadrons and nucleons inside the nuclei involved in the interaction. Nuclear potentials, Fermi motion, and relativistic effects are taken into account.

general-purpose particle interaction and transport Monte Carlo codes: Monte Carlo codes which allow the simulation of hadronic and electromagnetic cascades in matter in a wide energy range. They can therefore be used in a large variety of studies and is not restricted to certain applications.

impact parameter: In a nuclear collision between a target nucleus X and an impinging particle p, the distance between the locus of p and the straight line of the same direction that passes the center of X. The impact parameter is measured at a position far from X, where any force does not affect the locus of p.

interlock system: Interruption system of the particle beam

internal radiation: Secondary radiation produced in the patient

IOC: Computer dedicated communication (Input/Output)

isobar: A nucleus having the same mass number but having a different atomic number.

isobaric yield: The isobaric yield is the production probability of nuclei having a specific mass number after a nuclear collision.

Local PaSS: The local patient safety system of an area

MCS: Machine Control System

microscopic model: Description of nuclear interactions based on models for interactions between the constituents of the colliding hadrons and nuclei (*e.g.*, nucleons, quarks, and gluons).

MPSSC: Main Patient Safety Switch and Controller

nuclear fragmentation: The break-up of a nucleus as a consequence of an inelastic interaction.

operational quantity: A quantity with which, by means of its measurement, compliance with dose limits may be demonstrated. Examples of operational quantities are ambient dose equivalent, directional dose equivalent, and personal dose equivalent.

OPTIS: A proton therapy beam line dedicated for eye treatments.

out-of-field dose: Dose outside the area penetrated by the primary beam

PaSS: Patient Safety System

personal dose equivalent ($H_p(d)$): The dose equivalent in soft tissue at an appropriate depth, d, below a specified point on the body. The personal dose equivalent is measured in Sv.

PLC: Programmable Logic Controller

prompt radiation: Radiations that are immediately emitted by nuclear reactions of primary accelerated particles.

protection quantity: Dosimetric quantities specified in the human body by the ICRP. Examples of protection quantities are effective dose and equivalent dose.

PSI: Paul Scherrer Institute, Switzerland

PSS: Personnel Safety System

quality factor: Conservatively defined weighting factor to indicate the biological effectiveness as a function of linear energy transfer

radiation weighting factor: Conservatively defined weighting factor to indicate the biological effectiveness as a function of particle type and energy for external whole body exposure

relative biological effectiveness (RBE): Ratio of the doses required by two different types of radiation to cause the same level of effect for a specified end point

relative risk (RR): Rate of disease among groups with a specific risk factor divided by the rate among a group without that specific risk factor

residual radiation: Primary accelerated particles and their secondary radiations of neutrons and charged particles produce radionuclides. Radiations, such as photons and beta rays, which are emitted by disintegrations of these induced radionuclides are called residual radiations.

resonance: A phenomenon that occurs when the projectile particle energy coincides with the energy level of the target nucleus, and a large peak appears in the reaction cross section.

RF: Radiofrequency; the accelerating voltage of an accelerator

RPS: Run Permit System, also called accelerator/machine interlock system

RPSM: Dedicated modules in RPS having multiple I/O channels

saturation activity: The maximum radioactivity induced by irradiation. Saturation activity is reached when the irradiation time becomes longer than several times the half-life.

scattered radiation: Radiation caused by scattering of the primary beam

secondary radiation: Radiation by secondary particles produced when the primary beam interacts with beam-line components or within patients

SIL: Safety Integrity Level; the robustness of such a measure or a device

spallation: The process in which a heavy nucleus emits a large number of particles as a result of the collision. between the target nucleus and a high-energy heavy projectile nucleus. Any kind of nucleus lighter than the disintegrating heavy nucleus can be produced in a spallation reaction.

stylized phantoms: Computer representation of the human body using simple geometrical shapes

TCS: Treatment Control System

Thick Target Yield (TTY): Secondary radiation emission from a target, of which the thickness is slightly larger than the range of the irradiating charged particles. Examples of TTY quantities are the total neutron yield and the neutron energy angular distribution.

trip: A signal that switches the beam off.

tune: Predefined setting of the beam line

variance reduction techniques: One of several procedures used to increase the precision of the estimates that can be obtained for a given number of iterations.

voxelized phantom: Computer representation of the human body using a grid geometry

watchdog: Backup timer; electronic counters measuring the duration of dose application

References

AESJ (2004). Atomic Energy Society of Japan, *Radiation Dose Conversion Coefficients for Radiation Shielding Calculations*, AESJ-SC-R002:2004 (Atomic Energy Society of Japan, Tokyo).

Agosteo, S. (2001). "Radiation Protection at Medical Accelerators," *Radiat. Prot. Dosim.* **96,** 393-406.

Agosteo, S., Fasso, A., Ferrari, A., Sala, P., R., Silari, M. and Tabarelli de Fatis, P. (1995). “Double differential distributions attenuation lengths and source terms for proton accelerator shielding,” in *Proc. Shielding Aspects of Accelerators, Targets and Irradiation Facilities (SATIF-2)*, 12-13 October 1995, Geneva (Nuclear Energy Agency, Organization for Economic Co-operation and Development, Paris).

Agosteo, S., Fasso, A., Ferrari, A., Sala, P.,R., Silari, M., and Tabarelli de Fatis, P., (1996a). "Double differential distributions and attenuation in concrete for neutrons produced by 100-400 MeV protons on iron and tissue targets." *NIM Phys. Res.* **B114,** 70-80.

Agosteo, S. *et al.* (1996b). "Shielding Calculations for a 250 MeV Hospital-based Proton Accelerator," *NIM Phys. Res.* **A 374**, 254-268.

Agosteo, S., Birattari, C., Corrado, M.,G., and Silari, M., (1996c). “Maze design of a gantry room for proton therapy,” *NIM Phys. Res. A* **382**, 573-582.

Agosteo, S., Birattari, C., Caravaggio, M., Silari, M., and Tosi, G. (1998). "Secondary neutron and photon dose in proton therapy," *Radiother. Oncol.* **48,** 293-305.

Agosteo S., Nakamura, T., Silari, M., and Zajacova, Z. (2004a). “Attenuation curves in concrete of neutrons from 100 to 400 MeV per nucleon He, C, Ne, Ar, Fe and Xe ions on various targets,” *NIM Phys. Res.* **B217,** 221-236.

Agosteo, S., Magistris, M., Mereghetti, A., Silari, M., and Zajacova, Z. (2004b). “Shielding data for 100 to 250 MeV proton accelerators: double differential neutron distributions and attenuation in concrete,” *NIM Phys. Res.* **B265**, 581-589.

Agostinelli, S., *et al*. (2003). “GEANT4 - A simulation toolkit,” *NIM Phys. Res. A* **506**, 250-303.

Ahmed, S.N. (2007). *Physics and Engineering of Radiation Detection*, (Academic Press, San Diego, CA).

Alberts, W.G., Dietze, E., Guldbakke, S., Kluge, H., and Schuhmacher, H. (1989). “International intercomparison of TEPC systems used for radiation protection,” *Radiat. Prot. Dosim.* **29**, 47-53.

Alghamdi, A.A., Ma, A., Tzortzis, M., and Spyrou, N.M. (2005). "Neutron-fluence-to-dose conversion coefficients in an anthropomorphic phantom," *Radiat. Prot. Dosim.* **115,** 606-611.

Alghamdi, A.A., Ma, A., Marouli, M., Albarakati, Y., Kacperek, A., and Spyrou, N.M. (2007). "A high-resolution anthropomorphic voxel-based tomographic phantom for proton therapy of the eye," *Phys. Med. Biol*. **52,** N51-59.

Allison, J., *et al*. (2006). “GEANT4 Developments and Applications,” *IEEE Transactions on Nuclear Science* **53**, 270-278.

Amaldi, U. and Silari, M. (Eds.) (1995). *The TERA Project and the Centre for Oncological Hadrontherapy*, The TERA Foundation, (INFN, Frascati. II ed).

Amaldi, U. and Kraft, G. (2005). "Recent applications of Synchrotrons in cancer therapy with Carbon Ions," *Europhysics News* **36**, 114-118.

ASTM (2003). ASTM International, *Cement Standards and Concrete Standards*, ASTM Standard C657 (ASTM International, West Conshohocken, PA).

ASTM (2007) . ASTM International, *Standard Test Methods for Instrumental Determination of Carbon, Hydrogen, and Nitrogen in Petroleum Products and Lubricants*, ASTM Standard D5291 (ASTM International, West Conshohocken, PA).

Avery, S., Ainsley, C., Maughan, R., and McDonough, J. (2008). "Analytical Shielding Calculations for a Proton Therapy Facility," *Radiat. Prot. Dosim.* **131 (2),** 167-179.

Awschalom, M. (1987). *Radiation Shielding for 250 MeV Protons,* (Fermi National Accelerator Laboratory, USA).

Awschalom, M. and Sanna, R.S. (1985). “Applications of Bonner sphere detectors in neutron field dosimetry,” *Radiat. Prot. Dosim.* **10**, 89-101.

Azzam, E.I., Raaphorst, G.P., and Mitchel, R.E. (1994). "Radiation-induced adaptive response for protection against micronucleus formation and neoplastic transformation in C3H 10T1/2 mouse embryo cells," *Radiat. Res.* **138,** S28-31.

Ballarini, F., Biaggi, M., Ottolenghi, A., and Sapora, O. (2002). "Cellular communication and bystander effects: a critical review for modelling low-dose radiation action," *Mutat. Res.* **501,** 1-12.

Ban, S., Nakamura, H., and Hirayama, H. (2004). “Estimation of amount of residual radioactivity in high-energy electron accelerator component by measuring the gamma-ray dose rate,” *J. Nucl. Sci. Tech.*, Suppl. **4**, 168-171.

Barbier, M. (1969). *Induced Radioactivity,* (North Holland Publ. Co., Amsterdam).

Barcellos-Hoff, M.H. (2001). "It takes a tissue to make a tumor: epigenetics, cancer and the microenvironment," *J. Mammary Gland Biol. Neoplasia* **6,** 213-221.

Bassal, M., Mertens, A.C., Taylor, L., Neglia, J.P., Greffe, B.S., Hammond, S., Ronckers, C.M., Friedman, D.L., Stovall, M., Yasui, Y.Y., Robison L,L., Meadows, A.T., and Kadan-Lottick, N.S. (2006). "Risk of selected subsequent carcinomas in survivors of childhood cancer: a report from the Childhood Cancer Survivor Study," *J. Clin. Oncol.* **24,** 476-483.

Battistoni, G., Muraro, S., Sala, P.,R., Cerutti, F., Ferrari, A., Roesler, S., Fasso, A., and Ranft, J., (2007). "The FLUKA code: Description and benchmarking," in *Proc. of the Hadronic Shower Simulation Workshop 2006, Fermilab*, 6-8 September 2006, M., Albrow, R., Raja Eds., *AIP Conference Proceeding* **896**, 31-49.

Battistoni, G., *et al.* (2008). “The FLUKA code and its use in hadron therapy,” *Nuovo Cimento* C **31**, 69-75.

Bednarz, B. and Xu, X.G. (2008). "A feasibility study to calculate unshielded fetal doses to pregnant patients in 6-MV photon treatments using Monte Carlo methods and anatomically realistic phantoms," *Med. Phys.* **35** (7).

BEIR (2006). *Health risks from exposure to low levels of ionizing radiation, BEIR VII, Phase 2*, National Research Council of the National Academy of Science (National Academies Press, Washington, DC).

BfG (2004). Bundesamt für Gesundheit, Abteilung Strahlenschutz, Sektion Aufsicht und Bewilligung,*Richtwerte für Ortsdosisleistungen in nuklearmedizinischen Betrieben,* (Eidgenössisches Departement des Innern EDI, Switzerland).

Bhattacharjee, D. and Ito, A. (2001). "Deceleration of carcinogenic potential by adaptation with low dose gamma irradiation," *In Vivo* **15,** 87-92.

Binns, P.J. and Hough, J.H. (1997). "Secondary dose exposures during 200 MeV proton therapy," *Radiat. Prot. Dosim.* **70,** 441-444.

Birattari, C., Ferrari, A., Nuccetelli, C., Pelliccioni, M., and Silari, M. (1990). “An extended range neutron rem counter,” *Nucl. Instr. and Meth.*, **A297**, 250-257.

Blettner, M. and Boice, J.D., Jr. (1991). "Radiation dose and leukaemia risk: general relative risk techniques for dose-response models in a matched case-control study," *Stat. Med.* **10** 1511-1526.

Boag, J.W. (1975). "The statistical treatment of cell survival data," pp. 40-53 in *Proc. of the Sixth, L.H. Gray Conference: Cell survival after low doses of radiation*, Alper, T., Ed.

Boice, J.D., Jr., Blettner, M., Kleinerman, R.A., Stovall, M., Moloney, W.C., Engholm, G., Austin, D.F., Bosch, A., Cookfair, D.L., Krementz, E.T., and *et al.* (1987). "Radiation dose and leukemia risk in patients treated for cancer of the cervix," *J. Natl. Cancer Inst.* **79**, 1295-1311.

Bozkurt, A., Chao, T.C., and Xu, X.G. (2000). "Fluence-to-dose conversion coefficients from monoenergetic neutrons below 20 MeV based on the VIP-man anatomical model," *Phys. Med. Biol.* **45,** 3059-79.

Bozkurt, A., Chao, T.C., and Xu, X.G. (2001). "Fluence-to-dose conversion coefficients based on the VIP-man anatomical model and MCNPX code for monoenergetic neutrons above 20 MeV," *Health Phys.* **81,** 184-202.

Brada, M., Ford, D., Ashley, S., Bliss, J.M., Crowley, S., Mason, M., Rajan, B., and Traish, D. (1992). "Risk of second brain tumour after conservative surgery and radiotherapy for pituitary adenoma," *BMJ* **304,** 1343-1346.

Brandl, A., Hranitzky, C., and Rollet, S., (2005). "Shielding variation effects for 250 MeV protons on tissue targets," *Radiat. Prot. Dosim.* **115**, 195–199.

Brenner, D.J. and Hall, E.J. (1992). "Commentary 2 to Cox and Little: radiation-induced oncogenic transformation: the interplay between dose, dose protraction, and radiation quality," *Adv. Radiat. Biol.* **16,** 167-179.

Brenner, D.J. and Hall, E.J. (2008) "Secondary neutrons in clinical proton radiotherapy:, A.charged issue," *Radiother. Oncol.* 86 (2), 165-170.

Brenner, D.J., Curtis, R.E., Hall, E.J., and Ron, E. (2000). "Second malignancies in prostate carcinoma patients after radiotherapy compared with surgery," *Cancer* **88,** 398-406.

Brenner, D.J., Doll, R., Goodhead, D.T., Hall, E.J., Land, C.E., Little, J.B., Lubin, J.H., Preston, D.L., Preston, R.J., Puskin, J.S., Ron, E., Sachs, R.K., Samet, J.M., Setlow, R.B., and Zaider, M. (2003). "Cancer risks attributable to low doses of ionizing radiation: assessing what we really know," *Proc. Natl. Acad. Sci. U.S.A.* **100,** 13761-13766.

Broerse, J.J., Hennen, L.A., and Solleveld, H.A. (1986). "Actuarial analysis of the hazard for mamary carcinogenesis in different rat strains after X- and neutron irradiation," *Leukemia Research* **10,** 749-754.

Broniscer, A., Ke, W., Fuller, C.E., Wu, J., Gajjar, A. and Kun, L.E. (2004). "Second neoplasms in pediatric patients with primary central nervous system tumors: the St. Jude Children's Research Hospital experience," *Cancer* **100**, 2246-2252.

Brugger, M., Khater, H., Mayer, S., Prinz, A., Roesler, S., Ulrici, L., and Vincke, H., (2005). “Benchmark studies of induced radioactivity produced in LHC materials, Part II: remanent dose rates,” *Radiat. Prot. Dosim.* **116**, 12-15.

Brugger, M., Ferrari, A., Roesler, S., and Ulrici, L., (2006). “Validation of the FLUKA Monte Carlo code for predicting induced radioactivity at high-energy accelerators,” *NIM Phys. Res. A* **562**, 814-818.

Calabrese, E.J. and Baldwin, L.A. (2000). "The effects of gamma rays on longevity," *Biogerontology* **1,** 309-319.

Calabrese, E.J. and Baldwin, L.A. (2003). "The hormetic dose-response model is more common than the threshold model in toxicology," *Toxicol. Sci.* **71,** 246-250.

Caon, M., Bibbo, G. and Pattison, J. (1999). "An EGS4-ready tomographic computational model of a 14-year-old female torso for calculating organ doses from CT examinations," *Phys. Med. Biol.* **44,** 2213-2225.

Caporaso, G. (2009). “High Gradient Induction Linacs for Hadron Therapy,” *1st International Workshop on Hadron Therapy for Cancer* 24 April – 1 May 2009, Erice, Sicily. http://erice2009.na.infn.it/TalkContributions/Caporoso.pdf, accessed May 15, 2009.

Carter, L.,L., and Cashwell, E.,D. (1975). “Particle-transport simulation with the Monte Carlo method,” *ERDA Crit. Rev. Ser*., (National Technical Information Service, Springfield, VA).

CFR (2007). Code of Federal Regulations, Title 10, Part 835, *Occupational Radiation Protection*, (U.S. Department of Energy, Washington, DC).

Chadwick, M.B., Oblozinsky, P., Herman, M., *et al.* (2006). “ENDF/B-VII.0: Next generation evaluated nuclear data library for nuclear science and technology,” *Nuclear Data Sheets* **107**, 2931-3060.

Chao, T.C. and Xu, X.G. (2001). "Specific absorbed fractions from the image-based VIP-Man body model and EGS4-VLSI Monte Carlo code: Internal electron emitters," *Phys. Med. Biol.* **46,** 901-927.

Chao, T.C., Bozkurt, A. and Xu, X.G. (2001a). "Conversion coefficients based on the VIP-Man anatomical model and GS4-VLSI code for external monoenergetic photons from 10 keV to 10 MeV," *Health Phys.* **81,** 163-183.

Chao, T.C., Bozkurt, A. and Xu, X.G. (2001b) "Organ dose conversion coefficients for 0.1-10 MeV external electrons calculated for the VIP-Man anatomical model," *Health Phys.* **81,** 203-214.

Chaturvedi, A.K., Engels, E.A., Gilbert, E.S., Chen, B.E., Storm, H., Lynch, C.F., Hall, P., Langmark, F., Pukkala, E., Kaijser, M., Andersson, M., Fossa, S.D., Joensuu, H., Boice, J.D., Kleinerman, R.A and Travis, L.B (2007). "Second cancers among 104,760 survivors of cervical cancer: evaluation of long-term risk," *J. Natl. Cancer Inst.* **99**, 1634-1643.

Chen, J. (2006). "Fluence-to-absorbed dose conversion coefficients for use in radiological protection of embryo and foetus against external exposure to protons from 100 MeV to 100 GeV," *Radiat. Prot. Dosim.* **118,** 378-383.

Chilton, A.B., Shultis, J.K., and Faw, R.E. (1984). *Principles of Radiation Shielding,* (Prentice-Hall Inc, Englewood Cliffs, NJ).

Cho, S.H., Vassiliev, O.N., Lee, S., Liu, H.H., Ibbott, G.S., and Mohan, R. (2005). "Reference photon dosimetry data and reference phase space data for the 6 MV photon beam from varian clinac 2100 series linear accelerators," *Med. Phys.* **32,** 137-148.

Chung, C.S., Keating, N., Yock, T. and Tarbell, N. (2008). "Comparative Analysis of Second Malignancy Risk in Patients Treated with Proton Therapy versus Conventional Photon Therapy," *Int. J. Radiat. Oncol. Biol. Phys.* **72** S8.

Cloth, P. *et al*. (1983). "The KFA-Version of the High-Energy Transport Code HETC and the generalized Evaluation Code SIMPLE," *Kernforschungsanlage Jülich*, Jül-Spez **196**.

Coutrakon, G..B. (2007). “Accelerators for heavy-charged particle radiation therapy,” *Technology in Cancer Research and Treatment,* **6(4)** Supplement.

Coutrakon, G., Bauman, M., Lesyna, D., Miller, D., Nusbaum, J., Slater, J., Johanning, J., Miranda, J., DeLuca, P.M., Siebers, J., and Ludewigt, B. (1990). "A prototype beam delivery system for the proton medical accelerator at Loma Linda," *Med. Phys.* **18 (6)**, 1093-1099.

Cristy, M. and Eckerman, K.F. (1987). "Specific absorbed fractions of energy at various ages from internal photon sources," Report ORNL/TM-8381/I-VII (Oak Ridge National Laboratory, Battelle, TN, USA).

Curtis, R.E., Rowlings, P.A., Deeg, H.J., Shriner, D.A., Socie, G., Travis, L.B., Horowitz, M.M., Witherspoon, R.P., Hoover, R.N., Sobocinski, K.A., Fraumeni, J.F. Jr. and Boice, J.D., Jr. (1997). "Solid cancers after bone marrow transplantation," *N. Engl. J. Med.* **336,** 897-904.

de Vathaire, F., Francois, P., Hill, C., Schweisguth, O., Rodary, C., Sarrazin, D., Oberlin, O., Beurtheret, C., Dutreix, A. and Flamant, R. (1989). "Role of radiotherapy and chemotherapy in the risk of second malignant neoplasms after cancer in childhood," *Br. J. Cancer* **59,** 792-796.

Debus, J. (1998). *Proposal for a dedicated Ion Beam Facility for Cancer Theray*, Groß, K.D., Pavlovic, M., Eds. (GSI, Darmstadt, Germany).

Dementyev, A.,V., and Sobolevsky, N.,M. (1990). “SHIELD-universal Monte Carlo hadron transport code: scope and applications,” *Radiation Measurements* **30**, 553-557.

Dennis, J.A. (1987). "The relative biological effectiveness of neutron radiation and its implications for quality factor and dose limitation," *Progress in Nuclear Energy* **20,** 133-149.

Diallo, I., Lamon, A., Shamsaldin, A., Grimaud, E., de Vathaire, F. and Chavaudra, J. (1996). "Estimation of the radiation dose delivered to any point outside the target volume per patient treated with external beam radiotherapy," *Radiother. Oncol.* **38,** 269-271.

DIN (2003). Deutsches Institut für Normung, e.V., *Medical Electron Accelerators – Part 2: Radiation Protection Rules for Installation*, German Technical Standards 6847 (Deutsches Institut für Normung, e.V., Berlin).

Dinter, H., Dworak, D., Tesch, K. (1993). "Attenuation of the neutron dose equivalent in labyrinths through an accelerator shield," *NIM Phys. Res.* A **330,** 507-512.

Dittrich, W. and Hansmann, T. (2006). "Radiation Measurements at the RPTC in Munich for Verification of Shielding Measures around the Cyclotron Area," in *Proc. Shielding Aspects of Accelerators, Targets and Irradiation Facilities (SATIF 8),* 22-24 May 2006, Gyongbuk, Republic of Korea (Nuclear Energy Agency, Organization for Economic Co-operation and Development, Paris).

Dorr, W. and Herrmann, T. (2002). "Second primary tumors after radiotherapy for malignancies. Treatment-related parameters," *Strahlenther Onkol* **178,** 357-362.

Edwards, A.A. (1999). "Neutron RBE values and their relationship to judgements in radiological protection," *J. Radiol. Prot.* **19,** 93-105.

Egbert, S.D., Kerr, G.D. and Cullings, H.M. (2007). "DS02 fluence spectra for neutrons and gamma rays at Hiroshima and Nagasaki with fluence-to-kerma coefficients and transmission factors for sample measurements," *Radiat. Environ. Biophys.* **46,** 311-325.

Eickhoff, H., Haberer, T., Schlitt, B., and Weinrich, U. (2003). "HICAT – The German Hospital- based light Ion Cancer Therapy Project," in *Proc. of the Particle Accelerator Conference (PAC03)*, 12-16 May 2003, Portland, Oregon.

Endo, S., Tanaka, K., Takada, M., Onizuka, Y., Miyahara, N., Sato, T., Ishikawa, M., Maeda, N., Hayabuchi, N., Shizuma, K. and Hoshi, M. (2007). "Microdosimetric study for secondary neutrons in phantom produced by, a.290 MeV/nucleon carbon beam," *Med. Phys.* **34,** 3571-3578.

Engle, W.A. Jr. (1967). "A User's Manual for ANISN, A one-dimensional discrete Ordinates Transport Code with anisotropic Scattering," *USAEC Report* **K-1963**.

EPA (1994). Environmental Protection Agency, *Estimating radiogenic cancer risks,* EPA 402-R-93-076 (Environmental Protection Agency, Washington, DC).

EPA (1999). Environmental Protection Agency, *Estimating radiogenic cancer risks. Addendum: Uncertainty analysis*, EPA 402-R-99-003 (Environmental Protection Agency, Washington, DC).

Epstein, R., Hanham, I. and Dale, R. (1997). "Radiotherapy-induced second cancers: are we doing enough to protect young patients?" *Eur. J. Cancer* **33,** 526-530.

EURATOM (1996). "Council Directive 96/29/Euratom, Laying down basic safety standards for the Protection of the Health of Workers and the General Public against the Dangers arising from ionizing Radiation," *Official Journal L* **159**, *29.6.1996*, 1–114.

Fan, J., Luo, , W., Fourkal, E., Lin, T., Li, J., Veltchev, I. and Ma, C-M. (2007). "Shielding design for a laser-accelerated proton therapy system," *Phys. Med. Biol.* **52,** 3913–3930.

Fasso, A. *et al.* (1997). "FLUKA: New Developments in FLUKA, Modelling Hadronic and EM Interactions," in *Proc. of the 3rd Workshop on Simulating Accelerator Radiation Environments*, May 1997, Ed., H. Hirayama, KEK Proc. 97-5. 32-43 (KEK, Tsukuba, Japan).

Fasso, A., Ferrari, A., Ranft, J., and Sala, P.R. (2001). "FLUKA: status and prospective for hadronic applications," p.955 in *Proc. of the Monte Carlo 2000 Conference*, Lisbon, 23-26 October 2000 (Springer-Verlag, Berlin).

Fasso, A., Ferrari, A., Ranft, J., and Sala, P.R. (2005). "FLUKA: A Multi-Particle Transport Code," CERN-2005-10, INFN/TC_05/11, SLAC-R-773.

Fehrenbacher, G., Gutermuth, F., and Radon, T. (2001). "Neutron Dose Assessments for the Shielding of the planned heavy Ion Cancer Therapy Facility in Heidelberg," GSI Report 2001-05 (GSI, Darmstadt, Germany).

Fehrenbacher, G., Gutermuth, F., and Radon, T. (2002a). "Calculation of Dose Rates near the Horizontal Treatment Places of the heavy Ion Therapy Clinic in Heidelberg by means of Monte-Carlo-Methods," *unpublished internal note at GSI* (GSI, Darmstadt, Germany).

Fehrenbacher, G., Gutermuth, F., and Radon, T. (2002b), "Estimation of Carbon-Ion caused Radiation Levels by Calculating the Transport of the produced Neutrons through Shielding Layers," *GSI Scientific Report 2001*, **205**.

Fehrenbacher, G., Gutermuth, F., and Radon, T. (2007a). "Shielding Calculations for the Ion Therapy Facility HIT," pp. 33-36 in *Ion Beams in Biology and Medicine, 39, Annual Conference of the German-Swiss Association for Radiation Protection and 11th Workshop of Heavy Charged Particles in Biology and Medicine* (IRPA Fachverband für Strahlenschutz, Switzerland and Germany).

Fehrenbacher, G., Gutermuth, F., Kozlova, E., Radon, T., Aumann, T., Beceiro, S., Bleis, T. Le, Boretzky, K., Emling, H., Johansson, H., Kiselev, O., Simon, H., and Typel, S. (2007b). "Measurement of the fluence response of the GSI neutron ball in high-energy neutron fields produced by 500 AMeV and 800 AMeV deuterons," *Radiat. Prot. Dosim.* **126**, 497-500.

Fehrenbacher, G., Kozlova, E., Gutermuth, F., Radon, T., Schülz, R., Nolte, R., and Böttger, R. (2007c). "Measurement of the fluence response of the GSI neutron ball dosimeter in the energy range from thermal to 19 MeV," *Radiat. Prot. Dosim.* **126**, 546-548.

Fehrenbacher, G., Festag, J.G., Grosam, S., Vogt, K., and Becker, F. (2008). "Measurements of the ambient dose equivalent of produced X-rays at the linear accelerator UNILAC of GSI," in *Proc. of the 12th Congress of the International Radiation Protection Association, IRPA12* (Buenos Aires).

Feinendegen, L.E. (2005). "Evidence for beneficial low level radiation effects and radiation hormesis," *Br. J. Radiol.* **78,** 3-7.

Ferrari, A., Pelliccioni, M., and Pillon, M. (1996). "Fluence to effective dose and effective dose equivalent conversion coefficients for photons from 50 keV to 10 GeV," *Radiat. Prot. Dosim.*, **67**, 245-251.

Ferrari, A., Pelliccioni, M., and Pillon, M. (1997). “Fluence to effective dose conversion coefficients for neutrons up to 10 TeV,” *Radiat. Prot. Dosim.*, **71**, 165-173.

Ferrari, A., Sala, P.R., Fasso, A. and Ranft, J. (2005). "FLUKA: a multi-particle transport code," *CERN Yellow Report CERN 2005-10; INFN/TC 05/11, SLAC-R-773* (CERN, Geneva, Switzerland).

Ferrarini, M. (2007). personal communication, Politecnico di Milano, Dipatimento di Ingegneria Nucleare, Via Ponzio 34/3, 20133, Milano.

Firestone, R.B. (1999). *Table of Isotopes: 1999 Update*, 8th ed. CD-ROM (Wiley Interscience, Malden, MA).

Fix, M.K., Keall, P.J. and Siebers, J.V. (2005). "Photon-beam subsource sensitivity to the initial electron-beam parameters," *Med. Phys.* **32**, 1164-1175.

Flanz, J., Durlacher, S., Goitein, M., Levine, A., Reardon, P., and Smith, A. (1995) "Overview of the MGH-Northeast Proton Therapy Center plans and progress," *NIM Phys. Res.* B **99**, 830-834.

Flanz, J., DeLaney, T.F., and Kooy, H.M. (2008). "Particle Accelerators 27-32," *Proton and Charged Particle Radiotherapy* (Lippincott Williams & Wilkins, Philadelphia, USA).

Followill, D., Geis, P. and Boyer, A. (1997). "Estimates of whole-body dose equivalent produced by beam intensity modulated conformal therapy," *Int. J. Radiat. Oncol. Biol. Phys.* **38,** 667-672.

Fontenot, J., Taddei, P., Zheng, Y., Mirkovic, D., Jordan, T. and Newhauser, W. (2008). "Equivalent dose and effective dose from stray radiation during passively scattered proton radiotherapy for prostate cancer," *Phys. Med. Biol.* **53**, 1677-1688.

Forringer, E. and Blosser, H.G. (2001). "Emittance measurements of a cold cathode internal ion source for cyclotrons," in *Proc. of the 16th International Conference on Cyclotrons and their Applications*, Marti, F., Ed., *AIP Conference Proceedings*, **600**, 277-279.

Foss Abrahamsen, A., Andersen, A., Nome, O., Jacobsen, A.B., Holte, H., Foss Abrahamsen, J., and Kvaloy, S. (2002). "Long-term risk of second malignancy after treatment of Hodgkin's disease: the influence of treatment, age and follow-up time," *Ann. Oncol.* **13**, 1786-1791.

Francois, P., Beurtheret, C., and Dutreix, A. (1988a). "Calculation of the dose delivered to organs outside the radiation beams," *Med. Phys.* **15,** 879-883.

Francois, P., Beurtheret, C., Dutreix, A., and De Vathaire, F. (1988b) "A mathematical child phantom for the calculation of dose to the organs at risk," *Med. Phys.* **15,** 328-333.

Frankenberg, D., Kelnhofer, K., Baer, K., and Frankenberg-Schwager, M. (2002). "Enhanced Neoplastic Transformation by Mammography, X.Rays Relative to 200 kVp X Rays: Indication for a Strong Dependence on Photon Energy of the RBE(M) for various End Points," *Radiat. Res.* **157,** 99-105.

Freytag, E. (1972). "Strahlenschutz an Hochenergiebeschleunigern" *Reihe Wissenschaft und Technik: Nukleare Elektronik und Messtechnik,* Karlsruhe. **3** (G.Braun: Karlsruhe, Germany).

Fry, R.J. (1981). "Experimental radiation carcinogenesis: what have we learned?" *Radiat. Res.* **87,** 224-239.

Furukawa, T. *et al.* (2006). "Design of Synchrotron and Transport Line for Carbon Therapy Facility and related Machine Study at HIMAC," *NIM Phys. Res.* A **562**, 1050-1053.

Garrity, J.M., Segars, W.P., Knisley, S.B., and Tsui, B.M.W. (2003). "Development of, a.dynamic model for the lung lobes and airway tree in the NCAT phantom," *IEEE Transactions in Nuclear Science* **50,** 378-383.

Geisler, A.E., Hottenbacher, J., Klein, H.-U., Krischel, D., Röcken, H., Schillo, M., Stephani, T., Timmer, J.H. (2007). "Commissioning of the ACCEL 250 MeV Proton Cyclotron," *Cyclotrons and Their Applications* **18** (Accel Instruments GmbH, Bergich Gladbach, Germany).

Geithner, O., Andreo, P., Sobolevsky, N.,M., Hartmann, G., and Jäkel, O., (2006). “Calculation of stopping power ratios for carbon ion dosimetry,” *Phys. Med. Biol*. **51**, 2279-2292.

Gibbs, S.J., Pujol, A., Chen, T.S. and *et al.* (1984). "Computer-simulation of patient dose from dental radiography." *Journal of Dental Research* **63,** 209.

Gilbert, W.S., *et al.* (1968). "Shielding Experiment at the CERN Proton Synchrotron," *CERN-LBL-RHEL, Rep. UCRL-17941* (Lawrence Berkeley Lab., Berkeley, CA, USA).

Goebel, K., Stevenson, G.R., Routti, J.T., and Vogt, H.G. (1975). "Evaluating dose rates due to neutron leakage through the access tunnels of the SPS," CERN Internal Report LABII-RA/Note/75-10.

Gottschalk, B. (2006). "Neutron dose in scattered and scanned proton beams: in regard to Eric, J. Hall (Int., J. Radiat. Oncol. Biol. Phys. 2006;65:1-7)," *Int. J. Radiat. Oncol. Biol. Phys.* **66,** 1594; author reply 5.

Grahn, D., Fry, R.J., and Lea, R.A. (1972). "Analysis of survival and cause of death statistics for mice under single and duration-of-life gamma irradiation," *Life. Sci. Space. Res.* **10,** 175-186.

Gregoire, O. and Cleland, M.R. (2006). "Novel approach to analyzing the carcinogenic effect of ionizing radiations," *Int. J. Radiat. Biol.* **82,** 13-19.

GRPO (2005). German Radiation Protection Ordinance, *Veordnung über den Schutz vor Schäden durch ionisierende Strahlen (Strahlenschutzverordnung – StrlSchV).* (Bundesministerium der Justis, Germany).

Gudowska, I. and Sobolevsky, N. (2005). "Simulation of secondary particle production and absorbed dose to tissue in light ion beams," *Radiat. Prot. Dosim.* **116,** 301-306.

Gudowska, I., Andreo, P., and Sobolevsky, N. (2002). "Secondary particle production in tissue-like and shielding materials for light and heavy ions calculated with the Monte-Carlo code SHIELD-HIT," *J. Radiat. Res. (Tokyo)* **43 Suppl** S93-97.

Gudowska, I., Sobolevsky, N.,M., Andreo, P., Belkic D., and Brahme, A., (2004). "Ion beam transport in tissue-like media using the Monte Carlo code SHIELD-HIT," *Phys. Med. Biol*. **49**,1933-1958.

Gudowska, I., Kopec, M., and Sobolevsky, N. (2007). "Neutron production in tissue-like media and shielding materials irradiated with high-energy ion beams," *Radiat. Prot. Dosim.* **126,** 652-656.

Gunzert-Marx, K., Schardt, D., and Simon, R.S. (2004). "Fast neutrons produced by nuclear fragmentation in treatment irradiations with 12C beam," *Radiat. Prot. Dosim.* **110,** 595-600.

Gunzert-Marx, K., Iwase, H., Schardt, D., and Simon, R.S. (2008). "Secondary beam fragments produced by 200MeVu−1 12C ions in water and their dose contributions in carbon ion radiotherapy," *New Journal of Physics* **10,** 075003.

Haberer, T., Becher, W., Schardt, D., and Kraft, G. (1993). "Magnetic scanning system for heavy ion therapy," *NIM Phys. Res.* A **330,** 296-305**.**

Haettner, E., Iwase, H., and Schardt, D. (2006). "Experimental fragmentation studies with 12C therapy beams," *Radiat. Prot. Dosim.* **122,** 485-487.

Hagan, W.K., Colborn, B.L., Armstrong, T.W., and Allen, M. (1988). "Radiation Shielding Calculations for a 70- to 350-MeV Proton Therapy Facility," *Nuclear Science and Engineering* **98,** 272-278**.**

Hall, E.J. (2004). "Henry S. Kaplan Distinguished Scientist Award 2003: The crooked shall be made straight; dose response relationships for carcinogenesis," *Int. J. Radiat. Biol.* **80,** 327-337.

Hall, E.J. (2006). "Intensity-modulated radiation therapy, protons, and the risk of second cancers," *Int. J. Radiat. Oncol. Biol. Phys.* **65,** 1-7.

Hall, E.J. (2007). "The impact of protons on the incidence of second malignancies in radiotherapy," *Technol. Cancer Res. Treat.* **6,** 31-34.

Hall, E.J. and Wuu C-S. (2003). "Radiation-induced second cancers: The impact of 3D-CRT and IMRT," *Int. J. Radiat. Oncol. Biol. Phys.* **56,** 83-88.

Hall, E.J., Kellerer, A.M., Rossi, H.H., and Yuk-Ming, P.L. (1978). "The Relative Biological Effectiveness of 160 MeV Protons. II. Biological Data and Their Interpretation in Terms of Microdosimetry," *Int. J. Radiat. Oncol. Biol. Phys.* **4**, 1009-1013.

Han, A. and Elkind, M.M. (1979). "Transformation of mouse C3H/10T1/2 cells by single and fractionated doses of X-rays and fission-spectrum neutrons," *Cancer Res.* **39,** 123-130.

Hawkins, M.M., Draper, G.J., and Kingston, J.E. (1987). "Incidence of second primary tumours among childhood cancer survivors," *Br. J. Cancer* **56**, 339-347.

Heeg, P., Eickhoff, H., Haberer, T. (2004). "Die Konzeption der Heidelberger Ionentherapieanlage HICAT," in *Zeitschrift für Medizinische Physik* **14,** 17-24.

Heidenreich, W.F., Paretzke, H.G., and Jacob, P. (1997). "No evidence for increased tumor rates below 200 mSv in the atomic bomb survivors data," *Radiat. Environ. Biophys.* **36,** 205-207.

Hess, E., Takacs, S., Scholten, B., Tarkanyi, F., Coenen, H.H., and Qaim, S.M. (2001). "Excitation function of the $^{18}O(p, n)^{18}F$ nuclear reaction from threshold up to 30 MeV," *Radiochim. Acta.* **89**, 357-362.

Heyes, G.J. and Mill, A.J. (2004). "The neoplastic transformation potential of mammography X rays and atomic bomb spectrum radiation," *Radiat. Res.* **162,** 120-127.

Hirao, Y. (2001). "Results from HIMAC and other therapy facilities in Japan," pp.8-12 in *Proc. of Sixteenth International Conference on Cyclotrons and their Applications 2001, CP600,* 13-17 May 2001, Marti, F., Ed. (American Institute of Physics, East Lansing, MI, USA).

Hirao, Y. *et al.* (1992). "Heavy Ion Medical Accelerator in Chiba – A Design Summary and Update – Division of Accelerator Research," *Report NIRS-M-89, HIMAC-001* (National Institute of Radiological Sciences, Chiba, Japan).

Hofmann, W. and Dittrich, W. (2005). "Use of Isodose Rate Pictures for the Shielding Design of a Proton Therapy Centre," pp. 181-187 in *Proc. of Shielding Aspects of Accelerators, Targets and Irradiation Facilities (SATIF 7)*, 17-18 May 2004, Portugal.

Hranitzky, C., Stadtmann, H., and Kindl, P. (2002). "The use of the Monte Carlo simulation technique for the design of an H*(10) dosemeter based on TLD-100," *Radiat. Prot. Dosim.*, **101**, 279-282.

Hultqvist, M. and Gudowska, I. (2008). "Secondary doses in anthropomorphic phantoms irradiated with light ion beams," *Nuclear Technology* **10-057-151.**

IAEA (1987). International Atomic Energy Agency, *Handbook on Nuclear Activation Data*, IAEA Technical Report Series 273 (International Atomic Energy Agency, Vienna).

IAEA (1988). International Atomic Energy Agency, *Radiological Safety Aspects of the Operation of Proton Accelerators,* Technical Reports Series No. 283 (International Atomic Energy Agency, Vienna).

IAEA (1996). International Atomic Energy Agency, *International Basic Safety Standards for Protection against Ionizing Radiation and for the Safety of Radiation Sources*, IAEA Safety Series No. 115 (International Atomic Energy Agency, Vienna).

IAEA (2006). International Atomic Energy Agency, *Radiation Protection in the Design of Radiotherapy Facilities,* IAEA Safety Reports Series No. 47 (International Atomic Energy Agency, Vienna).

Iancu, G. and Kraemer, M. (2009). personal communication, Biologie, GSI Helmholtzzentrum für Schwerionenforschung GmbH, Hessen, Darmstadt.

ICRP (1973). International Commission on Radiological Protection, *Data for Protection Against Ionizing Radiation from External Sources* (Supplement to ICRP Publication 15), ICRP Publication 21, *Annals of the ICRP* **21** (1-3) (Pergamon Press, Oxford, UK).

ICRP (1975). International Commission on Radiological Protection, *Reference Man: Anatomical, Physiological and Metabolic Characteristics,* ICRP Publication 23, International Commission on Radiological Protection (Pergamon Press, Oxford, UK).

ICRP (1991). International Commission on Radiological Protection, *Recommendations of the International Commission on Radiological Protection*, ICRP Publication 60, *Annals of ICRP* **21**(1-3) (Pergamon Press, Oxford, UK).

ICRP (1996). International Commission on Radiological Protection, *Conversion Coefficients for use in Radiological Protection against External Radiation*, ICRP Publication 74 (Elsevier Science, Oxford, UK).

ICRP (1998). International Commission on Radiological Protection, *Radiation Dose to Patients from Radiopharmaceuticals,* ICRP Publication 53, *Annals of the ICRP* **18** (Elsevier Science, Oxford, UK).

ICRP (1999). International Commission on Radiological Protection, *Genetic Susceptibility to Cancer*, ICRP Publication 79, *Annals of the ICRP* **28** (Elsevier Science, Oxford, UK).

ICRP (2000). International Commission on Radiological Protection, *Prevention of Accidental Exposures to Patients Undergoing Radiation Therapy*, ICRP Publication 86, *Annals of the ICRP* **30** (Elsevier Science, Oxford, UK).

ICRP (2003a). International Commission on Radiological Protection, *Basic Anatomical and Physiological Data for Use in Radiological Protection: Reference Values*, ICRP Publication 89, *Annals of the ICRP* **33 (3-4)** (Elsevier Science, Oxford, UK).

ICRP (2003b). International Commission on Radiological Protection, *Relative Biological Effectiveness (RBE), QualityFactor (Q), and Radiation Weighting Factor (wR),* ICRP Publication 92, *Annals of the ICRP* **33** (4) (Elsevier Science, Oxford, UK).

ICRP (2007). International Commission on Radiological Protection, *Recommendations of the ICRP*, ICRP Publication 103, *Annals of the ICRP* (Elsevier Science, Oxford, UK).

ICRP (2008). International Commission on Radiological Protection, *Recommendations of the International Commission on Radiological Protection*, ICRP Publication 60, *Annals of the ICRP* **21** (1-3) (Elsevier Science, Oxford, UK).

ICRU (1978). International Commission on Radiation Units and Measurements, *Basic Aspects of High Energy Particle Interaction sand Radiation Dosimtery*, ICRU Report 28 (International Commission on Radiation Measurements and Units, Bethesda, MD).

ICRU (1986). International Commission on Radiation Units and Measures, *The Quality Factor in Radiation Protection*, ICRU Report 40 (International Commission on Radiation Units and Measurements, Bethesda, MD**).**

ICRU (1989). International Commission on Radiation Units and Measures, *Tissue Substitutes in Radiation Dosimetry and Measurement*, ICRU Report 44 (International Commission on Radiation Units and Measurements, Bethesda, MD**).**

ICRU (1992a). International Commission on Radiation Units and Measures, *Measurement of Dose Equivalents from External Photon and Electron Radiations*, ICRU Report 47 (International Commission on Radiation Units and Measurements, Bethesda, MD).

ICRU (1992b). International Commission on Radiation Units and Measures, *Photon, Electron, Proton and Neutron Interaction Data for Body Tissues*, ICRU Report 46 (International Commission on Radiation Units and Measurements, Bethesda, MD).

ICRU (1993). International Commission on Radiation Units and Measures, *Quantities and Units in Radiation Protection*, ICRU Report 51 (International Commission on Radiation Measurements and Units, Bethesda, MD).

ICRU (1998). International Commission on Radiation Units and Measures, *Conversion Coefficients for Use in Radiological Protection Against External Radiation*, ICRU Report 57 (International Commission on Radiation Units and Measurements, Bethesda, MD).

ICRU (2000). International Commission on Radiation Units and Measures, *Nuclear Data for Neutron and Proton Radiotherapy and for Radiation Protection*, ICRU Report 63 (International Commission on Radiation Units and Measurements, Bethesda, MD).

ICRU (2001). International Commission on Radiation Units and Measurements, *Determination of Dose Equivalent Quantities for Neutrons*, ICRU Report 47 (Nuclear Technology Publishing, Ashford).

ICRU (2007). International Commission on Radiation Units and Measures, *Prescribing, Recording, and Reporting Proton-Beam Therapy*, ICRU Report 78 (International Commission on Radiation Units and Measurements, Bethesda, MD).

IEC (1998). International Electrotechnical Commission, *Medical Electrical Equipment - Part 2-1, "Particular requirements for the safety of electron accelerators in the Range 1 MeV to 50 MeV*, International Standard IEC 60601-2-1(IHS, Englewood, CO, USA).

IEC (2005). International Electrotechnical Commission, Funnctional safety of electrical, electronic, and programmable electronic equipment, Internattional Standard IEC 61508-SER (Ed. 1.0) (International Electrotechnical Commission, Geneva, Switzerland).

IEC (2006) International Electrotechnical Commission, *Medical device software - Software life cycle processes*, IEC 62304 (International Electrotechnical Commission, Geneva, Switzerland).

Imaizumi, M., Usa, T., Tominaga, T., Neriishi, K., Akahoshi, M., Nakashima, E., Ashizawa, K., Hida, A., Soda, M., Fujiwara, S., Yamada, M., Ejima, E., Yokoyama, N., Okubo, M., Sugino, K., Suzuki, G., Maeda, R., Nagataki, S., and Eguchi, K. (2006). "Radiation dose-response relationships for thyroid nodules and autoimmune thyroid diseases in Hiroshima and Nagasaki atomic bomb survivors 55-58 years after radiation exposure," *JAMA* **295**, 1011-1022).

Ipe, N.E. (2008). "Particle accelerators in particle therapy: the new wave," in *Proc. of the 2008 Mid-Year Meeting of the Health Phys. Society on Radiation Generating Devices*, Oakland, CA (Health Phys. Society, McLean, VA).

Ipe, N.E. (2009a). "Transmission of Shielding Materials for Particle Therapy Facilities," in *Proc.of the ICRS-11 International Conference on Radiation Shielding and RPSD-2008 15th Topical Meeting of the Radiation Protection and Shielding Division of the ANS*, 1 3-18 April 2008, Pine Mountain, Georgia, USA.

Ipe, N.E. and Fasso, A., (2006). **"**Preliminary computational models for shielding design of particle therapy facilities," pp. in *Proc. of Shielding Aspects of Accelerators, Targets and Irradiation Facilities (SATIF 8),* 22-24 May 2006, Gyongbuk, Republic of Korea (Nuclear Energy Agency, Organization for Economic Co-operation and Development, Paris).

IRPL (2000). Italian Radiation Protection Laws, *Decreto Legislativo del Governo n° 230/1995 modificato dal 187/2000 e dal 241/2000* (Ministero dell'Ambiente e della Tutela del Territorio, Italy).

Ishikawa, T., Sugita, H., and Nakamura, T. (1991). “Thermalization of accelerator produced neutrons in concrete,” *Health Phys.* **60**, 209-221.

ISO (2007). International Organization for Stanzation, *Medical devices--Application of risk management to medical devices*, ISO Standard 14791 (International Organization for Standardization, Geneva, Switzerland).

Iwase, H., Niita, K., and Nakamura, T. (2002). "Development of General-Purpose Particle and heavy Ion Transport Monte Carlo Code," *J. Nucl. Sci. Technol.* **39**, 1142-1151.

Iwase, H., Gunzert-Marx, K., Haettner, E., Schardt, D., Gutermuth, F., Kraemer, M., and Kraft, G. (2007). "Experimental and theoretical study of the neutron dose produced by carbon ion therapy beams," *Radiat. Prot. Dosim.* **126,** 615-618.

Janssen, J.J., Korevaar, E.W., van Battum, L.J., Storchi, P.R., and Huizenga, H. (2001). "A model to determine the initial phase space of a clinical electron beam from measured beam data," *Phys. Med. Biol.* **46,** 269-286.

Jemal, A., Siegel, R., Ward, E., Murray, T., Xu, J., Smigal, C. and Thun, M.J. (2006). "Cancer statistics, 2006," *CA Cancer J. Clin.* **56,** 106-130.

Jenkinson, H.C., Hawkins, M.M., Stiller, C.A., Winter, D.L., Marsden, H.B., and Stevens, M.C. (2004). "Long-term population-based risks of second malignant neoplasms after childhood cancer in Britain," *Br. J. Cancer* **91**, 1905-1910.

Jiang, H., Wang, B., Xu, X.G., Suit, H.D., and Paganetti, H. (2005). "Simulation of Organ Specific Patient Effective Dose Due to Secondary Neutrons in Proton Radiation Treatment," *Phys. Med. Biol.* **50**, 4337-4353.

Jirousek, I. and *et al.* (2003). “The concept of the PROSCAN Patient Safety System,” in *Proc. of the IX International Conference on Accelerator and Large Experimental Physics Control Systems (ICALEPCS 2003)*, 13-17 October, 2003, Gyenongju, Republic of Republic of Korea.

Joiner, M.C., Marples, B., Lambin, P., Short, S.C., and Turesson, I. (2001). "Low-dose hypersensitivity: current status and possible mechanisms," *Int., J. Radiat. Oncol. Biol. Phys.* **49,** 379-389.

Jones, D.G (1998). "A realistic anthropomorhpic phantom for calculating specific absorbed fractions of energy deposited from internal gamma emitters," *Radiat. Prot. Dosim.* **79,** 411-414.

JORF (2006). "Arrêté du 15 mai 2006 relatif aux conditions de délimitation et de signalisatoin des zones surveillées et contrôlées et des zones spécialement réglementées ou interdites compte tenu de l'exposition aux rayonnements ionisants, ainsi qu'aux règles d'hygiène, de sécurité et d'entretien qui y sont imposées," *Journal Officiel de la Republique Française*, 15 juin 2006.

JRPL (2004). Japanese Radiation Protection Laws (Prevention Law), *Law concerning Prevention from Radiation Hazards due to Radioisotopes etc.* **167**.

Kaido, T., Hoshida, T., Uranishi, R., Akita, N., Kotani, A., Nishi, N., and Sakaki, T. (2001). "Radiosurgery-induced brain tumor. Case report," *J. Neurosurg.* **95,** 710-713.

Kaschten, B., Flandroy, P., Reznik, M., Hainaut, H., and Stevenaert, A. (1995). "Radiation-induced gliosarcoma. Case report and review of the literature," *J. Neurosurg.* **83,** 154-162.

Kato, T. and Nakamura, T. (1992). "Estimation of Neutron Yields from thick Targets by high- energy He Ions for the Design of Shielding for a heavy ion Medical Accelerator," *NIM Phys. Res.* A **311**, 548-557.

Kato, T., Kurosawa, K., Nakamura, T. (2002). "Systematic analysis of neutron yields from thick targets bombarded by heavy ions and protons with moving source model," *NIM Phys. Res.* A **480** 571-590.

Keall, P.J., Siebers, J.V., Libby, B. ,and Mohan, R. (2003). "Determining the incident electron fluence for Monte Carlo-based photon treatment planning using, a.standard measured data set," *Med. Phys.* **30,** 574-582.

Kellerer, A.M. (2000). "Risk estimates for radiation-induced cancer - the epidemiological evidence," *Radiat. Environ. Biophys.* **39,** 17-24.

Kellerer, A.M., Nekolla, E.A., and Walsh, L. (2001). "On the conversion of solid cancer excess relative risk into lifetime attributable risk," *Radiat. Environ. Biophys.* **40,** 249-257.

Kellerer, A.M., Ruhm, W., and Walsh, L. (2006). "Indications of the neutron effect contribution in the solid cancer data of the A-bomb survivors," *Health Phys.* **90,** 554-564.

Kenney, L.B., Yasui, Y., Inskip, P.D., Hammond, S., Neglia, J.P., Mertens, A.C., Meadows, A.T., Friedman, D., Robison, L.L., and Diller, L. (2004). "Breast cancer after childhood cancer: a report from the Childhood Cancer Survivor Study," *Ann. Intern. Med.* **141,** 590-597.

Kim, E., Nakamura, T., Uwamino, Y., Nakanishi, N., Imamura, M., Nakao, N., Shibata, S., and Tanaka, S. (1999). “Measurements of activation cross section on spallation reactions for ^{59}Co and ^{nat}Cu at incident neutron energies of 40 to 120 MeV," *J. Nucl. Sci. Technol*., **36** (1), 29-40.

Kim, J. (2003) "Proton Therapy Facility Project in National Cancer Center, Republic of Korea," *Journal of the Republic of Korean Physical Society*, **43, Sep**, 50-54.

Kinoshita, N., Masumoto, K., Matsumura, H., Bessho, K., Toyoda, A., Tosaki, Y., Tamari, M., Takahashi, T., Sueki, K., Oki, T., Mihara, S., Nagashima, Y., and Matsushi, Y. (2009). “Measurement and Monte Carlo simulation of radioactivity produced in concrete shield in EP-1 beamline at the 12-GeV proton synchrotron facility, KEK,” in *Proc. 5th International Symposium on Radiation Safety and Detection Technology* (ISORD-5), Kita-Kyushu, Japan.

Kirihara, Y., Hagiwara, M., Iwase, H., Ban, S., Itoga, T., and Nakamura, T. (2008). “Comparison of several Monte Carlo codes with neutron deep penetration experiments,” in *Proc. 11th International Conference on Radiation Shielding* (ICRS-11), Pine Mountain, Georgia, USA.

Kitwanga, S.W., Leleux, P., Lipnik, P., and Vanhorenbeeck, J. (1990). “Production of O-14,15, F-18 and Ne-19 radioactive nuclei from (p, n) reactions up to 30-MeV,” *Phys. Rev.* **C 42**, 748-752.

Klein, E.E., Maserang, B., Wood, R., and Mansur, D. (2006). "Peripheral doses from pediatric IMRT," *Med. Phys.* **33**, 2525-2531.

Knoll, G.F. (1999). *Radiation Detection and Measurement*, 3rd. ed., (John Wiley & Sons, Hoboken, NJ).

Ko, S.J., Liao, X.Y., Molloi, S., Elmore, E., and Redpath, J.L. (2004). "Neoplastic transformation in vitro after exposure to low doses of mammographic-energy X rays: quantitative and mechanistic aspects," *Radiat. Res.* **162,** 646-654.

Kocher, D.C., Apostoaei, A.I., and Hoffman, F.O. (2005). "Radiation effectiveness factors for use in calculating probability of causation of radiogenic cancers," *Health Phys.* **89,** 3-32.

Komori, M. *et al.* (2004). "Design of Compact Irradiation Port for Carbon Radiotherapy Facility," in *Proc. of the 3rd Asian Particle Accelerator Conference*, 22-26 March 2004, Gyeongju, Republic of Republic of Korea.

Kotegawa, H. *et al.* (1993). "Neutron-Photon Multigroup Cross Sections for Neutron Energies Up to 400 MeV: H1L086R- Revision of HIL086 Library," JAERI-M 93-020 (Japan Atomic Energy Research Institute).

Kraemer, M. *et al.* (2004) "Treatment planning for scanned ion beams," *Radiother. Oncol.* **73,** 80-85.

Kraft, G. (2000). "Tumor Therapy with Heavy Charged Particles," *Progress in Particle and Nuclear Physics* **45.**

Kramer, R., Zankl, M., Williams, G., and *et al.* (1982). "The calculation of dose from external photon exposures using reference human phantoms and Monte Carlo methods. Part I: The male (ADAM) and female (EVA) adult mathematical phantoms," *Gesellschaft fuer Strahlen- und Umweltforschung* **GSF-Bericht-S-885.**

Kramer, R., Vieira, J.W., Khoury, H.J., Lima, F.R., and Fuelle, D. (2003). "All about MAX: a male adult voxel phantom for Monte Carlo calculations in radiation protection dosimetry," *Phys. Med. Biol.* **48**, 1239-1262.

Kramer, R., Khoury, H.J., Vieira, J.W., and Lima, V.J. (2006). "MAX06 and FAX06: update of two adult human phantoms for radiation protection dosimetry," *Phys. Med. Biol.* **51**, 3331-3346.

Kry, S.F., Salehpour, M., Followill, D.S., Stovall, M., Kuban, D.A., White, R.A., and Rosen, I.I., (2005). "The calculated risk of fatal secondary malignancies from intensity-modulated radiation therapy," *Int. J. Radiat. Oncol. Biol. Phys.* **62**, 1195-1203.

Kry, S.F., Followill, D., White, R.A., Stovall, M., Kuban, D.A., and Salehpour, M. (2007). "Uncertainty of calculated risk estimates for secondary malignancies after radiotherapy," *Int. J. Radiat. Oncol. Biol. Phys.* **68**, 1265-1271.

Kurosawa, T. (1999). "Measurements of secondary neutrons produced from thick targets bombarded by high-energy neon ions," *J. Nucl. Sci. Technol.* **36**(1), 41-53.

Kurosawa, T. (2000). "Neutron yields from thick C, Al, Cu and Pb targets bombarded by 400MeV ar, Fe, Xe and 800MeV Si ions," *Phys. Rev*. C **62**

Kurosawa, T., Nakao, N., Nakamura, T., Uwamino, Y., Shibata, T., Nakanishi, N., Fukamura, A., and Murakami, K., (1999). "Measurements of secondary neutrons produced from thick targets bombarded by high-energy helium and carbon ions," *Nucl. Sci. and Eng.* **132,** 30-57**.**

Kuttesch, J.F. Jr., Wexler, L.H., Marcus, R.B., Fairclough, D., Weaver-McClure, L., White, M., Mao, L., Delaney, T.F., Pratt, C.B., Horowitz, M.E., and Kun, L.E. (1996). "Second malignancies after Ewing's sarcoma: radiation dose-dependency of secondary sarcomas," *J. Clin. Oncol.* **14**, 2818-2825.

Lee, C. and Bolch, W. (2003). "Construction of a tomographic computational model of a 9-mo-old and its Monte Carlo calculation time comparison between the MCNP4C and MCNPX codes," *Health Phys.* **84** S259.

Lee, C., Williams, J.L., Lee, C., and Bolch, W.E. (2005). "The UF series of tomographic computational phantoms of pediatric patients," *Med. Phys.* **32**, 3537-3548.

Lee, C., Lee, C., and Bolch, W.E. (2006a). "Age-dependent organ and effective dose coefficients for external photons: a comparison of stylized and voxel-based paediatric phantoms," *Phys. Med. Biol.* **51**, 4663-4688.

Lee, C., Lee, C., Williams, J.L .and Bolch, W.E. (2006b). "Whole-body voxel phantoms of paediatric patients--UF Series B," *Phys. Med. Biol.* **51**, 4649-4661.

Lee, C., Lee, C., Lodwick, D. and Bolch, W. (2007a). "A series of 4D pediatric hybrid phantoms developed from the US series B tomographic phantoms [Abstract]," *Med. Phys.* **33.**

Lee, C., Lodwick, D., Hasenauer, D., Williams, J.L., Lee, C., and Bolch, W. (2007b). "Hybrid computational phantoms of the male and female newborn patient: NURBS-based whole-body models," *Phys. Med. Biol.* **52**, 3309-3333.

Lee, C., Lodwick, D., Williams, J.L., and Bolch, W. (2008). "Hybrid computational phantoms of the 15-year male and female adolescent: Applications to CT organ dosimetry for patients of variable morphometry," *Med. Phys.* **35**, 2366-2382.

Lee, H.S. (2008). personal communication, Radiation Safety Office, Pohang Accelerator Laboratory, POSTECH, Nam-Gu Pohang, Gyongbuk, Republic of Republic of Korea.

Leroy, C. and Rancoita, P.G. (2005). *Principles of Radiation Interaction in Matter and Detection*, (World Scientific, Singapore).

Lim, S.M., DeNardo, G.L., DeNardo, D.A., Shen, S., Yuan, A., O'Donnell, R.T., and DeNardo, S.J. (1997). "Prediction of myelotoxicity using radiation doses to marrow from body, blood and marrow sources," *J. Nucl. Med.* **38**, 1374-1378.

Little, M.P. (1997). "Estimates of neutron relative biological effectiveness derived from the Japanese atomic bomb survivors," *Int. J. Radiat. Biol.***72,** 715-726.

Little, M.P. (2000). "A comparison of the degree of curvature in the cancer incidence dose-response in Japanese atomic bomb survivors with that in chromosome aberrations measured in vitro," *Int. J. Radiat. Biol.***76**, 1365-1375.

Little, M.P. (2001). "Comparison of the risks of cancer incidence and mortality following radiation therapy for benign and malignant disease with the cancer risks observed in the Japanese A-bomb survivors," *Int. J. Radiat. Biol.* **77,** 431-464.

Little, M.P. and Muirhead, C.R. (2000). "Derivation of low-dose extrapolation factors from analysis of curvature in the cancer incidence dose response in Japanese atomic bomb survivors," *Int. J. Radiat. Biol.* **76,** 939-953.

Liwnicz, B.H., Berger, T.S., Liwnicz, R.G, and Aron, B.S. (1985). "Radiation-associated gliomas: a report of four cases and analysis of postradiation tumors of the central nervous system," *Neurosurgery* **17,** 436-445.

Loeffler, J.S., Niemierko, A. and Chapman, P.H. (2003). "Second tumors after radiosurgery: tip of the iceberg or a bump in the road?" *Neurosurgery* **52**, 1436-1442.

Loncol, T., Cosgrove, V., Denis, J.M., Gueulette, J., Mazal, A., Menzel, H.G., Pihet, P., and Sabattier, R. (1994). "Radiobiological effectiveness of radiation beams with broad LET spectra: microdosimetric analysis using biological weighting functions," *Radiat. Prot. Dosim.* **52,** 347-352.

Lux, I., and Koblinger, L., (1991). *Monte Carlo particle transport methods: neutron and photon calculations* (CRC Press, Boca Raton, FL).

Maisin, J.R., Wambersie, A., Gerber, G.B., Mattelin, G., Lambiet-Collier, M., De Coster, B., and Gueulette, J. (1991). "Life-shortening and disease incidence in mice after exposure to g rays or high-energy neutrons," *Radiat. Res.* **128** S117-S23.

Mares, V., Leuthold, G., and Schraube, H. (1997). “Organ doses and dose equivalents for neutrons above 20 MeV,” *Radiat. Prot. Dosim.*, **70**, 391-394.

Marquez, L. (1952). “The yield of F-18 from medium and heavy elements with 420 MeV protons,” *Phys. Rev.* **86**, 405-407.

Mashnik, S.,G. (2009). “Overview and Validation of the CEM and LAQGSM Event Generators for MCNP6, MCNPX, and MARS15,” in *Proc. of the First International Workshop on Accelerator Radiation Induced Activation (ARIA'08), PSI, Switzerland*, PSI Proceedings 09-01, 20-29.

Masumoto, K., Matsumura, H., Bessho, K., and Toyoda, A. (2008). “Role of activation analysis for radiation control in accelerator facilities,” *Journal of Radioanalytical and Nuclear Chemistry*, **278**, 449–453.

Matsufuji, N., Fukumura, A., Komori, M., Kanai, T., and Kohno, T. (2003). "Influence of fragment reaction of relativistic heavy charged particles on heavy-ion radiotherapy," *Phys. Med. Biol.* **48**, 1605-1623.

Mazal, A., Gall, K., Bottollier-Depois, J.F., Michaud, S., Delacroix, D., Fracas, P., Clapier, F., Delacroix, S., Nauraye, C., Ferrand, R., Louis, M., and Habrand, J.L. (1997). “Shielding measurements for a proton therapy beam of 200 MeV: preliminary results,” *Radiat. Prot. Dosim.*, **70**, 429-436.

McKinney, G., *et al*. (2006). “Review of Monte Carlo all-particle transport codes and overview of recent MCNPX features,” in *Proc. of the International Workshop on Fast Neutron Detectors* (University of Cape Town, South Africa).

Meier, M.M., Goulding, C.A., Morgan, G.L., and Ullmann, J.L. (1990). "Neutron Yields from Stopping- and Near-Stopping-Length Targets for 256-MeV Protons," *Nucl. Sci. and Eng.* **104**, 339-363.

Mesoloras, G., Sandison, G.A., Stewart, R.D., Farr, J.B., and Hsi, W.C. (2006). "Neutron scattered dose equivalent to, a.fetus from proton radiotherapy of the mother," *Med. Phys.* **33**, 2479-2490.

Michel, R., *et al.* (1997). “Cross sections for the production of residual nuclides by low- and medium-energy protons from the target elements C, N, O Mg, Al, Si, Ca, Ti, V, Mn, Fe, Co, Ni, Cu, Sr, Y, Zr, Nb, Ba and Au,” *NIM Phys. Res.* **B129**, 153-193.

Minniti, G., Traish, D., Ashley, S., Gonsalves, A., and Brada, M. (2005). "Risk of second brain tumor after conservative surgery and radiotherapy for pituitary adenoma: update after an additional 10 years," *J. Clin. Endocrinol. Metab.* **90,** 800-804.

Miralbell, R., Lomax, A., Cella, L., and Schneider, U. (2002). "Potential reduction of the incidence of radiation-induced second cancers by using proton beams in the treatment of pediatric tumors," *Int. J. Radiat. Phys. Med. Biol.* **54,** 824-829.

Mokhov, N.V. (1995). "The MARS Code System User's Guide," Fermilab-FN-628 (1995).

Mokhov, N.V. (2009). "MARS Code System," Version 15 (2009), http://www-ap.fnal.gov/MARS, accessed 20 September 2009.

Mokhov, N.V. and Striganov, S.I. (2007). "MARS15 Overview," in *Proc. of the Hadronic Shower Simulation Workshop 2006, Fermilab* 6-8 September 2006, M., Albrow, R., Raja Eds., *AIP Conference Proceeding* **896** .

Moritz, L.E. (1994). "Summarized experimental results of neutron shielding and attenuation length," pp. in *Proc. Shielding Aspects of Accelerators, Targets and Irradiation Facilities (SATIF),* 28-29 April 1998, Arlington, Texas (Nuclear Energy Agency, Organization for Economic Co-operation and Development, Paris).

Moritz, L.E. (2001). "Radiation protection at low energy proton accelerators," *Radiat. Prot. Dosim.* **96(4),** 297-309.

Morone, M.C., Calabretta, L., Cuttone, G., and Fiorini, F. (2008). "Monte Carlo simulation to evaluate the contamination in an energy modulated carbon ion beam for hadron therapy delivered by cyclotron," *Phys. Med. Biol.* **53**, 6045-6053.

Morstin, K., and Olko, P. (1994). "Calculation of neutron energy deposition in nanometric sites," *Radiat. Prot. Dosim.* **52**, 89-92.

Moyer, B.J. (1957) "University of California Radiation Laboratory Proton Synchrotron", *Rep. TID-7545,* **38** (U.S. Army Environmental Command, Washington, DC).

Moyers, M.F., Benton, E.R., Ghebremedhin, A., and Coutrakon, G. (2008). "Leakage and scatter radiation from a double scattering based proton beamline," *Med. Phys.* **35,** 128-144.

Nakamura, T. (2000). “Neutron production from thin and thick targets by high-energy heavy ion bombardment,” pp. in *Proc. Shielding Aspects of Accelerators, Targets and Irradiation Facilities (SATIF-5)*, 18-21 July 2000, Paris (Nuclear Energy Agency, Organization for Economic Co-operation and Development, Paris).

Nakamura, T. (2002). “Double differential thick-target neutron yields bombarded by high-energy heavy ions,”pp. 19–25 in *Proc. Shielding Aspects of Accelerators, Targets and Irradiation Facilities (SATIF-6)*, 10–12 April 2002, Stanford, CA (Nuclear Energy Agency, Organization for Economic Co-operation and Development, Paris).

Nakamura, T. (2004). "Summarized experimental results of neutron shielding and attenuation length," pp. 129-146 in *Proc. Shielding Aspects of Accelerators, Targets and Irradiation Facilities (SATIF-7)*, 17–18 May 2004, Portugal (Nuclear Energy Agency, Organization for Economic Co-operation and Development, Paris).

Nakamura T., and Heilbronn, L. (2006). *Handbook on Secondary Particle Production and Transport by High-Energy Heavy Ions*, (World Scientific, Singapore).

Nakamura, T., Nunomiya, T., Yashima, H., and Yonai, S. (2004). "Overview of recent experimental works on high energy neutron shielding,” *Progress in Nuclear Energy*, **44(2),** 85-187.

Nakashima, H., Takada, H., Meigo, S., Maekawa, F., Fukahori, T., Chiba, S., Sakamoto, Y., Sasamoto, N., Tanaka, S., Hayashi, K., Odano, N.,   Yoshizawa, N., Sato, O., Suzuoki, Y., Iwai, S., Uehara, T., Takahashi, H., Uwamino, Y., Namito, Y., Ban, S., Hirayama, H., Shin, K. and Nakamura, T. (1995). “Accelerator shielding benchmark experiment analyses,” in *Proc. Shielding Aspects of Accelerators, Targets and Irradiation Facilities (SATIF-2)*, 12-13 October 1995, CERN, Geneva (Nuclear Energy Agency, Organization for Economic Co-operation and Development, Paris).

Nasagawa, H. and Little, J.B. (1999). "Unexpected sensitivity to the induction of mutations by very low doses of alpha-particle radiation: evidence for a bystander effect," *Radiat. Res.* **152,** 552-557.

NCRP (1971). National Council on Radiation Protection and Measurements, *Protection Against Neutron Radiation*, NCRP Report 38 (National Council on Radiation Protection and Measurements, Bethesda, MD).

NCRP (1977). National Council on Radiation Protection and Measurements, *Radiation Protection Design Guidelines for 0.1-100 MeV Particle Accelerator Facilities*, NCRP Report 51 (National Council on Radiation Protection and Measurements, Bethesda, MD).

NCRP (1990). National Council on Radiation Protection and Measurements, *The Relative Biological Effectiveness of Radiations of Different Quality*, NCRP Report 104 (National Council on Radiation Protection and Measurements, Bethesda, MD).

NCRP (1991). National Council on Radiation Protection and Measurements, *Calibration of Survey Instruments Used in Radiation Protection for the Assessment of Ionizing Radiation Fields and Radioactive Surface Contamination,* NCRP Report 112 (National Council on Radiation Protection and Measurements, Bethesda, MD).

NCRP (1993). National Council on Radiation Protection and Measurements, *Limitation of Exposure to Ionizing Radiation (Supersedes NCRP Report No. 91),* NCRP Report 116 (National Council on Radiation Protection and Measurements, Bethesda, MD).

NCRP (1996). National Council on Radiation Protection and Measurements, *Dosimetry of X-Ray and Gamma-Ray Beams for Radiation Therapy in the Energy Range 10 keV to 50 MeV,* NCRP Report 69 (National Council on Radiation Protection and Measurements, Bethesda, MD).

NCRP (2001). National Council on Radiation Protection and Measurements, *Evaluation of the Linear-Nonthreshold Dose-Response Model for Ionizing Radiation*, NCRP Report 136 (National Council on Radiation Protection and Measurements, Bethesda, MD).

NCRP (2003). National Council on Radiation Protection and Measurements, *Radiation Protection for Particle Accelerator Facilities*, NCRP Report 144 (National Council on Radiation Protection and Measurements, Bethesda, MD).

NCRP (2005). National Council on Radiation Protection and Measurements, *Structural Shielding Design and Evaluation for Megavoltage X- and Gamma-Ray Radiotherapy Facilities*, NCRP Report 151 (National Council on Radiation Protection and Measurements, Bethesda, MD).

Neglia, J.P., Meadows, A.T., Robison, L.L., Kim, T.H., Newton, W.A., Ruymann, F.B., Sather, H.N., and Hammond, G.D. (1991). "Second neoplasms after acute lymphoblastic leukemia in childhood," *N. Engl. J. Med.* **325**, 1330-1336.

Neglia, J.P., Friedman, D.L., Yasui, Y., Mertens, A.C., Hammond, S., Stovall, M., Donaldson, S.S., Meadows, A.T., and Robison, L.L. (2001). "Second malignant neoplasms in five-year survivors of childhood cancer: childhood cancer survivor study," *J. Natl. Cancer Inst.* **93,** 618-629.

Newhauser, W.D., Titt, U., Dexheimer, D., Yan, X. and Nill, S. (2002). "Neutron shielding verification measurements and simulations for a 235-MeV proton therapy center," *NIM Phys. Res.* A **476,** 80-84.

Newhauser, W.D., Ding, X., Giragosian, D., Nill, S., and Titt, U., (2005a). “Neutron radiation area monitoring system for proton therapy facilities,” *Radiat. Prot. Dosim.* **115**, 149–153.

Newhauser, W., Koch, N., Hummel, S., Ziegler, M., and Titt, U. (2005b). "Monte Carlo simulations of a nozzle for the treatment of ocular tumours with high-energy proton beams," *Phys. Med. Biol.* **50,** 5229-5249.

Newhauser, W.D., Fontenot, J.D., Mahajan, A., Kornguth, D., Stovall, M., Zheng, Y., Taddei, P.J., Mirkovic, D., Mohan, R., Cox, J.D., and Woo, S. (2009). "The risk of developing a second cancer after receiving craniospinal proton irradiation," *Phys. Med. Biol.* **54**, 2277-2291.

Niita, K., Meigo, S., Takada, H., and Ikeda, Y. (2001). “High energy particle transport code NMTC/JAM,” *NIM Phys. Res.* **B184**, 406-420.

Niita, K., Sato, T., Iwase, H., Nose, H., Nakashima, H., and Sihver, L. (2006). "PHITS: a particle and heavy ion transport code system," *Radiation Measurements* **41,** 1080-1090.

Nipper, J.C., Williams, J.L., and Bolch, W.E. (2002). "Creation of two tomographic voxel models of paediatric patients in the first year of life," *Phys. Med. Biol.* **47**, 3143-3164.

Nishimura, H., Miyamoto, T., Yamamoto, N., Koto, M., Sugimura, K., and Tsujii, H. (2003). "Radiographic pulmonary and pleural changes after carbon ion irradiation," *Int. J. Radiat. Oncol. Biol. Phys.* **55,** 861-866.

Noda, K. (2004). "HIMAC and new Facility Design for Widespread Use of Carbon Cancer Therapy," pp 552-556 in *Proc. of the 3rd Asian Particle Accelerator Conference*, 22-26 March 2004, Gyeongju, Republic of Korea.

Noda, K. *et al.* (2006a). "Development for new Carbon Cancer-Therapy Facility and Future Plan of HIMAC," in *Proc. of EPAC 2006, 995-957* (Applications of Accelerators, Technology Transfer and Industrial Relations, Edinburgh, Scotland).

Noda, K. *et al.* (2006b). "Design of Carbon Therapy Facility Based on 10 Years Experience at HIMAC," *NIM Phys. Res.* A **562**, 1038-1041.

Nolte, E., Ruhm, W., Loosli, H.H., Tolstikhin, I., Kato, K., Huber, T.C., and Egbert, S.D. (2006). "Measurements of fast neutrons in Hiroshima by use of (39)Ar," *Radiat. Environ. Biophys.* **44,** 261-271.

Norosinski, S. (2006). *Erstellung eines Handbuches zur Abschätzung von Abschirmungen*, Diploma thesis 31 May 2006, Zittau, Görlitz.

Numajiri, M. (2007). "Evaluation of the radioactivity of the pre-dominant gamma emitters in components used at high-energy proton accelerator facilities," *Radiat. Prot. Dosim*. **23 (4)**, 417-425.

Oishi, K., Nakao, N., Kosako, K., Yamakawa, H., Nakashima, H, Kawai, M., Yashima, H., Sanami, T., Numajiri, M., Shibata, T., Hirayama, H., and Nakamura, T. (2005). "Measurement and anylysis of induced activities in concrete irradiated using high-energy neutrons at KENS neutron spallation source facility," *Radiat. Prot. Dosim*. **115**, 623–629.

Olsen, J.H., Garwicz, S., Hertz, H., Jonmundsson, G., Langmark, F., Lanning, M., Lie, S.O., Moe, P.J., Moller, T., Sankila, R., and *et al.* (1993). "Second malignant neoplasms after cancer in childhood or adolescence. Nordic Society of Paediatric Haematology and Oncology Association of the Nordic Cancer Registries," *BMJ* **307**, 1030-1036.

Olsher, R.H., Hsu, H.H., Beverding, A, Kleck, J.H., Casson, W.H., Vasilik, D.G., and Devine, R.T. (2000). "WENDI: An improved neutron rem meter," *Health Phys*. **70**, 171-181.

Olsher, R.H., Seagraves, D.T., Eisele, S.L., Bjork, C.W., Martinez, W.A., Romero, L.L., Mallett, M.W., Duran, M.A., and Hurlbut, C.R. (2004). "PRESCILA: A new, lightweight neutron rem meter," *Health Phys*. **86**, 603-612.

Paganetti, H. (1998). "Monte Carlo method to study the proton fluence for treatment planning," *Med. Phys.* **25**, 2370-2375.

Paganetti, H. (2002). "Nuclear Interactions in Proton Therapy: Dose and Relative Biological Effect Distributions Originating From Primary and Secondary Particles," *Phys. Med. Biol.* **47,** 747-764.

Paganetti, H. (2005). "Changes in tumor cell response due to prolonged dose delivery times in fractionated radiation therapy," *Int. J. Radiat. Oncol. Biol. Phys.* **63,** 892-900.

Paganetti, H. (2006). "Monte Carlo calculations for absolute dosimetry to determine output factors for proton therapy treatments," *Phys. Med. Biol.* **51,** 2801-2812.

Paganetti, H., Olko, P., Kobus, H., Becker, R., Schmitz, T., Waligorski, M.P.R., Filges, D., and Mueller-Gaertner, H.W. (1997). "Calculation of RBE for Proton beams Using Biological Weighting Functions," *Int. J. Radiat. Oncol. Biol. Phys.* **37,** 719-729.

Paganetti, H., Jiang, H., Lee S-Y., and Kooy, H. (2004). "Accurate Monte Carlo for nozzle design, commissioning, and quality assurance in proton therapy," *Med. Phys.* **31**, 2107-2118.

Paganetti, H., Bortfeld, T., and Delaney, T.F. (2006). "Neutron dose in proton radiation therapy: in regard to Eric, J. Hall (Int., J. Radiat. Oncol. Biol. Phys. 2006;65:1-7)," *Int. J. Radiat. Oncol. Biol. Phys.* **66,** 1594-5; author reply 5.

Paganetti, H., Jiang, H., Parodi, K., Slopsema, R., and Engelsman, M. (2008). "Clinical implementation of full Monte Carlo dose calculation in proton beam therapy," *Phys. Med. Biol.* **53,** 4825-4853.

Palm, A. and Johansson, K.A. (2007). "A.review of the impact of photon and proton external beam radiotherapy treatment modalities on the dose distribution in field and out-of-field; implications for the long-term morbidity of cancer survivors," *Acta. Oncol.* **46,** 462-473.

Parodi, K., Ferrari, A., Sommerer, F., and Paganetti, H., (2007). "Clinical CT-based calculations of dose and positron emitter distributions in proton therapy using the FLUKA Monte Carlo code," *Phys. Med. Biol*. **52**, 3369-3387.

Pedroni, E. *et al*. (2005). "The 200 MeV proton therapy project at the Paul Scherrer Institute: conceptual design and practical realization," *Med. Phys.* **22**, 37-53.

Pelliccioni, M. (2000). "Overview of fluence-to-effective dose and fluence-to-ambient dose equivalent conversion coefficients for high energy radiation calculated using the FLUKA Code," *Radiat. Prot. Dosim.* **88(4)**, 277-297.

Pelowitz, D.B., ed. (2005). "MCNPX User's Manual, Version 2.5.0," Los Alamos National Laboratory report, LA-CP-05-0369, http://mcnpx.lanl.gov (accessed 18 September 2009).

Perez-Andujar, A., Newhauser, W.D., and Deluca, P.M. (2009). "Neutron production from beam-modifying devices in a modern double scattering proton therapy beam delivery system," *Phys. Med. Biol.* **54,** 993-1008.

Petoussi-Henss, N., Zanki, M., Fill, U., and Regulla, D. (2002). "The GSF family of voxel phantoms," *Phys. Med. Biol.* **47,** 89-106.

Piegl, L. (1991). "On NURBS: A survey," *IEEE Computer Graphics and Applications* **11,** 55-71.

Pierce, D.A. and Preston, D.L. (2000). "Radiation-related cancer risks at low doses among atomic bomb survivors," *Radiat. Res.* **154,** 178-186.

Pierce, D.A., Shimizu, Y., Preston, D.L., Vaeth, M., and Mabuchi, K. (1996). "Studies of the mortality of atomic bomb survivors. Report 12, Part, I. Cancer: 1950-1990," *Radiat. Res.* **146,** 1-27.

Polf, J.C. and Newhauser, W.D. (2005). "Calculations of neutron dose equivalent exposures from range-modulated proton therapy beams," *Phys. Med. Biol.* **50,** 3859-3873.

Polf, J.C., Newhauser, W.D., and Titt, U., (2005). “Patient neutron dose equivalent exposures outside of the proton therapy treatment field,” *Radiat. Prot. Dosim.* **115**, 154–158.

Popova, I.I. (2005). ”MCNPX vs DORT for SNS shielding design studies,” *Radiat. Prot. Dosim.* **115**, 559-563.

Porta, A., Agosteo, S., and Campi, F. (2005). "Monte Carlo Simulations for the Design of the Treatment Rooms and Synchrotron Access Mazes in the CNAO Hadrontherapy Facility," *Rad. Prot. Dosim.* **113 (3)** 266-274.

Porta, A., Agosteo, S., Campi, F., and Caresana, M. (2008). “Double-differential spectra of secondary particles from hadrons on tissue equivalent targets,” *Radiat. Prot. Dosim.* **132 (1),** 29-41.

Potish, R.A., Dehner, L.P., Haselow, R.E., Kim, T.H., Levitt, S.H., and Nesbit, M. (1985). "The incidence of second neoplasms following megavoltage radiation for pediatric tumors," *Cancer* **56**, 1534-1537.

Preston, D.L., Shimizu, Y., Pierce, D.A., Suyama, A., and Mabuchi, K. (2003). "Studies of mortality of atomic bomb survivors. Report 13: Solid cancer and noncancer disease mortality: 1950-1997," *Radiat. Res.* **160,** 381-407.

Preston, D.L., Pierce, D.A., Shimizu, Y., Cullings, H.M., Fujita, S., Funamoto S, .and Kodama, K. (2004). "Effect of Recent Changes in Atomic Bomb Survivor Dosimetry on Cancer Mortality Risk Estimates," *Radiat. Res.* **162,** 377-389.

Pshenichnov, I., Mishustin, I., and Greiner, W. (2005). "Neutrons from fragmentation of light nuclei in tissue-like media: a study with the GEANT4 toolkit," *Phys. Med. Biol.* **50,** 5493-5507.

Pshenichnov, I., Larionov, A., Mishustin, I., and Greiner, W. (2007). “PET monitoring of cancer therapy with ^{3}He and ^{12}C beams: a study with the GEANT4 toolkit,” *Phys. Med. Biol.* **52**, 7295-7312.

PTCOG (2009). Particle Theory Co-Operative Group, http://www.psi.org.ch/ Accessed 4 May 09.

Raju, M.R. (1980). *Heavy Particle Radiotherapy*, (Academic Press, New York).

Reft, C.S., Runkel-Muller, R., and Myrianthopoulos, L. (2006). "In vivo and phantom measurements of the secondary photon and neutron doses for prostate patients undergoing 18 MV IMRT," *Med. Phys.* **33**, 3734-3742.

RIBF (2005). “Radiation safety assessment for RI Bean Factory,” Promotion Office of RI Beam Factory, Nishina Center for Accelerator-Based Science, RIKEN (Wako, Japan).

Ries, L.A.G., Eisner, M.P., Kosary, C.L., Hankey, B.F., Miller, B.A., Clegg, L., Mariotto, A., Fay, M.P., Feuer, E.J., Edwards, B.K., eds. (2003). *SEER Cancer Statistics Review*, *1975-2000*, http://seer.cancer.gov/csr/1975_2000/, accessed 20 September 2009 (National Cancer Institute. Bethesda, MD).

Ries, L.A.G., Harkins, D., Krapcho, M., Mariotto, A., Miller, B.A., Feuer, E.J. and *et al.* eds. (2006). *SEER cancer statistics review*, *1975-2003*, http://seer.cancer.gov/csr/1975_2003/, accessed 20 September 2009 (National Cancer Institute. Bethesda, MD).

Rijkee, A.G., Zoetelief, J., Raaijmakers, C.P., Van Der Marck, S.C. and Van Der Zee, W. (2006). "Assessment of induction of secondary tumours due to various radiotherapy modalities," *Radiat. Prot. Dosim.* **118,** 219-226.

Rinecker, H. (2005). *Protonentherapie – Neue Chance bei Krebs* ,(F.A. Herbig Verlagsbuchhandlung GmbH: Munich, Germany).

Rogers, J., Stabin, M., and Gesner, J., (2007). “Use of GEANT4 for Monte Carlo studies in voxel-based anthropomorphic models,” *J. Nucl. Med*. **48**, Suppl. 2, 295P.

Ron, E. (2006). "Childhood cancer--treatment at a cost," *J. Natl. Cancer Inst.* **98,** 1510-1511.

Ron, E. and Hoffmann, F.O. (1997). "Uncertainty in radiation dosimetry and their impact on dose-response analysis," *National Cancer Institute, National Institute of Health Workshop Proceedings.* 99-4541.

Ron, E., Modan, B., Boice, J.D., Alfandary, E., Stovall, M., Chetrit, A., and Katz, L. (1988). "Tumors of the brain and nervous system after radiotherapy in childhood," *N. Eng. J. Med.* **319,** 1033-1039.

Ron, E., Lubin, J.H., Shore, R.E., Mabuchi, K., Modan, B., Pottern, L.M., Schneider, A.B., Tucker, M.A., and Boice, J.D., Jr. (1995). "Thyroid cancer after exposure to external radiation:, a.pooled analysis of seven studies," *Radiat. Res.* **141,** 259-277.

Roy, S.C. and Sandison, G.A. (2004). "Scattered neutron dose equivalent to a fetus from proton therapy of the mother," *Radiat. Phys. Chem.* **71,** 997-998.

Ruth, T.J. and Wolf, A.P. (1979). "Absolute cross sections for the production of ^{18}F via the ^{18}O (p, n) ^{18}F peaction," *Radiochim. Acta.* **26**, 21-24.

Sadetzki, S., Flint-Richter, P., Ben-Tal, T., and Nass, D. (2002). "Radiation-induced meningioma: a descriptive study of 253 cases," *J. Neurosurg.* **97,** 1078-1082.

Sakamoto, Y., Sato, O., Tsuda, S., Yoshizawa, N., Iwai, S., Tanaka, S., and Yamaguchi, Y. (2003). "Dose conversion coefficients for high-energy photons, electrons, neutrons and protons," JAERI-1345 (Japan Atomic Energy Research Institute, Tokai).

Sasaki, S. and Fukuda, N. (1999). "Dose-response relationship for induction of solid tumors in female B6C3F1 mice irradiated neonatally with a single dose of gamma rays," *J. Radiat. Res. (Tokyo)* **40,** 229-241.

Sato, O., Yoshizawa, N., Takagi, S., Iwai, S., Uehara, T., Sakamoto, Y., Yamaguchi, Y., and Tanaka, S. (1999). "Calculations of effective dose and ambient dose equivalent conversion coefficients for high energy photons," *J. Nucl. Sci. Tech.*, **36**, 977-987.

Sato, T., Endo, A., Zankl, M., Petoussi-Henss, N., and Niita, K. (2009). "Fluence-to-dose conversion coefficients for neutrons and protons calculated using the PHITS code and ICRP/ICRU adult reference computational phantoms," *Phys. Med. Biol.* **54**, 1997-2014.

Schardt, D., Iwase, H., Simon, R.S., and Gunzert-Marx, K. (2006). "Experimental investigation of secondary fast neutrons produced in carbon ion radiotherapy," in *Proc. of the International*

Workshop on Fast Neutron Detectors and Applications, 3-6 April 2006, University of Cape Town, South Africa.

Scharf, W.H. and Wieszczycka, W. (2001). *Proton Radiotherapy Accelerators* (World Scientific Publishing Co., London, UK).

Schimmerling, W., Miller, J., Wong, M., Rapkin, M., Howard, J., Spieler, H.G., and Jarret, B.V. (1989). "The fragmentation of 670A MeV neon-20 as afunction of depth in water. I Experiment," *Radiat. Res.* **120,** 36-71.

Schippers, J.M. *et al.*, (2007). "The SC cyclotron and beam lines of PSI's new proton therapy facility PROSCAN," *NIM Phys. Res.* **B 261,** 773–776.

Schneider, U. and Kaser-Hotz, B. (2005). "Radiation risk estimates after radiotherapy: application of the organ equivalent dose concept to plateau dose-response relationships," *Radiat. Environ. Biophys.* **44,** 235-239.

Schneider, U., Agosteo, S., Pedroni, E., and Besserer, J. (2002). "Secondary neutron dose during proton therapy using spot scanning," *Int. J. Radiat. Oncol. Biol. Phys.* **53,** 244-251.

Schneider, U., Fiechtner, A., Besserer, J. and Lomax, A. (2004). "Neutron dose from prostheses material during radiotherapy with protons and photons," *Phys. Med. Biol.* **49,** N119-N24

Schneider, U., Lomax, A., Hauser, B. and Kaser-Hotz, B. (2006). "Is the risk for secondary cancers after proton therapy enhanced distal to the Planning Target Volume? A two-case report with possible explanations," *Radiat. Environ. Biophys.* **45**, 39-43.

Schneider, U., Lomax, A., Besserer, J., Pemler, P., Lombriser, N., and Kaser-Hotz, B. (2007). "The impact of dose escalation on secondary cancer risk after radiotherapy of prostate cancer," *Int. J. Radiat. Oncol. Biol. Phys.* **68,** 892-897.

Schottenfeld, D. and Beebe-Dimmer, J.L. (2006). "Multiple cancers," *Cancer epidemiology and prevention.* Schottenfeld, D. and Fraumeni, J.F., Jr., Eds., 1269-1280.

Schultz-Ertner, D. *et al.* (2004). "Results of Carbon Ion Radiotherapy in 152 Patients," *Int., J. Radiation Onc. Biol. Phys.* **58 (2)** 631-640.

Schwarz, R., (2008). “Graphical User Interface for High Energy Multi-Particle Transport,” http://www.mcnpvised.com, accessed 20 September 2009.

Segars, W.P (2001). "Development and application of the new dynamic NURBS-based cardiac-torso (NCAT) phantom.," Dissertation in Biomedical Engineering. (University of North Carolina, NC, USA).

Segars, W.P. and Tsui, B.M.W. (2002). "Study of the efficacy of respiratory gating in myocardial SPECT using the new 4-D NCAT phantom," *IEEE Transactions in Nuclear Science* **49,** 675-679.

Segars, W.P., Lalush, D.S., and Tsui, B.M.W. (1999). "A realistic spline-based dynamic heart phantom," *IEEE Transactions in Nuclear Science* **46,** 503-506.

Shamisa, A., Bance, M., Nag, S., Tator, C., Wong, S., Noren, G., and Guha, A. (2001). "Glioblastoma multiforme occurring in a patient treated with gamma knife surgery. Case report and review of the literature," *J. Neurosurg.* **94,** 816-821.

Shellabarger, C.J., Chmelevsky, D., and Kellerer, A.M. (1980). "Induction of mammary neoplasms in the Sprague-Dawley rat by 430keV neutrons and X-rays," *J. Natl. Cancer Inst.* **64,** 821-833.

Shi, C. and Xu, X.G. (2004). "Development of a 30-week-pregnant female tomographic model from computed tomography (CT) images for Monte Carlo organ dose calculations," *Med. Phys.* **31,** 2491-2497.

Shi, C.Y., Xu, X.G., and Stabin, M.G. (2004). "Specific absorbed fractions for internal photon emitters calculated for a tomographic model of a pregnant woman," *Health Phys.* **87,** 507-511.

Shin, K, Ono, S., Ishibashi, K., Meigo, S., Takada, H., Sasa, N., Nakashima, H., Tanaka, S., Nakao, N., Kurosawa, T., Nakamura, N., and Uwamino, Y. (1997). “Thick target yield measurements in Tiara, KEK and HIMAC,” in *Proc. Shielding Aspects of Accelerators, Targets and Irradiation Facilities (SATIF-3),* 12-13 May 1997, Tohoko University, Sendai, Japan (Nuclear Energy

Agency, Organization for Economic Co-operation and Development, Paris).

Shin, M., Ueki, K., Kurita, H., and Kirino, T. (2002). "Malignant transformation of a vestibular schwannoma after gamma knife radiosurgery," *Lancet* **360,** 309-310.

Siebers, J.V. (1990). "Shielding Measurements for a 230-MeV Proton Beam," Doctoral Thesis, Department of Med. Phys. (University of Wisconsin, Madison, WI).

Siebers, J.V., DeLuca, P.M., Pearson, D.W., and Coutrakon, G. (1992). "Measurement of Neutron Dose Equivalent and Penetration in Concrete for 230 MeV Proton Bombardment of Al, Fe and Pb Targets," *Radiat. Prot. Dosim.* **44 (1)**, 247-251.

Siebers, J.V., DeLuca, P.M., Pearson, D.W., and Coutrakon, G. (1993). "Shielding Measurements for 230-MeV Protons," *Nucl. Sci. and Eng.* **115**, 13-23.

Sigurdson, A.J., Ronckers, C.M., Mertens, A.C., Stovall, M., Smith, S.A., Liu, Y., Berkow, R.L., Hammond, S., Neglia, J.P., Meadows, A.T., Sklar, C.A., Robison, L.L., and Inskip, P.D. (2005). "Primary thyroid cancer after a first tumour in childhood (the Childhood Cancer Survivor Study): a nested case-control study," *Lancet* **365**, 2014-2023.

Simmons, N.E. and Laws, E.R., Jr. (1998). "Glioma occurrence after sellar irradiation: case report and review," *Neurosurgery* **42,** 172-178.

Sisterson, J.M., Brooks, F.D., Buffler, A. Allie, M.S., Jones, D.T.L., and Chadwick, M.B. (2005).”Cross-section measurements for neutron-induced reactions in copper at neutron energies of 70.7 and 110.8 MeV,” *NIM Phys. Res.* **B240**, 617-624.

Slater, J.M, Archambeau, J.O., Miller, D.W., Notarus, M.I., Preston, W., and Slater, J.D. (1991). "The Proton Treatment Center at Loma Linda University Medical Center: Rationale for and Description of its Development," *Int. J. Radiat. Oncol. Biol. Phys.* **22**, 383-389.

Smith, A.R. (2009). **“**Vision 20/20: Proton therapy,” *Med. Phys.* **36** (2), 556-568.

Snyder, W.S., Fisher, H.L., Jr., Ford, M.R., and Warner, G.G. (1969). "Estimates of absorbed fractions for monoenergetic photon sources uniformly distributed in various organs of a heterogeneous phantom," *J. Nucl. Med.* **10** (Suppl 3), 7-52.

Sobolevsky, N.M. (2008) “Multipurpose hadron transport code SHIELD,” http://www.inr.ru/shield, accessed 20 September 2009.

Sorge, H. (1995). "Flavor production in Pb (160A GeV.) on Pb collisions: Effect of color ropes and hadronic rescattering," *Phys. Rev.* C **52**, 3291-3314.

Spitzer, V.M. and Whitlock, D.G. (1998). "The Visible Human Dataset: the anatomical platform for human simulation," *Anat. Rec.* **253,** 49-57.

Stabin, M.G., Watson, E., Cristy, M., and *et al.* (1995). "Mathematical models and specific absorbed fractions of photon energy in the nonpregnant adult female and at the end of each trimester of pregnancy," **ORNL/TM-12907.**

Stabin, M.G., Yoriyaz, H., Brill, A.B., and Dawant, M. (1999). "Monte Carlo calculations of dose conversion factors for a new generation of dosimetry phantoms," *J. Nucl. Med.* **40,** 310-311.

Stapleton, G.B., O’Brien, K., and Thomas, R.H. (1994). "Accelerator skyshine: Tyger, tiger, burning bright," *Part. Accel.* **44.**

Staton, R.J., Pazik, F.D., Nipper, J.C., Williams, J.L., and Bolch, W.E. (2003). "A comparison of newborn stylized and tomographic models for dose assessment in paediatric radiology," *Phys. Med. Biol.* **48,** 805-820.

Stevenson, G.R. (1999). “The shielding of high-energy accelerators,” CERN-TIS-99-RP-CF8 (CERN, Geneva).

Stevenson, G.R. (2001). “Shielding high-energy accelerators,” *Radiat. Prot. Dosim.* **96,** 359-371.

Stevenson, G.R. and Thomas, R.H. (1984). "A simple procedure for the estimation of neutron skyshine from proton accelerators," *Health Phys.* **46**, 155.

Stichelbaut, F., Canon, T., and Yongen, Y. (2009). "Shielding Studies for a Hadron Therapy Center," in *Proc. of the ICRS-11 International Conference on Radiation Shielding and RPSD-2008 15th Topical Meeting of the Radiation Protection and Shielding Division of the ANS,* 13-18 April 2008 (Pine Mountain, Georgia, USA).

Stovall, M., Smith, S.A., and Rosenstein, M. (1989). "Tissue doses from radiotherapy of cancer of the uterine cervix," *Med. Phys.* **16,** 726-733.

Stovall, M., Donaldson, S.S., Weathers, R.E., Robison, L.L., Mertens, A.C., Winther, J.F., Olsen, J.H., and Boice, J.D., Jr. (2004). "Genetic effects of radiotherapy for childhood cancer: gonadal dose reconstruction," *Int. J. Radiat. Oncol. Biol. Phys.* **60,** 542-552.

Strong, L.C., Herson, J., Osborne, B.M. and Sutow, W.W. (1979). "Risk of radiation-related subsequent malignant tumors in survivors of Ewing's sarcoma," *J. Natl. Cancer Inst.* **62,** 1401-1406.

Suit, H., Goldberg, S., Niemierko, A., Ancukiewicz, M., Hall, E., Goitien, M., Wong, W., and Paganetti, H. (2007). "Secondary Carcinogenesis in Patients Treated with Radiation:, A.Review of Data on Radiation-Induced Cancers in Human, Non-human Primate, Canine and Rodent Subjects," *Radiat. Res.* **167,** 12-42.

Sullivan, A.H. (1992). *A Guide to Radiation and Radioactivity Levels Near High-Energy Particle Accelerators,* (Nuclear Technology Publishing, Kent, UK).

Sutton, M.R., Hertel, N.E., and Waters, L.S. (2000). “A high-energy neutron depth-dose experiment performed at the LANSCE/WNR facility,” pp. 231-240 in *Proc. 5th Meeting of the Task Force on Shielding Aspects of Accelerators, Targets and Irradiation Facilities*, Paris.

Taddei, P.J., Fontenot, J.D., Zheng, Y., Mirkovic, D., Lee, A.K., Titt, U., and Newhauser, W.D. (2008). "Reducing stray radiation dose to patients receiving passively scattered proton radiotherapy for prostate cancer," *Phys. Med. Biol.* **53** 2131-2147.

Taddei, P.J., Mirkovic, D., Fontenot, J.D., Giebeler, A., Zheng, Y., Kornguth, D., Mohan, R., and Newhauser, W.D. (2009). "Stray radiation dose and second cancer risk for a pediatric patient receiving craniospinal irradiation with proton beams," *Phys. Med. Biol.* **54,** 2259-2275.

Takacs, S., Tarkanyi, F., Hermanne, A., and Paviotti de Corcuera, R. (2003). “Validation and upgrade of the recommended cross section data of charged particle reactions used for production pet radioisotopes,” *NIM Phys. Res.* **B 211**, 169-189.

Tayama, R., Nakano, H., Handa, H., Hayashi, K., Hirayama, H., Shin, K., Masukawa, H., Nakashima, H., and Sasamoto, N. (2001). "DUCT-III: A simple Design Code for Duct-Streaming Radiations," KEK Internal Report (Tsukuba, Japan).

Tayama, R., Handa, H., Hayashi, H., Nakano, H., Sasmoto, N., Nakashima, H., and Masukawa, F. (2002). "Benchmark calculations of neutron yields and dose equivalent from thick iron target fro 52-256 MeV protons," *Nucl. Eng. and Design* **213**, 119-131.

Tayama, R., Hayashi, K., and Hirayama, H. (2004) "BULK-I Radiation Shielding Tool for Accelerator Facilities," KEK Internal, Report, NEA-1727/01 (Tsukuba, Japan).

Tayama, R., Fujita, Y., Tadokoro, M., Fujimaki, H., Sakae, T., and Terunuma, T. (2006). "Measurement of neutron dose distribution for apassive scattering nozzle at the Proton Medical Research Center (PMRC)," *NIM Phys. Res. A.* **564,** 532-536.

Teichmann, S. (2002) "Shielding Calculations for Proscan," *PSI – Scientific and Technical Report* **6,** 58-59.

Teichmann, S. (2006). "Shielding Parameters of Concrete and Polyethylene for the PSI Proton Accelerator Facilities," in *Proc. Shielding Aspects of Accelerators, Targets and Irradiation Facilities (SATIF 8),* 22-24 May 2006, Gyongbuk, Republic of Korea (Nuclear Energy Agency, Organization for Economic Co-operation and Development, Paris).

Tesch, K. (1982) "The attenuation of the neutron dose equivalent in a labyrinth through an accelerator shield," *Part. Accel.*, **12 (N 3),** 169-175.

Tesch, K. (1985). “A simple estimation of the lateral shielding for proton accelerators in the energy range 50 to 1000 MeV,” *Radiat. Prot. Dosim.* **11(3),** 165-172.

Theis, C., Buchegger, K.,H., Brugger, M., Forkel-Wirth, D., Roesler, S., and Vincke, H., (2006). “Interactive three dimensional visualization and creation of geometries for Monte Carlo calculations,” *NIM Phys. Res. A* **562,** 827-829, http://theis.web.cern.ch/theis/simplegeo/, accessed 20 September 2009.

Thomas, R.H. (1993). “Practical Aspects of Shielding High-Energy Particle Accelerators,” Report UCRL-JC-115068 (U.S. Department of Energy, Washington DC).

Titt, U., and Newhauser, W.D. (2005). “Neutron shielding calculations in a proton therapy facility based on Monte Carlo simulations and analytical models: criterion for selecting the method of choice,” *Radiat. Prot. Dosim.* **115**, 144–148.

Tsoulfanidis, N. (1995). *Measurement and Detection of Radiation*, (Hemisphere Publishing, Washington, D.C.)

Tsui, B.M.W., Zhao, X.D., Gregoriou, G.K., and *et al.* (1994). "Quantitative cardiac SPECT reconstruction with reduced image degradation due to patient anatomy," *IEEE Transactions in Nuclear Science* **41,** 2838-2844.

Tubiana, M. (2005). "Dose-effect relationship and estimation of the carcinogenic effects of low doses of ionizing radiation: the joint report of the Academie des Sciences (Paris) and of the Academie Nationale de Medecine," *Int. J. Radiat. Oncol. Biol. Phys.* **63,** 317-319.

Tubiana, M. (2009). "Can we reduce the incidence of second primary malignancies occurring after radiotherapy? A critical review," *Radiother. Oncol.* **91,** 4-15, discussion 1-3.

Tubiana, M., Feinendegen, L.E., Yang, C., and Kaminski, J.M. (2009). "The linear no-threshold relationship is inconsistent with radiation biologic and experimental data," *Radiology* **251,** 13-22.

Tucker, M.A., Meadows, A.T., Boice, J.D., Jr., and *et al.* (1984). "Cancer risk following treatment of childhood cancer," *Radiation carcinogenesis: Epidemiology and biological significance.* Boice, J.D., Jr., and Fraumeni, J.F., Jr., Eds. 211-224.

Tucker, M.A., D'Angio, G.J., Boice, J.D., Jr., Strong, L.C., Li, F.P., Stovall, M., Stone, B.J., Green, D.M., Lombardi, F., Newton, W., and *et al.* (1987). "Bone sarcomas linked to radiotherapy and chemotherapy in children," *N. Engl. J. Med.* **317** 588-593.

Tujii, H., Akagi, T., Akahane, K., Uwamino, Y., Ono, T., Kanai, T., Kohno, R., Sakae, T., Shimizu, M., Urakabe, E., Nakayama, T., Nakamura, T., Nishio, T., Nishizawa, Ka., Nishizawa, Ku., Fukuda, S., Matsufuji, N., Yamashita, H., and Yonai, S. (2009). "Research on radiation protection in the application of new technologies for proton and heavy ion radiotherapy," *Jpn., J. Med. Phys.*, **28**, 172-206.

Turner, J.E. (1986). *Atoms, Radiation, and Radiation Protection*, (Pergamon Press, New York).

Ueno, A.M., Vannais, D.B., Gustafson, D.L., Wong, J.C., and Waldren, C.A. (1996). "A low, adaptive dose of gamma-rays reduced the number and altered the spectrum of S1-mutants in human-hamster hybrid AL cells," *Mutat. Res.* **358,** 161-169.

Ullrich, R.L. (1980). "Effects of split doses of x rays or neutrons on lung tumor formation in RFM mice," *Radiat. Res.* **83,** 138-145.

Ullrich, R.L. and Davis, C.M. (1999). "Radiation-induced cytogenetic instability in vivo," *Radiat. Res.* **152,** 170-173.

Ullrich, R.L., Jernigan, M.C., Satterfield, L.C., and Bowles, N.D. (1987). "Radiation carcinogenesis: time-dose relationships," *Radiat. Res.* **111,** 179-184.

Upton, A.C. (2001). "Radiation hormesis: data and interpretations," *Crit. Rev. Toxicol.* **31,** 681-695.

USNRC (2009). United States Nuclear Regulatory Commission, *Standards for Protection Against Radiation 10CFR20, Code of Federal Regulations*, www.nrc.gov/reading-rm/doc-collections/cfr/part020/, accessed 18 September 2009.

Uwamino, Y. (2007) personal communication, RIKEN, Safety Management Group (RIKEN, Japan).

Uwamino, Y. and Nakamura, T. (1985). “Two types of multi-moderator neutron spectrometers: gamma-ray insensitive type and high-efficiency type,” *NIM Phys. Res.* **A239**, 299-309.

Uwamino, Y., Fujita, S., Sakamoto, H., Ito, S., Fukunishi, N., Yabutani, T., Yamano, T., and Fukumura, A. (2005). “Radiation protection system at the Riken RI Beam Factory,” *Radiat. Prot. Dosim.*, **115**, 279-283.

van Leeuwen, F.E. and Travis, L.B. (2005). "Second cancers," *Cancer: Principles and practice of oncology, 7th edition.* Devita, V.T. *et al.* (Eds.) 2575-2602.

Verellen, D. and Vanhavere, F. (1999). "Risk assessment of radiation-induced malignancies based on whole-body equivalent dose estimates for IMRT treatment in the head and neck region," *Radiother. Oncol.* **53,** 199-203.

Vlachoudis, V., (2009). “FLAIR: FLUKA Advanced Interface,” http://www.fluka.org/flair/, accessed 20 September 2009.

Wang, Q.B., Masumoto, K., Bessho, K., Matsumura, H., Miura, T., and Shibata, T. (2004). “Tritium activity induced in the accelerator building and its correlation to radioactivity of gamma-nuclides,” *Journal of Radioanalytical and Nuclear Chemistry*, **262**, 587–592.

Weber, U. (2007). "The Particle Therapy Centre of Rhön Klinikum AG at the University Hospital Marburg," pp. 242-243 in *Ion Beams in Biology and Medicine, 39. Annual Conference of the German-Swiss Association for Radiation Protection and 11th Workshop of Heavy Charged Particles in Biology and Medicine* (IRPA Fachverband für Strahlenschutz, Switzerland and Germany).

White, R.G., Raabe, O.G., Culbertson, M.R., Parks, N.J., Samuels, S.J., and Rosenblatt, L.S. (1993). "Bone sarcoma characteristics and distribution in beagles fed strontium-90," *Radiat. Res.* **136,** 178-189.

Wiegel, B. and Alevra, A.V. (2002). “NEMUS – the PTB neutron multisphere spectrometer: Bonner spheres and more,” *NIM Phys. Res.* **A476**, 36-41.

Wolff, S. (1998). "The adaptive response in radiobiology: evolving insights and implications," *Environ. Health Perspect.* **106 (Suppl 1),** 277-283.

Wood, D.H. (1991). "Long-term mortality and cancer risk in irradiated rhesus monkeys," *Radiat. Res.* **126,** 132-140.

Wroe, A., Rosenfeld, A., and Schulte, R. (2007). "Out-of-field dose equivalents delivered by proton therapy of prostate cancer," *Med. Phys.* **34**, 3449-3456.

Wroe, A., Clasie, B., Kooy, H., Flanz, J., Schulte, R., and Rosenfeld, A. (2009). "Out-of-field dose equivalents delivered by passively scattered therapeutic proton beams for clinically relevant field configurations," *Int. J. Radiat. Oncol. Biol. Phys.* **73,** 306-313.

Xu, X.G., Chao, T.C., and Bozkurt, A. (2000). "VIP-MAN: an image-based whole-body adult male model constructed from color photographs of the Visible Human Project for multi-particle Monte Carlo calculations," *Health Phys.* **78,** 476-485.

Xu, X.G., Chao, T.C., and Bozkurt, A. (2005). "Comparison of effective doses from various monoenergetic particles based on the stylised and the VIP-Man tomographic models," *Radiat. Prot. Dosim.* **115,** 530-535.

Xu, X.G., Taranenko, V., Zhang, J., and Shi, C. (2007). "A boundary-representation method for designing whole-body radiation dosimetry models: pregnant females at the ends of three gestational periods—RPI-P3, -P6 and -P9," *Phys. Med. Biol.* **52,** 7023-7044.

Xu, X.G., Bednarz, B., and Paganetti, H. (2008). "A Review of Dosimetry Studies on External-Beam Radiation Treatment with Respect to Second Cancer Induction," *Phys. Med. Biol.* **53,** R193-R241.

Yan, X., Titt, U., Koehler, A.M., and Newhauser, W.D, (2002). "Measurement of neutron dose equivalent to proton therapy patients outside of the proton radiation field," *NIM Phys. Res.* **A 476,** 429-434.

Yashima, H., Uwamino, Y., Sugita, H., Nakamura, T., Ito, S., and Fukumura, A. (2002). ”Projectile dependence of radioactive spallation products induced in copper by high-energy heavy ions,“ *Phys. Rev*. **C66**, 044607-1 to 11.

Yashima, H., Uwamino, Y., Iwase, H., Sugita, H., Nakamura, T., Ito, S., and Fukumura, A. (2003). “Measurement and calculation of radioactivities of spallation products by high-energy heavy ions,” *Radiochim. Acta*, **91**, 689-696.

Yashima, H., Uwamino, Y., Iwase, H., Sugita, H., Nakamura, T., Ito, S., and Fukumura, A. (2004a). “Cross sections for the production of residual nuclides by high-energy heavy ions,” *NIM Phys. Res.* **B226**, 243-263.

Yashima, H., Uwamino, Y., Sugita, H., Ito, S., Nakamura, T., and Fukumura, A. (2004b). “Induced radioactivity in Cu targets produced by high-energy heavy ions and the corresponding estimated photon dose rates,” *Radiat. Protec. Dosim.* **112**, 195-208.

Yonai, S., Matsufuji, N., Kanai, T., Matsui, Y., Matsushita, K., Yamashita, H., Numano, M., Sakae, T., Terunuma, T., Nishio, T., Kohno, R., and Akagi, T. (2008). "Measurement of neutron ambient dose equivalent in passive carbon-ion and proton radiotherapies," *Med. Phys.* **35**, 4782-4792.

Yu, J.S., Yong, W.H., Wilson, D., and Black, K.L. (2000). "Glioblastoma induction after radiosurgery for meningioma," *Lancet* **356**, 1576-1577.

Zacharatou Jarlskog, C. and Paganetti, H. (2008a). "Sensitivity of different dose scoring methods on organ specific neutron doses calculations in proton therapy," *Phys. Med. Biol.* **53,** 4523-4532.

Zacharatou Jarlskog, C. and Paganetti, H. (2008b). "The risk of developing second cancer due to neutron dose in proton therapy as a function of field characteristics, organ, and patient age," *Int. J. Radiat. Oncol. Biol. Phys.* **69,** 228-235.

Zacharatou Jarlskog, C., Lee, C., Bolch, W., Xu, X.G., and Paganetti, H. (2008). "Assessment of organ specific neutron doses in proton therapy using whole-body age-dependent voxel phantoms," *Phys. Med. Biol.* **53,** 693-714.

Zaidi, H. and Xu, X.G. (2007). "Computational anthropomorphic models of the human anatomy: the path to realistic monte carlo modeling in radiological sciences," *Ann. Rev. Biomed. Eng.* **9,** 471-500.

Zankl, M., Veit, R., Williams, G., Schneider, K., Fendel, H., Petoussi, N., and Drexler, G. (1988). "The construction of computer tomographic phantoms and their application in radiology and radiation protection," *Radiat. Environ. Biophys.* **27,** 153-164.

Zhang, G., Liu, Q., Zeng, S., and Luo, Q. (2008). "Organ dose calculations by Monte Carlo modeling of the updated VCH adult male phantom against idealized external proton exposure," *Phys. Med. Biol.* **53**, 3697-3722.

Zheng, Y., Newhauser, W., Fontenot, J., Taddei, P., and Mohan, R. (2007). "Monte Carlo study of neutron dose equivalent during passive scattering proton therapy," *Phys. Med. Biol.* **52**, 4481-4496.

Zheng, Y., Fontenot, J., Taddei, P., Mirkovic, D., and Newhauser, W. (2008). "Monte Carlo simulations of neutron spectral fluence, radiation weighting factor and ambient dose equivalent for a passively scattered proton therapy unit," *Phys. Med. Biol.* **53,** 187-201.

Zubal, I.G. and Harell, C.H. (1992). "Voxel based Monte Carlo calculations of nuclear medicine images and applied variance reduction techniques," *Image and Vision Computing* **10,** 342-348.